

DISSERTATION

MALDI Mass Spectrometric Imaging - Aspects of Sample Preparation

ausgeführt zum Zwecke der Erlangung des akademischen Grades eines

Doktors der technischen Wissenschaften

Unter der Leitung von

Assoc. Prof. Dr. Martina Marchetti-Deschmann

IAC-164

Institute of Chemical Technologies and Analytics

eingereicht an der Technischen Universität Wien

Fakultät für Technische Chemie

von

DI Matthias Holzlechner

0640751

Wien, Mai 2018

Diese Dissertation haben begutachtet:

Univ. Prof. Dr. Gunda Köllensperger
Universität Wien

Ao. Univ. Prof. Dr. Herbert Hutter
Technische Universität Wien

Name des Kandidaten: DI Matthias Holzlechner
Namen der PrüferInnen: Assoc. Prof. Dr. Martina Marchetti-Deschmann
Univ. Prof. Dr. Gunda Köllensperger
Titel der Dissertation: MALDI mass spectrometric imaging - aspects of sample preparation.

Zusammenfassung:

Der Schwerpunkt der vorgelegten Dissertation liegt in der optimierten Probenpräparation von Rohgewebeproben für die bildgebende matrix-unterstützte Laser Desorptions/Ionisations Massenspektrometrie (MALDI MSI). Um qualitativ hochwertige MSI-Analysen zu gewährleisten, muss die Gewebeintegrität erhalten bleiben. Mit anderen Worten, die Analyten müssen in den Gewebeproben exakt lokalisiert bleiben, während die Empfindlichkeit der Messung durch optimierte Einbettung von Molekülen in die MALDI-Matrixkristalle erhöht wird.

Eine der Haupteinschränkungen und -herausforderungen in MALDI MSI ist die räumliche Auflösung. Matrixkristalle, die kleiner als der emittierte Laserstrahl sind, stellen einen Schlüsselparameter für eine Mikrometerauflösung in MALDI MSI dar. In der vorgelegten Dissertation wird eine selbstgebaute Sublimationsapparatur vorgestellt, die eine optimierte Matrixapplikation mit kleinen Kristallgrößen für verschiedene gängige Matrices ermöglicht. Sublimationsbedingungen für hochvakuumstabile MALDI-Matrices wurden für eine quantitative Sublimation etabliert und in Kombination mit einem verbesserten Matrix-Rekristallisationsverfahren konnte eine Standardisierung des Matrixauftrages sowie eine einfache Handhabung erreicht werden. Eine umfassende, theoriegeleitete Studie zur Reproduzierbarkeit und Homogenität des Auftrages sowie zur Matrixkristallisation, die von unterschiedlichen Oberflächen, Kühltemperaturen und Rekristallisation beeinflusst wird, wird vorgestellt.

Die Implementierung des neu entwickelten Matrix-Sublimations- / Rekristallisationsprozesses in MSI führte zu einer schnellen und robusten Probenvorbereitungsstrategie, geeignet für verschiedene Probentypen. Folgenden Projekte profitierten wesentlich von der entwickelten Methodik: (a) Sekundärmetaboliten, freigesetzt von *Rhizoctonia solani* und *Trichoderma atroviride* während Mykoparasit-Wirt-Wechselwirkungen, wurden direkt auf Kultivierungsmedien untersucht, (b) Immunzellansammlungen wurden in humanem Kolongewebe visualisiert und mehrere proteinartige Marker spezifischen Kolonstrukturen zugeordnet, (c) humane, bösartige Pleuramesotheliom (MPM) -proben von einem mit Cisplatin als Zytostatikum behandelten Patienten wurden analysiert. Letzteres Projekt diente dazu, die Methodik an ihre Grenzen zu bringen. In einem multimodalen Bildgebungsverfahren (MMI), das zwei komplementäre MSI-Modalitäten kombiniert, nämlich Laserablation mit einem induktiv gekoppelten Plasma als Ionenquelle für die Massenspektrometrie (LA-ICP-MS) und MALDI MS, konnte ein Maximum an Information von einem einzelnen Gewebeschnitt erfasst werden. Die entwickelte Strategie zur Probenvorbereitung ermöglichte die Erzeugung von Bildern durch MALDI MSI, die die Verteilung von Lipidspezies zeigen, die vorzugsweise im positiven oder negativen Ionenmodus gemessen werden können. Ein Arbeitsablauf wurde entwickelt, der MALDI MSI und LA-ICP-MSI Daten mit fortgeschrittener statistischer Analyse kombiniert, um vollständige Informationen über Lipidverteilungen und Quantifizierung von Elementen mit Fokus auf Phosphor und Platin zu liefern.

Abstract:

The focus of the present thesis lies on optimized sample preparation of raw tissue samples for matrix-assisted laser desorption/ionization mass spectrometric imaging (MALDI MSI). For high quality MSI analyses tissue integrity has to be preserved. In other words, analytes have to be kept correctly localized within the tissue samples while increasing the sensitivity of the measurement by optimized embedding of molecules in the MALDI matrix crystals.

One of the major limitations and main challenges in MALDI MSI is spatial resolution. Matrix crystals being smaller than the emitted laser beam are one key parameter for micrometer-resolution in MALDI MSI. In the present thesis an in-house built sublimation apparatus is introduced allowing for optimized matrix application exhibiting small crystal sizes for various commonly used matrices. Sublimation conditions for high-vacuum stable MALDI matrices were established for quantitative sublimation and in combination with an enhanced matrix recrystallization process, standardization of matrix application and ease of handling was achieved. A comprehensive, theory-driven study on deposition reproducibility and homogeneity as well as matrix crystallization affected by differing surfaces, cooling temperatures and recrystallization is presented. Implementation of the newly developed matrix sublimation/recrystallization process in MSI led to a quick and robust sample preparation strategy suitable for various sample types. The following projects essentially benefited from the developed methodology: (a) secondary metabolites released during mycoparasite-host interactions of *Rhizoctonia solani* and *Trichoderma atroviride* were studied directly from cultivation media, (b) immune cell accumulations in human colon tissue were visualized and several proteinaceous markers for specific colon structures could be identified, (c) human malignant pleural mesothelioma (MPM) samples from a patient treated with cisplatin as cytostatic agent were analyzed. The latter project was key to test the methodology for its limits. In a multi-modal imaging (MMI) approach that combined two complementary MSI modalities, namely laser ablation inductively coupled plasma mass spectrometry (LA-ICP-MS) and MALDI MS, maximum information was gathered from a single tissue section. The developed sample preparation strategy allowed to generate images by MALDI MSI showing lipid distribution of species preferentially measured in positive or negative ion mode. A workflow combining MALDI MSI and LA-ICP-MSI data in combination with advanced statistical analysis was also developed to provide full information on lipid distributions and quantification of elements, with a focus on phosphorus and platinum.

Für Magdalena (03.07.2017)*

TABLE OF CONTENTS

1	MASS SPECTROMETRIC IMAGING	1
	I General Remarks and Thesis Outline	4
	A Sample Acquisition and Prehandling: Raw Tissue	5
	I Embedding of Tissue	5
	II Sectioning of Tissue	6
	III Mounting of Tissue Sections	7
	IV Washing of Tissue Sections To Remove Salt and Other Interferences	7
	V Specific Molecular Modifications	9
	<i>Formalin Fixation of Tissue</i>	9
	<i>Chemical Staining of Tissue Sections</i>	9
	<i>On-tissue Digestion</i>	11
	<i>Chemical Derivatization</i>	12
	B MALDI Matrix Choice and Application	13
	I Solvent-based Matrix Application	13
	<i>Chemical Printers</i>	14
	<i>Manual Spraying</i>	14
	<i>Automated Spraying</i>	15
	II Solvent-free Matrix Application	16
	<i>Sublimation</i>	16
	C Mass Analyzers in MALDI MSI	19
	D Data Analysis	20
2	METHODOLOGICAL CONSIDERATIONS	22
	A Spatial Resolution	22
	B Surface Morphology & Sample Complexity	23

C	On-tissue Identification	24
D	Throughput	25
E	Ion Suppression Effects	26
F	Normalization	26
G	Quantitative MALDI MSI	28
	I Incorporation of Internal Standards	28
	II Relative Quantitation	28
	III Absolute Quantitation	29
H	Multi-modal Imaging	30
	REFERENCES	32
3	SUMMARY OF RESULTS	44
4	SUBLIMATION APPARATUS TO PUSH MALDI MS IMAGING BELOW THE CELLULAR LEVEL	54
5	VISUALIZING FUNGAL METABOLITES DURING MYCOPARASITIC INTERACTION BY MALDI MASS SPECTROMETRY IMAGING	77
6	IN SITU CHARACTERIZATION OF TISSUE-RESIDENT IMMUNE CELLS BY MALDI MASS SPECTROMETRY IMAGING	92
7	MULTI-SENSOR IMAGING– FROM SAMPLE PREPARATION TO INTEGRATED MULTI-MODAL INTERPRETATION OF LA-ICP-MS AND MALDI MS IMAGING DATA	136
8	PHOSPHONATE COATING OF SiO₂ NANOPARTICLES ABROGATES INFLAMMATORY EFFECTS AND LOCAL CHANGES OF THE LIPID COMPOSITION IN THE RAT LUNG: A COMPLEMENTARY BIOIMAGING STUDY	175
	ABBREVIATIONS	207
	CURRICULUM VITAE	209

LIST OF FIGURES

Figure 1: Simplified representation of a MALDI MSI workflow - from tissue section to the visualization of selected ions.	2
Figure 2: Selected ion distributions exhibit no visible analyte delocalization at a spatial resolution of 10 μm .	3
Figure 3: Direct comparison of 2 washing procedures applied to visualize peptides/proteins in human colon tissue.	8
Figure 4: Post-MSI H&E stain of (A) a horizontal mouse brain section and (B) a sagittal rat brain section.	10
Figure 5: Comparison of solvent-based (airbrush) and solvent-free (sublimation) matrix application.	16
Figure 6: Subsequent recrystallization of sublimed surfaces on human colon tissue sections.	17
Figure 7: Sublimation and influence of recrystallization on ion signals of selected lipids.	18
Figure 8: Influence of varying lateral resolutions on a horizontal mouse brain tissue section.	22
Figure 9: TIC normalization compensating for a gradual decrease in ion transmission during 10 h of image acquisition.	27
Figure 10: <i>Sublimation Apparatus to Push MALDI MS Imaging Below the Cellular Level</i> , graphical abstract.	44
Figure 11: <i>Visualizing Fungal Metabolites During Mycoparasitic Interaction bay MALDI Mass Spectrometry Imaging</i> , graphical abstract.	46
Figure 12: <i>In Situ Characterization of Tissue Resident Immune Cells by MALDI Mass Spectrometry Imaging</i> , graphical abstract.	48
Figure 13: <i>Multi-Sensor Imaging – from Sample Preparation to Integrated Multi-Modal Interpretation pf LA-ICP-MS and MALDI MS Imaging Data</i> , graphical abstract.	50
Figure 14: <i>Phosphonate Coating of SiO₂ Nanoparticles Abrogates Inflammatory Effects and Local Changes of the Lipid Composition in the Rat Lung: A Complementary Bioimaging Study</i> , graphical abstract.	52

1 **MASS SPECTROMETRIC IMAGING**

Mass spectrometric imaging (MSI) is a powerful imaging technique for visualizing the spatial distribution of chemical components in samples, from inorganic to organic materials. MSI is a label-free technique and enables to monitor thousands of compounds in a single experiment¹⁻³. Owing to its unique characteristics, especially the non-targeted detection of analytes, MSI has been rapidly and continuously developed to meet the expectations and needs of various research areas. The most relevant mass spectrometry techniques for molecular and elemental imaging currently are MALDI MS (matrix-assisted laser desorption/ionization mass spectrometry), DESI MS (desorption electrospray ionization mass spectrometry), SIMS (secondary ion mass spectrometry), and LA-ICP-MS (laser ablation inductively coupled plasma mass spectrometry).

Among the several mass spectrometric ionization techniques that can be used to directly analyze tissues, MALDI has led the way in the development of biological and clinical applications for MSI and is therein one of the most commonly used techniques⁴⁻⁹. By using appropriate sample preparation for biological samples, distributional information on a wide range of molecules, e.g., metabolites, glycans, lipids, or proteins can be recorded *in situ*. These biomolecules are essential components that control both the structural and functional behavior of every cell within every tissue of a living organism, making MALDI MSI a promising discovery tool.

MALDI is based on the application of a matrix on the top of the sample, facilitating co-crystallization of matrix and analytes. Herein, the MALDI matrix must be capable of strongly absorbing the photon energy emitted by the laser pulse to promote efficient desorption and subsequent ionization of analytes¹⁰ (detailed reviews of the mechanisms of MALDI can be found elsewhere¹¹⁻¹⁴). Commercially available lasers include pulsed nitrogen (N₂, $\lambda = 337$ nm), frequency tripled neodymium-doped yttrium aluminum garnet (Nd:YAG, $\lambda = 355$ nm) and neodymium-doped yttrium lithium fluoride (Nd:YLF, $\lambda = 349$ nm) lasers for UV radiation.

Figure 1 depicts the MALDI MSI workflow in a simplified manner. In principal, a frozen tissue is cut in sections, mounted on target plates suitable for MALDI, and homogeneously covered with matrix. Next, a laser beam is rastering spot-by-spot over a defined surface area, thereby desorbing/ionizing analytes that are subsequently extracted into the mass spectrometer for analysis. Images of single ions are then generated with the relative abundances displayed as a false color image across the analyzed region of interest (ROI)¹⁵.

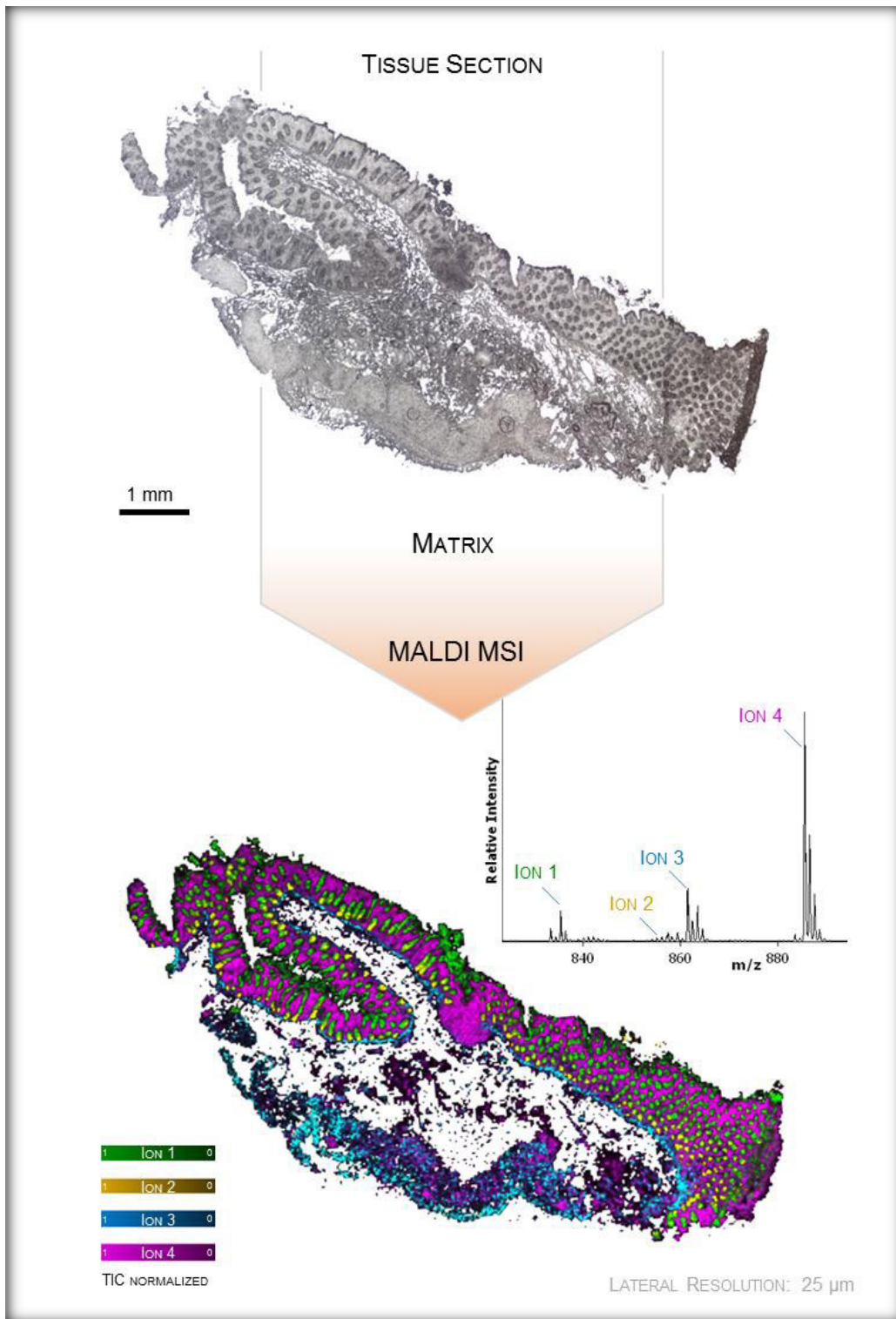


Figure 1: Simplified representation of a MALDI MSI workflow - from tissue section to the visualization of selected ions. Sublimation of 1,5-DAN (0.24 mg/cm²), negative ion mode (reflectron geometry), 100 shots/spot, 48354 spots. Data is normalized to the total ion current.

As with any methodology, one of the most crucial steps for analytical success is proper sample preparation. In MSI experiments, sample preparation aims to generate reliable data directly from tissue sections. The structural integrity and morphology of the tissue must be maintained from the time of sample collection and pre-handling until analysis without delocalization and degradation of the analytes of interest. In other words, the chemical distribution image must resemble the original biological state *in situ* as accurate as possible (Figure 2). The sample handling must be consequently optimized regarding the characteristics of the MSI instrument, the nature of the sample and the analytes of interest. Herein, one has to keep in mind that “*small mistakes can lead to big consequences*”¹⁶. Thus, a considerable number of excellent overview papers have been published that discuss the different sample preparation approaches and possibly occurring problems^{5, 17-21}.

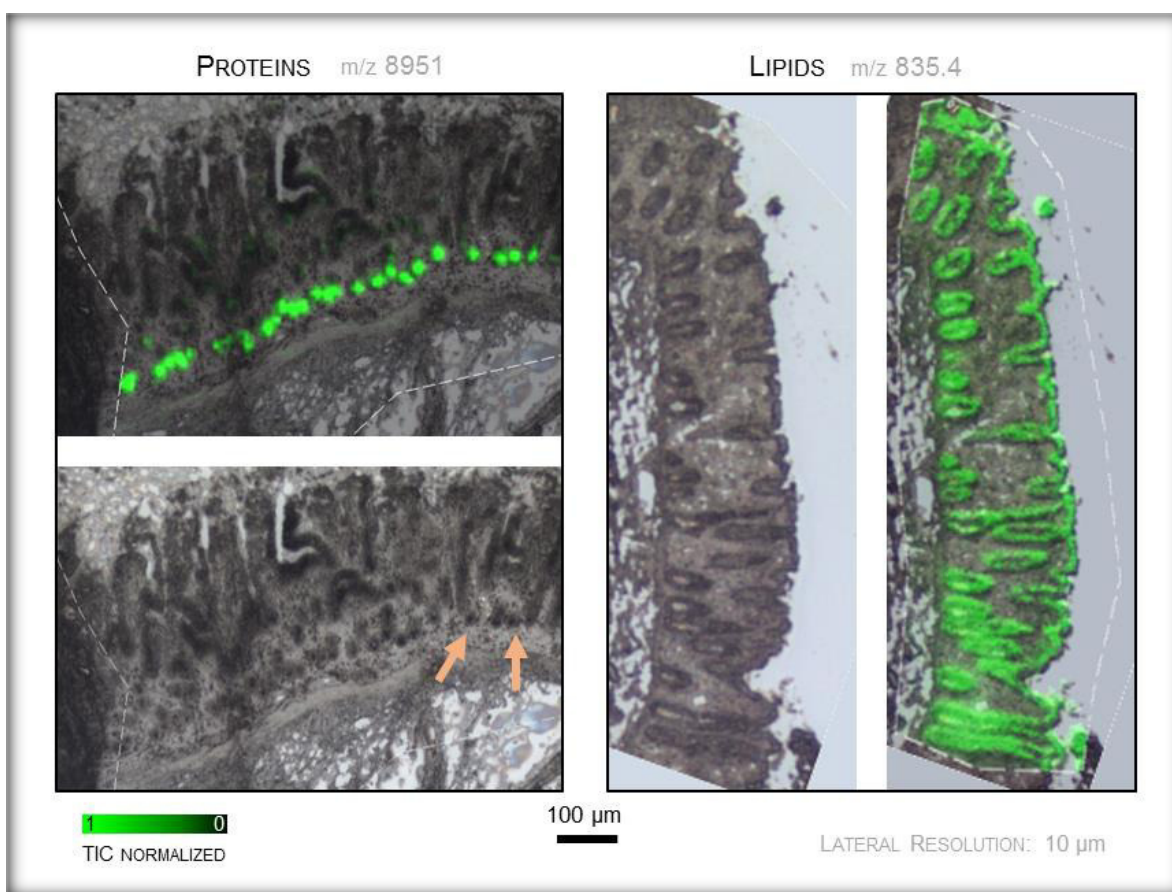


Figure 2: Selected ion distributions exhibit no visible analyte delocalization at a spatial resolution of 10 μm . Proteins: sublimation of SA (0.25 mg/cm^2) and recrystallization with 5% AcOH (3.8 min), positive ion mode (linear geometry). Lipids: sublimation of 1,5-DAN (0.24 mg/cm^2) and recrystallization with 5% AcOH (1 min), negative ion mode (reflectron geometry). For further information on sublimation and recrystallization refer to *chapter 4, p. 54*.

Several factors are critical for successful sample preparation in MSI, ranging from sample collection and storage, sectioning and mounting to the selection and application of the appropriate matrix¹⁶. MALDI matrix application is one of the main challenges as it directly affects the attainable spatial resolution. Consequently, in MALDI MSI, most of the focus for sample preparation has been on the matrix application process. Particularly matrix crystal size and application consistency^{16, 22-23} prove difficult to reach subcellular resolution, i.e., imaging at a lateral resolution below 10 μm . Thus, matrix application strategies providing highly reproducible matrix depositions along with crystals being significantly smaller in diameter than both the laser spot and the single cell are mandatory for MALDI MSI below the cellular level. The matrix deposition technique has to be carefully considered with respect to the investigated molecules and the spatial resolution desired¹⁹. Matrix preparation must produce a uniform coating of crystals with sufficient amount and density to permit sampling of the surface without having regions that are absent of signal. Most important, the localization of the analytes of interest throughout the tissue must be conserved. Furthermore, the best matrix application method would provide appropriate analyte extraction without any lateral diffusion, small crystal sizes, as well as homogeneous application. Unfortunately, to date no universal method exists and matrix deposition must be optimized in function of the objective of the analysis.

MALDI MSI has several limitations, some of which are inherent in the LDI process and others in the performance of instrumentation. Besides tissue heterogeneity and sample topography, one of the inherent limitations is the ion suppression effect that hampers direct quantitation from a tissue section, demanding for sophisticated quantitation strategies. A further limitation is the laser spot size and the trade-off between image resolution and sensitivity. The smaller the spot size the less material is desorbed/ionized, significantly decreasing signal intensity.

I GENERAL REMARKS AND THESIS OUTLINE

Rodent brain tissue remains the most commonly analyzed tissue type in MSI because of its wide availability²⁴⁻²⁵ and was used as specimen for method development throughout the whole thesis.

All MALDI experiments have been performed using a TOF/RTOF mass spectrometer from Bruker (ultrafleXtreme™). If not otherwise stated, tissue sections were prepared at a thickness of 10 μm and imaging data are normalized to the total ion current.

Chapter 1 gives a brief overview of MSI and discusses sample preparation for MALDI MS imaging with focus on fresh frozen tissue, pretreatment of tissue sections, and MALDI matrix application. Optional chemical and molecular tissue modifications are briefly overviewed but not discussed in detail, as they were not of special interest for this thesis. Specific issues of mass analyzers and data analysis in MALDI MSI are also discussed in this chapter. **Chapter 2** provides specific methodological considerations for MALDI MSI. **Chapter 3** summarizes all manuscripts published and drafted during this thesis. These manuscripts and articles are provided in **Chapter 4, 5, 6, 7, and 8**.

A SAMPLE ACQUISITION AND PREHANDLING: RAW TISSUE

Sample collection and treatment procedures need to be sufficiently fast in order to prevent tissue degradation²⁶. Subsequent stabilization/fixation steps are necessary to keep the morphology and analytes preserved²⁷. So, time is a critical factor to protect samples from potential endogenous enzymatic degradation²⁸⁻³¹.

The most common and fastest stabilization method is snap-freezing by exposing the tissue to a cryogen such as liquid nitrogen, liquid isopentane or a dry ice-solvent (e.g., ethanol/hexane)^{19, 32-33}. Immediate freezing of tissue samples after dissection minimizes tissue degradation as well as oxidation of biomolecules³⁴⁻³⁵.

Generally, rapid plunging of the tissue into cryogenic solutions should be avoided as the freezing process can lead to sample cracking and tattering as different parts of the tissue cool down at different rates. Instead, depending on the nature of the tissue and the feasibility, the sample should be wrapped in loose foil (e.g., aluminum) and gently floated or immersed in the cryogenic solution to prevent tissue damage^{26, 36}. Additional care must be taken to avoid deformation of the tissue by the freezing container. Another promising approach applied is tissue freezing on a dry-ice chilled steel plate. However, freezing must be rapid as too long freezing times may induce the formation of sizeable ice crystals within the tissue causing cell disruption and consequently tissue tearing during cryo-sectioning.

Unfixed, frozen tissue samples can be stored for a minimum of a year (below -80 °C) without any significant degradation of proteins and lipids but is not advised longer^{34, 37}. For long-term storage, effective deactivation of proteolytic enzymes by microwave irradiation³⁸ or heat denaturation is recommended to minimize the sample aging effect. For the latter, a heat fixation device was introduced, utilizing conductive heating under reduced pressure to rapidly eliminate enzymatic degradation in tissue samples³⁹⁻⁴⁰. Concerning photosensitive samples, exposure to light must be avoided not only during preparation but also during storage to omit potential molecular degradation.

I EMBEDDING OF TISSUE

As for histological analysis, also for MSI tissue samples have to be sectioned using a microtome. While snap-frozen tissue can be cryo-sectioned and analyzed advantageously without any embedding, in most cases morphologically very inhomogeneous tissues or fragile samples demand for supporting media. Thus, prior to sectioning, embedding of such tissues is highly recommended. Workflows developed for microscopy and histology are straight forward and have been successfully adapted also for MSI⁷. Yet, there are a few considerations being unique to tissue analysis by MALDI MSI. Unfortunately, many of the embedding media used in conventional histopathology practice are polymer-based and thus are incompatible with MALDI MS³⁶. Common examples include optimal cutting temperature (OCT TissueTek) media and carboxymethylcellulose (CMC). OCT has been

associated with smearing across the tissue surface during sectioning³³. These polymers are then easily ionized by the MALDI process and are likely to cause contamination and ion suppression^{36, 41}. In contrast to OCT, a low percentage of CMC (2 - 4%) in solution produces only little chemical contamination⁴² during the MALDI process.

However, as OCT comprises a mixture of water-soluble polyethylene glycols and resins, it is well suited for MSI analysis of hydrophobic species such as lipids, which are not affected by aqueous washing procedures such as immersing tissue sections in a 50 mM ammonium acetate solution (pH 6.7, 4 °C)⁴³ prior to MSI analysis. Besides, OCT can be used to affix the tissue to the sample holder of the cryotome. By leaving sufficient distance between the polymer and the blade passing through the tissue, the sample can be sectioned without contamination.

Paraffin is a widely used embedding medium providing morphological stability and analyte preservation. So, paraffin is the most common used medium in pathology and histology. However, paraffin shows high background signals in MALDI and so tissue sections must be de-paraffinized after cutting, e.g., by washing extensively in organic solvents such as xylene and alcohols⁴⁴.

The use of gelatin⁴⁵⁻⁴⁶ or sucrose⁴⁷ is applied to facilitate precise sectioning of tissue samples without introducing interferences to the MS analysis. Additionally, ice has been successfully employed as MSI compatible embedding medium⁴⁸ and is often used in sectioning whole animals for MALDI MSI⁴⁹⁻⁵⁰.

II SECTIONING OF TISSUE

MS imaging requires thin, flat tissue sections (see *Surface Morphology & Sample Complexity, chapter 2B, p.23*). In case of MALDI, the aim during tissue sectioning is to cut through the majority of cells and expose their contents to enable analyte co-crystallization with ionization assisting matrices. Optimization of the cutting temperature and thickness are required to produce high-quality sections for MALDI MS imaging. The sample stage temperature is typically maintained between -5 and -25 °C, depending on the tissue type. For tissues comprising high fat content (e.g., rodent brain) lower temperatures are required to achieve high quality sections⁵¹. Tissues are generally sliced to the typical thickness of mammalian cells (10 - 20 µm) to obtain representative cuts through the majority of cells, exposing their intracellular contents for analysis³⁶. In TOF-based MS analysis, sectioning of tissues is typically performed between 3 and 20 µm. Tissue sections thinner than 3 µm may show a decrease in signal intensities, whereas sections thicker than 30 µm may cause surface charge effects attended by signal decay⁵² along with increased background signals. Besides, thicker tissue sections take longer to dry which can cause cracking of the sections³⁶, and, because they are insulating samples, can adversely affect the performance of the mass analyzer⁵¹.

III MOUNTING OF TISSUE SECTIONS

After sectioning, the sample is transferred to an appropriate substrate. For MSI, tissue sections are mounted onto stainless steel MALDI plates or indium tin oxide (ITO)-coated glass slides⁵³⁻⁵⁴. ITO-coated targets are more routinely used to analyze tissue samples since their transparent surface allows for microscopic analysis and still provides electrical conductivity obligatory for instrument geometries applying high voltage on the sample holder for proper analysis. Prior to sample attachment, ITO-coated targets can be lysine coated to improve adhesive properties of the sections. Preferably, tissue sections are transferred onto the substrate either by thaw-mounting³⁶ or through direct fixation to adhesive double-sided conductive tapes either with incorporated steel filaments or simply copper bands allowing efficient electrical field transfer. The latter approach is rather used when dealing with very fragile tissue or whole-body sections by enhancing stability and reducing section distortion and dislocation of analytes⁵⁵⁻⁵⁶. Thaw-mounting, whereby the frozen tissue is picked up by gently bringing it in contact with a warm surface of a glass slide, is most common in MSI. The glass slide with the applied tissue section is then dried for ≥ 30 min under reduced pressure mostly at room temperature. Hereafter, glass slides can be mounted on common stainless steel MALDI target holders carrying up to 5 slides or can be transferred to 50 mL falcon tubes accepting up to 2 slides which are then stored at -80°C until further use. For the falcon tubes, one must be aware that the mounted tissue sections are not facing each other to omit harming of the sample. Glass slides holding tissue samples should be oxygen free, so an exchange to nitrogen is advised to prevent biomolecules from potential oxidation. Thawing of sectioned tissue after storage is a critical point in order to preserve sample and analyte stability. During thawing, especially water soluble analytes at the tissue surface are prone to relocation resulting from water condensation⁵⁷. To alleviate this problem, thawing under reduced pressure or air-drying using a gentle stream of N_2 is recommended^{16, 27, 58}.

IV WASHING OF TISSUE SECTIONS TO REMOVE SALT AND OTHER INTERFERENCES

MS imaging depends on efficient desorption/ionization of the surface molecules where some of the most abundant species can hamper the analysis of some of the minor abundant ones. Lipids and salts are the major interfering components for protein and peptide analysis^{15, 59-60} as they are highly abundant in many classes of biological tissue.

Salts are usually omnipresent, either derived from interstitial fluids or released from ruptured cells during sectioning⁶¹. Even though MALDI is a technique known to be moderately sensitive to salt residues, large quantities decrease signal quality as they suppress ionization through gas-phase adduct formation as well as negatively affect matrix crystallization^{15, 62-63}. Additionally, lipids with charged headgroups (e.g. phospholipids) are favored in ionization and thus lead to ion suppression for many analytes. Consequently, washing tissue sections with organic solvents is recommended to increase ion yields for peptides/proteins.

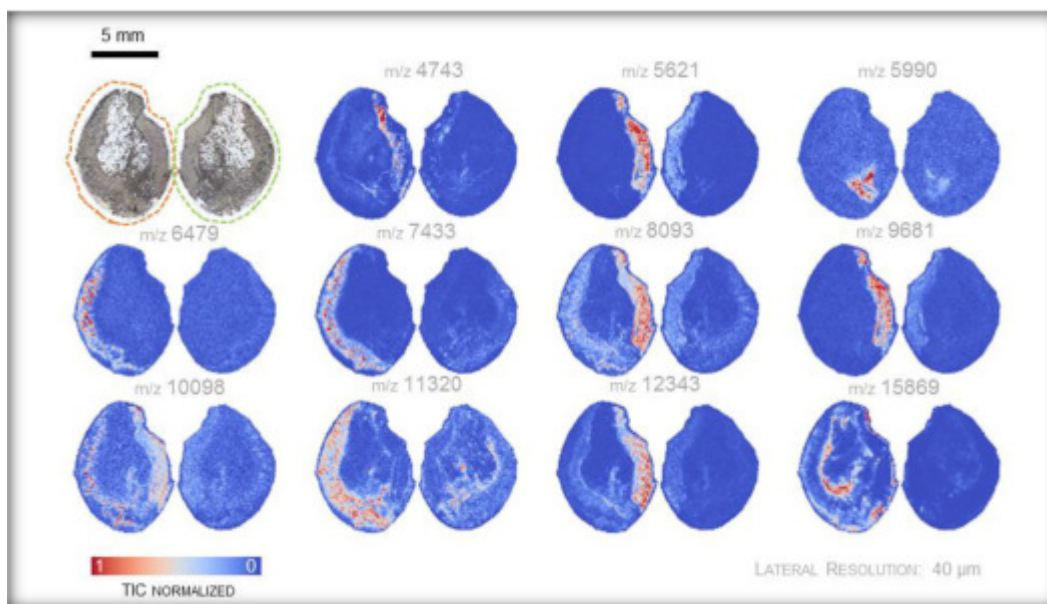


Figure 3: Direct comparison of 2 washing procedures applied to visualize peptides/proteins in human colon tissue. m/z values between 4 and 16 kDa are visualized. Left side, outlined in orange: 70% EtOH (30s), 100% EtOH (30s), Carnoy's fluid (2 min), 100% EtOH (30s), ddH₂O (30s), 100% EtOH (30s)⁶⁴. Right side, outlined in green: 2x70% EtOH (30s), 100% EtOH (30s). Sublimation of SA (0.25 mg/cm²) and recrystallization with 5% AcOH (3.8 min), lat.res. 40 μ m, positive ion mode (linear geometry), 100 shots/spot, ~17200 spots each.

Commonly applied tissue procedures employ a brief 70% ethanol wash to remove salts and debris followed by immersion in increasingly higher percentages of ethanol (90-100%)^{36, 65-68}. Under these conditions, proteins show no significant delocalization³⁶ but a significant raise of signal to noise ratios for the mass range above 20 kDa⁶⁹. For tissues exhibiting high lipid content additional washes with less polar organic solvents such as chloroform and xylene are preferred⁷⁰. An approach that utilizes Carnoy's fluid, a mixture comprising ethanol, chloroform and acetic acid (6:3:1, v/v/v), has been reported to yield superior results for imaging proteins^{64, 71}. Conversely, on-tissue detection of lipid species can be enhanced by washing cycles using aqueous buffer solutions such as 50 mM ammonium acetate (pH 6.7, 4°C)^{43, 63, 72-73}.

Figure 3 shows a comparison of two washing procedures, a standard one (right images), and a more sophisticated protocol (left images), which removes salts and lipids while increasing sensitivity for masses in the higher mass range (peptides/proteins). Significantly increased ion intensities can be observed for protein species between 4 and 16 kDa.

Nevertheless, the washing procedure must be optimized for the analyte and tissue of interest, as different classes of molecules require different treatments. Most important, washing must retain analyte localization within the tissue while enhancing detection, either by formation of adducts, or by removing sample constituents that interfere with the ionization process.

V SPECIFIC MOLECULAR MODIFICATIONS

Besides all the concerns mentioned above further sample preparation issues have to be considered. The following sections are giving a brief overview of the most important ones.

Formalin Fixation of Tissue

Formalin fixation is a very important procedure in histology and pathology for preserving tissue samples, owing to the superior preservation of tissue morphology and subsequent ease of storage. Formaldehyde induces cross-linking of neutral amino groups using methyl bridging⁷⁴. The process preserves the tissues' cellular organizations and anticipates proteolytic degradation. Fixation is performed by immersing the fresh biological sample in a formaldehyde solution (typically 4% v/v formalin in water)⁷⁴ at room temperature. The process requires several hours for the fixative to fully penetrate the tissue⁷⁵. Thus, potential protein and small molecule degradation can occur³⁴. Formalin fixation has been shown to be compatible with MALDI MSI by preserving the distribution of metabolites⁷⁶ and commonly detected polar lipids⁷⁷⁻⁷⁹. Prior to MSI experiments, peptides/proteins cross-linked in tissue must get accessible and denatured to be available for desorption/ionization, similar to antigen-retrieval methods established for histological analysis⁸⁰. Among the washing procedures being applied for antigen-retrieval, the use of citric acid buffers and extreme pH values showed good results for at least partially reversing the cross-linking and thus reversing the effect of formalin fixation in part. Nevertheless, large proteins remain bound by the remaining formalin cross-linking network and proteolytic digestion becomes thus indispensable in order to thoroughly analyze proteins by MSI⁸¹. In 2010, an alternative, non-crosslinking tissue fixative has been introduced, enabling comprehensive proteomic analyses by MALDI MSI⁸².

Chemical Staining of Tissue Sections

Histological or immunohistochemical staining of the tissue section is an optional step in the MALDI MSI workflow. However, it may be necessary in order to confidently target regions of interest within the tissue and it definitely is a must if correlation of histology features with the acquired ion images has to be made⁸³. Basically, this step can be performed prior to matrix application (pre-MSI) or after data acquisition (post-MSI).

Pre-MSI tissue staining will ensure the best quality of optical images along with the best correlation because the tissue is not impaired by the MALDI MS workflow (i.e., tissue preprocessing, matrix application, laser irradiation). Besides, a number of stains have been shown to be compatible with MALDI including methylene blue and cresyl violet, unlike the commonly used combination of Hematoxylin and Eosin (H&E) dyes (Figure 4) known to suppress protein signals⁸³⁻⁸⁴. However, most staining protocols require numerous incubation steps in aqueous and organic solvents and thus must be carefully selected and approached with caution as they may impair the molecular composition and integrity of the tissue.

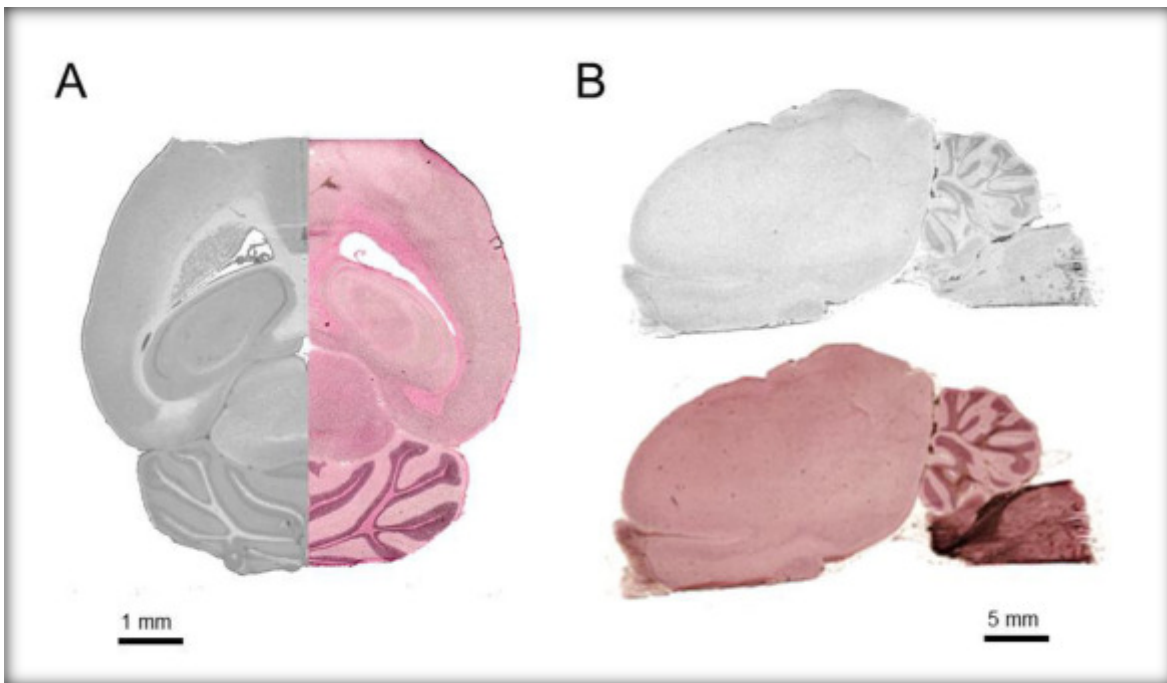


Figure 4: Post-MSI H&E stain of (A) a horizontal mouse brain section and (B) a sagittal rat brain section. Darker regions mark the presence of cell nuclei (Hematoxylin), the pink areas basic structures (Eosin). Matrix removal: rinsing with 100% ACE (15s), followed by 70% EtOH (15s). Staining: 100% EtOH (30s), 70% EtOH (30s), Hematoxylin (2 min), tab water (5 min), Eosin (1 min), 2x 70% EtOH (30s), 100% EtOH (30s), 100% iPrOH (1 min).

Performing post-MSI histology has practically no limitations in the choice of staining. Indeed, due to the high solubility of most matrices in alcohol-water mixtures, the deposited matrix can be easily removed by immersion in 70% ethanol for 1–2 min⁶⁵. If performed without excessive laser fluence laser irradiation does not cause significant loss of histological features within the ablated area⁸⁵. The main drawback of this approach is that the tissue sections are often slightly damaged after both, MALDI MSI analyses and matrix removal⁵. So most often, a consecutive tissue section is stained for image co-registration (MALDI MSI and histology) and used for data acquisition and subsequent data analysis. However, slight variations in size and shape of the consecutive tissue section may be problematic for reliable matching of ion and optical images.

On-tissue Digestion

Direct analysis and imaging of intact proteins is inhibited by the current practical upper limit of TOF-mass analyzers of about 30 kDa although the theoretical limit for singly charged species is much larger. In order to bring these proteins into the MS range *in situ* tryptic digestion has to be performed. This requires application of a proteolytic enzyme on the surface of the tissue section. For optimal proteolytic enzyme activity, the sample needs to remain moist at appropriate temperature and pH according to the enzyme's preferences. The incubation period ranges from 1 hour up to overnight depending on the research target. Yet enzyme application is still critical for on-tissue digestion as excess liquid applied can lead to analyte diffusion during the incubation process and consequently to a loss in spatial resolution of the underlying proteins. To prevent analyte dislocation, enzymes are usually applied similar to the MALDI matrix. In general, two methods were generally optimized for enzyme application: discrete spotting and homogenous spray coating which will be discussed in more detail in ***Solvent-based Matrix Application*** (chapter BI, p.13). In 2016, a novel approach was introduced that incorporates the MALDI matrix and the proteolytic enzyme onto the target surface prior to section mounting, thus minimizing the risk of analyte dislocation and simplifying the sample preparation process ⁸⁶.

The approach most frequently used in MSI experiments involves application of trypsin to the tissue surface. The cleaving sites for trypsin, arginine and lysine are very frequent in every protein. Consequently, accessibility of potential cleavage sites is improved, and digestion is more efficient.

On-tissue digestion generates proteolytic peptides of 400 to 3500 Da, which is a mass range where instrumental sensitivity is higher than that for intact proteins ⁸⁷. Protein identification can be performed using tandem mass spectrometry (MS/MS) by efficient fragmentation of selected peptides (e.g., by collision induced dissociation). However, MS/MS identification may be complicated due to multiple fragments originating from isobaric peptide ions. On-tissue protein digestion may necessitate further washing steps, primarily to avoid peptide ion signal suppression and spectra complexity by the presence of high concentrations of enzymatic autolytic products. Also salts and other ionic compounds are typically washed off the tissue section after enzymatic cleavage and prior to MALDI matrix application.

Chemical Derivatization

Although significant amounts of information can be obtained, several classes of molecules are difficult to ionize and thus analyzed directly by MS. For instance, the main challenges for the detection and localization of drugs and metabolites within tissue sections rely on low molecular weight background signals (e.g., matrix induced), poor ionization efficiency and ion suppression, as well as potential isobaric interferences of endogenous molecules. MALDI MSI usually leads to the detection of the most abundant, desorbable and ionizable compounds such as soluble proteins below 30 kDa and, consequently, does not provide access to the less abundant or higher mass molecules ⁸⁸.

Chemical derivatization is therefore a common process to improve analyte detection in MS techniques ⁸⁹. Herein, the addition of a chemical tagging reagent to a specific functional group of the analytes of interest changes the physicochemical properties of the molecules, converting them *in situ* to high ionization-efficiency derivatives. Besides, when referring to small molecules, derivatization may shift the MW of the target analytes beyond the spectral region of matrix interferences ⁹⁰. Chemical derivatization has been applied successfully for the on-tissue detection of steroids ⁹¹⁻⁹³, neurotransmitters ⁹⁴ and fatty acids ⁹⁵ but also for large molecules including N-glycans ⁹⁶, mRNAs ⁹⁷ as well as high mass proteins ⁹⁸. Compared to traditional spraying, electrospray deposition has been successfully applied for derivatization while achieving a high spatial resolution of 20 μm ⁹⁵.

B MALDI MATRIX CHOICE AND APPLICATION

Numerous matrices have been evaluated to date, each of these specifically applied to certain classes of molecules. Among these, several matrices have found popularity for their universal use in MALDI MSI in positive ion mode including SA (sinapic acid, 3,5-dimethoxy-4-hydroxycinnamic acid) for the analysis of large molecules such as proteins¹⁹, CHCA (alpha-cyano-4-hydroxycinnamic acid) is well appropriate for lower molecular weight compounds such as peptides⁹⁹ but also metabolites¹⁰⁰. 2,5-DHB (2,5-dihydroxybenzoic acid) is also suited for imaging small molecules⁴⁹ and is particularly used for lipid analysis. 1,5-DAN (1,5-diaminonaphtalene) and proton stripping matrices such as 9-AA (9-aminoacridine) are the matrices of choice for analysis of small compounds in the negative ion mode¹⁰¹⁻¹⁰². 1,5-DAN is also commonly used for lipid analysis in both positive and negative ion mode⁴³. 9-AA is reported to facilitate analyzes of small compounds due to absence of matrix ions in the low molecular mass range¹⁰³.

First described for use in MALDI¹⁰⁴, ionic liquid matrices have also been investigated for MSI. This class of matrix comprise a conventional matrix (CHCA, SA) mixed with an equimolar content of a base (e.g., N,N-dimethylaniline). Its use has been reported for analytes exhibiting critical ion yield¹⁰⁵, enabling improved ionization properties combined with increased S/N ratios¹⁰⁶. The stable state of liquid matrices facilitates the removal of so-called "matrix hot spots", allowing analytes to distribute homogenously inside the applied droplets. However, volatility of the liquid, especially under high vacuum, can be unpredictable¹⁰⁷.

A range of inorganic compounds has been used as novel MALDI matrices¹⁰⁸⁻¹¹³. Since these compounds are usually in a mass range below 100 Da, interferences of matrix ions in the low mass range are limited to a minimum¹¹⁴.

I SOLVENT-BASED MATRIX APPLICATION

In solvent-based matrix application methods, the solvent system and the matrix-to-solvent ratio directly relate to ionization efficiency and crystal size, parameters that must be optimized to match the analytes of interest and type of tissue under investigation. Solvent systems are ideally very quickly evaporating to accelerate matrix crystallization and thus favor small crystal sizes while inducing efficient analyte solvation/extraction and avoiding lateral diffusion of analytes across the tissue surface. Although it is well established that molar analyte:matrix ratios are important for MALDI, today in general saturated matrix concentrations are used¹¹⁵⁻¹¹⁶. Matrix solutions are commonly prepared in a mixture of water and organic solvent such as methanol, ethanol, acetonitrile or acetone (i.e., 50 - 70%) with a weak percentage (i.e., 0.1 - 0.2%) of acetic or trifluoroacetic acid³⁶. The latter has been shown to significantly increase the ionization yield for peptides and proteins in the positive ion mode¹¹⁷. However, hydrophobic or transmembrane proteins cannot be solubilized using common sample preparation conditions. For this purpose, MALDI-compatible detergents can be applied, including low

percentages (i.e., 2 - 3%) of ionic detergents such as sodium dodecyl sulfate (SDS) ¹¹⁸, or non-ionic detergents such as triton X-100 ¹¹⁸ and *n*-octyl glucoside ¹¹⁹.

Chemical Printers

Automated spotters are used to prepare samples for MSI by precisely depositing microdroplet arrays on tissue sections. Two different commercial instruments are the Chemical Inkjet Printer (Chip-1000, Shimadzu) and the Portrait 630 Spotter (Labcyte). The Chip-1000 utilizes piezoelectric elements embedded in the print heads, while the Portrait 630 uses focused acoustic energy to transfer droplets from a matrix reservoir to the sample surface. Both instruments exhibit similar specifications, ejecting matrix droplets with approximately 100 pL in volume, resulting in spots that are less than 150 μm in cross section dimensions. The sample is placed on a mechanical stage and moved in x-y direction, to print high crystal density matrix spots in different locations on the tissue section. Contrary to spray methods, the spatial resolution is in that case limited to the center-to-center spacing between adjacent microspots. However, the spacing between each spot restricts analyte delocalization to occur within the given spot size only. Multiple droplet passes favor analyte incorporation and thus result in significantly improved S/N ratios, particularly for proteins.

Besides tissue profiling, where imaging the whole sample surface is not mandatory, spotting is well suited for enzyme application prior to matrix deposition on the exact same raster positions ¹²⁰. By using this approach, a significant increase in the overall number of proteolytic peptides was reported ⁸⁷.

Manual Spraying

Using an artistic airbrush for liquid matrix deposition is the simplest and least expensive method available and therefore has been widely used in MALDI MSI ¹²¹⁻¹²³. Yet it is not fully automated and thus limited in terms of comparability and reproducibility. Classically, the sprayer is gently moved over a tissue section mounted on a static sample plate using multiple coating steps. During each spraying circle the tissue is minimally wetted to avoid molecular diffusion, whilst providing sufficient solvent amount for analyte extraction to occur. The matrix is permitted to dry on the tissue surface between passes and coating is repeated until the whole sample is homogeneously covered with matrix.

While this can be reproducible between applications by the same trained analyst, person-to-person variability is high, as there is only limited control of angle adjustment as well as spraying distance and pressure. Since the focus of the spray is not adjustable and liquid loss during spraying is significantly high, huge amounts of matrix/solvent volumes are required for airbrush applications. Besides, commercial airbrush devices typically have metal surfaces which can corrode and consequently changing the performance over time. Besides the disadvantages mentioned above, manual spraying usually produces low spatial resolution ($> 100 \mu\text{m}$), thus this method is not favored for MSI.

Automated Spraying

To improve consistency from one analysis to another, the matrix amount deposited on tissue must be controlled and reproducible, explaining the development of automated devices. Several commercial solutions exist including the SunCollect (SunChrom), ImagePrep (Bruker), and TM Sprayer (HTX Technologies) ¹²⁴⁻¹²⁵. Besides differing in mechanism, these systems allow the matrix to be sprayed as a fine aerosol to coat the tissue sample, while controlling conditions such as spray pattern, flow rate, temperature, humidity, drying time or spray focus. Once the methodology is optimized for a tissue type, parameters may be fixed as a method and recalled, allowing reasonable reproducibility to be achieved on large sample sets. However, inhomogeneity in crystal size and formation still limits lateral resolution to $\geq 20 \mu\text{m}$ ¹²⁵ and the aerosol-based coating can favor analyte diffusion ¹²⁶.

II SOLVENT-FREE MATRIX APPLICATION

Sublimation

Matrix sublimation was first reported by Kim et al. in 1998¹²⁷. Since then this method was improved for several matrices¹²⁸ and in recent years it was found that many matrices do not decompose at elevated temperature under reduced pressure. Sublimation generally yields dry matrix crystals at the sub-micrometer to 3 μm level^{64, 129-130} allowing an increased lateral resolution down to 1.4 μm ¹³¹ and limited lateral migration of molecules in tissue^{17, 19, 132}.

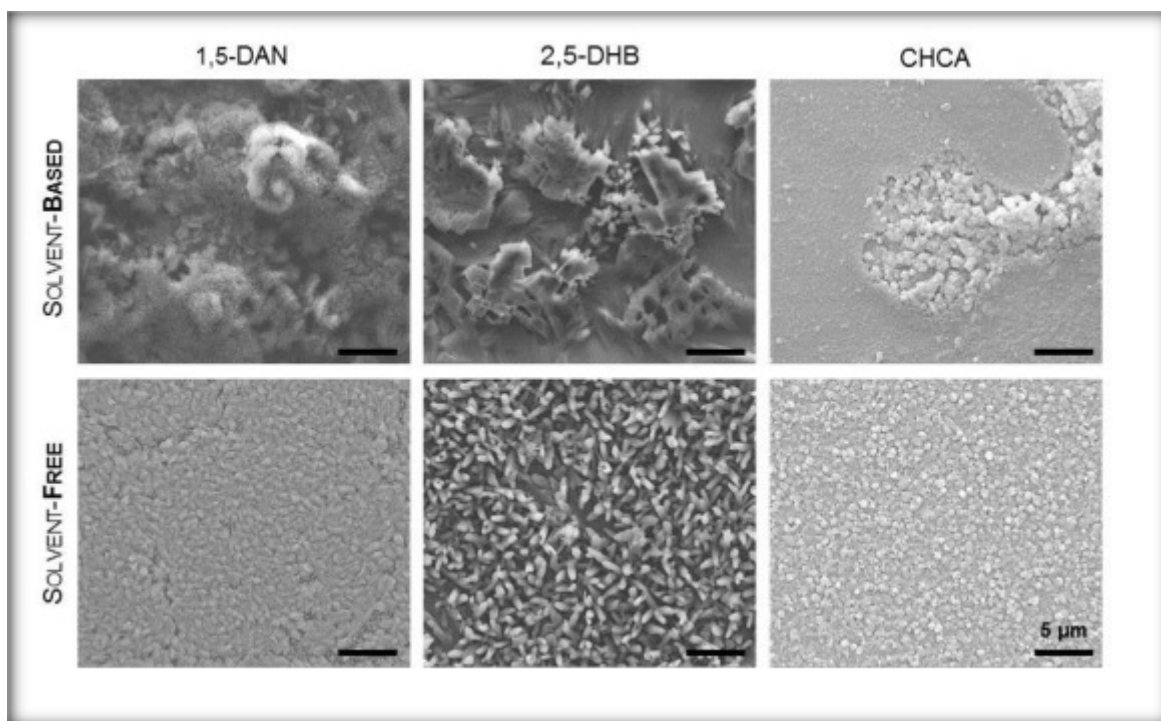


Figure 5: Comparison of solvent-based (airbrush) and solvent-free (sublimation) matrix application. 0.25 ± 0.02 mg of matrix per cm^2 glass slide were applied by both methods. Solvent-based: EtOH/ddH₂O (9:1, v/v), 1.5 bar, angle 45°, distance 30 cm. Solvent-free: sublimation of 25 mg per matrix resulted in a coating of 0.25 ± 0.01 mg/ cm^2 . For details on sublimation parameters refer to *chapter 4, p. 54*.

Besides significant smaller crystal sizes, sublimation decreases interstitial crystal volume to a minimum when compared to solvent-based deposition (Figure 5). Recent work suggests that narrow size distribution of crystals enhances reproducibility, resolution, sensitivity and S/N ratios in MALDI MS¹³³⁻¹³⁴. Moreover, it has been reasoned that decreased crystal sizes possess higher effective temperatures within each of the microcrystals irradiated by a laser pulse, and thus cause entire volatilization¹³⁵. In addition, sublimation has the effect of purifying matrix of any involatile compounds during application¹³², and thus reducing chemical noise resulting from impurities.

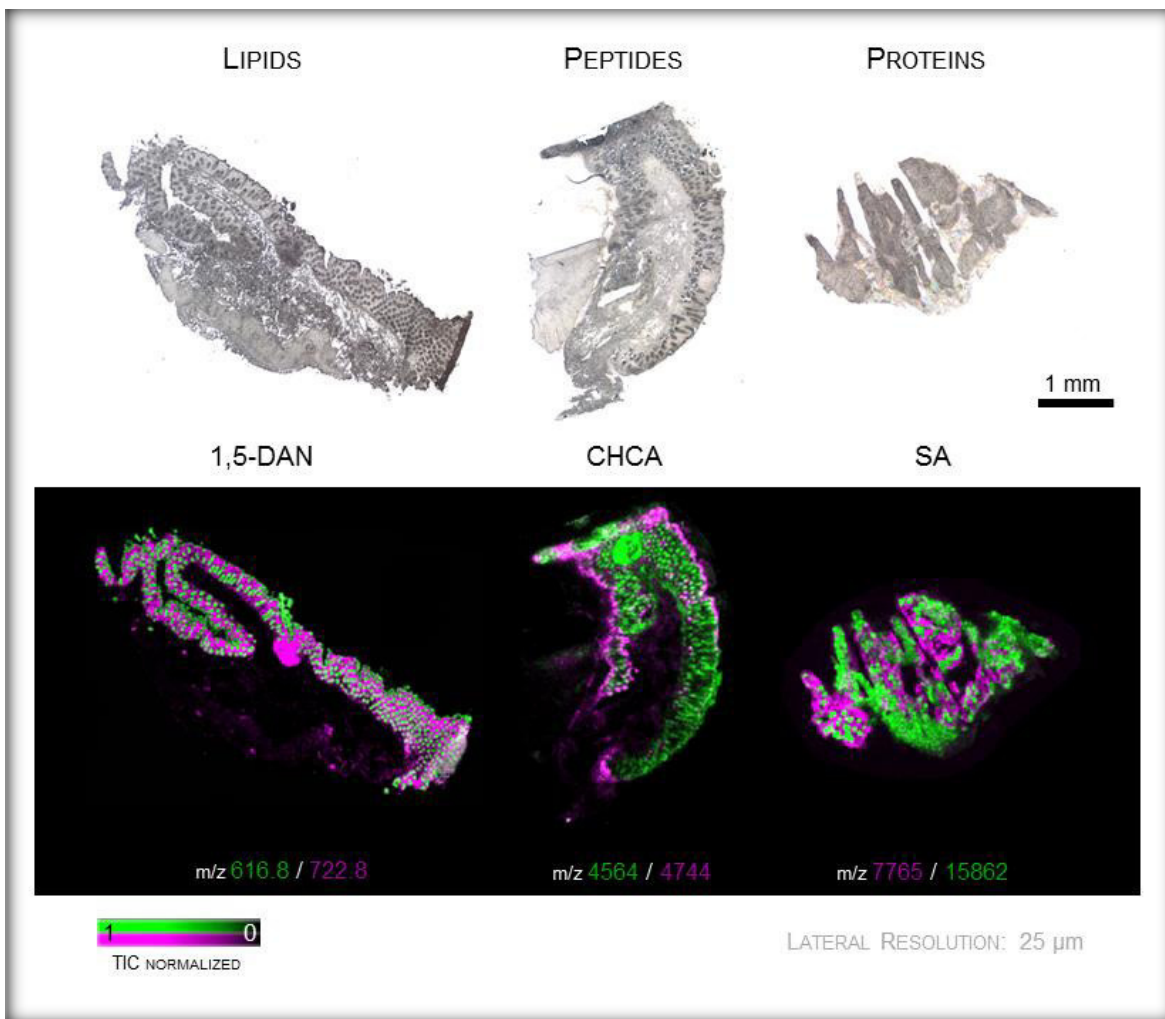


Figure 6: Subsequent recrystallization of sublimed surfaces on human colon tissue sections. Lipids: sublimation of 1,5-DAN (0.24 mg/cm²) and recrystallization with 5% AcOH (1 min), lat.res. 25 μm, negative ion mode (reflectron geometry), 100 shots/spot, 48354 spots. Peptides: sublimation of CHCA (0.23 mg/cm²) and recrystallization with 5% AcOH (4 min), lat.res. 30 μm, positive ion mode (reflectron geometry), 100 shots/spot, 34652 spots. Proteins: sublimation of SA (0.25 mg/cm²) and recrystallization with 5% AcOH (3.8 min), lat.res. 30 μm, positive ion mode (linear geometry), 100 shots/spot, 16487 spots.

However, the solvent-free deposition mechanism results in poor extraction of analytes from the tissue. Recrystallization of applied matrix layers has been reported to significantly increase the extraction efficiency and sensitivity of analytes^{64, 136}. Figure 6 shows sublimation and subsequent recrystallization of common MALDI matrices on human colon tissue. Visualization of lipids, peptides and proteins at a spatial resolution of 25 μm proves the robustness of the method. Rehydration of the sublimed surface is mandatory for peptide and protein analyses but has also shown to significantly increase ion intensities when applied to lipids (Figure 7).

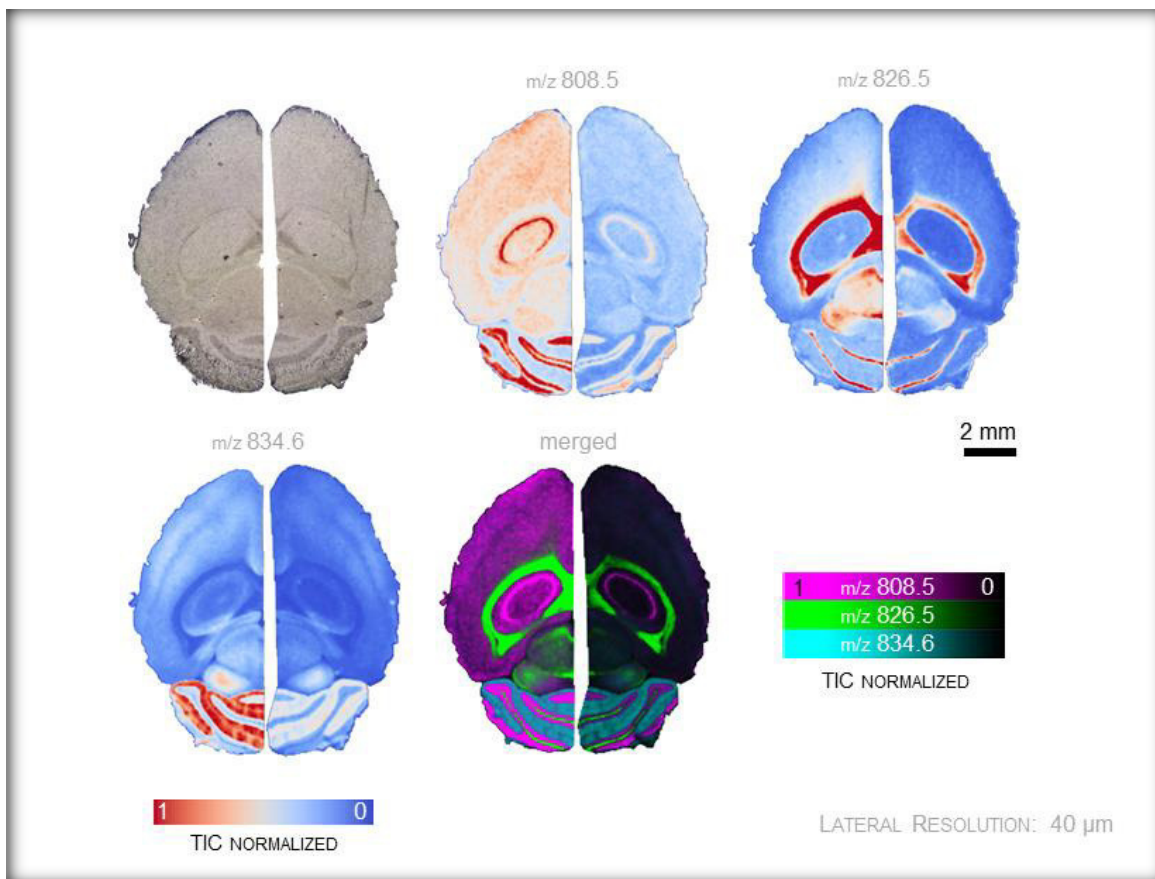


Figure 7: Sublimation and influence of recrystallization on ion signals of selected lipids. Left hemisphere with recrystallization (5% AcOH, 1 min), right hemisphere without recrystallization. 1,5-DAN (sublimation, 0.23 mg/cm²), lat.res. 40 μm, positive ion mode (reflectron geometry), 100 shots/spot, 24500 spots. For details on sublimation and recrystallization parameters please refer to *chapter 4, p. 54*.

Sublimation devices used for MALDI matrix coating reported in literature^{122, 132, 137} are primarily modified glass devices originally designed for bulk chemicals and therefore provide limited control over reproducibility, crystallization and number of MALDI targets to be prepared simultaneously. Furthermore, matrix layer thickness and in-plane homogeneity of the matrix are not manageable. Today one sublimation device is commercialized¹³⁸, a system controlling temperature, pressure and a laser light source which measures the thickness of the deposited matrix layer. But this system is restricted to one sample holder, three matrix components, a certain thickness of matrix layer and the matrix amount deposited¹³⁹. Furthermore, matrix consumption is exceptionally high (100 - 600 mg/run)^{43, 102, 139}. In **chapter 4** (p.54), we introduce a home-built sublimation setup requiring minor matrix amounts, allowing exceptional reproducibility and homogenous matrix deposition on up to three full-sized microscope slides.

C MASS ANALYZERS IN MALDI MSI

Once the molecular ions have been generated the mass analyzer measures the physical property of the introduced ions based on their mass-to-charge ratio (m/z). The most common types of mass analyzers used for MALDI MSI are time-of-flight (TOF), quadrupole time-of-flight (qTOF), ion trap, and Fourier transform-based MS including Fourier transform ion cyclotron resonance (FTICR) instruments and FT-orbitraps. The complexity of biological samples (i.e., isobaric ions) analyzed with MALDI MSI demands high mass accuracy and mass resolution (see

Surface Morphology & Sample Complexity, chapter 2B, p. 23), given by the geometry of the mass analyzer. In general, it is easier to achieve both performance characteristics when the source of the mass spectrometer is decoupled from the mass analyzer. In axial TOF instruments, the source forms part of the flight tube, whereas in most other MALDI mass spectrometer designs, including orthogonal TOF (oTOF) geometry, the link between ionization source and mass analyzer is indirect making it easier to achieve high mass resolution and mass accuracy¹⁴⁰. Because of its simple use, high speed of analysis and comparable low costs, most laser-based MSI work is performed on TOF instruments. The TOF mass analyzer in its simplest form comprises an evacuated flight tube with a pulsed ion source and a detector. Herein, the pulsed ion source is ideally suited to the pulsed nature of TOF analysis. The m/z of an ion is determined by accelerating it in an electric field towards a field-free drift region and measuring the time it takes to traverse the distance from the source to the detector¹⁴¹. Since all ions are accelerated with the same kinetic energy, their m/z ratio can be easily calculated. Besides being the fastest mass analyzers and thus facilitating larger areas to be ablated, TOF analyzers provide an exceptional high mass range which makes them well suited for MALDI MSI of large biomolecules.

However, inherent to MALDI, different starting locations of desorbed ions at the point of acceleration lead to variations in internal energy and, thus, drift times of given ions, resulting in decreased mass resolution and mass accuracy in TOF analyzers. Hence, the TOF-based instrumentation demanded for two technical implementations, the delayed extraction (DE) and the reflector TOF (RTOF). DE, also referred to pulsed (ion) extraction or time-lag-focusing, is a method widely used for MALDI TOF¹⁴¹⁻¹⁴². When applying DE, an initial pulse is implemented on the ion plume to compensate internal energy variations and thus correct for velocity distributions¹⁴³. The integration of the RTOF geometry elongates the ion flight path and further compensates for the internal energy distribution through an ion mirror, leading to enhanced mass resolution and mass accuracy. Yet, development of TOF-based imaging systems is still ongoing.

High performance MS methods, such as FTICR and FTOrbitrap offer significantly higher mass resolution and mass accuracy than a RTOF analyzer, mainly because the mass determination is independent of the initial energy distribution of the ions after laser irradiation¹⁴⁴. However, the long

acquisition time due to in-cell ion accumulation hampers the use of FTMS for high throughput imaging¹⁴⁵, restricting its applications in MSI to direct profiling or to limited ablation areas. Yet, today the benefit of high confidence identification and separation of ions at the same nominal mass is well recognized so that the number of FTMS instruments is steadily increasing in the field.

D DATA ANALYSIS

The principal of MSI is to qualitatively and quantitatively visualize distributions of selected ion signal abundances. Thus, prior to data processing, preprocessing should be applied to ensure accurate and efficient data analysis¹⁴⁶⁻¹⁴⁷. Preprocessing includes normalization (see **Normalization**, *chapter 2G*, *p. 26*), baseline correction, spectra recalibration, smoothing, and unsupervised or supervised data compression^{124, 148}. Normalization of the whole dataset is relevant to compensate for the instrument performance over time, surface inhomogeneities and ion suppression effects and, thus, reduce pixel-to-pixel variation. Herein, each spectrum is divided by a normalization factor generated on, e.g., the total ion current (TIC), the root-mean-square (RMS) or the median of all data points. Following normalization, baseline subtraction and spectral recalibration can be performed to ensure accurate interpretation of the data¹²⁴. Smoothing algorithms such as Savitsky Golay or Gaussian Smoothing are applied to the dataset to increase S/N and remove fluctuations between pixels.

In MSI acquisitions there is a clear trend towards large data files, which complicates data processing because of limited computational resources and storage capabilities. To alleviate this problem, unsupervised and supervised classification approaches are used to reduce data to the most important m/z distributions, while retaining relevant information for statistical analysis.

Unsupervised clustering uses spectral similarity to compress data into features prior to statistical analysis. For instance, principal component analysis (PCA) can be used to reduce the dimensionality of the data set, allowing to distinguish principal components that cause the greatest variance in the data¹⁴⁹. Another option would be hierarchical clustering of the data, to bin together similar spectra into regions of interests and to identify colocalized m/z values¹⁵⁰.

For supervised clustering a specified set of classes should be known in advance. Using this method, a new data set may be classified into one of those classes. In the field of supervised classification, machine learning is getting more and more present in making predictions for new data sets. Data are analyzed using algorithms that look for correlated structures in the data that also correlate with a target outcome. Models used for classification include supervised neuronal networks, support vector machine, genetic algorithms and random decision forest¹⁵¹. Among these, random decision forest (RDF)-based classifiers are often used statistical models that use training data to predict the classification of new data sets (see *manuscript*, **chapter 7**, *p. 136*).

MALDI imaging data can be generated from a variety of instrument platforms, each providing customized tools for acquisition built on proprietary data formats controlled by the manufacturers. The data format is crucial with respect to its portability and the way in which data is stored. To date, no standards exist for data formats, but numerous formats. In 2011, the data format imzML has been introduced in order to allow for flexible exchange of MS imaging data between different instrument vendors and data analysis software ¹⁵². The objective is to provide the user with the best suited processing software for a specific question or application. MS imaging data from different instruments can be converted to imzML ¹⁵³, and open source converters are available (i.e., imzMLConverter ¹⁵⁴).

2 METHODOLOGICAL CONSIDERATIONS

A SPATIAL RESOLUTION

The image resolution (i.e., the spatial resolution) of an MSI experiment decisively influences the ability to distinguish distributions of components within tissue sections. Herein, the recorded pixel size is key for whether two adjacent regions are perceived as unique and distinct.

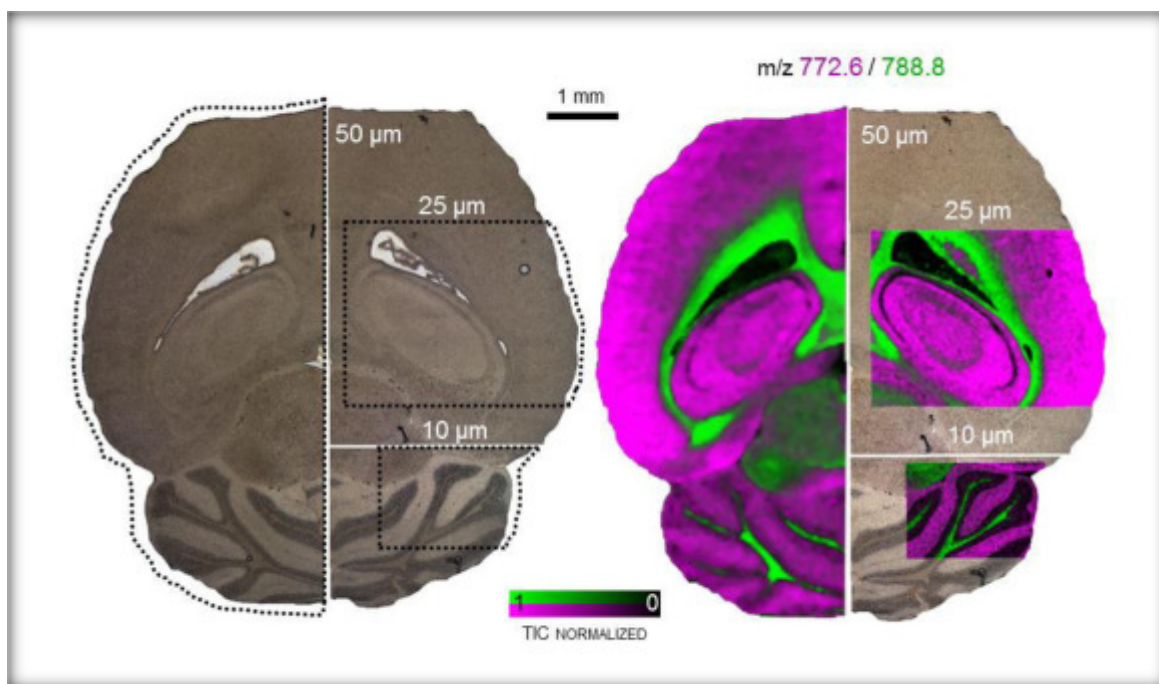


Figure 8: Influence of varying lateral resolutions on a horizontal mouse brain tissue section. Sublimation of 1,5-DAN (0.24 mg/cm²), MALDI MSI in positive ion mode (reflectron geometry) and at spatial resolutions of 50, 25 and 10 μm.

Figure 8 demonstrates the impact of spatial resolution on the quality of the resulting ion image - improving the spatial resolution enables more discrete localization patterns observed throughout the tissue section. The ion image looks less blurry.

Today, SIMS generally offers the highest spatial resolution among all MSI approaches (<50 nm)¹⁵⁵, yet is not a soft ionization technique allowing for desorption/ionization of intact molecules like MALDI. Although significantly increased recently¹⁵⁶⁻¹⁵⁹, spatial resolution has its main challenges in (1) sample preparation, and (2) instrumental parameters. Herein, the laser beam diameter is the limiting factor, as it determines the ablation area and thus the attainable lateral resolution in an imaging experiment. Several instrumental improvements and other notable advancements in spatial resolution have been reported recently^{131, 160-162}. For instance, by adjusting the optics of the ion source along with

changes in the geometry on an atmospheric pressure MALDI, a lateral resolution of 1.4 μm was reported, allowing for the visualization of lipids, metabolites, and peptides on a sub-cellular level ¹³¹. Besides instrument modifications, oversampling is a commonly used approach to technically increase spatial resolution in MALDI MSI ¹⁶³⁻¹⁶⁴. Oversampling means that the raster step size of the sample stage is set to a value lower than the laser beam dimensions with complete ablation of matrix at every spot. Recently, a lateral resolution of 5 μm was reported by the use of a 20 μm laser diameter and oversampling ¹⁶⁵.

However, improving spatial resolution has also its drawbacks, as it decreases the area of ablation, and thus decreases signal intensity while increasing data acquisition times combined with the amount of data generated ¹⁶⁶. Consequently, spatial resolution should always be adjusted to the aim of the study.

B SURFACE MORPHOLOGY & SAMPLE COMPLEXITY

In MALDI TOF-based analysis, the complex nature of many biological samples means that instrument parameters such as mass accuracy and mass resolution become very important to measure as many analyte species as possible by distinguishing analytes solely on their accurate mass. Except for MALDI coupled to ion mobility separation (IMS), MSI is *per se* not separating analytes. Thus, chemical interferences induced by the MALDI matrix overcomplicate mass spectra interpretation in the lower mass range (~100 - 600 Da).

Since the source in axial TOF instruments forms a part of the flight tube, mass spectral quality is significantly influenced by the given surface morphology of the section to be analyzed. Hence, inhomogeneity of matrix and crystal sizes, or specimens inherently providing highly irregular surfaces (see article, **chapter 5**, p. 77) are all considered challenges in this field as notably different starting locations of desorbed ions at the time of acceleration lead to a deviation in the drift time, and thus negatively affect mass resolution and accuracy (see **Mass Analyzers in MALDI MSI**, chapter 1C, p. 19). For instance, calibration standards applied rather on the blank glass slide than atop of a control tissue induces height differences and thus variations in the times of given ions consequently leading to spectral mass shifts during analysis. Recently, a TOF-based “ghosting” effect has been reported originating from a tissue section comprising uneven surface topography. A significant shift in mass and intensity from one end of a tissue section to the other was observed ¹⁶⁷.

C ON-TISSUE IDENTIFICATION

Analyte identification in MALDI MS typically relies either on the use of enzymes (see ***On-tissue Digestion***, chapter 1AV, p. 9), high-resolution mass spectrometry (HRMS), or tissue lysis in combination with liquid chromatography tandem mass spectrometry (LC-MS/MS). One of the most critical issues in MALDI TOF-based MSI is the fact, that analyte concentrations per pixel are extremely low usually resulting in fragment ion spectra of poor quality (S/N, mass accuracy). In addition, not only the most abundant analyte is desorbed and ionized from each measured spot. In the given ion selection window, numerous low abundant components increase the number of background signals which ultimately results in MS/MS spectra exhibiting mixed structural information. Using a conventional TOF/RTOF instrument, identification directly from the tissue is only applicable for compound classes providing easily insight into their structural nature by tandem mass spectrometry or post-source decay analysis. Particularly fragmentation of phospholipids, which induces formation of daughter ions being characteristic for the lipid's headgroup.

Typically, for detailed structural and fragment information, acquired mass values are compared with theoretical m/z values according to databases like LIPID MAPS Structure Database (The LIPID MAPS Lipidomics Gateway, <http://www.lipidmaps.org/>) and [Metabolomics Workbench Metabolite Database](http://www.metabolomicsworkbench.org/) (<http://www.metabolomicsworkbench.org/>, both University of California, San Diego, USA).

D THROUGHPUT

Another frequently discussed challenge for MALDI MSI are long analyses times, limiting the practicality for routine applications. Yet, the acquisition time and the resulting data load mainly depend on the spatial resolution (i.e., point-to-point distance), the mass resolution in case of high-resolution mass analyzers, and the size of the region of interest (ROI). Besides mass resolution, which is now routinely reduced via automated feature identification, improvements in signal digitization electronics and the implementation of frequency-tripled 355 nm Nd:YAG lasers with repetition rates up to 10 kHz¹⁶⁸ and 349 nm Nd:YLF lasers with a repetition rate of 5 kHz¹⁶⁹ have been made for increased throughput without sacrificing image quality. A novel MALDI TOF/RTOF instrument equipped with a solid state laser firing at a 10 kHz repetition rate was recently reported to scan up to 50 pixels per second^{168, 170}, compared to 3 - 7 pixels scanned by conventional lasers at the same time.

Throughput becomes even more of a challenge when molecules in the same tissue ionize differently, thus require different polarities for acquisition. This is particularly the case for lipid analysis, as lipids are a diverse analyte class with high structural variability and, thus, being preferentially detected as either positive or negative ions depending on the headgroup of the different classes. For instance, phosphatidylcholine (PC) and sphingomyelin (SM) contain positively charged headgroups, whereas phosphatidylethanolamine (PE) and phosphatidylinositol (PI) are present in permanently neutral or negative charge states. As a result, for comprehensive lipid analyses, MALDI MSI studies have to be performed in both, negative- and positive-ion mode to gain maximum information for phospholipid distributions within a single tissue section. Classically, the tissue section is first scanned in one of the ion modes, followed by offsetting the x- and y-raster positions and scanning the tissue in the opposite polarity mode. However, using this strategy demands twice the time for data acquisition. Recently, methods have been employed for imaging using both modes of polarity simultaneously while minimizing analysis time using high speed MALDI MSI technology and precise laser control¹⁷¹.

E ION SUPPRESSION EFFECTS

When considering the analyte of interest in its biological environment, ion suppression can be understood as a competition for ionization based on secondary reactions^{12, 115-116, 172}. The relative concentrations of analyte to MALDI matrix as well analytes to each other can adversely affect the resulting mass spectrum. Hence, if ionization of a certain endogenous compound is thermodynamically favored and/or this substance is highly abundant in tissue, other ions may be totally masked or ionization may be depleted to insignificance. For instance, highly abundant phospholipids omnipresent in lipid membranes may lead to intense lipid signaling which may mask other molecules including the targeted analyte¹⁷². Besides the competition of charges with matrix or other endogenous species, the tissue itself can have a significant impact on the resulting ionization yield¹⁷³. The analyte of interest, being trapped in a complex biomatrix, undergoes various noncovalent interactions, resulting in extraction efficiencies varying in function of both, the local position within the tissue as well as the type of tissue. Thus, the response factor for each targeted analyte is also truly tissue specific.

F NORMALIZATION

Normalization is critically important for the proper interpretation of MALDI imaging datasets. Normalization is the process of multiplying a mass spectrum with an intensity-scaling factor to expand or reduce the range of the intensity axis. It is used to remove instrumental and systemic artifacts that impact signal intensities by projecting spectra of varying intensity onto a common intensity scale^{124, 174-176}. Artifacts may originate from matrix application, crystal heterogeneity or ion source contamination that steadily attenuates the total ion count (TIC) as a function of time during which the ion transmission is influenced and therefore can gradually decrease the image brightness (Figure 9).

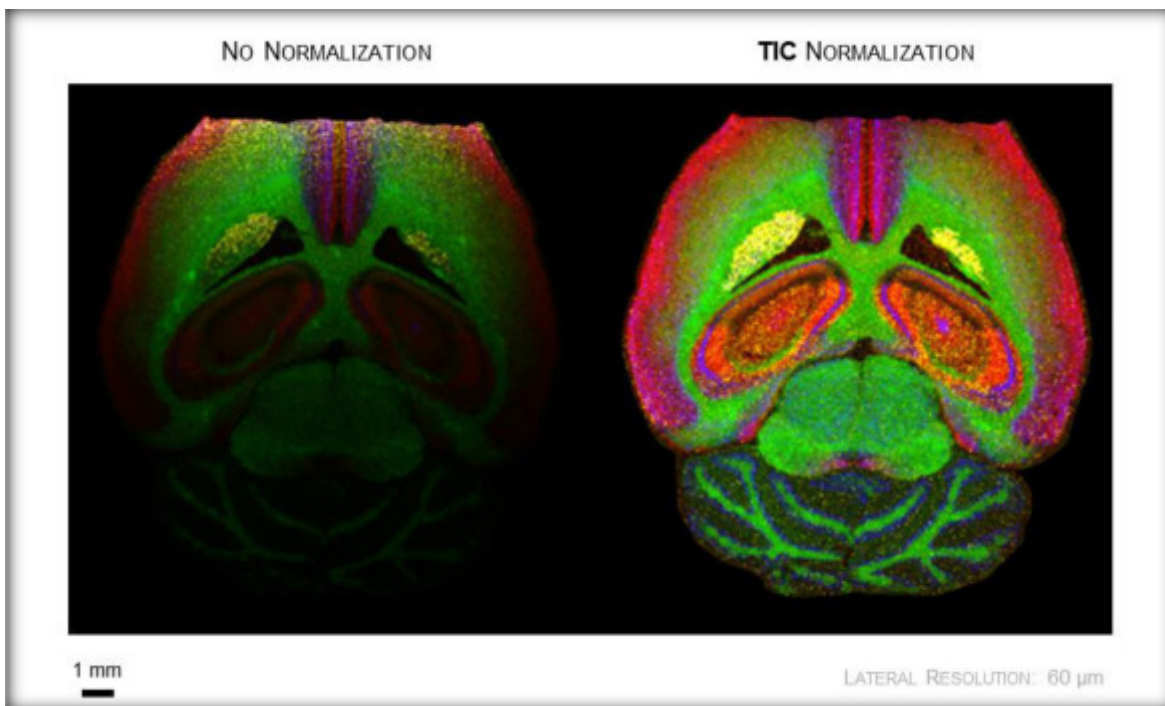


Figure 9: TIC normalization compensating for a gradual decrease in ion transmission during 10 hours of image acquisition. Horizontal mouse brain section (10 μm), Sublimation of SA (0.25 mg/cm^2) and recrystallization with 5% AcOH (3.8 min), lat.res. 60 μm , positive ion mode (linear geometry), 100 shots/spot, 55640 spots.

Among the few different normalization strategies for MSI datasets, TIC normalization is the most commonly implemented algorithm¹⁷⁷. For this, all mass spectra are divided by their TIC so that all spectra in a dataset have the same integrated area under the spectrum, based on the assumption that there is a comparable number of signals in each spectrum^{124, 146}, limiting signal comparison to similar types of tissue¹⁷⁷. MALDI data can be further normalized to matrix related peaks to account for inhomogeneous matrix coating, which mainly depends on the performance of the used matrix application method¹²².

For samples comprising tissue heterogeneity, e.g., whole body sections, normalization to an internal standard (IS) should be considered (*see Incorporation of Internal Standards, chapter GI, p.28*)¹⁷⁸. Each acquired spectrum is normalized to the intensity of the IS, correcting for compound-dependent ionization effects. Preferably, the IS is applied to the tissue prior to matrix application, e.g., by automated spraying^{92, 94, 179}, to ensure consistent dosing over the entire tissue section. However, this strategy may lead to inaccurate results when the targeted analyte is compartmentalized in tissue. Incorporation of isotopically labeled analytes as IS was reported to significantly improve normalization and pixel-to-pixel precision in tissue sections¹⁸⁰⁻¹⁸¹.

G QUANTITATIVE MALDI MSI

Extracting quantitative information from MSI data has proven to be difficult. This is largely due to the high dependency of the MS signal on both, the type of analyte and the local composition of the surface, the previously discussed ion suppression effects (see *Ion Suppression Effects*, chapter 2E, p.26)¹⁸².

While appropriate sample preparation is central to any MSI study, the use of a matrix introduces an additional preparation step for MALDI and has important implications for quantitative analysis¹⁶. The matrix must be homogeneously applied across the entire tissue section while preserving analyte localization (see *MALDI Matrix Choice and Application*, chapter 1B, p.13). The method of matrix application and the matrix itself have also been shown to impact the types of analytes observed¹⁸³. Consequently, matrix and application technique require careful optimization prior to quantitative MSI.

I INCORPORATION OF INTERNAL STANDARDS

One help in the effort for correct quantitation is again the application of an IS against which the signal from the targeted analyte is normalized or calibrated. Incorporation of an IS compensates differences in ionization efficiencies. Furthermore, by external calibration procedures analyte signals can be related to absolute surface concentration. The molecular structure of the IS should be similar to that of the targeted analyte, to ensure similar extraction and ionization efficiencies. IS are ideally labeled versions of the analyte¹⁸⁴, or a structural analog¹⁸⁵. However, one must be aware that the requirement of calibration standards for quantitative MSI demands a targeted analysis that is only applicable to a small fraction of ions observed in the spectrum.

II RELATIVE QUANTITATION

Most studies that utilize MSI use relative quantitation to examine molecular differences in tissues. Ideally, the tissue sections to be compared are measured in a single experiment on the same glass slide, ensuring identical conditions for sample preparation (e.g., standard and matrix application), data acquisition as well as data processing (e.g., normalization). For this, ion signals have to be TIC normalized and the normalized spectral intensities are then compared amongst tissues¹⁸⁶. However, this approach is not without drawbacks, for instance if different regions within a heterogenous sample have to be compared¹⁸² or if abundant signals compartmentalize within a tissue section¹⁷⁷ (see *Ion Suppression Effects*, chapter 2E, p.26). Normalization of the analyte signal can be improved by the addition of an internal standard⁹⁶, enabling confident comparisons of the same molecule even when normalized within different tissue sections⁹³.

III ABSOLUTE QUANTITATION

The simplest method is direct spotting of a standard solution on the blank target, e.g., next to the investigated tissue section, prior to matrix application and data acquisition. Although this technique does not reflect the actual situation for a given analyte being trapped in a complex biomatrix, it allows to determine a tissue extinction coefficient (TEC). The TEC presents an analyte and tissue-specific normalization factor and is calculated via comparison between signal intensities of the analyte spotted on the target versus the same analyte spotted on the tissue section ^{173, 187}. Next, a calibration curve is built on varying standard concentrations (i.e., spotting a dilution series near the dosed tissue) by taking into account the TEC and the mean intensity values of the standards. The TEC approach allows for correlation of the amount of analyte per surface unit ¹⁸⁸. However, the inherent specificity of signal suppression in the function of both the tissue type and analyte demands each analyte of interest to be calibrated in a separate experiment ¹⁷³.

Tissue spotting techniques have been introduced, aiming for analogous extraction of the IS to the analyte present within the tissue ^{184, 181, 189-190}. Therefore, the standards of interest are applied onto or under a separate tissue section, usually a consecutive one mimicking similar biological matrix conditions which are mandatory for reliable quantitation ¹⁸². Yet, tissue spotting approaches do not consider droplet dispersions on the glass slide or tissue. As a consequence, the signal recorded at each level of concentration is plotted against the amount spotted (actual analyte concentration is expressed in mol or g). However, applying an internal standard on the top of the tissue might not accurately reflect the analyte being extracted from beneath the tissue sample, as it may reside atop the tissue and thus provide elevated response for the IS relative to the analyte.

Matrix-matched standards are approaches that incorporate a known amount of IS in a homogenized matrix comprising similar properties to that of the sample ^{182, 191}. In terms of biomedical studies, this homogenized matrix is widely generated from cell or tissue homogenates of the same origin as the sample. Since ion suppression effects and tissue matrix interferences are expected to be similar for the spiked standard and the endogenous analytes, this method is probably the most reliable for determining absolute quantities in MSI. In addition, this calibration strategy holds the advantage of expressing the actual concentration of analyte per gram of tissue. However, for whole body sections, time-consuming sample preparation steps are limiting factors as homogenates must be prepared from each tissue type of interest.

Yet, to confirm absolute quantitation achieved by MSI, results must be cross-validated with an established quantification method, such as traditional LC-MS analysis of tissue extracts ^{184, 181, 190-191}.

H MULTI-MODAL IMAGING

The combination of different modalities offers a comprehensive analytical tool to answer biological questions that could otherwise not be answered. In the field of laterally resolved chemical analysis there is a trend towards the combination of two or more technologies, so called multi-modal imaging (MMI) approaches, to provide more information than offered by a single modality.

While MSI offers high chemical specificity for visualizing and identifying distributions of several molecular species, it lacks the molecular depth that other methods provide and, thus, is typically combined with modalities that complement these features. MSI is often combined with microscopy¹⁹², fluorescence microscopy¹⁹³, near-field infrared microscopy¹⁹⁴, electron microscopy¹⁹⁵, coherent anti-Stokes Raman spectroscopy¹⁹⁶ or Fourier transform infrared (FTIR) spectroscopy¹⁹⁷ to provide high-resolution morphological and structural information.

Because of the variety of ionization modalities, MSI can be multiplexed with itself to analyze different groups of compounds. In particular MALDI can be combined with a range of ionization mechanisms such as SIMS¹⁹⁸⁻¹⁹⁹, DESI²⁰⁰, or LA-ICP-MS²⁰¹⁻²⁰² providing a more comprehensive analysis of the sample.

However, different imaging platforms often demand for distinct sample preparation protocols, which can cause interference for different imaging modalities.

In this case, using consecutive tissue sections might seem most straight-forward. Yet, even two consecutive tissue sections, cut at some tens of micrometer distance show most likely variations in analyte distributions. These differences may originate from the sample itself, because different cells may have different compositions, or from the sample preparation process where tissue sections are not cut accurately enough and have different thicknesses. Therefore, analyzing the same tissue section using two different methods is highly desirable to exclude inter-sample variations but also to guarantee appropriate quality after data combination. The latter is an issue, because image co-registration is challenging especially if data are not acquired at the same spatial resolutions or from the same sample, demanding for sophisticated data processing methods²⁰³.

Therefore, in multi-modal analysis, it is of the utmost importance to adjust the sample preparation strategy for the needs of each imaging modality. LA-ICP-MS is a widely-accepted method for elemental analysis of solid samples²⁰⁴⁻²⁰⁵. Due to its exceptional limits of detection (below the $\mu\text{g g}^{-1}$ -range for most elements), achievable lateral resolutions down to the single-digit μm -scale and a quite extensive range of available possibilities for quantification, this technique has found its way into many disciplines of science²⁰⁶⁻²⁰⁸. Among them, Life Sciences have recently become a wide application range, with LA-ICP-MS offering the possibility of depicting lateral distribution of trace elements in various types of biological samples²⁰⁹⁻²¹¹.

Since LA-ICP-MS and MALDI MS offer complementary analyte information on elements and molecules, excellent insight into the chemical nature of a single tissue section can be gained by combination of these two techniques in a multi-modal imaging approach.

The challenge for combining these two methods is manifold: (a) MSI requires matrix application and mostly sample carriers providing conductive surfaces, (b) on the other hand, LA-ICP-MS is usually completely consuming the sample during analysis. Additionally, MALDI matrices have to be free of the targeted elements, so highly purified matrices have to be used. As a consequence, background signals originating from conductive glass slides have to be studied for elemental analysis (*see manuscript, chapter 7, p.136*).

As FT-IR imaging provides direct molecular specific information in a non-destructive way, no application of a special matrix is needed. Unlike in MALDI MSI, FTIR imaging methods do not instantaneously generate molecular information, but by studying the spectral fingerprint region (700 – 3000 cm⁻¹) particular functional groups in the building blocks of biological tissues can be assigned, i.e., lipids, proteins, carbohydrates, or nucleic acids. Thus, the use of FTIR spectroscopy is ideally suited to, e.g., verify results from MALDI MSI studies. FTIR imaging enables the distinction between healthy and initial-to-advanced states of disease after applying sophisticated data processing routines²¹² and allows only then the discrimination between, e.g., viable and dead cells²¹³. The complementary use of MALDI MS and FTIR imaging is assumed to hold a great potential for the examination of health and disease states in biological tissue samples (*see manuscript, chapter 8, p.175*).

REFERENCES

1. Caprioli, R.M., Farmer, T.B., Gile, J., *Molecular Imaging of Biological Samples: Localization of Peptides and Proteins Using MALDI-TOF MS*, Anal. Chem., **1997**. 69 (23): p. 4751.
2. Chaurand, P., Stoeckli, M., Caprioli, R.M., *Direct Profiling of Proteins in Biological Tissue Sections by MALDI Mass Spectrometry*, Anal. Chem., **1999**. 71 (23): p. 5263.
3. Stoeckli, M., Farmer, T.B., Caprioli, R.M., *Automated mass spectrometry imaging with a matrix-assisted laser desorption ionization time-of-flight instrument*, J. Am. Soc. Mass Spectrom., **1999**. 10 (1): p. 67.
4. Caprioli, R.M., *Perspectives on imaging mass spectrometry in biology and medicine*, Proteomics, **2008**. 8 (18): p. 3679.
5. Norris, J.L., Caprioli, R.M., *Analysis of Tissue Specimens by Matrix-Assisted Laser Desorption/Ionization Imaging Mass Spectrometry in Biological and Clinical Research*, Chem. Rev. , **2013**. 113 (4): p. 2309.
6. Ye, H., Gemperline, E., Li, L., *A vision for better health: Mass spectrometry imaging for clinical diagnostics*, Clin. Chim. Acta, **2013**. 420: p. 11.
7. Stoeckli, M., Chaurand, P., Hallahan, D.E., Caprioli, R.M., *Imaging mass spectrometry: A new technology for the analysis of protein expression in mammalian tissues*, Nat. Med. , **2001**. 7 (4): p. 493.
8. Dreisewerd, K., *Recent methodological advances in MALDI mass spectrometry*, Anal. Bioanal. Chem., **2014**. 406 (9-10): p. 2261.
9. Spengler, B., *Mass Spectrometry Imaging of Biomolecular Information*, Anal. Chem., **2015**. 87 (1): p. 64.
10. Zenobi, R., Knochenmuss, R., *Ion formation in MALDI mass spectrometry*, Mass Spectrom. Rev., **1999**. 17 (5): p. 337.
11. Dreisewerd, K., *The desorption process in MALDI*, Chem. Rev. , **2003**. 103 (2): p. 395.
12. Knochenmuss, R., *Ion formation mechanisms in UV-MALDI*, Analyst, **2006**. 131 (9): p. 966.
13. Knochenmuss, R., Zenobi, R., *MALDI ionization: The role of in-plume processes*, Chem. Rev., **2003**. 103 (2): p. 441.
14. Karas, M., Krueger, R., *Ion formation in MALDI: The cluster ionization mechanism*, Chem. Rev. , **2003**. 103 (2): p. 427.
15. Goodwin, R.J.A., Pennington, S.R., Pitt, A.R., *Protein and peptides in pictures: imaging with MALDI mass spectrometry*, Proteomics, **2008**. 8 (18): p. 3785.
16. Goodwin, R.J.A., *Sample preparation for mass spectrometry imaging: small mistakes can lead to big consequences*, J. Proteomics, **2012**. 75 (16): p. 4893.
17. Chughtai, K., *Mass Spectrometric Imaging for Biomedical Tissue Analysis*, Chem. Rev., **2010**. 110 (5): p. 3237.
18. Zemski, B.K.A., Hankin, J.A., Barkley, R.M., Spraggins, J.M., Caprioli, R.M., Murphy, R.C., *MALDI Imaging of Lipid Biochemistry in Tissues by Mass Spectrometry*, Chem. Rev. , **2011**. 111 (10): p. 6491.
19. Kaletas, B.K., van, d.W.I.M., Stauber, J., Guezell, C., Kros, J.M., Luidier, T.M., Heeren, R.M.A., *Sample preparation issues for tissue imaging by imaging MS*, Proteomics, **2009**. 9 (10): p. 2622.
20. Li, B., Dunham, S.J.B., Dong, Y., Yoon, S., Zeng, M., Sweedler, J.V., *Analytical capabilities of mass spectrometry imaging and its potential applications in food science*, Trends Food Sci. Technol., **2016**. 47: p. 50.
21. Dong, Y., Li, B., Malitsky, S., Rogachev, I., Aharoni, A., Kaftan, F., Svatos, A., Franceschi, P., *Sample Preparation for Mass Spectrometry Imaging of Plant Tissues: A Review*, Front Plant Sci., **2016**. 7: p. 60.
22. Balluff, B., Schoene, C., Hoefler, H., Walch, A., *MALDI imaging mass spectrometry for direct tissue analysis: technological advancements and recent applications*, Histochem. Cell Biol., **2011**. 136 (3): p. 227.

23. Trimpin, S., Herath, T.N., Inutan, E.D., Wager-Miller, J., Kowalski, P., Claude, E., Walker, J.M., Mackie, K., *Automated Solvent-Free Matrix Deposition for Tissue Imaging by Mass Spectrometry*, *Anal. Chem.*, **2010**. *82* (1): p. 359.
24. Hafezparast, M., Ahmad-Annuar, A., Wood, N.W., Tabrizi, S.J., Fisher, E.M.C., *Mouse models for neurological disease*, *Lancet Neurol.*, **2002**. *1* (4): p. 215.
25. Waerzeggers, Y., Monfared, P., Viel, T., Winkeler, A., Jacobs, A.H., *Mouse models in neurological disorders: Applications of non-invasive imaging*, *Biochim. Biophys. Acta*, **2010**. *1802* (10): p. 819.
26. Nimesh, S., Mohottalage, S., Vincent, R., Kumarathasan, P., *Current status and future perspectives of mass spectrometry imaging*, *Int. J. Mol. Sci.*, **2013**. *14* (6): p. 11277.
27. Goodwin, R.J.A., Lang, A.M., Allingham, H., Boren, M., Pitt, A.R., *Stopping the clock on proteomic degradation by heat treatment at the point of tissue excision*, *Proteomics*, **2010**. *10* (9): p. 1751.
28. Franzen, B., Yang, Y., Sunnemark, D., Wickman, M., Ottervald, J., Oppermann, M., Sandberg, K., *Dihydropyrimidinase related protein-2 as a biomarker for temperature and time dependent post mortem changes in the mouse brain proteome*, *Proteomics*, **2003**. *3* (10): p. 1920.
29. Ferrer, I., Santpere, G., Arzberger, T., Bell, J., Blanco, R., Boluda, S., Budka, H., Carmona, M., Giaccone, G., Krebs, B., Limido, L., Parchi, P., Puig, B., Strammiello, R., Stroebel, T., Kretzschmar, H., *Brain protein preservation largely depends on the postmortem storage temperature: implications for study of proteins in human neurologic diseases and management of brain banks: a BrainNet Europe study*, *J. Neuropathol. Exp. Neurol.*, **2007**. *66* (1): p. 35.
30. Crecelius, A., Gotz, A., Arzberger, T., Frohlich, T., Arnold, G.J., Ferrer, I., Kretzschmar, H.A., *Assessing quantitative post-mortem changes in the gray matter of the human frontal cortex proteome by 2-D DIGE*, *Proteomics*, **2008**. *8* (6): p. 1276.
31. Skold, K., Svensson, M., Norrman, M., Sjogren, B., Svenningsson, P., Andren, P.E., *The significance of biochemical and molecular sample integrity in brain proteomics and peptidomics: stathmin 2-20 and peptides as sample quality indicators*, *Proteomics*, **2007**. *7* (24): p. 4445.
32. Jehl, B., Bauer, R., Doerge, A., Rick, R., *The use of propane/isopentane mixtures for rapid freezing of biological specimens*, *J. Microsc.*, **1981**. *123* (3): p. 307.
33. Zaima, N., Hayasaka, T., Goto-Inoue, N., Setou, M., *Matrix-assisted laser desorption/ionization imaging mass spectrometry*, *Int. J. Mol. Sci.*, **2010**. *11*: p. 5040.
34. Chaurand, P., Cornett, D.S., Caprioli, R.M., *Molecular imaging of thin mammalian tissue sections by mass spectrometry*, *Curr. Opin. Biotechnol.*, **2006**. *17* (4): p. 431.
35. Chaurand, P., Sanders, M.E., Jensen, R.A., Caprioli, R.M., *Proteomics in diagnostic pathology: profiling and imaging proteins directly in tissue sections*, *Am. J. Pathol.*, **2004**. *165* (4): p. 1057.
36. Schwartz, S.A., Reyzer, M.L., Caprioli, R.M., *Direct tissue analysis using matrix-assisted laser desorption/ionization mass spectrometry: Practical aspects of sample preparation*, *J. Mass Spectrom.*, **2003**. *38* (7): p. 699.
37. Qing, Z., E, L.-L., Wang, D.-S., Liu, H.-C., *Relationship of advanced oxidative protein products in human saliva and plasma: age- and gender-related changes and stability during storage*, *Free Radical Res.*, **2012**. *46* (10): p. 1201.
38. Che, F.-Y., Lim, J., Pan, H., Biswas, R., Fricker, L.D., *Quantitative neuropeptidomics of microwave-irradiated mouse brain and pituitary*, *Mol. Cell. Proteomics*, **2005**. *4* (9): p. 1391.
39. Svensson, M., Boren, M., Skold, K., Faelth, M., Sjoegren, B., Andersson, M., Svenningsson, P., Andren, P.E., *Heat Stabilization of the Tissue Proteome: A New Technology for Improved Proteomics*, *J. Proteome Res.*, **2009**. *8* (2): p. 974.
40. Rountree, C.B., Van Kirk, C.A., You, H., Ding, W., Dang, H., Van Guilder, H.D., Freeman, W.M., *Clinical application for the preservation of phospho-proteins through in-situ tissue stabilization*, *Proteome Sci.*, **2010**. *8*: p. 61.

41. Crecelius, A.C., Cornett, D.S., Caprioli, R.M., Williams, B., Dawant, B.M., Bodenheimer, B., *Three-Dimensional Visualization of Protein Expression in Mouse Brain Structures Using Imaging Mass Spectrometry*, J. Am. Soc. Mass Spectrom., **2005**. 16 (7): p. 1093.
42. Goto-Inoue, N., Hayasaka, T., Zaima, N., Nakajima, K., Holleran, W.M., Sano, S., Uchida, Y., Setou, M., *Imaging mass spectrometry visualizes ceramides and the pathogenesis of Dorfman-Chanarin syndrome due to ceramide metabolic abnormality in the skin*, PLoS One, **2012**. 7(11): p. e49519.
43. Angel, P.M., Spraggins, J.M., Baldwin, H.S., Caprioli, R., *Enhanced Sensitivity for High Spatial Resolution Lipid Analysis by Negative Ion Mode Matrix Assisted Laser Desorption Ionization Imaging Mass Spectrometry*, Anal. Chem. , **2012**. 84 (3): p. 1557.
44. Wisztorski, M., Franck, J., Salzet, M., Fournier, I., *MALDI direct analysis and imaging of frozen versus FFPE tissues: what strategy for which sample?*, Methods Mol. Biol. , **2010**. 656 (Mass Spectrometry Imaging): p. 303.
45. Chen, R., Hui, L., Sturm, R.M., Li, L., *Three Dimensional Mapping of Neuropeptides and Lipids in Crustacean Brain by Mass Spectral Imaging*, J. Am. Soc. Mass Spectrom., **2009**. 20 (6): p. 1068.
46. Gemperline, E., Jayaraman, D., Maeda, J., Ane, J.-M., Li, L., *Multifaceted Investigation of Metabolites During Nitrogen Fixation in Medicago via High Resolution MALDI-MS Imaging and ESI-MS*, J. Am. Soc. Mass Spectrom., **2015**. 26 (1): p. 149.
47. Verhaert, P.D.E.M., Pinkse, M.W.H., Strupat, K., Conaway, M.C.P., *Imaging of similar mass neuropeptides in neuronal tissue by enhanced resolution MALDI MS with an ion trap - Orbitrap hybrid instrument*, Methods Mol. Biol. , **2010**. 656 (Mass Spectrometry Imaging): p. 433.
48. Gorzolka, K., Bednarz, H., Niehaus, K., *Detection and localization of novel hordatine-like compounds and glycosylated derivatives of hordatines by imaging mass spectrometry of barley seeds*, Planta, **2014**. 239 (6): p. 1321.
49. Khatib-Shahidi, S., Andersson, M., Herman, J.L., Gillespie, T.A., Caprioli, R.M., *Direct Molecular Analysis of Whole-Body Animal Tissue Sections by Imaging MALDI Mass Spectrometry*, Anal. Chem., **2006**. 78 (18): p. 6448.
50. Reyzer, M.L., Chaurand, P., Angel, P.M., Caprioli, R.M., *Direct molecular analysis of whole-body animal tissue sections by MALDI imaging mass spectrometry*, Methods Mol. Biol. , **2010**. 656 (Mass Spectrometry Imaging): p. 285.
51. Caldwell, R.L., Caprioli, R.M., *Tissue profiling by mass spectrometry: A review of methodology and applications*, Mol. Cell. Proteomics, **2005**. 4 (4): p. 394.
52. Peukert, M., Matros, A., Lattanzio, G., Kaspar, S., Abadia, J., Mock, H.-P., *Spatially resolved analysis of small molecules by matrix-assisted laser desorption/ionization mass spectrometric imaging (MALDI-MSI)*, New Phytol., **2012**. 193 (3): p. 806.
53. Chaurand, P., Fouchecourt, S., DaGue, B.B., Xu, B.J., Reyzer, M.L., Orgebin-crist, M.-c., Caprioli, R.M., *Profiling and imaging proteins in the mouse epididymis by imaging mass spectrometry*, Proteomics, **2003**. 3 (11): p. 2221.
54. Chaurand, P., Schriver, K.E., Caprioli, R.M., *Instrument design and characterization for high resolution MALDI-MS imaging of tissue sections*, J. Mass Spectrom., **2007**. 42 (4): p. 476.
55. Goodwin, R.J.A., Nilsson, A., Borg, D., Langridge-Smith, P.R.R., Harrison, D.J., Mackay, C.L., Iverson, S.L., Andren, P.E., *Conductive carbon tape used for support and mounting of both whole animal and fragile heat-treated tissue sections for MALDI MS imaging and quantitation*, J. Proteomics, **2012**. 75 (16): p. 4912.
56. Kawamoto, T., *Use of a new adhesive film for the preparation of multi-purpose fresh-frozen sections from hard tissues, whole-animals, insects and plants*, Arch. Histol. Cytol., **2003**. 66 (2): p. 123.
57. Cha, S., Zhang, H., Ilarslan, H.I., Wurtele, E.S., Brachova, L., Nikolau, B.J., Yeung, E.S., *Direct profiling and imaging of plant metabolites in intact tissues by using colloidal graphite-assisted laser desorption ionization mass spectrometry*, Plant J., **2008**. 55 (2): p. 348.
58. Goodwin, R.J.A., Mackay, C.L., Nilsson, A., Harrison, D.J., Farde, L., Andren, P.E., Iverson, S.L., *Qualitative and Quantitative MALDI Imaging of the Positron Emission Tomography*

- Ligands Raclopride (a D2 Dopamine Antagonist) and SCH 23390 (a D1 Dopamine Antagonist) in Rat Brain Tissue Sections Using a Solvent-Free Dry Matrix Application Method*, Anal. Chem. , **2011**. 83 (24): p. 9694.
59. Castaing, R., Slodzian, G., *Microanalysis by secondary ionic emission*, J. Microsc., **1962**. 1 (6): p. 395.
 60. Bornsen, K.O., *Influence of salts, buffers, detergents, solvents, and matrices on MALDI-MS protein analysis in complex mixtures*, Methods Mol. Biol. , **2000**. 146 (Mass Spectrometry of Proteins and Peptides): p. 387.
 61. Mahboob, T., Mumtaz, M., Haleem, M.A., *Electrolyte content of serum, erythrocyte, kidney and heart tissue in salt induced hypertensive rats*, Life Sci., **1996**. 59 (9): p. 731.
 62. Berman, E.S.F., Fortson, S.L., Checchi, K.D., Wu, L., Felton, J.S., Wu, K.J.J., Kulp, K.S., *Preparation of Single Cells for Imaging/Profiling Mass Spectrometry*, J. Am. Soc. Mass Spectrom., **2008**. 19 (8): p. 1230.
 63. Wang, H.-Y.J., Liu, C.B., Wu, H.-W., *A simple desalting method for direct MALDI mass spectrometry profiling of tissue lipids*, J. Lipid Res., **2011**. 52 (4): p. 840.
 64. Yang, J., Caprioli, R.M., *Matrix Sublimation/Recrystallization for Imaging Proteins by Mass Spectrometry at High Spatial Resolution*, Anal. Chem. , **2011**. 83 (14): p. 5728.
 65. Chaurand, P., Schwartz, S.A., Caprioli, R.M., *Profiling and imaging proteins in tissue sections by MS*, Anal. Chem., **2004**. 76 (5): p. 86A.
 66. Chaurand, P., Norris, J.L., Cornett, D.S., Mobley, J.A., Caprioli, R.M., *New Developments in Profiling and Imaging of Proteins from Tissue Sections by MALDI Mass Spectrometry*, J. Proteome Res., **2006**. 5 (11): p. 2889.
 67. Aerni, H.-R., Cornett, D.S., Caprioli, R.M., *Automated Acoustic Matrix Deposition for MALDI Sample Preparation*, Anal. Chem., **2006**. 78 (3): p. 827.
 68. Seeley, E.H., Oppenheimer, S.R., Mi, D., Chaurand, P., Caprioli, R.M., *Enhancement of Protein Sensitivity for MALDI Imaging Mass Spectrometry After Chemical Treatment of Tissue Sections*, J. Am. Soc. Mass Spectrom., **2008**. 19 (8): p. 1069.
 69. Mainini, V., Bovo, G., Chinello, C., Gianazza, E., Grasso, M., Cattoretti, G., Magni, F., *Detection of high molecular weight proteins by MALDI imaging mass spectrometry*, Mol. BioSyst., **2013**. 9 (6): p. 1101.
 70. Lemaire, R., Wisztorski, M., Desmons, A., Tabet, J.C., Day, R., Salzet, M., Fournier, I., *MALDI-MS Direct Tissue Analysis of Proteins: Improving Signal Sensitivity Using Organic Treatments*, Anal. Chem., **2006**. 78 (20): p. 7145.
 71. Deutskens, F., Yang, J., Caprioli, R.M., *High spatial resolution imaging mass spectrometry and classical histology on a single tissue section*, J. Mass Spectrom., **2011**. 46 (6): p. 568.
 72. Wang, H.-Y.J., Wu, H.-W., Tsai, P.-J., Liu, C.B., *MALDI-mass spectrometry imaging of desalted rat brain sections reveals ischemia-mediated changes of lipids*, Anal. Bioanal. Chem., **2012**. 404 (1): p. 113.
 73. Ellis, S.R., Brown, S.H., in het Panhuis, M., Blanksby, S.J., Mitchell, T.W., *Surface analysis of lipids by mass spectrometry: More than just imaging*, Prog. Lipid Res., **2013**. 52 (4): p. 329.
 74. Holt, S.J., Hicks, R.M., *Studies on formalin fixation for electron microscopy and cytochemical staining purposes*, J. Biophys. Biochem. Cytol., **1961**. 11: p. 31.
 75. De Marzo, A.M., Fedor, H.H., Gage, W.R., Rubin, M.A., *Inadequate formalin fixation decreases reliability of p27Kip1 immunohistochemical staining: probing optimal fixation time using high-density tissue microarrays*, Hum. Pathol., **2002**. 33 (7): p. 756.
 76. Achim, B., Alice, L., Benjamin, B., Na, S., Karin, G., Annette, F., Klaus-Peter, J., JK, K.P., JH, v.d.V.C., Gregor, W., Franziska, E., Rupert, L., Michaela, A., Horst, Z., Michaela, A., Axel, W., *High-resolution MALDI-FT-ICR MS imaging for the analysis of metabolites from formalin-fixed, paraffin-embedded clinical tissue samples*, The Journal of Pathology, **2015**. 237 (1): p. 123.
 77. Carter, C.L., McLeod, C.W., Bunch, J., *Imaging of phospholipids in formalin fixed rat brain sections by matrix assisted laser desorption/ionization mass spectrometry*, J. Am. Soc. Mass Spectrom., **2011**. 22 (11): p. 1991.

78. Griffiths, R.L., Sarsby, J., Guggenheim, E.J., Race, A.M., Steven, R.T., Fear, J., Lalor, P.F., Bunch, J., *Formal Lithium Fixation Improves Direct Analysis of Lipids in Tissue by Mass Spectrometry*, *Anal. Chem.*, **2013**. 85 (15): p. 7146.
79. Palmer, A.D., Griffiths, R., Styles, I., Claridge, E., Calcagni, A., Bunch, J., *Sucrose cryo-protection facilitates imaging of whole eye sections by MALDI mass spectrometry*, *J. Mass Spectrom.*, **2012**. 47 (2): p. 237.
80. Otali, D., Stockard, C.R., Oelschlager, D.K., Wan, W., Manne, U., Watts, S.A., Grizzle, W.E., *Combined effects of formalin fixation and tissue processing on immunorecognition*, *Biotech. Histochem.*, **2009**. 84 (5): p. 223.
81. Kiernan, J.A., *Formaldehyde, formalin, paraformaldehyde and glutaraldehyde: what they are and what they do*, *Microsc. Today*, **2000**. (00-1): p. 8.
82. Ergin, B., Meding, S., Langer, R., Kap, M., Viertler, C., Schott, C., Ferch, U., Riegman, P., Zatloukal, K., Walch, A., Becker, K.-F., *Proteomic Analysis of PAXgene-Fixed Tissues*, *J. Proteome Res.*, **2010**. 9 (10): p. 5188.
83. Chaurand, P., Schwartz, S.A., Billheimer, D., Xu, B.J., Crecelius, A., Caprioli, R.M., *Integrating histology and imaging mass spectrometry*, *Anal. Chem.*, **2004**. 76 (4): p. 1145.
84. Xu, B.J., Caprioli, R.M., Sanders, M.E., Jensen, R.A., *Direct analysis of laser capture microdissected cells by MALDI mass spectrometry*, *J. Am. Soc. Mass Spectrom.*, **2002**. 13 (11): p. 1292.
85. Carreira, R.J., Shyti, R., Balluff, B., Abdelmoula, W.M., van Heiningen, S.H., van Zeijl, R.J., Dijkstra, J., Ferrari, M.D., Tolner, E.A., McDonnell, L.A., van den Maagdenberg, A.M., *Large-scale mass spectrometry imaging investigation of consequences of cortical spreading depression in a transgenic mouse model of migraine*, *J. Am. Soc. Mass Spectrom.*, **2015**. 26 (6): p. 853.
86. Zubair, F., Laibinis, P.E., Swisher, W.G., Yang, J., Spraggins, J.M., Norris, J.L., Caprioli, R.M., *Trypsin and MALDI matrix pre-coated targets simplify sample preparation for mapping proteomic distributions within biological tissues by imaging mass spectrometry*, *J. Mass Spectrom.*, **2016**. 51 (12): p. 1168.
87. Stauber, J., MacAleese, L., Franck, J., Claude, E., Snel, M., Kaletas, B.K., Wiel, I.M.V.D., Wisztorski, M., Fournier, I., Heeren, R.M.A., *On-Tissue Protein Identification and Imaging by MALDI-Ion Mobility Mass Spectrometry*, *J. Am. Soc. Mass Spectrom.*, **2010**. 21 (3): p. 338.
88. Stauber, J., El Ayed, M., Wisztorski, M., Salzet, M., Fournier, I., *Specific MALDI-MSI: TAG-MASS*, *Methods Mol. Biol.*, **2010**. 656 (Mass Spectrometry Imaging): p. 339.
89. Chaurand, P., *Imaging mass spectrometry of thin tissue sections: A decade of collective efforts*, *J. Proteomics*, **2012**. 75 (16): p. 4883.
90. Manier, M.L., Reyzer, M.L., Goh, A., Dartois, V., Via, L.E., Barry, C.E., Caprioli, R.M., *Reagent precoated targets for rapid in-tissue derivatization of the anti-tuberculosis drug isoniazid followed by MALDI imaging mass spectrometry*, *J. Am. Soc. Mass Spectrom.*, **2011**. 22 (8): p. 1409.
91. Beasley, E., Francese, S., Bassindale, T., *Detection and Mapping of Cannabinoids in Single Hair Samples through Rapid Derivatization and Matrix-Assisted Laser Desorption Ionization Mass Spectrometry*, *Anal. Chem.*, **2016**. 88 (20): p. 10328.
92. Barre, F.P.Y., Flinders, B., Garcia, J.P., Jansen, I., Huizing, L.R.S., Porta, T., Creemers, L.B., Heeren, R.M.A., Cillero-Pastor, B., *Derivatization Strategies for the Detection of Triamcinolone Acetonide in Cartilage by Using Matrix-Assisted Laser Desorption/Ionization Mass Spectrometry Imaging*, *Anal. Chem.*, **2016**. 88 (24): p. 12051.
93. Cobice, D.F., Livingstone, D.E.W., Mackay, C.L., Goodwin, R.J.A., Smith, L.B., Walker, B.R., Andrew, R., *Spatial Localization and Quantitation of Androgens in Mouse Testis by Mass Spectrometry Imaging*, *Anal. Chem.*, **2016**. 88 (21): p. 10362.
94. Shariatgorji, M., Nilsson, A., Kallback, P., Goodwin, R.J.A., Schintu, N., Zhang, X., Svenningsson, P., Crossman, A.R., Bezard, E., Andren, P.E., *Direct targeted quantitative molecular imaging of neurotransmitters in brain tissue sections*, *Neuron*, **2014**. 84 (4): p. 697.
95. Wu, Q., Comi, T.J., Li, B., Rubakhin, S.S., Sweedler, J.V., *On-Tissue Derivatization via Electro Spray Deposition for Matrix-Assisted Laser Desorption/Ionization Mass Spectrometry*

- Imaging of Endogenous Fatty Acids in Rat Brain Tissues*, Anal. Chem., **2016**. 88 (11): p. 5988.
96. Holst, S., Heijs, B., de Haan, N., van Zeijl, R.J.M., Briaire-de Bruijn, I.H., van Pelt, G.W., Mehta, A.S., Angel, P.M., Mesker, W.E., Tollenaar, R.A., Drake, R.R., Bovee, J.V.M.G., McDonnell, L.A., Wuhrer, M., *Linkage-Specific in Situ Sialic Acid Derivatization for N-Glycan Mass Spectrometry Imaging of Formalin-Fixed Paraffin-Embedded Tissues*, Anal. Chem. , **2016**. 88 (11): p. 5904.
 97. Gagnon, H., Franck, J., Wisztorski, M., Day, R., Fournier, I., Salzet, M., *Targeted mass spectrometry imaging: specific targeting mass spectrometry imaging technologies from history to perspective*, Prog. Histochem. Cytochem., **2012**. 47 (3): p. 133.
 98. Thiery, G., Shchepinov, M.S., Southern, E.M., Audebourg, A., Audard, V., Terris, B., Gut, I.G., *Multiplex target protein imaging in tissue sections by mass spectrometry - TAMSIM*, Rapid Commun. Mass Spectrom., **2007**. 21 (6): p. 823.
 99. Stoeckli, M., Staab, D., Schweitzer, A., Gardiner, J., Seebach, D., *Imaging of a β -Peptide Distribution in Whole-Body Mice Sections by MALDI Mass Spectrometry*, J. Am. Soc. Mass Spectrom., **2007**. 18 (11): p. 1921.
 100. Hopfgartner, G., Varesio, E., Stoeckli, M., *Matrix-assisted laser desorption/ionization mass spectrometric imaging of complete rat sections using a triple quadrupole linear ion trap*, Rapid Commun. Mass Spectrom., **2009**. 23 (6): p. 733.
 101. Benabdellah, F., Seyer, A., Quinton, L., Touboul, D., Brunelle, A., Laprevote, O., *Mass spectrometry imaging of rat brain sections: nanomolar sensitivity with MALDI versus nanometer resolution by TOF-SIMS*, Anal. Bioanal. Chem., **2010**. 396 (1): p. 151.
 102. Thomas, A., Charbonneau, J.L., Fournaise, E., Chaurand, P., *Sublimation of New Matrix Candidates for High Spatial Resolution Imaging Mass Spectrometry of Lipids: Enhanced Information in Both Positive and Negative Polarities after 1,5-Diaminonaphthalene Deposition*, Anal. Chem. , **2012**. 84 (4): p. 2048.
 103. Sun, G., Yang, K., Zhao, Z., Guan, S., Han, X., Gross, R.W., *Shotgun metabolomics approach for the analysis of negatively charged water-soluble cellular metabolites from mouse heart tissue*, Anal. Chem., **2007**. 79 (17): p. 6629.
 104. Armstrong, D.W., Zhang, L.-K., He, L., Gross, M.L., *Ionic liquids as matrixes for matrix-assisted laser desorption/ionization mass spectrometry*, Anal. Chem., **2001**. 73 (15): p. 3679.
 105. Meriaux, C., Franck, J., Wisztorski, M., Salzet, M., Fournier, I., *Liquid ionic matrixes for MALDI mass spectrometry imaging of lipids*, J. Proteomics, **2010**. 73 (6): p. 1204.
 106. Lemaire, R., Tabet, J.C., Ducoroy, P., Hendra, J.B., Salzet, M., Fournier, I., *Solid Ionic Matrixes for Direct Tissue Analysis and MALDI Imaging*, Anal. Chem., **2006**. 78 (3): p. 809.
 107. Li, Y.L., Gross, M.L., *Ionic-liquid matrices for quantitative analysis by MALDI-TOF mass spectrometry*, J. Am. Soc. Mass Spectrom., **2004**. 15 (12): p. 1833.
 108. Fleith, C., Cantel, S., Subra, G., Mehdi, A., Ciccione, J., Martinez, J., Enjalbal, C., *Laser desorption ionization mass spectrometry of peptides on a hybrid CHCA organic-inorganic matrix*, Analyst, **2014**. 139 (15): p. 3748.
 109. Hou, J., Chen, S., Zhang, N., Liu, H., Wang, J., He, Q., Wang, J., Xiong, S., Nie, Z., *Organic salt NEDC (N-naphthylethylenediamine dihydrochloride) assisted laser desorption ionization mass spectrometry for identification of metal ions in real samples*, Analyst, **2014**. 139 (13): p. 3469.
 110. Bernier, M.C., Wysocki, V.H., Dagan, S., *Laser desorption ionization of small molecules assisted by tungsten oxide and rhenium oxide particles*, J. Mass Spectrom., **2015**. 50 (7): p. 891.
 111. Kruegel, A., Pavlov, J., Attygalle, A.B., *Enhancement of laser desorption ionization mass spectrometric signals of cesium iodide by elemental sulfur*, Rapid Commun. Mass Spectrom., **2013**. 27 (7): p. 763.
 112. Marsico, A.L., Creran, B., Duncan, B., Elci, S.G., Jiang, Y., Onasch, T.B., Wormhoudt, J., Rotello, V.M., Vachet, R.W., *Inkjet-printed gold nanoparticle surfaces for the detection of low molecular weight biomolecules by laser desorption/ionization mass spectrometry*, J. Am. Soc. Mass Spectrom., **2015**. 26 (11): p. 1931.

113. Friesen, W.L., Schultz, B.J., Destino, J.F., Alivio, T.E., Steet, J.R., Banerjee, S., Wood, T.D., *Two-dimensional graphene as a matrix for MALDI imaging mass spectrometry*, J. Am. Soc. Mass Spectrom., **2015**. 26 (11): p. 1963.
114. Dong, X., Cheng, J., Li, J., Wang, Y., *Graphene as a novel matrix for the analysis of small molecules by MALDI-TOF MS*, Anal. Chem., **2010**. 82 (14): p. 6208.
115. Knochenmuss, R., *The matrix suppression effect in matrix-assisted laser desorption/ionization: Application to negative ions and further characteristics*, Rapid Commun. Mass Spectrom., **1998**. 12 p. 529.
116. Knochenmuss, R., Dubois, F., Dale, M.J., Zenobi, R., *The Matrix Suppression Effect and Ionization Mechanisms in Matrix-assisted Laser Desorption/Ionization*, Rapid Commun. Mass Spectrom., **1996**. 10 (8): p. 871.
117. Schwamborn, K., Caprioli, R.M., *Molecular imaging by mass spectrometry - looking beyond classical histology*, Nat. Rev. Cancer, **2010**. 10 (9): p. 639.
118. Mainini, V., Angel, P., Magni, F., Caprioli, R.M., *Detergent enhancement of on-tissue protein analysis by matrix-assisted laser desorption/ionization imaging mass spectrometry*, Rapid Commun. Mass Spectrom., **2011**. 25 (1): p. 199.
119. Djidja, M.-C., Francese, S., Loadman, P.M., Sutton, C.W., Scriven, P., Claude, E., Snel, M.F., Franck, J., Salzet, M., Clench, M.R., *Detergent addition to tryptic digests and ion mobility separation prior to MS/MS improves peptide yield and protein identification for in situ proteomic investigation of frozen and formalin-fixed paraffin-embedded adenocarcinoma tissue sections*, Proteomics, **2009**. 9 (10): p. 2750.
120. Tucker, K.R., Serebryanny, L.A., Zimmerman, T.A., Rubakhin, S.S., Sweedler, J.V., *The modified-bead stretched sample method: Development and application to MALDI-MS imaging of protein localization in the spinal cord*, Chem. Sci., **2011**. 2 (4): p. 785.
121. DeKeyser, S.S., Kutz-Naber, K.K., Schmidt, J.J., Barrett-Wilt, G.A., Li, L., *Imaging Mass Spectrometry of Neuropeptides in Decapod Crustacean Neuronal Tissues*, J. Proteome Res., **2007**. 6 (5): p. 1782.
122. Gemperline, E., Rawson, S., Li, L., *Optimization and Comparison of Multiple MALDI Matrix Application Methods for Small Molecule Mass Spectrometric Imaging*, Anal. Chem. , **2014**. 86 (20): p. 10030.
123. Shimma, S., Sugiura, Y., Hayasaka, T., Hoshikawa, Y., Noda, T., Setou, M., *MALDI-based imaging mass spectrometry revealed abnormal distribution of phospholipids in colon cancer liver metastasis*, J. Chromatogr. B: Anal. Technol. Biomed. Life Sci., **2007**. 855 (1): p. 98.
124. Norris, J.L., Cornett, D.S., Mobley, J.A., Andersson, M., Seeley, E.H., Chaurand, P., Caprioli, R.M., *Processing MALDI mass spectra to improve mass spectral direct tissue analysis*, Int. J. Mass Spectrom., **2007**. 260 (2-3): p. 212.
125. Lagarrigue, M., Becker, M., Lavigne, R., Deininger, S.-O., Walch, A., Aubry, F., Suckau, D., Pineau, C., *Revisiting rat spermatogenesis with MALDI imaging at 20- μ m resolution*, Mol. Cell. Proteomics, **2011**. 10 (3): p. 1.
126. Baluya, D.L., Garrett, T.J., Yost, R.A., *Automated MALDI Matrix Deposition Method with Inkjet Printing for Imaging Mass Spectrometry*, Anal. Chem. , **2007**. 79 (17): p. 6862.
127. Kim, S.H., Shin, C.M., Yoo, J.S., *First application of thermal vapor deposition method to matrix-assisted laser desorption ionization mass spectrometry: determination of molecular mass of bis(p-methyl benzylidene) sorbitol*, Rapid Commun. Mass Spectrom., **1998**. 12 (11): p. 701.
128. Stevenson, E., Breuker, K., Zenobi, R., *Internal energies of analyte ions generated from different matrix-assisted laser desorption/ionization matrices*, J. Mass Spectrom., **2000**. 35 (8): p. 1035.
129. Poetsch, A., Schlusener, D., Florizone, C., Eltis, L., Menzel, C., Rogner, M., Steinert, K., Roth, U., *Improved identification of membrane proteins by MALDI-TOF MS/MS using vacuum sublimated matrix spots on an ultraphobic chip surface*, J. Biomol. Tech., **2008**. 19 (2): p. 129.
130. Roth, M.J., Kim, J., Maresh, E.M., Plymire, D.A., Corbett, J.R., Zhang, J., Patrie, S.M., *Thin-Layer Matrix Sublimation with Vapor-Sorption Induced Co-Crystallization for Sensitive and*

- Reproducible SAMDI-TOF MS Analysis of Protein Biosensors*, J. Am. Soc. Mass Spectrom., **2012**. 23 (10): p. 1661.
131. Kompauer, M., Heiles, S., Spengler, B., *Atmospheric pressure MALDI mass spectrometry imaging of tissues and cells at 1.4- μ m lateral resolution*, Nat. Methods, **2017**. 14 (1): p. 90.
 132. Hankin, J.A., Barkley, R.M., Murphy, R.C., *Sublimation as a Method of Matrix Application for Mass Spectrometric Imaging*, J. Am. Soc. Mass Spectrom., **2007**. 18 (9): p. 1646.
 133. Sadeghi, M., Vertes, A., *Crystallite size dependence of volatilization in matrix-assisted laser desorption ionization*, Appl. Surf. Sci., **1998**. 127-129: p. 226.
 134. Qiao, H., Piyadasa, G., Spicer, V., Ens, W., *Analyte distributions in MALDI samples using MALDI imaging mass spectrometry*, Int. J. Mass Spectrom., **2009**. 281 (1-2): p. 41.
 135. Jaskolla, T.W., Karas, M., Roth, U., Steinert, K., Menzel, C., Reihls, K., *Comparison between vacuum sublimed matrices and conventional dried droplet preparation in MALDI-TOF mass spectrometry*, J. Am. Soc. Mass Spectrom., **2009**. 20 (6): p. 1104.
 136. Bouschen, W., Schulz, O., Eikel, D., Spengler, B., *Matrix vapor deposition/recrystallization and dedicated spray preparation for high-resolution scanning microprobe matrix-assisted laser desorption/ionization imaging mass spectrometry (SMALDI-MS) of tissue and single cells*, Rapid Commun. Mass Spectrom., **2010**. 24 (3): p. 355.
 137. O'Rourke, M.B., Djordjevic, S.P., Padula, M.P., *A non-instrument-based method for the analysis of formalin-fixed paraffin-embedded human spinal cord via matrix-assisted laser desorption/ionisation imaging mass spectrometry*, Rapid Commun. Mass Spectrom., **2015**. 29 (19): p. 1836.
 138. Yamamoto, T., *Study of experimental conditions for MALDI Imaging by using highly controlled sublimation technique*, ASMS **2015**. p.
 139. Shimadzu, *Matrix Vapor Deposition System iMLayer*, **2015**. p.
 140. Garrett, T.J., Prieto-Conaway, M.C., Kovtoun, V., Bui, H., Izgarian, N., Stafford, G., Yost, R.A., *Imaging of small molecules in tissue sections with a new intermediate-pressure MALDI linear ion trap mass spectrometer*, Int. J. Mass Spectrom., **2007**. 260 (2): p. 166.
 141. Wiley, W.C., McLaren, I.H., *Time-of-flight mass spectrometer with improved resolution*, Rev. Sci. Instrum., **1955**. 26: p. 1150.
 142. Whittall, R.M., Li, L., *High-Resolution Matrix-Assisted Laser Desorption/Ionization in a Linear Time-of-Flight Mass Spectrometer*, Anal. Chem., **1995**. 67 (13): p. 1950.
 143. Juhasz, P., Roskey, M.T., Smirnov, I.P., Haff, L.A., Vestal, M.L., Martin, S.A., *Applications of Delayed Extraction Matrix-Assisted Laser Desorption Ionization Time-of-Flight Mass Spectrometry to Oligonucleotide Analysis*, Anal. Chem., **1996**. 68 (6): p. 941.
 144. Jungmann, J.H., Heeren, R.M., *Emerging technologies in mass spectrometry imaging*, J. Proteomics, **2012**. 75 (16): p. 5077.
 145. Taban, I.M., Altelaar, A.F., van der Burgt, Y.E., McDonnell, L.A., Heeren, R.M., Fuchser, J., Baykut, G., *Imaging of peptides in the rat brain using MALDI-FTICR mass spectrometry*, J. Am. Soc. Mass Spectrom., **2007**. 18 (1): p. 145.
 146. Fonville, J.M., Carter, C., Cloarec, O., Nicholson, J.K., Lindon, J.C., Bunch, J., Holmes, E., *Robust data processing and normalization strategy for MALDI mass spectrometric imaging*, Anal. Chem., **2012**. 84 (3): p. 1310.
 147. Fonville, J.M., Carter, C.L., Pizarro, L., Steven, R.T., Palmer, A.D., Griffiths, R.L., Lalor, P.F., Lindon, J.C., Nicholson, J.K., Holmes, E., Bunch, J., *Hyperspectral visualization of mass spectrometry imaging data*, Anal. Chem., **2013**. 85 (3): p. 1415.
 148. Källback, P., Shariatgorji, M., Nilsson, A., Andren, P.E., *Novel mass spectrometry imaging software assisting labeled normalization and quantitation of drugs and neuropeptides directly in tissue sections*, J. Proteomics, **2012**. 75 (16): p. 4941.
 149. Bro, R., Smilde, A.K., *Principal component analysis*, Anal. Methods, **2014**. 6 (9): p. 2812.
 150. Deininger, S.O., Ebert, M.P., Futterer, A., Gerhard, M., Rocken, C., *MALDI imaging combined with hierarchical clustering as a new tool for the interpretation of complex human cancers*, J. Proteome Res., **2008**. 7 (12): p. 5230.
 151. Deininger, S.O., Becker, M., Suckau, D., *Tutorial: multivariate statistical treatment of imaging data for clinical biomarker discovery*, Methods Mol. Biol., **2010**. 656: p. 385.

152. Rompp, A., Guenther, S., Takats, Z., Spengler, B., *Mass spectrometry imaging with high resolution in mass and space (HR(2) MSI) for reliable investigation of drug compound distributions on the cellular level*, *Anal. Bioanal. Chem.*, **2011**. 401 (1): p. 65.
153. Schramm, T., Hester, A., Klinkert, I., Both, J.P., Heeren, R.M., Brunelle, A., Laprevote, O., Desbenoit, N., Robbe, M.F., Stoeckli, M., Spengler, B., Rompp, A., *imzML--a common data format for the flexible exchange and processing of mass spectrometry imaging data*, *J. Proteomics*, **2012**. 75 (16): p. 5106.
154. Race, A.M., Styles, I.B., Bunch, J., *Inclusive sharing of mass spectrometry imaging data requires a converter for all*, *J. Proteomics*, **2012**. 75 (16): p. 5111.
155. Boxer, S.G., Kraft, M.L., Weber, P.K., *Advances in imaging secondary ion mass spectrometry for biological samples*, *Annu. Rev. Biophys.*, **2009**. 38: p. 53.
156. Yang, J., Caprioli, R.M., *Matrix Sublimation/Recrystallization for Imaging Proteins by Mass Spectrometry at High Spatial Resolution*, *Anal. Chem. (Washington, DC, U. S.)*, **2011**. 83 (14): p. 5728.
157. Guenther, S., Roempp, A., Kummer, W., Spengler, B., *AP-MALDI imaging of neuropeptides in mouse pituitary gland with 5 μ m spatial resolution and high mass accuracy*, *Int. J. Mass Spectrom.*, **2011**. 305 (2-3): p. 228.
158. Schober, Y., Guenther, S., Spengler, B., Roempp, A., *Single Cell Matrix-Assisted Laser Desorption/Ionization Mass Spectrometry Imaging*, *Anal. Chem.*, **2012**. 84 (15): p. 6293.
159. Murray, K.K., Seneviratne, C.A., Ghorai, S., *High resolution laser mass spectrometry bioimaging*, *Methods* **2016**. 104: p. 118.
160. Cahill, J.F., Kertesz, V., Van Berkel, G.J., *Characterization and Application of a Hybrid Optical Microscopy/Laser Ablation Liquid Vortex Capture/Electrospray Ionization System for Mass Spectrometry Imaging with Sub-micrometer Spatial Resolution*, *Anal. Chem.*, **2015**. 87 (21): p. 11113.
161. Hieta, J.-P., Vaikkinen, A., Auno, S., Raikkonen, H., Haapala, M., Scotti, G., Kopra, J., Piepponen, P., Kauppila, T.J., *A Simple Method for Improving the Spatial Resolution in Infrared Laser Ablation Mass Spectrometry Imaging*, *J. Am. Soc. Mass Spectrom.*, **2017**. 28 (6): p. 1060.
162. Feenstra, A.D., Duenas, M.E., Lee, Y.J., *Five Micron High Resolution MALDI Mass Spectrometry Imaging with Simple, Interchangeable, Multi-Resolution Optical System*, *J. Am. Soc. Mass Spectrom.*, **2017**. 28 (3): p. 434.
163. Jurchen, J.C., Rubakhin, S.S., Sweedler, J.V., *MALDI-MS Imaging of Features Smaller than the Size of the Laser Beam*, *J. Am. Soc. Mass Spectrom.*, **2005**. 16 (10): p. 1654.
164. Snel, M.F., Fuller, M., *High-Spatial Resolution Matrix-Assisted Laser Desorption Ionization Imaging Analysis of Glucosylceramide in Spleen Sections from a Mouse Model of Gaucher Disease*, *Anal. Chem.*, **2010**. 82 (9): p. 3664.
165. Thiery-Lavenant, G., Zavalin, A.I., Caprioli, R.M., *Targeted Multiplex Imaging Mass Spectrometry in Transmission Geometry for Subcellular Spatial Resolution*, *J. Am. Soc. Mass Spectrom.*, **2013**. 24 (4): p. 609.
166. Spraggins, J.M., Caprioli, R.M., *High-Speed MALDI-TOF Imaging Mass Spectrometry: Rapid Ion Image Acquisition and Considerations for Next Generation Instrumentation*, *J. Am. Soc. Mass Spectrom.*, **2011**. 22 (6): p. 1022.
167. O'Rourke, M.B., Djordjevic, S.P., Padula, M.P., *The quest for improved reproducibility in MALDI mass spectrometry*, *Mass Spectrom. Rev.*, **2016**. 37 (2): p. 217.
168. Potočník, N.O., Porta, T., Becker, M., Heeren, R.M.A., Ellis, S.R., *Use of advantageous, volatile matrices enabled by next-generation high-speed matrix-assisted laser desorption/ionization time-of-flight imaging employing a scanning laser beam*, *Rapid Commun. Mass Spectrom.*, **2015**. 29 (23): p. 2195.
169. Prentice, B.M., Chumbley, C.W., Caprioli, R.M., *High-speed MALDI MS/MS imaging mass spectrometry using continuous raster sampling*, *J. Mass Spectrom.*, **2015**. 50 (4): p. 703.
170. Prentice, B.M., Caprioli, R.M., *The Need for Speed in Matrix-Assisted Laser Desorption/Ionization Imaging Mass Spectrometry*, *Postdoc J.*, **2016**. 4 (3): p. 3.

171. Ellis, S.R., Cappell, J., Potocnik, N.O., Balluff, B., Hamaide, J., Van der Linden, A., Heeren, R.M.A., *More from less: high-throughput dual polarity lipid imaging of biological tissues*, *Analyst*, **2016**. 141 (12): p. 3832.
172. Knochenmuss, R., *MALDI and Related Methods: A Solved Problem or Still a Mystery?*, *Mass Spectrom.*, **2013**. 2 (Spec Iss): p. S0006.
173. Stoeckli, M., Staab, D., Schweitzer, A., *Compound and metabolite distribution measured by MALDI mass spectrometric imaging in whole-body tissue sections*, *Int. J. Mass Spectrom.*, **2007**. 260 (2): p. 195.
174. Baggerly, K.A., Morris, J.S., Wang, J., Gold, D., Xiao, L.C., Coombes, K.R., *A comprehensive approach to the analysis of matrix-assisted laser desorption/ionization-time of flight proteomics spectra from serum samples*, *Proteomics*, **2003**. 3 (9): p. 1667.
175. Morris, J.S., Coombes, K.R., Koomen, J., Baggerly, K.A., Kobayashi, R., *Feature extraction and quantification for mass spectrometry in biomedical applications using the mean spectrum*, *Bioinformatics*, **2005**. 21 (9): p. 1764.
176. Villanueva, J., Philip, J., Chaparro, C.A., Li, Y., Toledo-Crow, R., DeNoyer, L., Fleisher, M., Robbins, R.J., Tempst, P., *Correcting common errors in identifying cancer-specific serum peptide signatures*, *J. Proteome Res.*, **2005**. 4 (4): p. 1060.
177. Deininger, S.-O., Cornett, D.S., Paape, R., Becker, M., Pineau, C., Rauser, S., Walch, A., Wolski, E., *Normalization in MALDI-TOF imaging datasets of proteins: practical considerations*, *Anal. Bioanal. Chem.*, **2011**. 401 (1): p. 167.
178. Bokhart, M.T., Rosen, E., Thompson, C., Sykes, C., Kashuba, A.D.M., Muddiman, D.C., *Quantitative mass spectrometry imaging of emtricitabine in cervical tissue model using infrared matrix-assisted laser desorption electrospray ionization*, *Anal. Bioanal. Chem.*, **2015**. 407 (8): p. 2073.
179. Heijs, B., Tolner, E.A., Bovee, J.V.M.G., van den Maagdenberg, A.M.J.M., McDonnell, L.A., *Brain Region-Specific Dynamics of On-Tissue Protein Digestion Using MALDI Mass Spectrometry Imaging*, *J. Proteome Res.*, **2015**. 14 (12): p. 5348.
180. Källback, P., Nilsson, A., Shariatgorji, M., Andrén, P.E., *mslQuant – Quantitation Software for Mass Spectrometry Imaging Enabling Fast Access, Visualization, and Analysis of Large Data Sets*, *Anal. Chem.*, **2016**. 88 (8): p. 4346.
181. Chumbley, C.W., Reyzer, M.L., Allen, J.L., Marriner, G.A., Via, L.E., Barry, C.E., Caprioli, R.M., *Absolute Quantitative MALDI Imaging Mass Spectrometry: A Case of Rifampicin in Liver Tissues*, *Anal. Chem.*, **2016**. 88 (4): p. 2392.
182. Hansen, H.T., Janfelt, C., *Aspects of Quantitation in Mass Spectrometry Imaging Investigated on Cryo-Sections of Spiked Tissue Homogenates*, *Anal. Chem.*, **2016**. 88 (23): p. 11513.
183. Goodwin, R.J.A., Scullion, P., MacIntyre, L., Watson, D.G., Pitt, A.R., *Use of a Solvent-Free Dry Matrix Coating for Quantitative Matrix-Assisted Laser Desorption Ionization Imaging of 4-Bromophenyl-1,4-diazabicyclo(3.2.2)nonane-4-carboxylate in Rat Brain and Quantitative Analysis of the Drug from Laser Microdissected Tissue Regions*, *Anal. Chem.*, **2010**. 82 (9): p. 3868.
184. Pirman, D.A., Reich, R.F., Kiss, A., Heeren, R.M.A., Yost, R.A., *Quantitative MALDI Tandem Mass Spectrometric Imaging of Cocaine from Brain Tissue with a Deuterated Internal Standard*, *Anal. Chem.*, **2013**. 85 (2): p. 1081.
185. Prideaux, B., Dartois, V., Staab, D., Weiner, D.M., Goh, A., Via, L.E., Barry, C.E., 3rd, Stoeckli, M., *High-sensitivity MALDI-MRM-MS imaging of moxifloxacin distribution in tuberculosis-infected rabbit lungs and granulomatous lesions*, *Anal. Chem.*, **2011**. 83 (6): p. 2112.
186. Lazova, R., Seeley, E.H., Keenan, M., Gueorguieva, R., Caprioli, R.M., *Imaging Mass Spectrometry—A New and Promising Method to Differentiate Spitz Nevi From Spitzoid Malignant Melanomas*, *Am. J. Dermatopathol.*, **2012**. 34 (1): p. 82.
187. Hamm, G., Bonnel, D., Michel, C., Legouffe, R., Pamelard, F., Hochart, G., Stauber, J., *Toward Quantitative Imaging Mass Spectrometry*, *Curr. Mass Spectrom.*, **2012**. p. 36.

188. Hamm, G., Bonnel, D., Legouffe, R., Pamelard, F., Delbos, J.M., Bouzom, F., Stauber, J., *Quantitative mass spectrometry imaging of propranolol and olanzapine using tissue extinction calculation as normalization factor*, *J. Proteomics*, **2012**. 75 (16): p. 4952.
189. Nilsson, A., Fehniger, T.E., Gustavsson, L., Andersson, M., Kenne, K., Marko-Varga, G., Andrén, P.E., *Fine Mapping the Spatial Distribution and Concentration of Unlabeled Drugs within Tissue Micro-Compartments Using Imaging Mass Spectrometry*, *PLoS One*, **2010**. 5 (7): p. e11411.
190. Prentice, B.M., Chumbley, C.W., Caprioli, R.M., *Absolute Quantification of Rifampicin by MALDI Imaging Mass Spectrometry Using Multiple TOF/TOF Events in a Single Laser Shot*, *J. Am. Soc. Mass Spectrom.*, **2017**. 28 (1): p. 136.
191. Groseclose, M.R., Castellino, S., *A Mimetic Tissue Model for the Quantification of Drug Distributions by MALDI Imaging Mass Spectrometry*, *Anal. Chem.*, **2013**. 85 (21): p. 10099.
192. Van de Plas, R., Yang, J., Spraggins, J., Caprioli, R.M., *Image fusion of mass spectrometry and microscopy: a multimodality paradigm for molecular tissue mapping*, *Nat. Methods*, **2015**. 12 (4): p. 366.
193. Mascini, N.E., Cheng, M., Jiang, L., Rizwan, A., Podmore, H., Bhandari, D.R., Roempp, A., Glunde, K., Heeren, R.M.A., *Mass Spectrometry Imaging of the Hypoxia Marker Pimonidazole in a Breast Tumor Model*, *Anal. Chem.*, **2016**. 88 (6): p. 3107.
194. Aoyagi, S., Abe, K., Yamagishi, T., Iwai, H., Yamaguchi, S., Sunohara, T., *Evaluation of blood adsorption onto dialysis membranes by time-of-flight secondary ion mass spectrometry and near-field infrared microscopy*, *Anal. Bioanal. Chem.*, **2017**. 409 (27): p. 6387.
195. Vollnhals, F., Audinot, J.-N., Wirtz, T., Mercier-Bonin, M., Fourquaux, I., Schroepel, B., Kraushaar, U., Lev-Ram, V., Ellisman, M.H., Eswara, S., *Correlative Microscopy Combining Secondary Ion Mass Spectrometry and Electron Microscopy: Comparison of Intensity-Hue-Saturation and Laplacian Pyramid Methods for Image Fusion*, *Anal. Chem.*, **2017**. 89 (20): p. 10702.
196. Marty, F., Rago, G., Smith, D.F., Gao, X., Eijkel, G.B., MacAleese, L., Bonn, M., Brunner, E., Basler, K., Heeren, R.M.A., *Combining Time-of-Flight Secondary Ion Mass Spectrometry Imaging Mass Spectrometry and CARS Microspectroscopy Reveals Lipid Patterns Reminiscent of Gene Expression Patterns in the Wing Imaginal Disc of *Drosophila melanogaster**, *Anal. Chem.*, **2017**. 89 (18): p. 9664.
197. Balbekova, A., Bonta, M., Toeroek, S., Ofner, J., Doeme, B., Limbeck, A., Lendl, B., *FTIR-spectroscopic and LA-ICP-MS imaging for combined hyperspectral image analysis of tumor models*, *Anal. Methods*, **2017**. 9 (37): p. 5464.
198. Lanni, E.J., Dunham, S.J.B., Nemes, P., Rubakhin, S.S., Sweedler, J.V., *Biomolecular Imaging with a C60-SIMS/MALDI Dual Ion Source Hybrid Mass Spectrometer: Instrumentation, Matrix Enhancement, and Single Cell Analysis*, *J. Am. Soc. Mass Spectrom.*, **2014**. 25 (11): p. 1897.
199. Desbenoit, N., Walch, A., Spengler, B., Brunelle, A., Römpf, A., *Correlative mass spectrometry imaging, applying time-of-flight secondary ion mass spectrometry and atmospheric pressure matrix-assisted laser desorption/ionization to a single tissue section*, *Rapid Commun. Mass Spectrom.*, **2018**. 32 (2): p. 159.
200. Eberlin, L.S., Liu, X., Ferreira, C.R., Santagata, S., Agar, N.Y.R., Cooks, R.G., *Desorption Electrospray Ionization then MALDI Mass Spectrometry Imaging of Lipid and Protein Distributions in Single Tissue Sections*, *Anal. Chem.*, **2011**. 83 (22): p. 8366.
201. Bianga, J., Bouslimani, A., Bec, N., Quenet, F., Mounicou, S., Szpunar, J., Bouyssiere, B., Lobinski, R., Larroque, C., *Complementarity of MALDI and LA ICP mass spectrometry for platinum anticancer imaging in human tumor*, *Metallomics*, **2014**. 6 (8): p. 1382.
202. Niehoff, A.-C., Schulz, J., Soltwisch, J., Meyer, S., Kettling, H., Sperling, M., Jeibmann, A., Dreisewerd, K., Francesconi, K.A., Schwerdtle, T., Karst, U., *Imaging by Elemental and Molecular Mass Spectrometry Reveals the Uptake of an Arsenolipid in the Brain of *Drosophila melanogaster**, *Anal. Chem.*, **2016**. 88 (10): p. 5258.

203. Eliceiri, K.W., Berthold, M.R., Goldberg, I.G., Ibanez, L., Manjunath, B.S., Martone, M.E., Murphy, R.F., Peng, H., Plant, A.L., Roysam, B., Stuurmann, N., Swedlow, J.R., Tomancak, P., Carpenter, A.E., *Biological imaging software tools*, Nat. Methods, **2012**. 9 (10): p. 1031.
204. Russo, R.E., Mao, X., Liu, H., Gonzalez, J., Mao, S.S., *Laser ablation in analytical chemistry - a review*, Talanta, **2002**. 57 (3): p. 425.
205. Günther, D., Hattendorf, B., *Solid sample analysis using laser ablation inductively coupled plasma mass spectrometry*, TrAC **2005**. 24 (3): p. 255.
206. Becker, J.S., *Applications of inductively coupled plasma mass spectrometry and laser ablation inductively coupled plasma mass spectrometry in materials science*, Spectrochim. Acta B, **2002**. 57 (12): p. 1805.
207. Resano, M., Garcia-Ruiz, E., Vanhaecke, F., *Laser ablation-inductively coupled plasma mass spectrometry in archaeometric research*, Mass Spectrom. Rev., **2009**. 29 (1): p. 55.
208. Orellana, F.A., Gálvez, C.G., Orellana, F.A., Gálvez, C.G., Roldán, M.T., García-Ruiz, C., Roldán, M.T., García-Ruiz, C., *Applications of laser-ablation-inductively-coupled plasma-mass spectrometry in chemical analysis of forensic evidence*, TrAC **2013**. 42: p. 1.
209. Limbeck, A., Galler, P., Bonta, M., Bauer, G., Nischkauer, W., Vanhaecke, F., *Recent advances in quantitative LA-ICP-MS analysis: challenges and solutions in the life sciences and environmental chemistry*, Anal. Bioanal. Chem., **2015**. 407 (22): p. 6593.
210. Becker, J.S., Zoriy, M., Matusch, A., Wu, B., Salber, D., Palm, C., Becker, J.S., *Bioimaging of metals by laser ablation inductively coupled plasma mass spectrometry (LA-ICP-MS)*, Mass Spectrom. Rev., **2009**. 29 (1): p. 156.
211. Drescher, D., Giesen, C., Traub, H., Panne, U., Kneipp, J., Jakubowski, N., *Quantitative Imaging of Gold and Silver Nanoparticles in Single Eukaryotic Cells by Laser Ablation ICP-MS*, Anal. Chem. , **2012**. 84 (22): p. 9684.
212. Naumann, D., *FT-infrared and FT-Raman spectroscopy in biomedical research*, Appl. Spectrosc. Rev., **2001**. 36 (2 & 3): p. 239.
213. Zelig, U., Kapelushnik, J., Moreh, R., Mordechai, S., Nathan, I., *Diagnosis of Cell Death by Means of Infrared Spectroscopy*, Biophys. J., **2009**. 97 (7): p. 2107.

3 SUMMARY OF RESULTS

In this section, a brief summary of the manuscripts and articles included in this thesis is presented.

MANUSCRIPT:

DETAILS SEE CHAPTER 4, P. 54

| for submission to *Angewandte Chemie, International Edition* |

SUBLIMATION APPARATUS TO PUSH MALDI MS IMAGING BELOW THE CELLULAR LEVEL.

Matthias Holzlechner, Johannes Frank, Kurt Piplits, Theo Luider, Günter Allmaier, and Martina Marchetti-Deschmann.

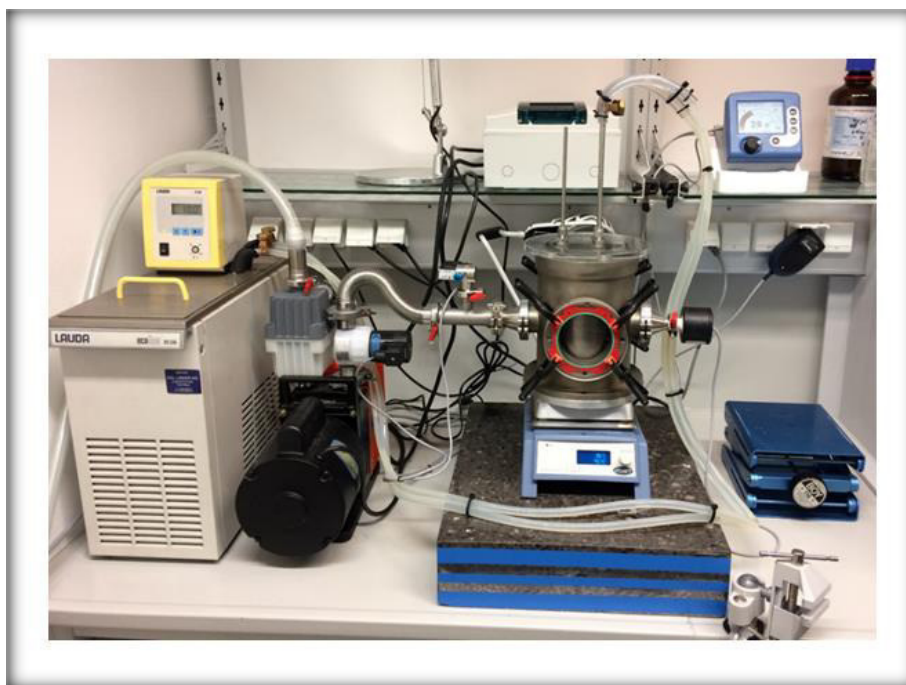


Figure 10: *Sublimation Apparatus to Push MALDI MS Imaging Below the Cellular Level*, graphical abstract. Inhouse-built sublimation apparatus.

In MALDI MSI, matrix deposition is a critical issue in terms of reproducibility and crystal size, both limiting the obtainable spatial resolution. Many different techniques have been published and sublimation was successfully applied for lipid analysis and tissue sections, using with the latter one a subsequent hydration/recrystallization process for peptide/protein analysis. Commercial sublimation devices are limited in availability and in number of glass slides to be prepared in parallel. In order to

overcome this limitation, we built a sublimation device allowing reproducible sample preparation on several ITO slides simultaneously.

Matrix deposition in the home-built sublimation apparatus showed a high reproducibility (RSD < 5%) on up to 3 ITO slides in parallel due to a vacuum-sealed, pressure-controlled matrix deposition chamber with constant heating for matrix vaporization and controlled cooling of the sample plate. Using predefined matrix concentrations and volumes give well defined coatings per unit areas. Secondary electron microscopy (SEM) analysis of the prepared surfaces showed significantly reduced matrix crystal sizes (< 1 μm) compared to aerosol-based application leading ultimately to improved lateral MALDI MSI resolution, because it is now restricted only to the laser spot diameter. Matrix crystal size and shape did not differ significantly when sublimed on ITO slides or tissue, not even after hydration/recrystallization. White light interferometer (WLI) investigations showed homogenous thickness of matrix coating and deposition across the ITO surface, the latter also confirmed by MALDI MSI.

INNOVATIVE ASPECTS

- high reproducibility of sublimation was obtained by predefining matrix concentrations and volumes; sublimation of 1 slide (1.2% RSD), 2 slides (2.4% RSD) and 3 slides (4.9% RSD)
- sub- μm to nm-scaled matrix crystals for matrices SA, CHCA, 2,5-DHB and 1,5-DAN
- significant decrease of sublimation temperatures and time (< 15min)
- minor matrix amount needed (< 25.5 mg per matrix) due to quantitative evaporation

OWN CONTRIBUTION

In this work, I

- was involved in planning the experiment,
- contributed to the design and set up the sublimation device,
- performed MALDI MSI studies, evaluated and interpreted the data,
- drafted and wrote major parts of the manuscript.

| published in *Proteomics* (2016) 16(11-12), 1742-1746 |

VISUALIZING FUNGAL METABOLITES DURING MYCOPARASITIC INTERACTION BY MALDI MASS SPECTROMETRY IMAGING.

Matthias Holzlechner, Sonja Reitschmidt, Sabine Gruber, Susanne Zeilinger-Migsich, and Martina Marchetti-Deschmann.

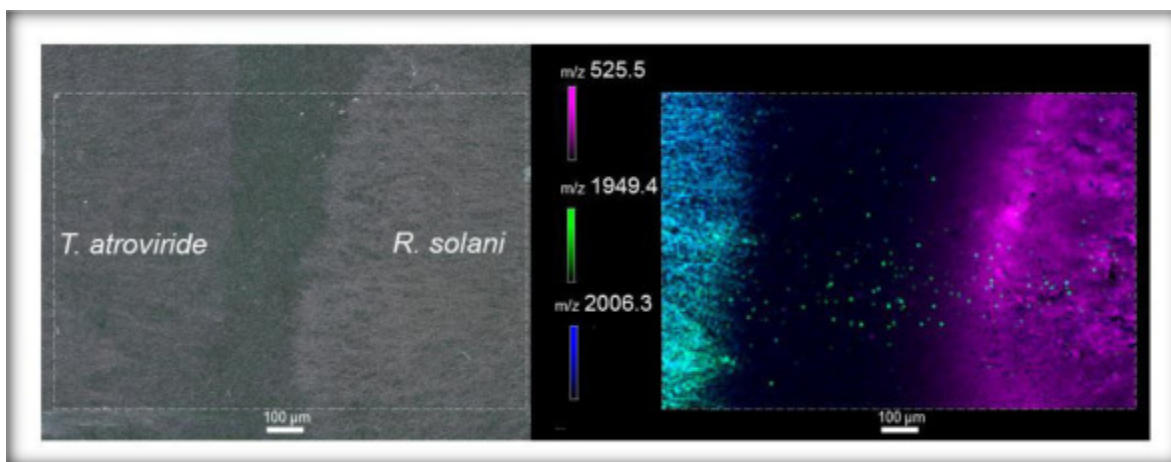


Figure 11: Visualizing Fungal Metabolites During Mycoparasitic Interaction by MALDI Mass Spectrometry Imaging, graphical abstract. Visualization of metabolites during the phase of host-sensing.

The use of antagonistic organisms interfering with plant pathogens is an environmentally friendly and sustainable alternative in plant disease control. *Trichoderma atroviride* is a mycoparasite, killing the pathogen while promoting growth and resistance of the host. The processes leading to mycoparasitism are rather complex, yet sensing of the host, the active release of small molecules and enzymes and the subsequent penetration of host hyphae are key events in a simplified 2-way model. However, studying microbial interactions by MALDI MSI directly from growing media is a difficult task if high sensitivity is demanded. Therefore, we developed a quick and robust sample preparation strategy suitable for studying mycoparasite-host interactions of *Rhizoctonia solani* and *Trichoderma atroviride* directly from cultivation.

MALDI MSI revealed several distinct local distributions of metabolites for both, non-interacting and physically interacting hyphae specifically assignable to either *T.atroviride* or *R.solani*. Potential representatives of peptaibols with chain lengths of 11, 18 and 20 residues could be detected along with metabolites being predominantly released by *R.solani*. Additionally, *T.atroviride* showed analytes being produced at an early growth stage to allow for migration towards *R.solani*. We attribute this

achievement to an enhanced sample preparation strategy facilitating a miniaturized confrontation assay carried out directly on glass slides. Furthermore, MALDI matrix application by sublimation in combination with thorough recrystallization/hydration ensured good analyte extraction from the agar medium and incorporation into the matrix crystals.

INNOVATIVE ASPECTS

- visualization of secondary metabolites during mycoparasitism
- miniaturized potato dextrose agar platform set up for a confrontation assay
- visualization of metabolite changes during host-pathogen interaction

OWN CONTRIBUTION

In this work, I

- was involved in planning and designing the MALDI MSI part of the experiment,
- performed the MALDI MS studies and visualized peptaibol distributions,
- drafted and wrote major parts of the manuscript.

| published in *Journal of Proteome Research* (2017), 16(1), 65-76 |

***IN SITU CHARACTERIZATION OF TISSUE-RESIDENT IMMUNE CELLS BY
MALDI MASS SPECTROMETRY IMAGING.***

Matthias Holzlechner, Katharina Strasser, Elitsa Zareva, Luise Steinhäuser, Hanna Birnleitner, Andrea Beer, Michael Bergmann, Rudolf Oehler, and Martina Marchetti-Deschmann.

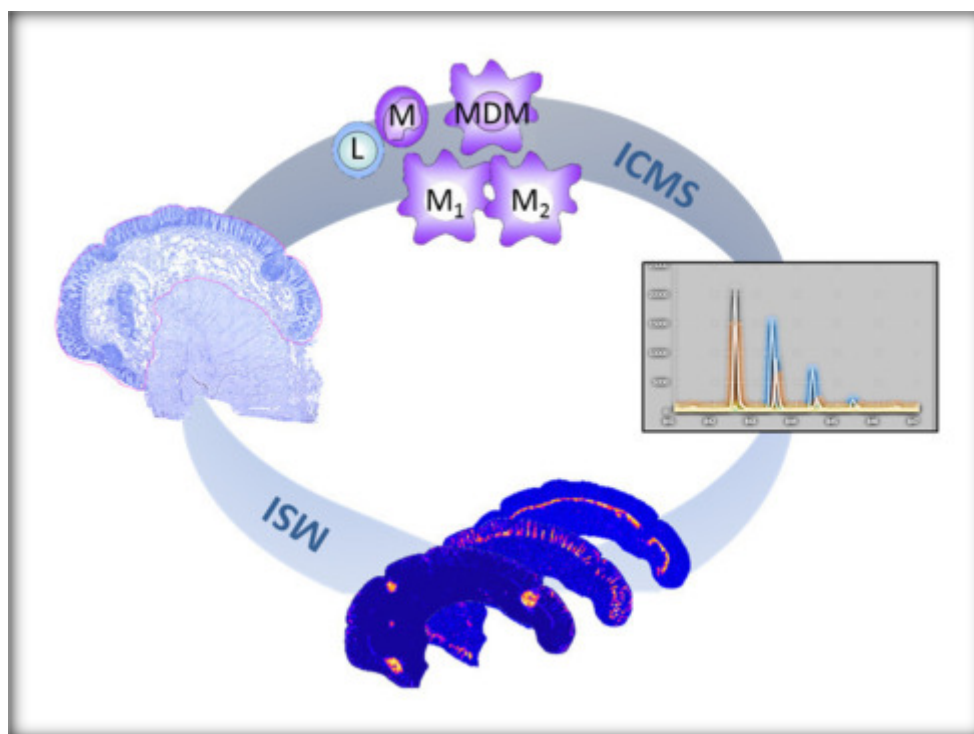


Figure 12: *In Situ Characterization of Tissue Resident Immune Cells by MALDI Mass Spectrometry Imaging*, graphical abstract.

The colon is infiltrated with a high number of immune cells which help to prevent spreading of bacteria from the gut lumen. The tissue-resident immune cells differ from the corresponding blood cells in many functional aspects. Although the proteome of blood immune cells is well investigated there are almost no data on tissue-resident lymphocytes and macrophages. Since these cells are still insufficiently described in the tissue we evaluated the potential of MSI and intact cell mass spectrometry (ICMS) to address this challenge.

Our data demonstrate that MSI is a suitable tool for characterization and *in situ* localization of immune cell accumulations without using antibodies, but on the basis of the protein expression of these cells. We could show that certain m/z values have the same spatial distribution as T lymphocytes in the lymphoid follicular structures or as macrophages in the lamina propria when compared to classical immunohistochemical (IHC) staining. In addition, MSI identified several proteinaceous markers that colocalized with specific structures of the colon, such as mucosa or muscularis mucosae. Statistical analysis of ICMS data of all 10 donor samples revealed a significant differentiation of monocytes and lymphocytes, showing certain m/z values to be characteristic for both cell types. Further we observed m/z values allowing for identification and discrimination of lymphocytes, monocytes, and polarized macrophages by ICMS. The combination of both MS approaches revealed m/z markers that are conserved between peripheral and tissue-resident immune cells, while others are only found within the tissue. We assume the latter to be derived from the adaptation of these cells to their microenvironment.

INNOVATIVE ASPECTS

- characterization and *in situ* visualization of immune cell accumulations
- identification of several proteinaceous markers that colocalize with specific structures of the colon
- robust sample preparation strategy facilitating reliable MSI data acquisition of multiple consecutive tissue sections

OWN CONTRIBUTION

In this work, I

- was involved in planning and designing the project and the MALDI MSI parts of the experiment,
- performed the MALDI MSI studies, evaluated, visualized and interpreted the data,
- drafted and wrote the MALDI MSI related parts of the manuscript.

| submitted to *Analytical Chemistry* |**MULTI-SENSOR IMAGING - FROM SAMPLE PREPARATION TO INTEGRATED MULTI-MODAL INTERPRETATION OF LA-ICP-MS AND MALDI MS IMAGING DATA.**

Matthias Holzlechner, Maximilian Bonta, Hans Lohninger, Andreas Limbeck, and Martina Marchetti-Deschmann.

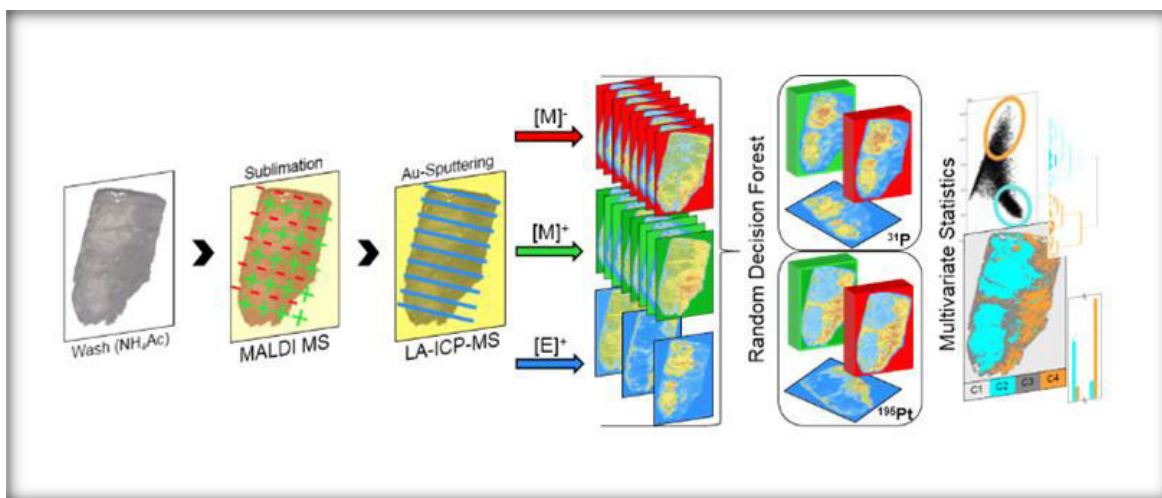


Figure 13: Multi-Sensor Imaging – from Sample Preparation to Integrated Multi-Modal Interpretation of LA-ICP-MS and MALDI MS Imaging Data, graphical abstract. Workflow of a MMI approach with integrated data evaluation.

Combination of two or more analysis techniques, so-called multi-sensor imaging, provides deeper information into the biochemical processes within one sample. In this work, a human malignant pleural mesothelioma (MPM) sample from a patient treated with cisplatin as cytostatic agent has been analyzed by combining LA-ICP-MS and MALDI MS in a multi-modal imaging (MMI) approach. The sample preparation strategy has been adjusted to fit the needs of each imaging method, whilst providing full information on lipid distributions and quantification of elements. An integrated data evaluation strategy has been developed combining LA-ICP-MS and MALDI MS data (positive and negative). The present proof-of-principle study demonstrates the benefit of data combination and highlights the value of advanced chemical imaging in the Life Sciences.

Examination of a blank ITO-coated glass slides and 1,5-DAN as MALDI matrix by LA-ICP-MS revealed an absence of signals for phosphorus and platinum. RDF-based classification exhibited 59 m/z values from MALDI MSI showing a correspondence to either the phosphorus (30 m/z values, all detected in negative mode) or the platinum distribution pattern (22 detected in the negative and 7 in

the positive ion mode) within the tissue. HCA of the PCA confirmed the correlation of analytes detected by MALDI MSI with the elemental distributions of phosphorus and platinum. Accordingly, results of the k-Means Clustering clearly reassembled the phosphorus and platinum pattern. Comparison of the average platinum concentration in the tissue used in the MSMMI approach (1.91 $\mu\text{g/g}$) with a consecutive section analyzed by LA-ICP-MS alone (1.75 $\mu\text{g/g}$) revealed a relative deviation of less than 10%. Thus, it can be stated that neither ablation by MALDI MS nor the washing step with ammonium acetate (AmAc) significantly interfered platinum quantification.

INNOVATIVE ASPECTS

- advanced statistical analysis allows the correlation of platinum distribution with certain lipids in an integrated data analysis approach
- MMI approach allows for reliable platinum quantification

OWN CONTRIBUTION

In this work, I

- was involved in planning and designing the project,
- designed the MALDI MSI parts of the experiment,
- performed the MALDI MSI experiments, evaluated and interpreted the data,
- visualized LA-ICP-MS and MALDI MSI data,
- drafted and wrote major parts the manuscript.

| submitted to *Particle and Fibre Toxicology* |

PHOSPHONATE COATING OF SiO₂ NANOPARTICLES ABROGATES INFLAMMATORY EFFECTS AND LOCAL CHANGES OF THE LIPID COMPOSITION IN THE RAT LUNG: A COMPLEMENTARY BIOIMAGING STUDY.

Mandy Großgarten, **Matthias Holzlechner**, Antje Vennemann, Anna Balbekova, Karin Wieland, Michael Sperling, Bernhard Lendl, Martina Marchetti-Deschmann, Uwe Karst, and Martin Wiemann.

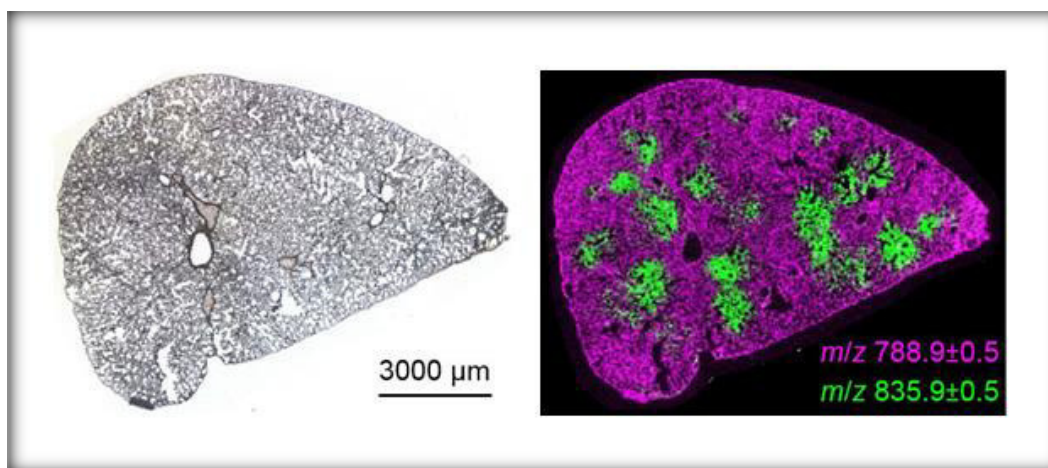


Figure 14: *Phosphonate Coating of SiO₂ Nanoparticles Abrogates Inflammatory Effects and Local Changes of the Lipid Composition in the Rat Lung: A Complementary Bioimaging Study*, graphical abstract. Ion images of local changes of lipid concentration in the SiO₂-FITC laden rat lung.

The well-known inflammatory and fibrogenic changes of the lung upon crystalline silica are accompanied by early changes of the phospholipid composition (PLC) as detected in broncho-alveolar lavage fluid (BALF). Silica (SiO₂) nanoparticles (NPs) evoke transient lung inflammation, but their effect on PLC is unknown. Here, we compared effects of unmodified and phosphonated SiO₂ NP and describe, for the first time, local changes of the PLC with innovative bioimaging tools.

MALDI MS analysis of rat lung tissue sections revealed a local overexpression of PIs and, to a lesser extent, PGs. The pattern of changes was largely congruent with the distribution pattern of SiO₂-FITC in the lung tissue. FTIR analyses of a neighboring cryosection combined with a subsequent hierarchical cluster analysis revealed regions representing enhanced lipid content, which corresponded invariably with the PI pattern. Notably, these observations were true only for FITC-coated and pristine nanoparticles, but not for phosphonated, i.e. TPMP-coated, NPs. This disparity was in excellent

accordance with in vitro and in vivo toxicity studies confirming a TPMP-mediated abrogation in SiO₂ NP induced cytotoxicity and lung inflammation. As the binding of major surfactant lipids to SiO₂ and SiO₂-P is virtually equal, we conclude that the locally increased PI/PG ratio is primarily due to early cytotoxic effects of instilled SiO₂ NPs, which are successfully masked in the phosphonated form.

INNOVATIVE ASPECTS

- combination of MALDI and FTIR spectroscopy revealed for the first time spatially resolved tissue remodeling of nanoparticle-affected tissue.

OWN CONTRIBUTION

In this work, I

- was involved in planning of the experiments and performed the MALDI MSI analyses,
- evaluated and visualized the MSI data,
- wrote parts of the manuscript related to MALDI MSI.

4 SUBLIMATION APPARATUS TO PUSH MALDI MS IMAGING BELOW THE CELLULAR LEVEL

| manuscript for submission to *Angewandte Chemie, International Edition* |

Sublimation Apparatus to Push MALDI MS Imaging Below the Cellular Level

Matthias Holzlechner[†], Johannes Frank[‡], Kurt Piplits[†], Theo Luider^{*}, Günter Allmaier[†] and Martina Marchetti-Deschmann^{**†}

[†]Institute of Chemical Technologies and Analytics, TU Wien, Getreidemarkt 9, 1060 Vienna, Austria

[‡]Joint Workshop Technical Chemistry, TU Wien, Getreidemarkt 9, 1060 Vienna, Austria

^{*}Department of Neurology, Erasmus University of Rotterdam, P.O. Box 1738, 3000 DR, Rotterdam, The Netherlands

Abstract: Sample preparation, especially reliable matrix application is probably the most critical step in MS imaging. Herein, matrix crystals being smaller than the laser beam are key for micrometer-resolution MALDI MSI. We report an in-house built sublimation apparatus along with optimized sublimation and rehydration conditions for commonly used MALDI matrices. We present a comprehensive study on matrix crystallization affected by differing surfaces, cooling temperatures and rehydration. Sublimation of the studied matrices enables cohesive layers comprising crystals at the sub-micrometer scale, exhibiting exceptional reproducibility and deposition uniformity. To showcase these capabilities, we demonstrate improvement in ion image quality after employing sublimation and HR image analysis.

MALDI mass spectrometry imaging (MSI) emerges as a powerful tool by providing chemical and distributional information on a wide range of molecules in biological samples *in situ*¹⁻². One of the major limitations and main challenges in MALDI MSI is spatial resolution. Although significantly increased recently³⁻⁶, spatial resolution is currently limited by (1) instrumentation, mostly laser spot diameter, raster step size of the sample holder and limit of detection, and (2) sample preparation, particularly matrix crystal size and application consistency⁷⁻⁹ prove difficult to reach subcellular resolution (< 10 μm). Yet, to provide new insights about molecular processes on the cellular level, spatial resolutions in the low μm ideally even nm range are required. Today, SIMS generally offers the highest spatial resolution among all MSI approaches (<50 nm)¹⁰, yet is not a soft ionization technique allowing for desorption/ionization of intact molecules like MALDI. Consequently, matrix application strategies providing highly reproducible matrix depositions along with crystals being significantly smaller in diameter than both the laser spot and the single cell are essential to push MALDI MSI to further limits. Various matrix deposition methods have been developed including manual and automated systems such as airbrushing, spraying, inkjet printing, and sublimation¹¹⁻¹². Using an airbrush is relatively simple, widely used¹³⁻¹⁵ yet not fully automated and thus limited by the skill of the user. Automated spray systems overcome some limitations by allowing a better control of deposition pattern across

tissue samples, yet inhomogeneity in crystal size and formation still limits lateral resolution to $\geq 20 \mu\text{m}$ ¹⁶ and the aerosol-based coating can favor analyte diffusion¹⁷. Matrix sublimation was first reported by Kim et al. in 1998¹⁸. Since then this method was improved for several matrices¹⁹ and in recent years it was found that many matrices do not decompose at elevated temperature under reduced pressure. Sublimation generally yields dry matrix crystals at the sub-micrometer to $3 \mu\text{m}$ level^{3, 20-21} of high purity, limiting lateral migration of molecules in tissue²²⁻²⁴ and chemical noise resulting from impurities. However, the solvent-free deposition mechanism results in poor extraction of analytes from the tissue. Rehydration of applied matrix layers has been reported to significantly increase the extraction efficiency and sensitivity of analytes^{3, 25}. However, sublimation devices used for MALDI matrix coating reported in literature^{14, 23, 26} are primarily modified glass devices originally designed for bulk chemicals and therefore provide limited control over reproducibility, crystallization and number of MALDI targets to be prepared simultaneously. Furthermore, matrix layer thickness and in-plane homogeneity of the matrix are not manageable. Today one sublimation device is commercialized²⁷, a system controlling temperature, pressure and a laser light source which measures the thickness of the deposited matrix layer. But this systems is restricted to one sample holder, three matrix components, a certain thickness of matrix layer and the matrix amount deposited²⁸. Furthermore, matrix consumption is exceptionally high (100 - 600 mg/run)²⁸⁻³⁰. To date, no systematic study on matrix layer homogeneity and reproducibility with respect to the physico-chemical process of sublimation is available. We introduce a home-built sublimation setup requiring minor matrix amounts, allowing exceptional reproducibility and homogenous MALDI matrix deposition on up to three full-sized microscope slides. We evaluated conditions for common high-vacuum stable MALDI matrices 2,5-DHB, 1,5-DAN, CHCA, and SA toward quantitative sublimation along with a modified matrix rehydration process facilitating standardization and ease of handling. We present a comprehensive, theory-driven study on matrix crystallization after sublimation on glass and biological tissue, at varying cooling temperatures and after rehydration. We address the necessity of high spatial resolution in MSI and compare high-resolution (HR) MALDI images achieved after aerosol deposition to samples prepared by sublimation.

Assembly of the in-house built sublimation apparatus is shown in the Supporting Information (Figure S1). Based on previous work³¹ we focused on reproducible and homogenous sublimation of MALDI matrices in respect of matrix concentration and crystallization conditions in the matrix well (solvent, temperature), distance between sample plate and matrix well, the sublimation temperature and the matrix amount deposited on the MALDI target(s) (max. size 8 x 10 cm, e.g. 3 ITO-coated glass slides). In general, 25.5 mg of matrix are dissolved in 3.5 mL ACE/ACN solution (7:3, v/v) and pipetted into the preheated matrix well (70°C). The elevated temperature accelerates evaporation of ACE (without boiling) leaving a thin film of ACN, overall promoting homogenous micro-crystallization of matrix in

the matrix well. MALDI targets, i.e. ITO-coated glass slides, are affixed to the sample plate holder. After reassembling the sublimation apparatus, vacuum is applied and after reaching the target pressure (37 mTorr, ca. 5 min) the sublimation temperature is set for each matrix individually (Table 1).

Table 1: Sublimation conditions for commonly used MALDI matrices.

MALDI Matrix	Solvent	Matrix Well [°C]	Sublimation Startpoint [°C]	Sublimation Setpoint [°C]	mp [°C]	Vacuum [mbar/mtorr]
1,5-DAN	ACE/ACN 7:3 (v/v)	68	125	145	187-190	5 × 10 ⁻² / 37
2,5-DHB			135	155	199.5	
SA			145	165	192	
CHCA			165	185	245 - 250	

All tested matrices are entirely volatilized during the sublimation process lasting less than 15 min. Sublimation of 25.5 mg matrix resulted in a coverage of 0.24 ± 0.01 mg/cm² (Table S1) when two targets are prepared at a time (one target serves as quality control). The distance between sample plate and matrix well had only a minor effect on the matrix amount deposited (decreasing amount with increasing distance, Table S2) but yielded most homogenous coatings at 3 cm. The respective melting points described for each matrix are in accordance to the applied sublimation temperatures under reduced pressure (Table 1). However, setpoint temperatures were fixed 20 °C above the empirically determined sublimation starting points to guarantee immediate and quantitative volatilization of matrices. Depositing dissolved matrix in the well and evaporating the solvent, instead of using matrix solids, introduces a further purification step allowing the use of chemicals of lower purity without introducing chemical noise into mass spectra. A direct comparison of profile spectra along with selected ion distributions from consecutive mouse brain sections acquired after using SA (purity $\geq 98\%$) and SA recrystallized before sublimation (2-times in ACN/ddH₂O, 7:3, v/v) show no significant difference (Figure S2).

Reproducibility of matrix deposition was determined by sublimation of 25.5 mg of SA on one target, or simultaneously on two or three targets. Each approach was repeated 5 times. In contrast to other reports^{27, 29}, exceptional reproducibility was achieved; 3.58 ± 0.04 mg per single slide (1.2 % RSD), 3.47 ± 0.05 mg (1.4% RSD) for two simultaneously covered slides and 3.11 ± 0.07 mg (2.4% RSD) for three slides. SA covered slides were further imaged by MALDI MS to check the homogeneity of the matrix coatings. Non-normalized ion images show constant signal intensities over the measured areas of 2 x 5 cm for the selected mass of SA (Figure S3). Additionally, the evaluation of matrix thickness for 18 ablated spots of a SA covered ITO target (2 x 5cm) and 9 silicon wafers partially

covered with SA (8 x 10 cm) (all 0.25 mg/cm²) revealed an average of 1598 ± 23 nm (1.4% RSD) and 1604 ± 78 nm (4.9% RSD), respectively (Figure S4).

Following the established sublimation protocol in this study allows for (1) matrix purification and application in one step, (2) uniform distribution of microcrystalline matrix in the matrix well providing maximum surface area for sublimation and best thermal conductivity from the heater to the sublimation substrate, therefore giving (3) a significant decrease of sublimation temperatures and time, as well as (4) homogenous matrix application over large areas in a highly reproducible manner because of pre-defined matrix amounts in the well.

Whilst small molecule analysis can be performed immediately after solvent-free matrix application by sublimation (analytes diffuse into matrix layer³²), a rehydration step is mandatory in order to extract larger molecules from the tissue and incorporate them into matrix crystals. As peptide/protein analysis is an integral part of MALDI MSI, rehydration conditions were studied comprehensively for 2,5-DHB, 1,5-DAN, CHCA, and SA. Care was taken to avoid condensation on sublimed surfaces and partial dissolving of the same during incubation. Beside optimization of incubation temperature and time, introduction of slight modifications to standard protocols³ resulted in simplified handling and increased reproducibility for all tested matrices (Table S3).

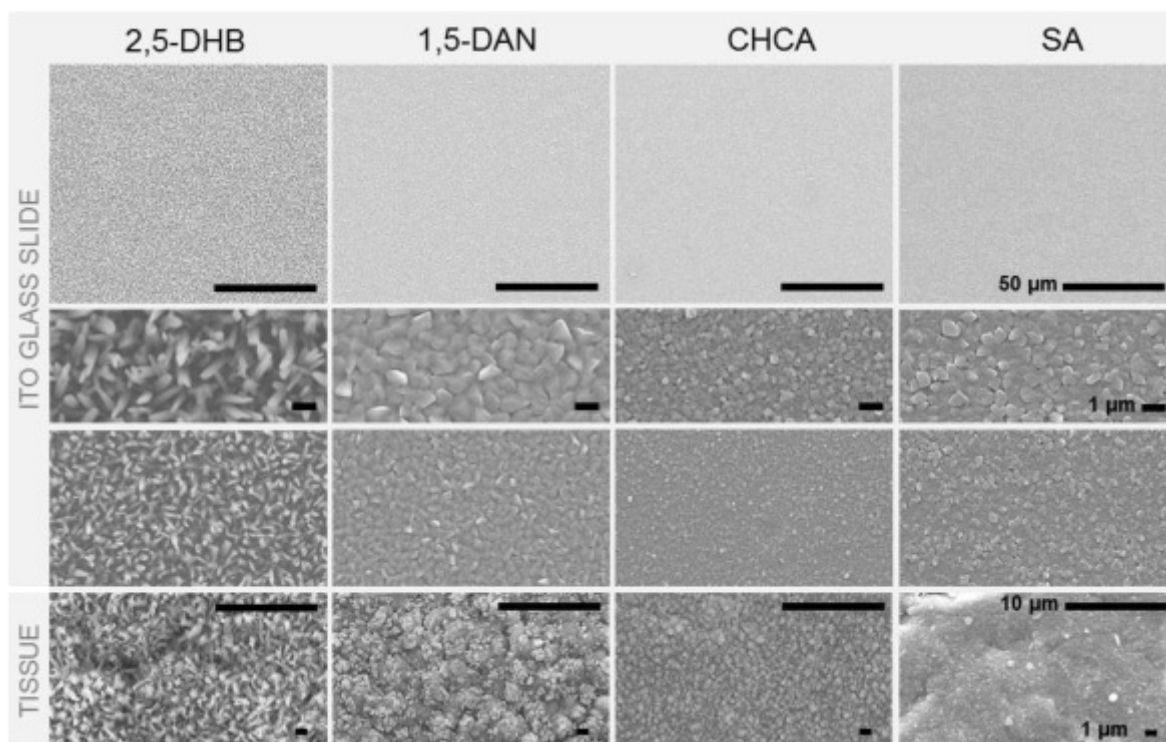


Figure 1: Condensation/crystallization of MALDI matrices on ITO glass slides and tissue.

SEM analysis shows matrix morphologies after sublimation on blank ITO glass slides (Figure 1). Application of 0.24 ± 0.01 mg matrix/cm² exhibits euhedral crystals in homogenous formations for all studied matrices. 2,5-DHB forms discrete needle-like crystals with up to approx. 2 μ m in length, inducing perceptible interstitial crystal volume. Sublimation of 1,5-DAN, CHCA and SA generates granular crystals embedded in more cohesive layers, exhibiting crystals at the 1 μ m to sub- μ m level for 1,5-DAN and SA, and even nm-scaled crystals for CHCA (< 500 nm). CHCA data correlate nicely with literature (granular shape, < 2 μ m)²¹, and the acquired results for SA and 1,5-DAN are corresponding. However, blank glass substrates present ideal surfaces for crystal growth and formation, compared to the heterogenous nature of biological tissue. For evaluation we focused on crystallization after sublimation on human colon thin cuts (0.24 ± 0.01 mg matrix/cm²) (Figure 1). Beside homogenous matrix crystal distributions, surface non-uniformities and tissue characteristics (e.g. cracks, < 5 μ m) become visual. The average particle size decreases to approx. 1 μ m for 2,5-DHB, and to the sub- μ m range for 1,5-DAN and SA. At the nanoscale, rough parts of the tissue surface may act as contact angles for nucleation. The reduced nucleation barrier may thus lead to a significant decrease in crystal size. Beside the sharper-edged appearance of 2,5-DHB crystals on tissue, matrix layers of 1,5-DAN, CHCA and especially SA exhibit subhedral textures possibly induced by endogenous salts hampering crystallization and thereby reducing the degree of structural perfection. Subsequent rehydration (5 % aqueous AcOH) notably affects sublimed surfaces neither on glass nor on tissue preparations (Figure S5). It is assumed that remaining matrix crystals close to the substrate act as seed layer during rehydration³³, consequently leading to comparable crystal habits, although now eventually containing analytes of interest. Recently, the authors demonstrated the reliability of the established sublimation/rehydration protocol in a HR study on peptide/protein distributions using a large stack of tissue thin cuts³⁴.

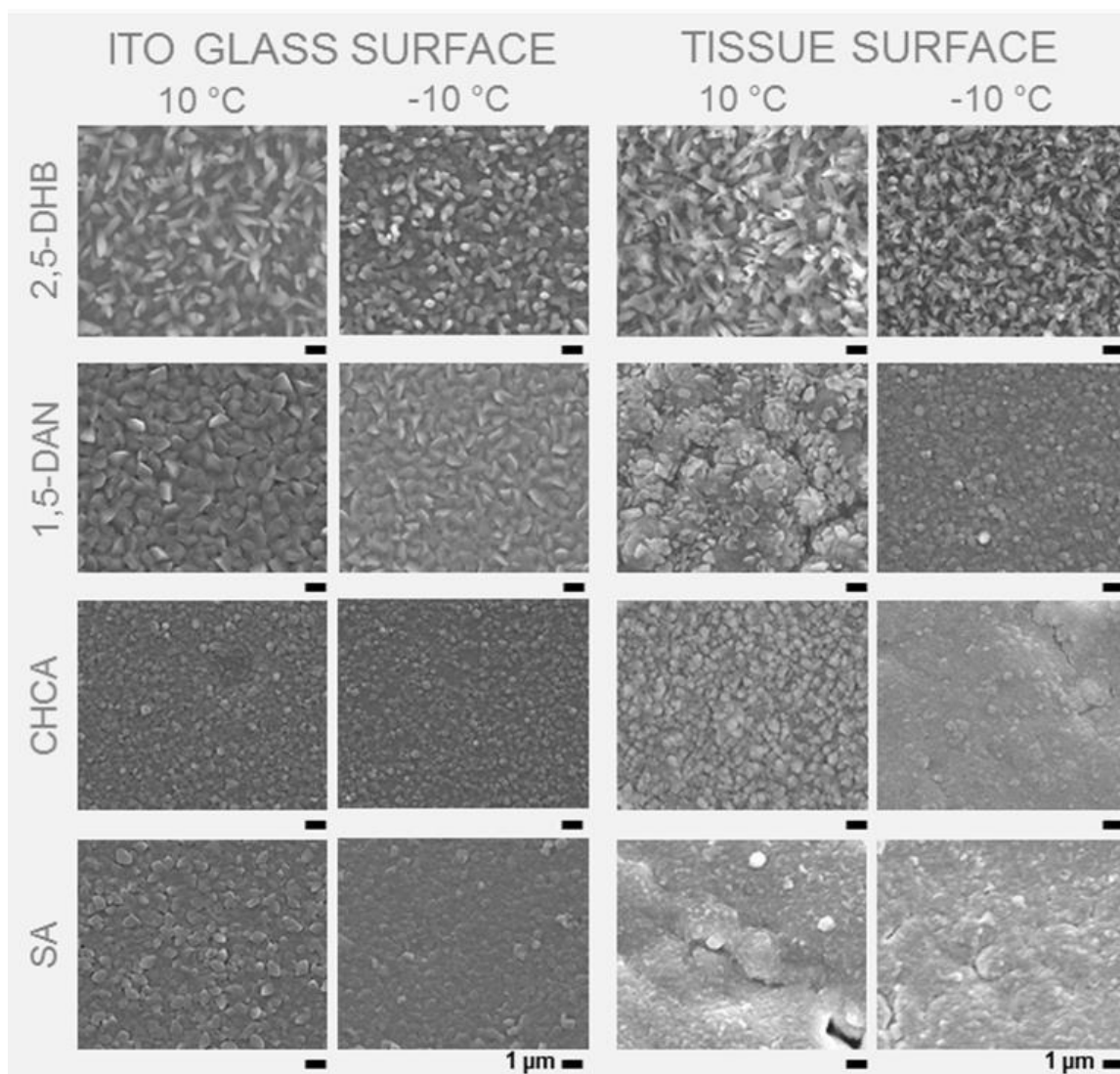


Figure 2: Influence of reduced cooling temperature on matrix crystallization on both glass and tissue surfaces.

For comprehensiveness, we tried to evaluate whether cooling has a beneficial effect on crystal size and layer formation of 2,5-DHB, 1,5-DAN, CHCA, and SA (Figure 2). Thus, sample plate temperature was set to -10°C for all matrices. Preparations were first done on blank ITO glass slides to favor unimpaired crystallization. Thereby, the appearance of 2,5-DHB changes from needle-like to more granular structures along with crystals by approx. half the length (sub- μm scale). Crystal sizes of 1,5-DAN and SA behave similarly at -10°C , forming crystallites at the sub- μm and 500 nm level, respectively. The average particle size of CHCA shows only a minor decrease on glass (sub-500 nm level). Tissue preparations at -10°C exhibit comparable crystal habits for 2,5-DHB and 1,5-DAN but formed crystals decrease to the sub- μm range. Beside CHCA forming anhedral to subhedral crystals on

tissue at -10°C , crystallization of SA does not differ significantly from preparations at plus 10°C . Applying reduced cooling temperature during sublimation did not influence the matrix amount deposited neither on glass nor on tissue (e.g. DHB: $0.23 \pm 0.01 \text{ mg/cm}^2$). However, interstitial crystal volume decreases to a minimum for all studied matrices. Besides, recent work suggests that narrow size distribution of crystals enhances reproducibility, resolution, sensitivity and S/N ratios in MALDI MS³⁵⁻³⁶. Moreover, it has been reasoned that decreased crystal sizes possess higher effective temperatures within each of the microcrystals irradiated by a laser pulse, and thus cause entire volatilization³³. Considering appropriate cooling temperatures, sublimation of all studied matrices yields crystals being significantly smaller than the smallest laser diameter reported today ($1.4 \mu\text{m}$ ³⁷) and thus eliminating crystal size as limiting factor for spatial resolution in MALDI MSI.

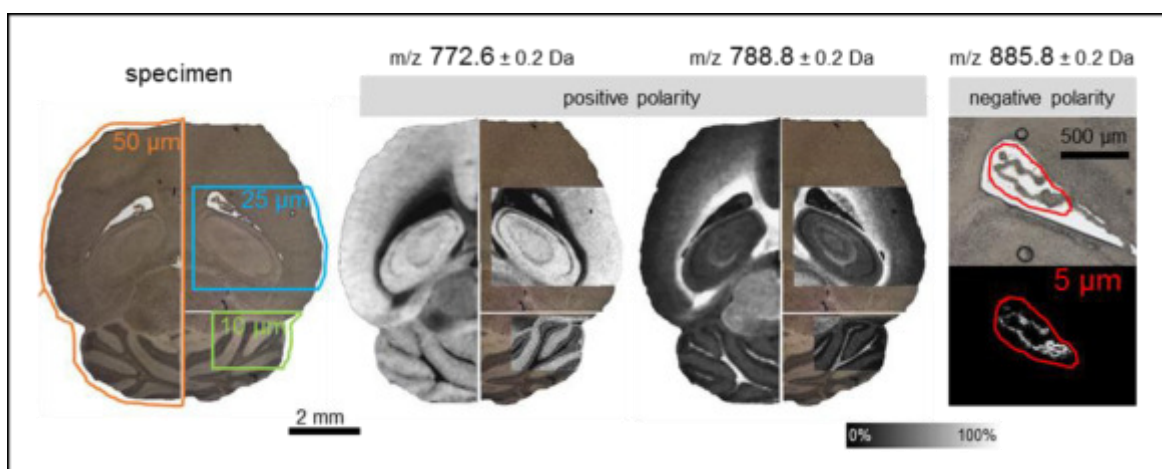


Figure 3: Effect of spatial resolution on spatial information of MS images.

In MS imaging, the spatial resolution (pixel size) of an experiment decisively influences the ability to distinguish distributions of components within tissue sections. Herein, the recorded pixel size is key for whether two adjacent regions are perceived as unique and distinct and thus should be adjusted according to the structure of interest. In Figure 3, we address the influence of varying spatial resolution in acquired MALDI images of a 1,5-DAN-coated mouse brain thin cut (0.24 mg/cm^2). Increasing lateral resolution from 50 to $5 \mu\text{m}$ reveals step by step the detailed molecular organization *in situ*. For comprehensiveness, the established sublimation method was compared to aerosol-based matrix application for lipid analysis on human colon tissue (Figure 4).

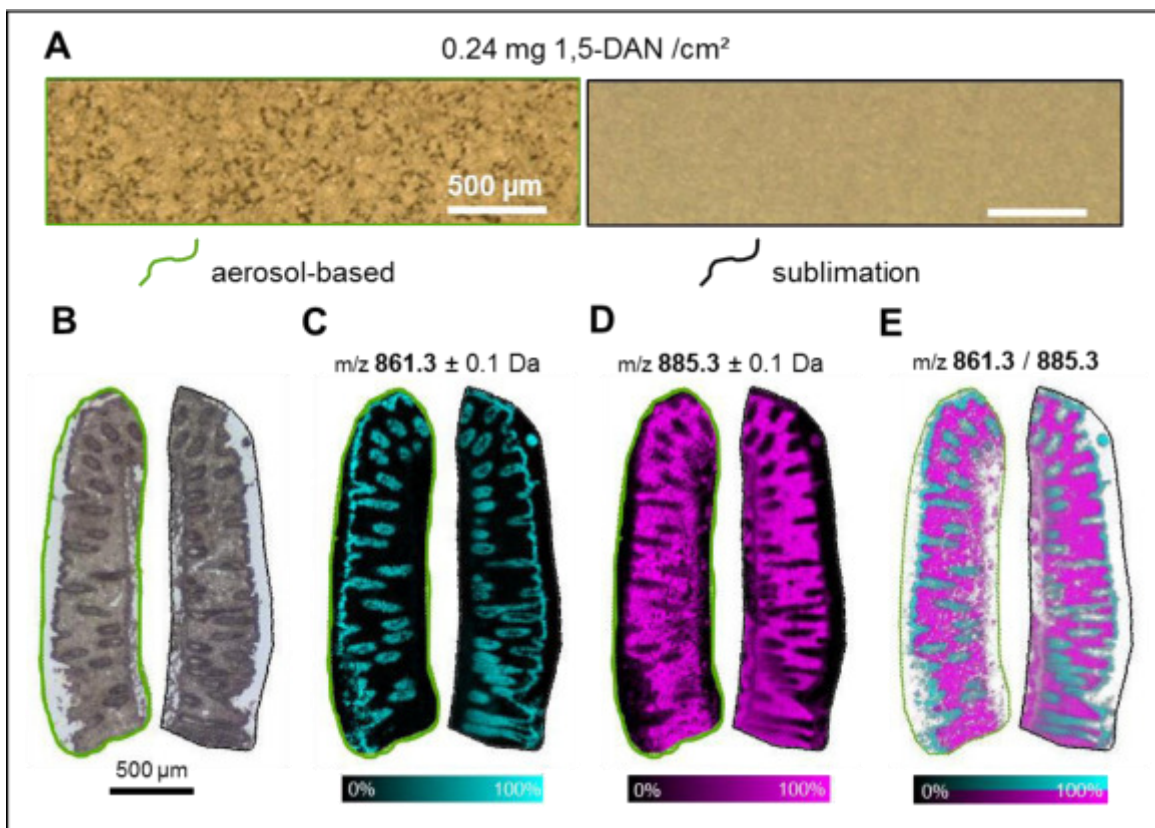


Figure 4: Comparison of sublimation and aerosol-based matrix application. 1,5-DAN applied on tissue (A), light micrograph of human colon section (B), ion distributions in crypts (C) and submucosa (D), ion distribution overlay (E).

Same amount of matrix was applied with both methods and MALDI MSI was performed under similar conditions at a lateral resolution of 10 μm . TIC normalized ion images acquired after sublimation reveal remarkable definition of anatomical regions of the colon tissue, as outlined by analyte distributions characteristic for submucosa (m/z 885.3) and crypt membranes (m/z 861.3), the latter being as thin as 5-10 μm . MSI data generated from aerosol-based matrix application appear to be blurred indicating analyte migration during sample preparation or missing data points as a consequence of matrix-free areas, i.e. interstitial volume. The individual profile spectra show similar peak patterns but with differing abundances (Figure S6). The significant increase in ion intensities achieved by using only 100 laser shots/pixel may arise from homogenous analyte ablation of the microcrystalline matrix layer after sublimation. Samples prepared by aerosol-based matrix application (crystal size up to 20 μm , Figure S7) showed comparable intensities only after the accumulation of 1000 shots/pixel, inevitably resulting in higher abundances of matrix cluster in the lower mass range.

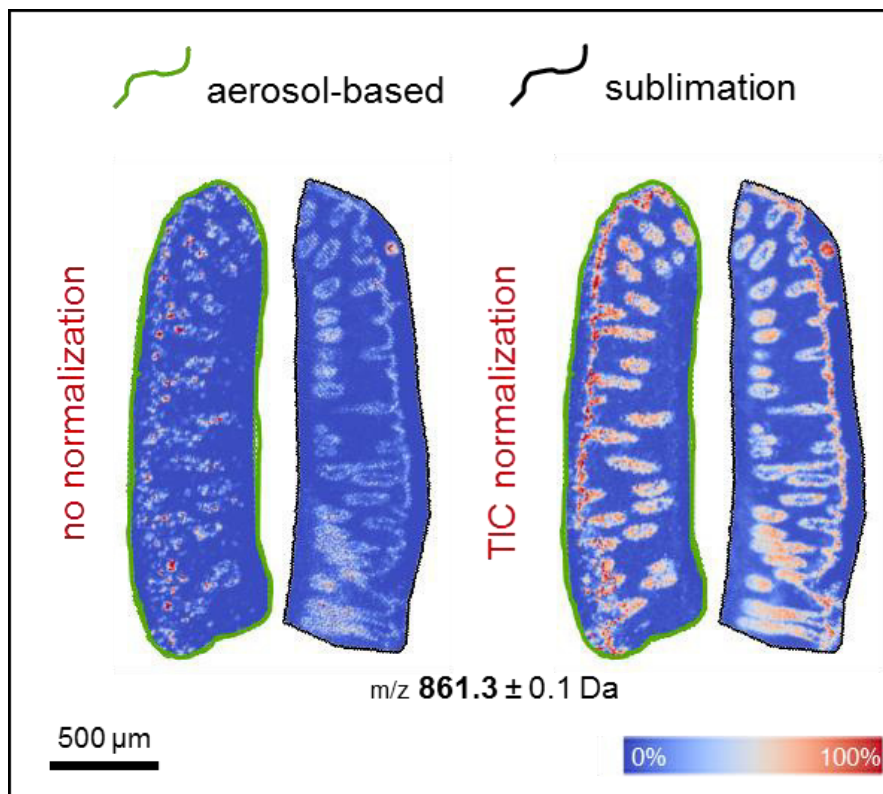


Figure 5: Effect of normalization on image quality.

Figure 5 shows the dramatic effect of homogenous, efficient analyte ionization from microcrystalline matrix layers when compared to aerosol-based application especially when data are not TIC normalized. Conventional normalization only enhances acquired imaging data, outlining the spatial localization of the thin crypt membranes and thus improving image quality.

In summary, the results of the current study outline the superior sublimation performance of the in-house built device, representing a vital link to high-quality HR MALDI ion images. Employing sublimation yields nm-scaled matrix crystals embedded in dense crystal layers, both being prerequisites for MS imaging below the sub-cellular level.

Experimental Section: please refer to Supporting Information.

Acknowledgments: The authors thank Elisabeth Eitenberger (TU Wien) for the support with SEM measurements.

REFERENCE

1. Chaurand, P., Schwartz, S.A., Caprioli, R.M., *Imaging mass spectrometry: a new tool to investigate the spatial organization of peptides and proteins in mammalian tissue sections*, *Curr. Opin. Chem. Biol.*, **2002**. 6 (5): p. 676.
2. Stoeckli, M., *Imaging mass spectrometry: A new technology for the analysis of protein expression in mammalian tissues*, *Nat. Med.*, **2001**. 7 (4): p. 493.
3. Yang, J., *Matrix Sublimation/Recrystallization for Imaging Proteins by Mass Spectrometry at High Spatial Resolution*, *Anal. Chem.*, **2011**. 83 (14): p. 5728.
4. Guenther, S., *AP-MALDI imaging of neuropeptides in mouse pituitary gland with 5 μ m spatial resolution and high mass accuracy*, *Int. J. Mass Spectrom.*, **2011**. 305 (2-3): p. 228.
5. Schober, Y., *Single Cell Matrix-Assisted Laser Desorption/Ionization Mass Spectrometry Imaging*, *Anal. Chem.*, **2012**. 84 (15): p. 6293.
6. Murray, K.K., *High resolution laser mass spectrometry bioimaging*, *Methods* **2016**. 104: p. 118.
7. Goodwin, R.J.A., *Sample preparation for mass spectrometry imaging: small mistakes can lead to big consequences*, *J Proteomics*, **2012**. 75 (16): p. 4893.
8. Balluff, B., *MALDI imaging mass spectrometry for direct tissue analysis: technological advancements and recent applications*, *Histochem. Cell Biol.*, **2011**. 136 (3): p. 227.
9. Trimpin, S., *Automated Solvent-Free Matrix Deposition for Tissue Imaging by Mass Spectrometry*, *Anal. Chem.*, **2010**. 82 (1): p. 359.
10. Boxer, S.G., *Advances in imaging secondary ion mass spectrometry for biological samples*, *Annu. Rev. Biophys.*, **2009**. 38: p. 53.
11. Cillero-Pastor, B., *Matrix-Assisted Laser Desorption Ionization Mass Spectrometry Imaging for Peptide and Protein Analyses: A Critical Review of On-Tissue Digestion*, *J. Proteome Res.*, **2014**. 13 (2): p. 325.
12. Thomas, A., *Advances in tissue section preparation for MALDI imaging MS*, *Bioanalysis*, **2014**. 6 (7): p. 967.
13. DeKeyser, S.S., *Imaging Mass Spectrometry of Neuropeptides in Decapod Crustacean Neuronal Tissues*, *J. Proteome Res.*, **2007**. 6 (5): p. 1782.
14. Gemperline, E., *Optimization and Comparison of Multiple MALDI Matrix Application Methods for Small Molecule Mass Spectrometric Imaging*, *Anal. Chem.*, **2014**. 86 (20): p. 10030.
15. Shimma, S., *MALDI-based imaging mass spectrometry revealed abnormal distribution of phospholipids in colon cancer liver metastasis*, *J. Chromatogr. B: Anal. Technol. Biomed. Life Sci.*, **2007**. 855 (1): p. 98.
16. Lagarrigue, M., *Revisiting rat spermatogenesis with MALDI imaging at 20- μ m resolution*, *Mol. Cell. Proteomics*, **2011**. 10 (3): p. 1.
17. Baluya, D.L., *Automated MALDI Matrix Deposition Method with Inkjet Printing for Imaging Mass Spectrometry*, *Anal. Chem.*, **2007**. 79 (17): p. 6862.
18. Kim, S.H., *First application of thermal vapor deposition method to matrix-assisted laser desorption ionization mass spectrometry: determination of molecular mass of bis(p-methyl benzylidene) sorbitol*, *Rapid Commun. Mass Spectrom.*, **1998**. 12 (11): p. 701.

19. Stevenson, E., *Internal energies of analyte ions generated from different matrix-assisted laser desorption/ionization matrices*, J. Mass Spectrom., **2000**. 35 (8): p. 1035.
20. Poetsch, A., *Improved identification of membrane proteins by MALDI-TOF MS/MS using vacuum sublimated matrix spots on an ultraphobic chip surface*, J Biomol Tech, **2008**. 19 (2): p. 129.
21. Roth, M.J., *Thin-Layer Matrix Sublimation with Vapor-Sorption Induced Co-Crystallization for Sensitive and Reproducible SAMDI-TOF MS Analysis of Protein Biosensors*, J. Am. Soc. Mass Spectrom., **2012**. 23 (10): p. 1661.
22. Chughtai, K., *Mass Spectrometric Imaging for Biomedical Tissue Analysis*, Chem. Rev., **2010**. 110 (5): p. 3237.
23. Hankin, J.A., *Sublimation as a Method of Matrix Application for Mass Spectrometric Imaging*, J. Am. Soc. Mass Spectrom., **2007**. 18 (9): p. 1646.
24. Kaletas, B.K., *Sample preparation issues for tissue imaging by imaging MS*, Proteomics, **2009**. 9 (10): p. 2622.
25. Bouschen, W., *Matrix vapor deposition/recrystallization and dedicated spray preparation for high-resolution scanning microprobe matrix-assisted laser desorption/ionization imaging mass spectrometry (SMALDI-MS) of tissue and single cells*, Rapid Commun. Mass Spectrom., **2010**. 24 (3): p. 355.
26. O'Rourke, M.B., Raymond, B.B.A., Djordjevic, S.P., Padula, M.P., *A versatile cost-effective method for the analysis of fresh frozen tissue sections via matrix-assisted laser desorption/ionisation imaging mass spectrometry*, Rapid Commun. Mass Spectrom., **2015**. 29 (7): p. 637.
27. Yamamoto, T., *Study of experimental conditions for MALDI Imaging by using highly controlled sublimation technique*, ASMS **2015**. p.
28. Shimadzu, *Matrix Vapor Deposition System iMLayer*, **2015**. p.
29. Angel, P.M., *Enhanced Sensitivity for High Spatial Resolution Lipid Analysis by Negative Ion Mode Matrix Assisted Laser Desorption Ionization Imaging Mass Spectrometry*, Anal. Chem. , **2012**. 84 (3): p. 1557.
30. Thomas, A., *Sublimation of New Matrix Candidates for High Spatial Resolution Imaging Mass Spectrometry of Lipids: Enhanced Information in Both Positive and Negative Polarities after 1,5-Diaminonaphthalene Deposition*, Anal. Chem. , **2012**. 84 (4): p. 2048.
31. Dekker, L.J.M., van Kampen, J.J.A., Reedijk, M.L., Burgers, P.C., Gruters, R.A., Osterhaus, A.D.M.E., Luiders, T.M., *A mass spectrometry based imaging method developed for the intracellular detection of HIV protease inhibitors*, Rapid Commun. Mass Spectrom., **2009**. 23 (8): p. 1183.
32. Van Nuffel, S., *Insights into the MALDI Process after Matrix Deposition by Sublimation Using 3D ToF-SIMS Imaging*, Anal. Chem. , **2018**. p. Ahead of Print.
33. Jaskolla, T.W., *Comparison between vacuum sublimed matrices and conventional dried droplet preparation in MALDI-TOF mass spectrometry*, J Am Soc Mass Spectrom, **2009**. 20 (6): p. 1104.
34. Holzlechner, M., *In Situ Characterization of Tissue-Resident Immune Cells by MALDI Mass Spectrometry Imaging*, J. Proteome Res., **2017**. 16 (1): p. 65.
35. Sadeghi, M., *Crystallite size dependence of volatilization in matrix-assisted laser desorption ionization*, Appl. Surf. Sci., **1998**. 127-129: p. 226.
36. Qiao, H., *Analyte distributions in MALDI samples using MALDI imaging mass spectrometry*, Int. J. Mass Spectrom., **2009**. 281 (1-2): p. 41.

37. Kompauer, M., *Atmospheric pressure MALDI mass spectrometry imaging of tissues and cells at 1.4- μm lateral resolution*, Nat. Methods, **2017**. 14 (1): p. 90.

Supporting Information

Sublimation Apparatus to Generate nm-scaled Matrix Crystals to Push MALDI MS Imaging Below the Cellular Level

Matthias Holzlechner[†], Johannes Frank[‡], Kurt Piplits[†], Theo Luider^{*}, Günter Allmaier[†] and Martina Marchetti-Deschmann^{**†}

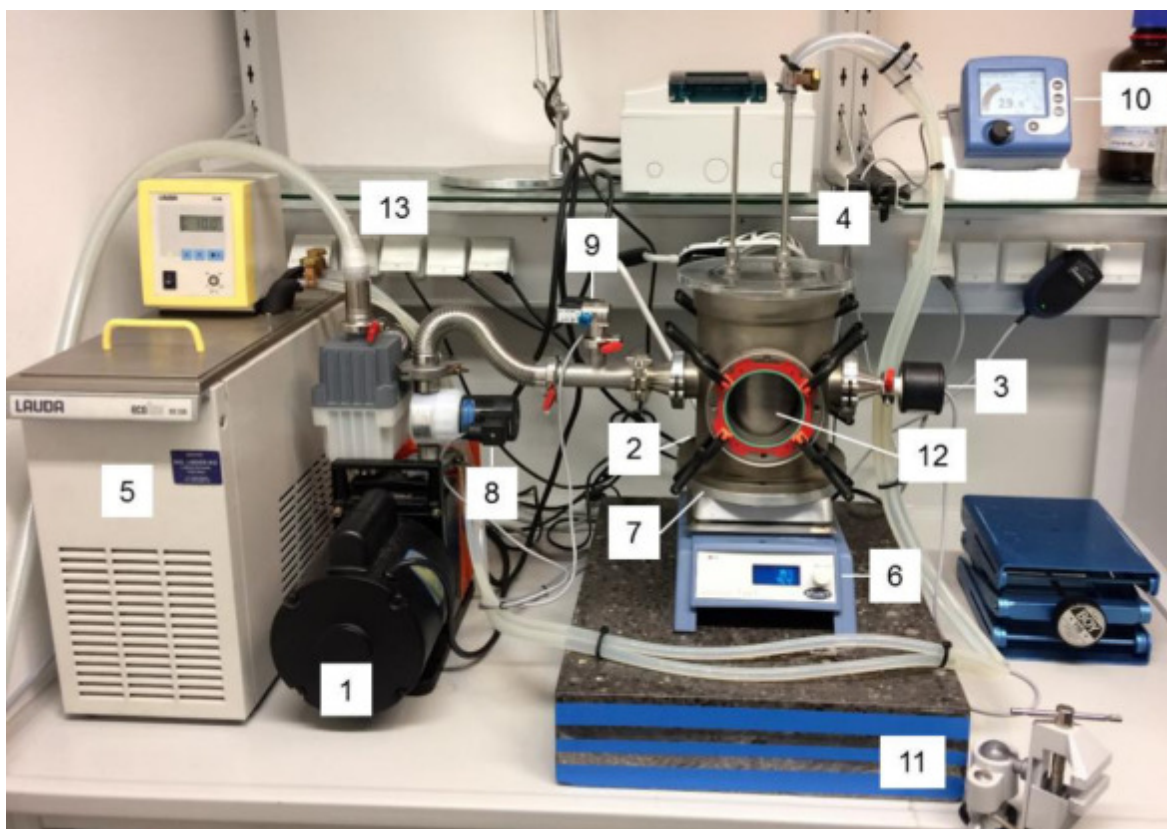
[†]Institute of Chemical Technologies and Analytics, TU Wien, Getreidemarkt 9, 1060 Vienna, Austria

[‡]Joint Workshop Technical Chemistry, TU Wien, Getreidemarkt 9, 1060 Vienna, Austria

^{*}Department of Neurology, Erasmus University of Rotterdam, P.O. Box 1738, 3000 DR, Rotterdam, The Netherlands

Materials. All reagents had a purity of at least 99%, if not otherwise stated. Fresh frozen human colon and mouse brain tissue was provided by the Department of Surgery and Comprehensive Cancer Center, Medical University of Vienna, and sectioned at a thickness of 10 μm using a Leica CM3050 cryostat (Leica Microsystems GmbH, Wetzlar, DE). Glacial acetic acid (AcOH), acetonitrile (ACN), methanol (MeOH), ethanol (EtOH), acetone (ACE), chloroform (CHCl_3), α -cyano-4-hydroxycinnamic acid (CHCA) (purity $\geq 98\%$), 2,5- dihydroxybenzoic acid (2,5-DHB) (98%), sinapinic acid (SA) ($\geq 98\%$), 1,5- diaminonaphthalene (1,5-DAN) (97%), and Whatman filter paper were purchased from Sigma-Aldrich (St. Louis, MO, US). Water (ddH₂O) was obtained from a Simplicity system (Millipore, Billerica, MA, US), resistivity $<18.2 \text{ M}\Omega \times \text{cm}$ @ 25°C. Indium tin oxide (ITO) -coated microscope glass slides were from Delta Technologies (Loveland, CO, US) and washed before use (sonicated in ACE, MeOH and ddH₂O, 15 min each, dried under vacuum). Gold-coated silicon wafer were supplied from Infineon Technologies Austria AG (Villach, AT). Double-sided copper tape was obtained from Advance Tapes (Leicester, GB), thermally conductive adhesive was purchased from Arctic silver (Visalia, CA, US), and conductive tape from Shimadzu Austria (Korneuburg, AT).

Figure S15: Setup of the in-house built sublimation apparatus for MALDI matrix application.



The in-house built sublimation device is composed of a (1) forevacuum pump connected to a (2) vacuum sealed stainless steel sublimation chamber equipped with a (3) pressure transducer, and a (4) modified fluid-cooled condenser defining the sample plate which is located in the sublimation chamber. A (5) recirculating fluid, controlled by a cooling unit, tempers the sample holder. A (6) hot-plate provides constant temperature to the (7) matrix well and a vacuum control system, consisting of a (8) solenoid operated in-line valve and an (9) air admittance valve monitored by a (10) vacuum controller, allows constant pressure levels and automated venting. A (11) granite slab is used as a heatsink, accelerating heat dissipation between experiments.

A (12) removable stainless steel hollow cylinder is implemented on top of the matrix well to prevent matrix condensation on the inner walls of the sublimation chamber ensuring long-term stability of the system and thus simplifies cleaning between runs. An additional (13) exhaust hose is installed to facilitate sublimation of toxic matrices (like 1,5-DAN) in the absence of a fume.

An aluminum plate (8 cm x 10 cm) is affixed to a fluid-cooled condenser using a thermally conductive adhesive (layer thickness approx. 35 μm) in combination with screw connections. This modification ensures a stable and uniform temperature distribution across the fluid-cooled sample plate. Additionally, the enlarged condensation area enables simultaneous matrix application to 3 full-sized MALDI slides (e.g. ITO slides) or any sample holder of max. 8 cm x 10 cm. For better control of sublimation results, the sample plate is adjustable in height allowing optimization of ITO target/matrix well distance.

The matrix well is sufficiently dimensioned (8 cm x 10 cm) to perfectly fit the sample plate and to take up a minimum of 3.5 mL of matrix solution for crystallization prior to sublimation. The vacuum control system allows operation of the sublimation process with preset pressure and time settings.

This setup in combination with conventional timers for the hotplate and the forevacuum pump enables semi-automated sample treatment and thus a user-friendly handling.

Tissue preparation. Tissue sections (10 μm) were thaw-mounted on ITO-coated slides, transferred into a vacuum desiccator for ≥ 2 h (complete dryness). Mouse brain tissue sections were washed in ascending ethanol concentrations (70% and 100% EtOH, followed by Carnoy's fluid (60 % EtOH, 30 % CHCl_3 , 10 % AcOH), 100% EtOH, ddH₂O, and 100% EtOH; 30 s each step, except for Carnoy's solution (2 min).¹ Human colon tissue sections were submerged 3-times in chilled ammonium acetate (4°C, 50mM, pH 6.7) for 5s each.² Tissue sections were dried under a gentle stream of N₂ and stored in a desiccator until matrix application (≥ 20 min).

Matrix application by sublimation. Sublimation conditions are listed in the main manuscript in Table 1 (see manuscript). All ITO-coated glass slides were weighed before use. 25.5 mg of matrix were dissolved in 3.5 mL ACE/ACN (7:3, v/v). After pipetting the solution into the preheated matrix well (70 °C) the solvent was allowed to evaporate, inducing crystals formation over the entire well. Sample

slides were mounted onto the sample plate using double-sided copper tape (width 1 cm). The adjustable distance between matrix well and sample plate was set to 3 cm. The sample plate was maintained at 10°C (unless otherwise stated) by a recirculating fluid cooler using dH₂O/glycol/isopropanol (4:2:0.5, v/v/v). The sublimation apparatus was reassembled, and vacuum was adjusted to 37 mTorr (5×10^{-2} mbar). System temperature was adjusted to matrix choice. Sublimation was proceeded until matrix crystals in the well volatilized entirely. Upon completion of sublimation, the heating was turned off and the device was vented to atmospheric pressure. After sublimation, the prepared ITO-slides were weighed again to determine average amount of matrix per cm². Matrix coverage was assessed by secondary electron microscopy (SEM).

Matrix application by airbrush. A high-end airbrush device (Grafo T3, Harder & Steenbeck, DE) with a 0.15 mm needle and connection to an oil-piston-compressor (Aero-pro HTC) providing constant air pressure levels (1.5 bar) was used for aerosol deposition of matrix. A saturated matrix solution of 1,5-DAN was prepared in ACE/ddH₂O (9:1, v/v) and manually applied on ITO glass slides by maintaining a distance of 30 cm and an angle of approx. 45° between nozzle and sample surface. Matrix coverage was again assessed by weight and SEM.

Matrix rehydration. After matrix sublimation was complete, subsequent recrystallization and hydration was performed according to J. Yang and R.M. Caprioli¹ with slight modifications. Briefly, the matrix covered ITO slide was attached to a stainless-steel target (Shimadzu Austria, Korneuburg, AT) on the bottom side of a Petri dish cover (100 mm x 15 mm depth; VWR, Darmstadt, DE). After placing a filter paper wetted with 5 % AcOH in the Petri dish the hydration chamber was reassembled and incubated with parameters adjusted for each matrix (Table S3). Besides, we introduced modifications to simplify handling and increase reproducibility. The stainless-steel target was attached to the underside of the Petri dish lid using conductive tape in combination with a thermally conductive adhesive to ensure a uniform heat sink across the entire steel target. The filter paper was cut to rectangular pieces (80 mm x 30 mm) to stick out the dimensions of the ITO-coated glass slide (75 x 25 mm) and placed in the Petri dish. 570 µL of 5% aqueous AcOH were pipetted evenly onto the filter paper to generate acidic, humidified atmosphere. The slide with the sublimed matrix was then attached to the steel target using 2 magnets. After reassembling, two additional magnets were placed on the top part of the Petri dish lid to prevent detachment of the steel target during longer incubation times. Conventional isolating tape (15 mm in width) used for sealing the reassembled Petri dish guaranteed constant humidity during recrystallization/hydration.

Purification of matrix prior to sublimation. Stock matrix material of SA (purity ≥ 98%) was purified by recrystallization prior to sublimation using either 2-times ACN/ddH₂O (7:3, v/v) or the same solution as used in the sublimation process developed in this manuscript, i.e. ACE/ACN (7:3, v/v).

Light and secondary electron microscopy. Optical images of human colon and mouse brain tissue were taken prior to MSI using a Leica DM 2500M light microscope (Leica Microsystems AG, Heerbrugg, CH) with a 2.5× objective lens. Matrix crystal morphologies of the sublimed surfaces were characterized by SEM, after sputtering-coating matrix-covered ITO glass slides with a thin gold film for 40 s (Agar Scientific Ltd., Stansted, Essex CM24 8GF, GB). SEM images were recorded at an acceleration voltage of 10 kV and a magnification between 2000 and 30000 on an XL 30 scanning electron microscope (FEI Philips, Hillsboro, OR, US).

Matrix coating homogeneity and thickness evaluation. For homogeneity testing, ITO glass slides were sublimed with SA (0.25 mg/cm²) prior to MSI measurements. Nine gold-coated silicon wafers (1 cm x 1 cm; 750 μm depth) were mounted on the aluminum sample plate (8 cm x 10 cm) using conductive tape. The wafers were partially covered with another wafer and SA was sublimed to obtain coatings at 0.25 mg/cm² (assessed by weight). After removing the covering wafer, the thickness of the matrix coating was measured across the coated and non-coated area using the profile line function of the DektakXT (Bruker Daltonics, Bremen, DE).

Mass spectrometry imaging and data analysis. MSI spectra were acquired on a MALDI-TOF/RTOF instrument (ultrafleXtreme™), equipped with a 2 kHz Smartbeam™ laser (355 nm) using flexControl v3.4 (all Bruker Daltonics). MSI measurements of mouse brain tissue: 4 – 18 kDa, positive linear ion mode, lateral resolution of 60 μm. High spatial resolution MSI data of human colon tissue: 450 – 950 Da, negative reflectron mode, lateral resolution of 10 μm. Matrix homogeneity testing by MSI: 100 – 300 Da, positive reflectron ion mode, lateral resolution of 1200 μm. In general, MS data acquisition parameters were kept identical for the individual tissue sections and regions of interest (ROI) of approximately the same area. One hundred shots per pixel were acquired at a laser repetition rate of 1 kHz without intraspot rastering, an array of approx. 5600 points for mouse brain and 15000 points for human colon tissue were covered. Imaging data for matrix homogeneity evaluation was acquired within an area of 2 x 5 cm of the sublimed ITO glass slides. Variations in spatial resolution were performed in order to limit the data size of the collected images. Mass spectra were calibrated externally using the cubic enhanced algorithm. Data acquisition and image representation were carried out using flexImaging software v3.0 and SCiLS Lab software v2015b (SCiLS GmbH, Bremen, DE). Acquired imaging data were normalized to the Total Ion Current (TIC) unless otherwise stated.

Figure S2: Comparison of applied non-purified and purified SA by MALDI MSI. Acquired profile spectra (A) and ion images of horizontal mouse brain (B).

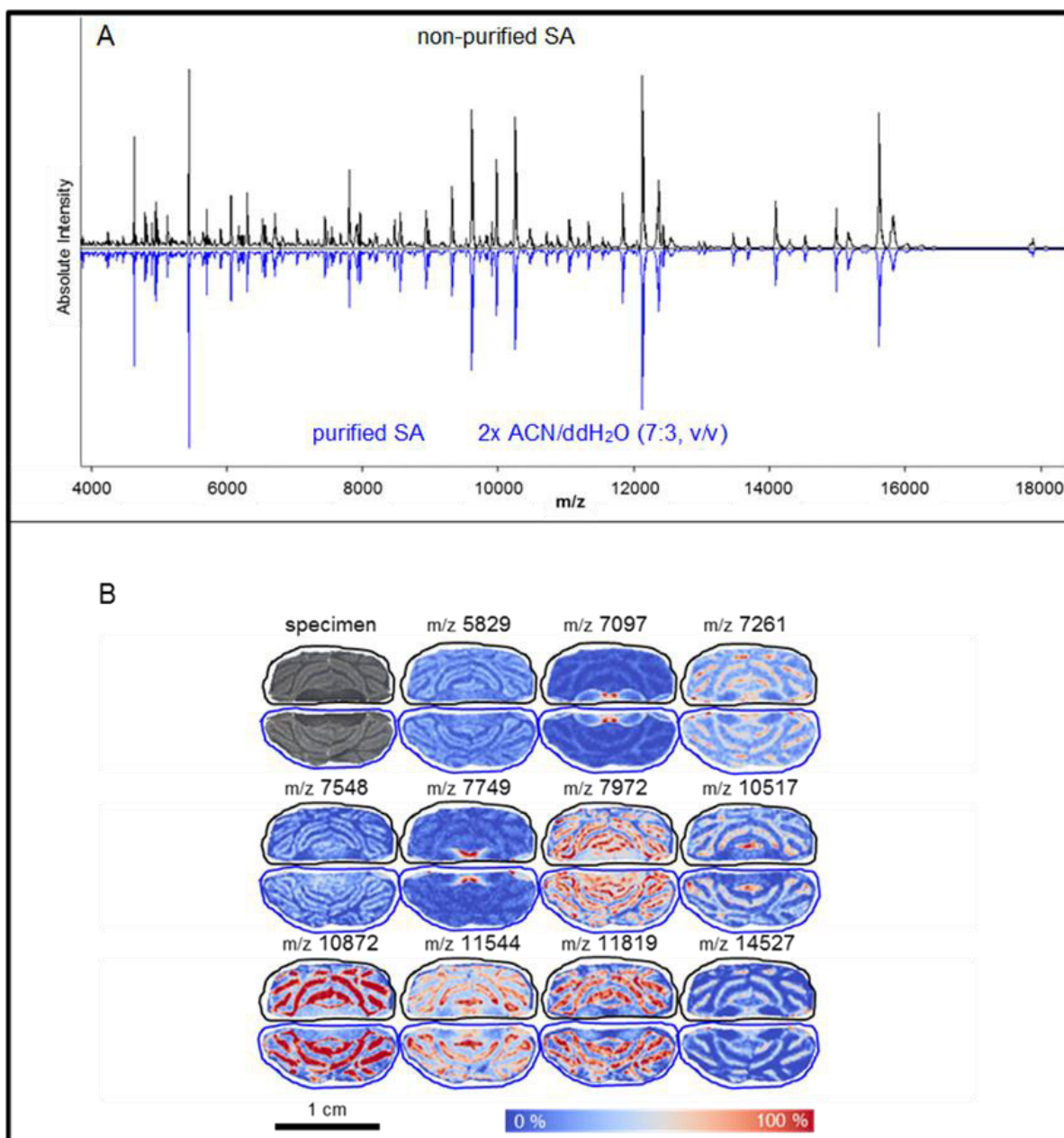


Figure S3: Testing the homogeneity of matrix coatings by the use of MALDI MSI.



Figure S4: Matrix thickness measurements of SA covered ITO target (A) and sample plate (B).

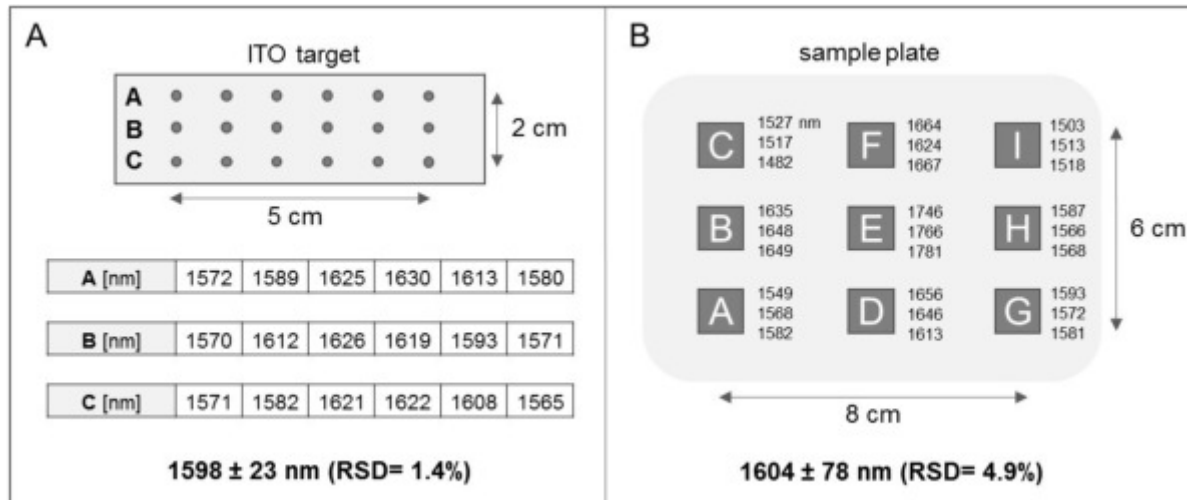


Figure S5: Effect of rehydration on sublimed ITO and tissue surfaces.

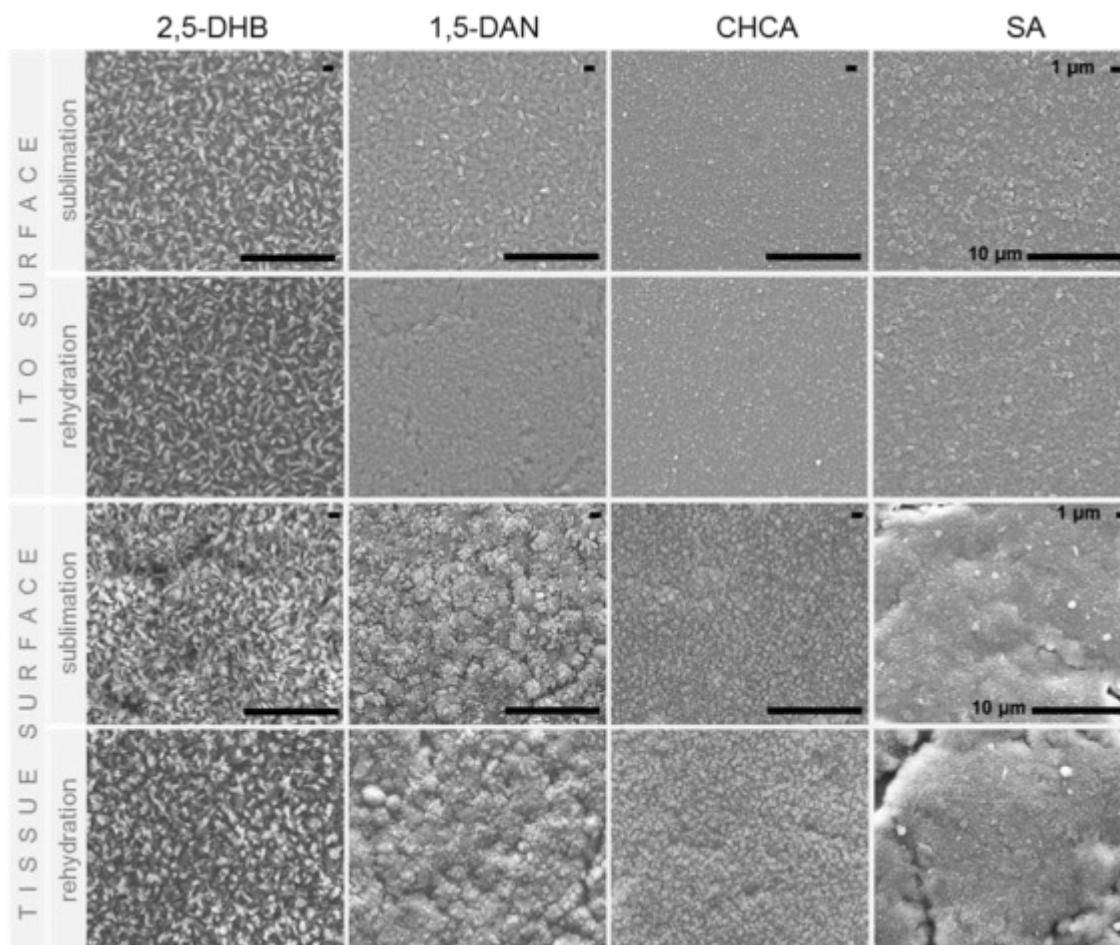


Figure S6: Comparison of sublimation and aerosol-based matrix application. MALDI MS profile spectra.

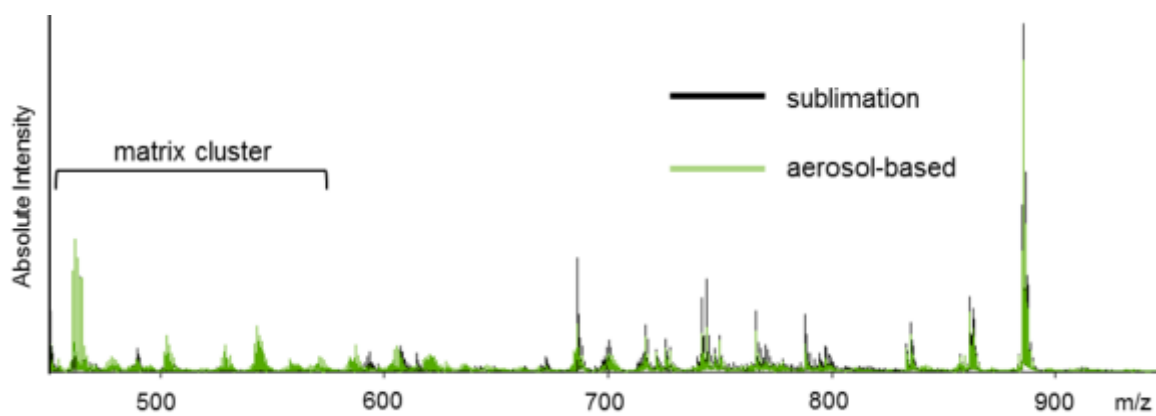


Figure S7: SEM micrographs of 1,5-DAN application by airbrush and sublimation.

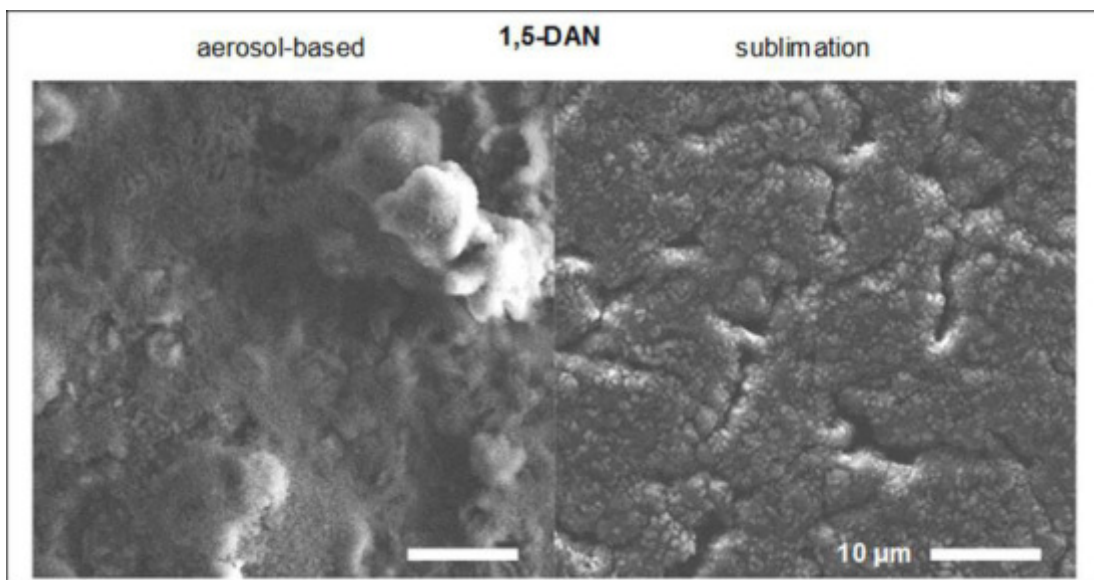


Table S1: Determined matrix coverage after sublimation of the same amount for each matrix used*.

MALDI Matrix	Matrix [mg]	Target 1 [mg]	Target 2 [mg]	Matrix Coating [mg/cm ²]
<i>1,5-DAN</i>	25.5	3.3	3.3	0.24
<i>2,5-DHB</i>		3.1	3.1	0.23
SA		3.5	3.5	0.25
<i>CHCA</i>		3.1	3.1	0.23

* sublimation conditions see Table 1 (manuscript).

Table S2: Matrix sublimation with varying distances between sample plate and matrix well*.

Distance [cm]	SA [mg]	Target 1 [mg]	Target 2 [mg]	Matrix Coating [mg/cm ²]
2		3.9	3.9	0.28
3	25.5	3.5	3.5	0.25
4		3.0	3.0	0.22

* sublimation conditions see Table 1 (manuscript).

Table S3: Rehydration conditions for commonly used MALDI matrices*.

MALDI Matrix	Incubation Temperature [°C]	Incubation Time [min]
<i>1,5-DAN</i>		1.5
<i>2,5-DHB</i>	85	1.5
SA		3.8
<i>CHCA</i>		4.0

*determined for a matrix coverage at 0.24 ± 0.01 mg/cm² and the use of 5% aqueous AcOH as solvent.

REFERENCES

1. Yang, J., Matrix Sublimation/Recrystallization for Imaging Proteins by Mass Spectrometry at High Spatial Resolution, *Anal. Chem.* , **2011**. 83 (14): p. 5728.
2. Angel, P.M., Enhanced Sensitivity for High Spatial Resolution Lipid Analysis by Negative Ion Mode Matrix Assisted Laser Desorption Ionization Imaging Mass Spectrometry, *Anal. Chem.* , **2012**. 84 (3): p. 1557.

5 VISUALIZING FUNGAL METABOLITES DURING MYCOPARASITIC INTERACTION BY MALDI MASS SPECTROMETRY IMAGING

| article published in *Proteomics* (2016), 16(11-12), 1742-1746 |

TECHNICAL BRIEF

Visualizing fungal metabolites during mycoparasitic interaction by MALDI mass spectrometry imaging

Matthias Holzlechner¹, Sonja Reitschmidt¹, Sabine Gruber², Susanne Zeilinger^{2,3} and Martina Marchetti-Deschmann¹

¹ Institute of Chemical Technologies and Analytics, Vienna University of Technology, Vienna, Austria

² Institute of Microbiology, University of Innsbruck, Innsbruck, Austria

³ Institute of Chemical Engineering, Vienna University of Technology, Vienna, Austria

Studying microbial interactions by MALDI mass spectrometry imaging (MSI) directly from growing media is a difficult task if high sensitivity is demanded. We present a quick and robust sample preparation strategy for growing fungi (*Trichoderma atroviride*, *Rhizoctonia solani*) on glass slides to establish a miniaturized confrontation assay. By this we were able to visualize metabolite distributions by MALDI MSI after matrix deposition with a home-built sublimation device and thorough recrystallization. We present for the first time MALDI MSI data for secondary metabolite release during active mycoparasitism.

Received: December 7, 2015

Revised: January 25, 2016

Accepted: February 17, 2016

Keywords:

Fungal communication / MALDI MSI / Mycoparasitism / Peptaibiotics / Rhizoctonia / Trichoderma



Additional supporting information may be found in the online version of this article at the publisher's web-site

Technical brief

We present that mass spectrometry imaging (MSI) is capable of visualizing the release of secondary metabolites upon host sensing and fungal interaction directly from a miniaturized potato-dextrose agar (PDA) platform set up for a confrontation assay.

Fungi are globally distributed and numerous occurring microorganisms exceeding an estimated total number of 1.0 to 1.5 million [1]. Besides their use as producers and agents for pharmaceuticals, enzymes, organic acids and foods [2] the fungal kingdom plays an essential role in natural ecosystems and also comprises pathogenic and parasitic species. Fungal phytopathogens like *Rhizoctonia spp.* account for 80% of plant diseases [3] and demand for sustainable, ecofriendly strategies to prevent crop loss. Several fungal species are specialized to attack and antagonize plant pathogens by impeding their growth or directly killing the pathogens. Such beneficial microorganisms are already commercially applied as biological control agents (BCAs) [4]. The fungus *T. atroviride*

can establish itself in the plant rhizosphere, thereby increasing plant growth and productivity [5, 6]. In addition to that, *Trichoderma* is able to directly parasitize a range of pathogens (e.g. *Rhizoctonia solani*) by a process called mycoparasitism, allowing for the effective use of *Trichoderma* as BCA [7]. The processes leading to mycoparasitism are rather complex, yet sensing of the host and growth towards it, the active release of small molecules and enzymes and the subsequent penetration and killing of the host are key events. It is already known that *Trichoderma* produces secondary metabolites contributing to the antagonistic potential towards plant pathogens [8–10], and peptaibiotics are one important group of significant concentration [11, 12]. Within peptaibiotics, peptaibols represent a subgroup of non-ribosomal, membrane-active linear chained polypeptides characterized by a C-terminal alcohol residue, an acylated N-terminus and a high level of unusual amino acids, like α -aminoisobutyric acid (Aib), 2-isovaline (Iva), and hydroxyproline (Hyp) [13, 14]. Up to now peptaibols were detected either from fungal spores by intact cell mass spectrometry (ICMS) [15] or by well-established HPLC-MS/MS methods after isolation from cell cultures [14, 16, 17]. Based on work using MSI in the field of microbiology [18], our objective was to develop a sample preparation

Correspondence: Dr. Martina Marchetti-Deschmann, Vienna University of Technology, Institute of Chemical Technologies and Analytics, Getreidemarkt 9/164-IAC, 1060 Vienna, Austria

E-mail: martina.marchetti-deschmann@tuwien.ac.at

Colour Online: See the article online to view Figs. 1 and 2 in colour.

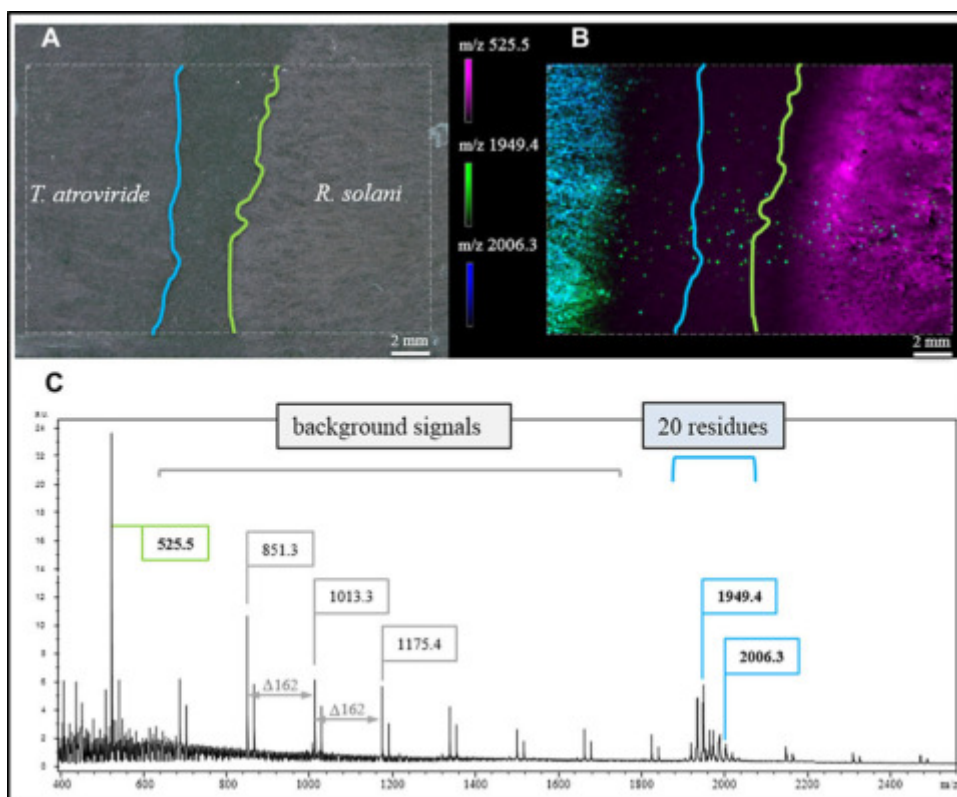


Figure 1. MALDI MSI of physically non-interacting *T. atroviride* and *R. solani* hyphae. (A) Light microscopic image showing non-interacting hyphae. (B) Distribution of selected m/z values representing characteristics for *T. atroviride* (m/z 1949.4 and 2006.3) and *R. solani* (m/z 525.5) (Supporting Information S1). (C) Mass profile for the selected ROI (outlined rectangle) exhibiting potato dextrose agar derived background signals with $\Delta m/z$ 162 and signals characteristic for each fungus (green ... *R. solani*, blue ... *T. atroviride*). Blue and green lines in (A) and (B) mark the outer rim of hyphal growth.

method suitable for studying *Trichoderma-Rhizoctonia* interactions directly from cultivation to visualize metabolite distributions induced by mycoparasite-host interaction to build a solid basis for future work in the field of fungal communication.

For our experiments we used chemicals of highest grade (supporting information). For the mycoparasitic *T. atroviride-R. solani* interaction, a miniaturized confrontation assay had to be established on conductive indium tin oxide (ITO) slides. *T. atroviride* and *R. solani* were first grown separately in petri dishes on PDA at 28°C. Then, an ITO slide was covered with a thin layer of PDA (approx. 400 μm) and mycelia plugs of each fungus were deposited on the glass slide approx. 1–2 cm apart and incubated at 28°C until (i) hyphae nearly reached each other (approx. 2–4 mm apart) or (ii) were clearly interacting which was monitored with a light microscope. After approx. 1–2 days, when fungal hyphae were grown towards each other, the sample was removed from the incubator and immediately stored at -70°C . For MALDI MSI the glass slides were removed from the freezer and thawed in a vacuum desiccator for 2 h. Matrix for MALDI MSI was deposited with a home-built sublimation apparatus in a vacuum-sealed, pressure-stabilized deposition chamber with constant heating for matrix vaporization and controlled sample plate cooling for deposition. 2,5-dihydroxy benzoic acid (2,5-DHB) dissolved in acetone was sublimed at 120°C and 35 mTorr to gain a matrix layer of 0.3 mg/cm². Recrystallization and hydration was done according to Yang et al. [19].

Finally, slides were dried for 2 min at 85°C and immediately used for analysis. Imaging measurements were performed on a MALDI TOF/RTOF mass spectrometer (ultraflextremeTM, Bruker Daltonics, Bremen, Germany) in a mass range from 100 to 2600 Da with ion suppression for ions below 50 Da. Images were normalized to the total ion current (TIC) (for full details on matrix deposition and MS analysis see Supporting Information).

MALDI MSI for PDA grown fungi is not straightforward. First metabolism has to be stopped, which was facilitated by immediate storing the sample at -70°C . Furthermore, the water content of the PDA layer had to be removed to prevent the vacuum system of the mass spectrometer from crashing. For this, samples were removed from the freezer and thawed while drying in a vacuum desiccator for 2 h. Then the glass slides were introduced into the fine vacuum of the sublimation unit guaranteeing completely dry samples for analysis.

Additionally, the hyphae-covered PDA layer does not provide an even surface. Most critical is the point of inoculation where height differences can be up to 1 mm. Because the points of inoculation were of lesser interest, only areas of similar height were investigated (rectangular shaped regions of interest (ROIs) in Figs. 1 and 2) to reduce signal broadening to a minimum due to differences in flight times.

By this we were for the first time able to visualize analyte distributions characteristic for both fungi directly from agar-covered ITO slides with good signal-to-noise (S/N) ratios (Fig. 1).

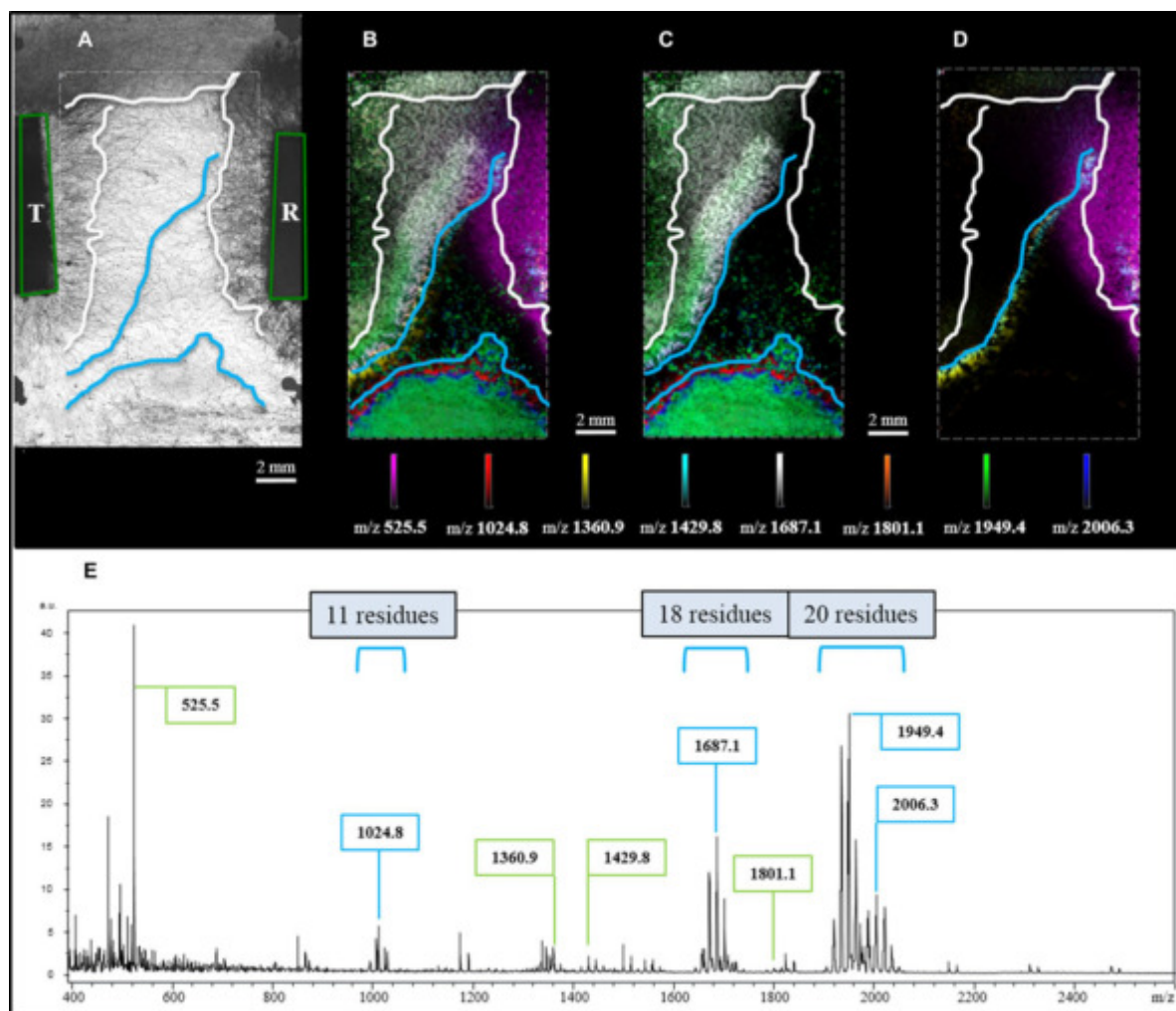


Figure 2. MALDI MSI of physically interacting *T. atroviride* (T) and *R. solani* (R) hyphae. (A) Light microscopic image showing points of inoculation (green tetragons), the outer rim of hyphal growth for both species (white lines) and borders for features detected by MSI (blue lines). (B) Molecular distributions of selected secondary metabolites localized by MALDI MSI. (C) *T. atroviride* specific metabolites (Supporting Information S3). (D) *R. solani* specific metabolites (Supporting Information S4). (E) Profile mass spectrum exhibiting signals assigned to *R. solani* (marked in green) and *T. atroviride* (marked in blue).

Figure 1A clearly shows that the fungal hyphae were not interacting (2–4 mm distance), yet already at this state characteristic analyte distributions could be determined (Fig. 1B). The exemplarily depicted distributions of m/z 525.5, 1949.4 and 2006.3 show that ions can specifically be assigned to either fungus. Interestingly, m/z 1949.4 and 2006.3 are present at apparent higher concentrations (higher signal intensities) in regions closer to the point of *T. atroviride* inoculation and almost not detected in the outer rim of the colony, while *R. solani* specific analytes were visible for the whole radially grown fungus. Yet m/z 1949.4 and 2006.3 seem to be released at an early growth stage to allow for migration towards *R. solani*. At this point we hypothesize that we have for the first time visualized metabolites released by *Trichoderma* during the phase of host sensing (details on single ion images see Supporting Information S1).

Compared with previous publications presenting antibiotic [20] or other chemical output [18] of fungi/bacteria grown on agar, this study presents signals with a very good S/N ratio (Fig. 1C), although background signals from PDA were not completely diminished (Supporting Information S2). We attribute this enhancement of detection to the fact that we established a miniaturized confrontation assay directly on glass slides, exhibiting therefore only a very thin layer of PDA providing nutrients. Even more important, matrix sublimation added the benefit of thorough sample drying and the rehydration step incorporated the analytes of interest very efficiently. At the current state of research we suspect the signals between m/z 1900 and 2000 to be representatives of above mentioned peptaibols because cultivation on solid media favors their production [21] and the observed m/z values correlate with data available in the

peptaibiotics database (<https://peptaibiotics-database.boku.ac.at/> [22]).

To strengthen our findings, MALDI MSI data were additionally collected from samples showing interacting hyphae (Fig. 2A). As can be seen in Fig. 2E metabolites were released to a high extent, suppressing the background signals from PDA. Figure 2B shows that the observed distributions correlate nicely with hyphal density. Again m/z 1949.4 and 2006.3 were observed, analytes considered to represent peptaibols containing 20 amino acid residues (details on single ion images see Supplemental S3). These m/z values are of high abundance also in an area far away from inoculation. This is caused by contamination coming from the inoculation procedure but not MALDI MSI sample preparation (Fig. 2B). This assumption is corroborated by light microscopy (Fig. 2A).

m/z 1024.8 and 1687.1 can be considered as peptaibols with chain lengths of 11 and 18 residues (Fig. 2C), from which 1024.8 was partially co-localized with 2006.3, while 1687.1 showed high prevalence in areas of *T. atroviride* hyphae of lesser density. Taking a closer look at the distribution of m/z 1024.8 one may hypothesize that this particular metabolite is released simultaneously with or even earlier than m/z 2006.3. Especially its distribution in the area of contamination is corroborating this assumption. For m/z 1024.8 first MS/MS spectra exhibited mass differences supporting the presence of Aib, therefore confirming the hypothesis that some compounds are indeed peptaibols (data not shown). Metabolites with m/z values of 1360.9, 1429.8 and 1801.1 (Fig. 2D) are predominantly present at the borders of fungal interaction and are most likely released by *R. solani*, especially when considering their presence near the point of inoculation (details on single ion images see Supporting Information S4).

With this technical brief we show for the first time that MALDI MSI can be used to visualize metabolites released during *T. atroviride*-*R. solani* interaction directly from PDA. First experiments show several distinct local distributions of metabolites for both, non-interacting and interacting hyphae. Characteristic masses correlating to known peptaibols with chain lengths of 11, 18 and 20 residues were detected. We attribute this achievement to an enhanced sample preparation strategy facilitating a miniaturized confrontation assay carried out directly on glass slides. Furthermore, MALDI matrix application by sublimation in combination with thorough recrystallization/hydration allows good analyte extraction from the agar medium and incorporation into the matrix crystals.

Based on these basic technical improvements, future work will focus on (i) biological aspects to obtain a better understanding of fungal sensing mechanisms and communication, and (ii) technical aspects to increase mass spectral quality by decreasing height differences of growing hyphae and preserving conductivity for the agar-coated targets.

Financial support by the Austrian Science Fund FWF (grant V139-B20) and the Vienna Science and Technology Fund (grant LS13-086) is acknowledged.

The authors have declared no conflict of interest.

References

- [1] Arora, D. K., (Ed.), Fungal biotechnology in agricultural, food, and environmental applications. *Mycol. Ser.* 2004, 21, 65–76.
- [2] Tkacz, J. S., Lange, L., (Eds.), *Advances in Fungal Biotechnology for Industry, Agriculture, and Medicine*, Kluwer Academic/Plenum Publishers 2004, 312–332.
- [3] Logemann, J., Schell, J., in: Chet, I. (Ed.), *Biotech. Plant Disease Control*. Wiley VCH 1993, 1–14.
- [4] Thakore, Y., The biopesticide market for global agricultural use. *Industrial Biotech.* 2006, 2, 194–208.
- [5] Harman, G. E., Howell, C. R., Viterbo, A., Chet, I., Lorito, M., Trichoderma species: opportunistic, avirulent plant symbionts. *Nat. Rev. Microbiol.* 2004, 2, 43–56.
- [6] Lorito, M., Woo, S. L., Harman, G. E., Monte, E., Translational research on trichoderma: from 'omics to the field. *Ann. Rev. Phytopathol.* 2010, 48, 395–417.
- [7] Benitez, T., Rincon, A. M., Limon, M. C., Codon, A. C., Biocontrol mechanisms of Trichoderma strains. *Int. Microbiol.* 2004, 7, 249–260.
- [8] Benhamou, N., Chet, I., Cellular and molecular mechanisms involved in the interaction between Trichoderma harzianum and Pythium ultimum. *Appl. Environ. Microbiol.* 1997, 63, 2095–2099.
- [9] Engelberth, J., Koch, T., Schuler, G., Bachmann, N. et al., Ion channel-forming alamethicin is a potent elicitor of volatile biosynthesis and tendrill coiling. Cross talk between jasmonate and salicylate signaling in lima bean. *Plant Physiol.* 2001, 125, 369–377.
- [10] Schirmbock, M., Lorito, M., Wang, Y. L., Hayes, C. K. et al., Parallel formation and synergism of hydrolytic enzymes and peptaibol antibiotics, molecular mechanisms involved in the antagonistic action of Trichoderma harzianum against phytopathogenic fungi. *Appl. Environ. Microbiol.* 1994, 60, 4364–4370.
- [11] Szekeres, A., Leitgeb, B., Kredics, L., Antal, Z. et al., Peptaibols and related peptaibiotics of Trichoderma. *Acta Microbiol. Immunol. Hung.* 2005, 52, 137–168.
- [12] Zeilinger, S., in: Gupta, V. K., Mach, R. L., Sreenivasaprasad, S. (Eds.), *Fungal Bio-Molecules: Sources, Applications and Recent Developments*, Wiley Blackwell, UK 2015, 101–113.
- [13] Chugh, J. K., Wallace, B. A., Peptaibols: models for ion channels. *Biochem. Soc. Trans.* 2001, 29, 565–570.
- [14] Roehrich, C. R., Iversen, A., Jaklitsch, W. M., Voglmayr, H. et al., Screening the biosphere: the fungicolous fungus Trichoderma phellinicola, a prolific source of hypophellins, new 17-, 18-, 19-, and 20-residue peptaibiotics. *Chem. Biodivers.* 2013, 10, 787–812.

- [15] Neuhof, T., Dieckmann, R., Druzhinina, I. S., Kubicek, C. P., von, D. H., Intact-cell MALDI-TOF mass spectrometry analysis of peptaibol formation by the genus *Trichoderma/Hypocrea*: can molecular phylogeny of species predict peptaibol structures? *Microbiology* 2007, 153, 3417–3437.
- [16] Stoppacher, N., Reithner, B., Omann, M., Zeilinger, S. et al., Profiling of trichorzianines in culture samples of *Trichoderma atroviride* by liquid chromatography/tandem mass spectrometry. *Rapid Commun. Mass Spectrom.* 2007, 21, 3963–3970.
- [17] Degenkolb, T., Fog Nielsen, K., Dieckmann, R., Branco-Rocha, F. et al., Peptaibol, secondary-metabolite, and hydrophobin pattern of commercial biocontrol agents formulated with species of the *Trichoderma harzianum* complex. *Chem. Biodivers.* 2015, 12, 662–684.
- [18] Watrous, J. D., Dorrestein, P. C., Imaging mass spectrometry in microbiology. *Nat. Rev. Microbiol.* 2011, 9, 683–694.
- [19] Yang, J., Caprioli, R. M., Matrix sublimation/recrystallization for imaging proteins by mass spectrometry at high spatial resolution. *Anal. Chem.* 2011, 83, 5728–5734.
- [20] Debois, D., Ongena, M., Cawoy, H., De Pauw, E., MALDI-FTICR MS imaging as a powerful tool to identify *paenibacillus* antibiotics involved in the inhibition of plant pathogens. *J. Am. Soc. Mass Spectrom.* 2013, 24, 1202–1213.
- [21] Kubicek, C. P., Komon-Zelazowska, M., Sandor, E., Druzhinina, I. S., Facts and challenges in the understanding of the biosynthesis of peptaibols by *Trichoderma*. *Chem. Biodivers.* 2007, 4, 1068–1082.
- [22] Neumann, N. K., Stoppacher, N., Zeilinger, S., Degenkolb, T. et al., The peptaibiotics database—a comprehensive online resource. *Chem. Biodivers.* 2015, 12, 743–751.

Supporting Information for Technical Brief

VISUALIZING FUNGAL METABOLITES DURING MYCOPARASITIC INTERACTION BY MALDI MASS SPECTROMETRY IMAGING

M. Holzlechner¹, S. Reitschmidt¹, S. Gruber², S. Zeilinger^{2,3}, M. Marchetti-Deschmann^{*1}

¹ *Institute of Chemical Technologies and Analytics, Vienna University of Technology, Vienna, Austria;*

² *Institute of Microbiology, University of Innsbruck, Innsbruck, Austria;*

³ *Institute of Chemical Engineering, Vienna University of Technology, Vienna, Austria*

Supporting Information on Chemicals and MALDI MSI Sample Preparation:

Chemicals

Glacial acetic acid and 2,5-dihydroxy benzoic (2,5-DHB) acid were obtained from Sigma Aldrich (St. Louis, MO, USA). Conductive indium tin oxide (ITO) glass targets were purchased from Delta Technologies (Loveland, CO, USA). MALDI MS calibrants, Angiotensin II, Neurotensin and the fragments Bradykinin 1-5 and ACTH 18-39, were obtained from LaserBio Labs (Sophia-Antipolis Cedox, F).

MALDI matrix deposition

Matrix was deposited with a home-built sublimation apparatus in a vacuum sealed, pressure controlled deposition chamber with constant heating for matrix vaporization and controlled sample plate cooling for deposition. 40.6 mg of 2,5-DHB per 7 mL acetone were placed in a preheated well (63 °C) forming a homogenous micro crystalline matrix layer after solvent evaporation. ITO slides with the dried fungi were mounted on the cooling plate and matrix was completely sublimed (120 °C, 35 mTorr). Amount of matrix coating per unit area was assessed with a balance and gave 0.3 mg/cm². Subsequent recrystallization and hydration according to Yang et al. [1] allowed analyte incorporation. Briefly, a filter paper soaked in 5 % aqueous acetic acid was placed in a glass petri dish. After attaching the matrix covered slide to a stainless steel plate and mounting it on the inner side of the cover, the petri dish was reassembled to form a hydration chamber and incubated in a constant temperature oven at 85 °C for 3 min. The slide was removed, dried at 85 °C for two minutes and immediately used for analysis.

Imaging MALDI Mass Spectrometry

Imaging measurements were performed on a MALDI TOF/RTOF mass spectrometer (UltrafleX-treme™, Bruker Daltonics, Bremen, Germany) using flexControl software v3.4. The Nd:YAG/355 nm smartbeam-II™ laser attenuator offset was adjusted to 65 % and laser fluency was operated at 55 %. Mass range was set from 100 – 2600 Da and ion suppression for ions below 50 Da. Data was collected at 0.50 Gs sampling rate. Pulsed ion extraction was adjusted to 120 ns. For reflectron positive ion mode, the source was set to an accelerating voltage of 20.00 kV with an extraction voltage of 17.95 kV, and a lens voltage of 7.50 kV. Imaging data were acquired with a spatial resolution of 120 μm by summing up 100 shots per array position without intraspot rastering using a laser repetition rate of 1 kHz. Mass spectra were calibrated externally using the cubic enhanced algorithm on the singly charged ions of 2,5-DHB (m/z 155.1), Angiotensin II (m/z 1046.5), Neurotensin (m/z 1673.9), Bradykinin fragment 1-5 (m/z 573.3) and ACTH 18-39 (m/z 2465.2).

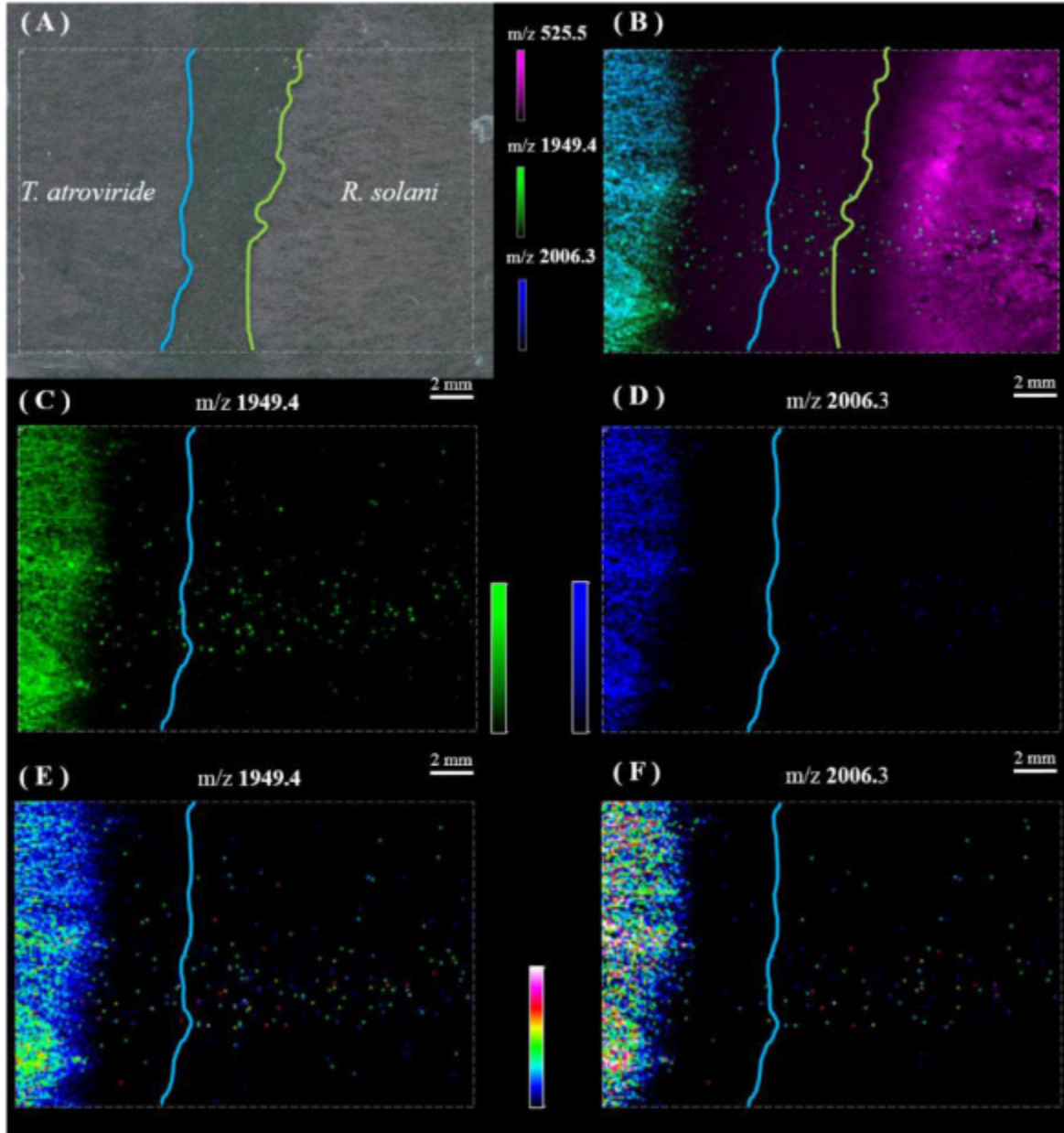
Image and Data Processing

Image acquisition and imaging data processing were carried out using flexImaging software v3.0 (Bruker Daltonics). Top Hat algorithm was used to subtract the baseline of the average spectra. Images were normalized to the total ion current. Intensity bars in figures represent ion intensity scalings from 0 to 100%. In supplemental figures, single color and rainbow color codes were displayed for highlighting the spatial and intensity distributions of ions, respectively.

[1] Yang, J., Caprioli, R. M., Matrix Sublimation/Recrystallization for Imaging Proteins by Mass Spectrometry at High Spatial Resolution. *Anal. Chem. (Washington, DC, U. S.)* 2011, 83, 5728-5734.

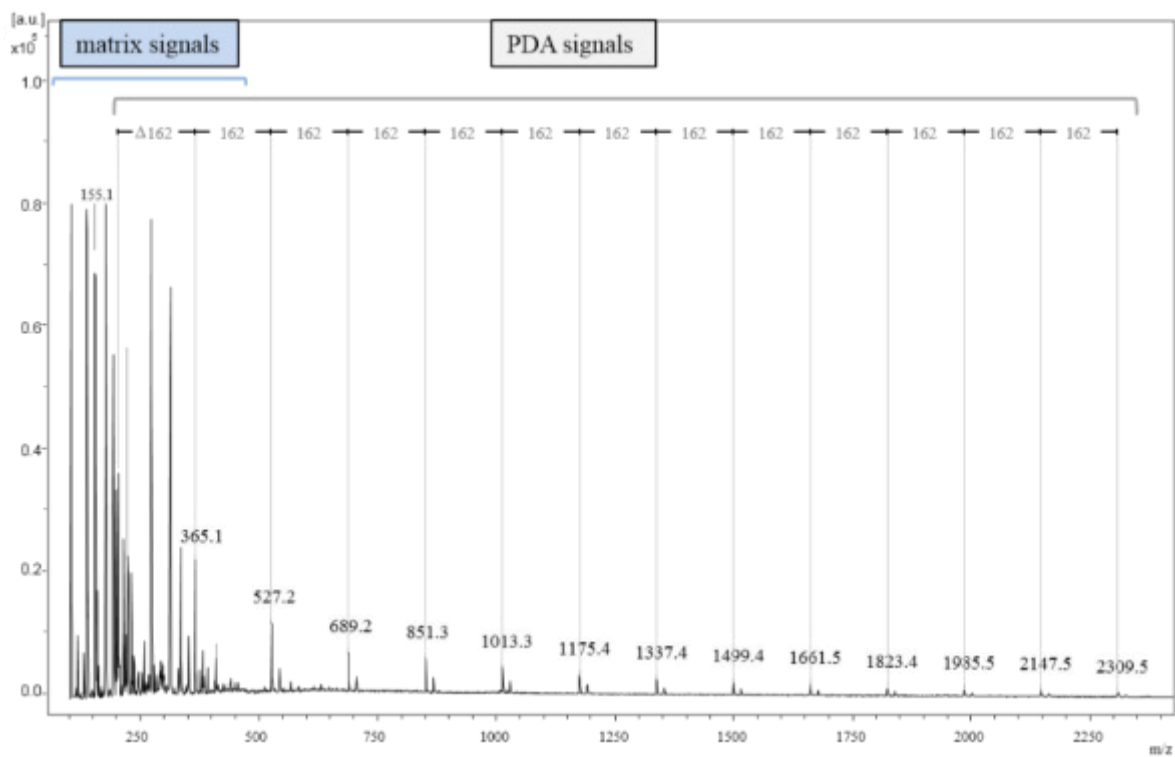
SUPPLEMENTARY FIGURES

Supplemental Figure 1



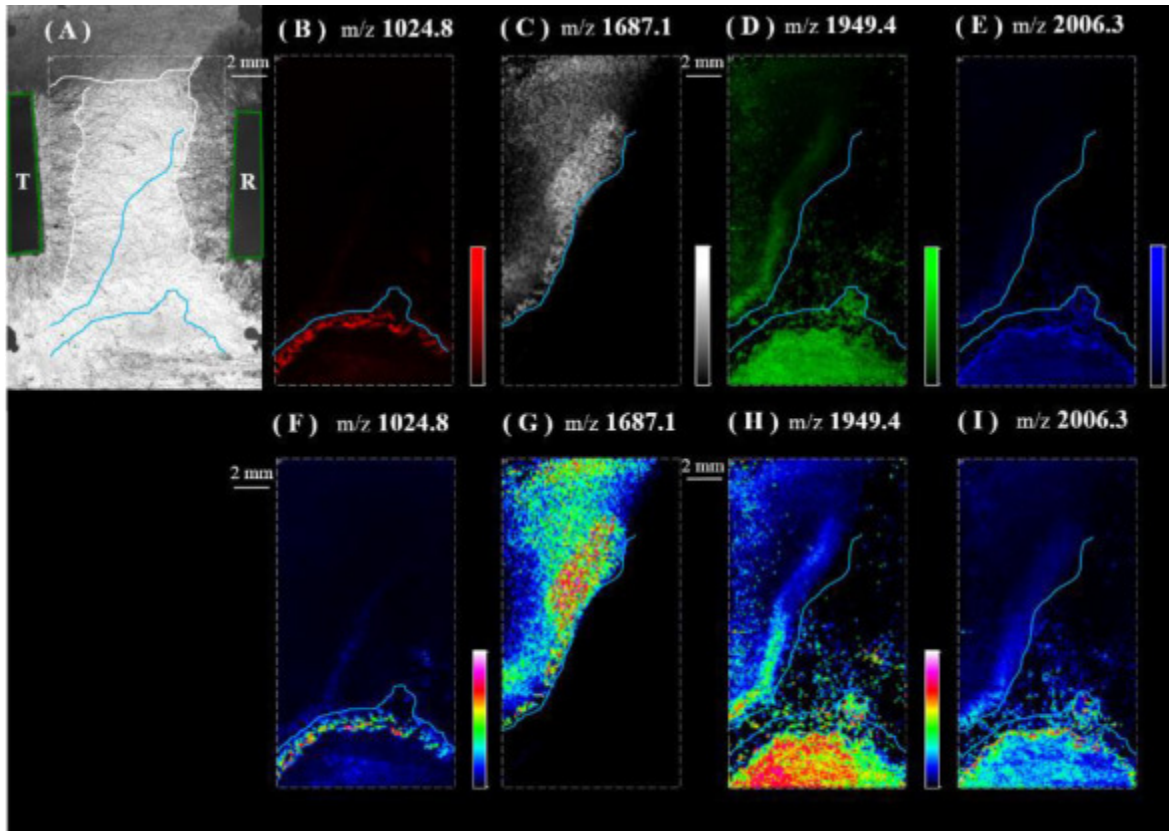
S1: MALDI MSI of physically non-interacting *T.atroviride* and *R.solani* hyphae. (A) Light microscopic image showing non-interacting hyphae. Blue and green lines mark the outer rim of hyphae growth. (B) Distribution of selected m/z values representing characteristics for *T.atroviride* (m/z 1949.4 and 2006.3) and *R.solani* (m/z 525.5). (C) and (D) visualize spatial distributed ions of m/z 1949.4 and m/z 2006.3. (E) and (F) show the respective ion intensity distributions.

Supplemental Figure 2



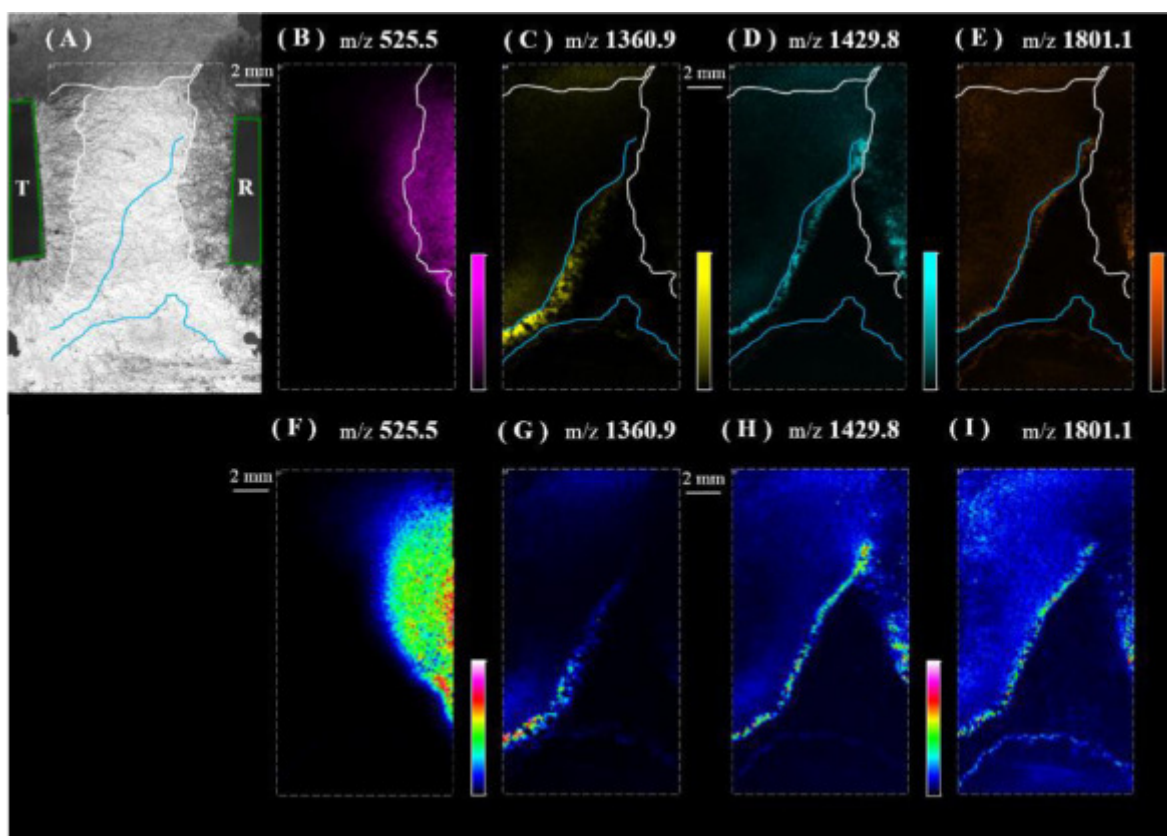
S2: Mass profile spectrum of potato dextrose agar exhibiting periodically occurring signals with $\Delta m/z$ 162 in grey and 2,5-DHB derived matrix signals in blue (mass range 100-2300 Da).

Supplemental Figure 3



S3: Single ion images of *T.atroviride* (T) specific metabolites derived during interaction with *R.solani* (R). (A) Light microscopic image showing points of inoculation (green tetragons), the outer rim of hyphal growth for both species (white lines) and borders for features detected by MSI (blue lines). Spatial distributions of metabolites with (B) m/z 1024.8, (C) m/z 1687.1, (D) m/z 1949.4 and (E) m/z 2006.3 are visualized. Images (F), (G), (H) and (I) highlight the respective ion intensity distributions.

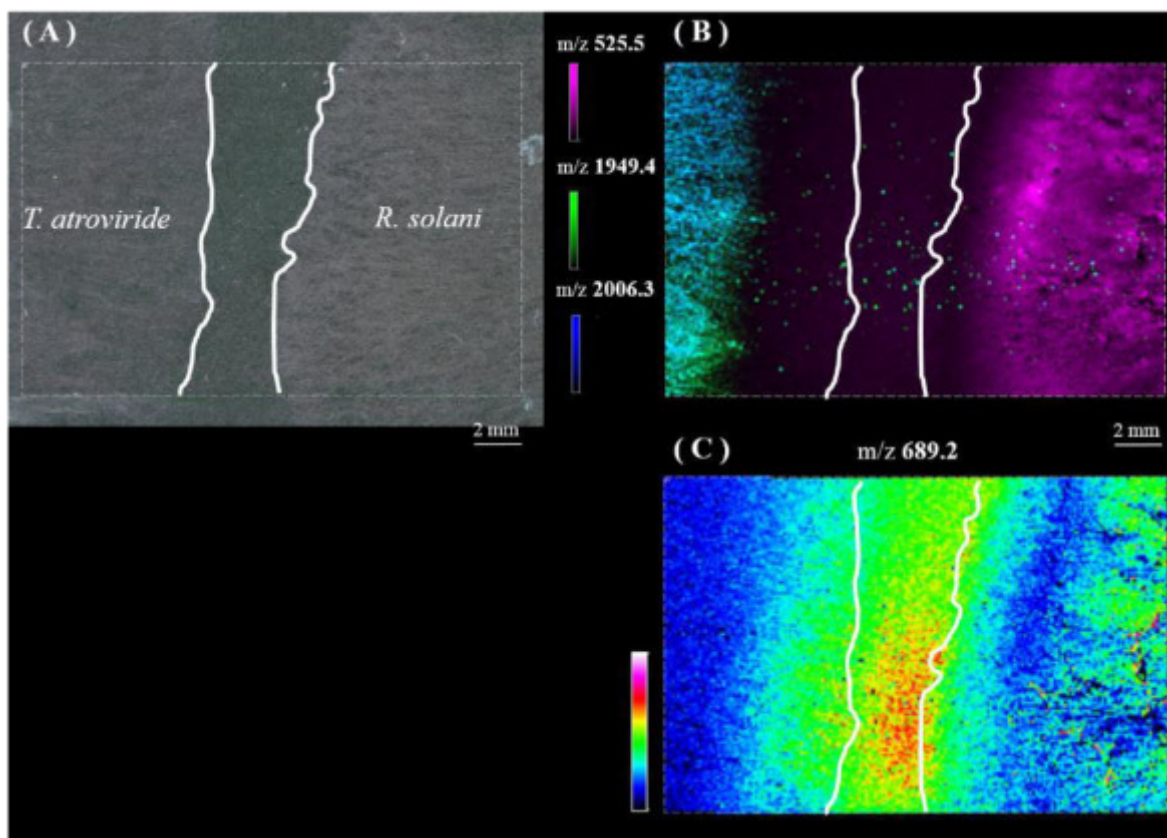
Supplemental Figure 4



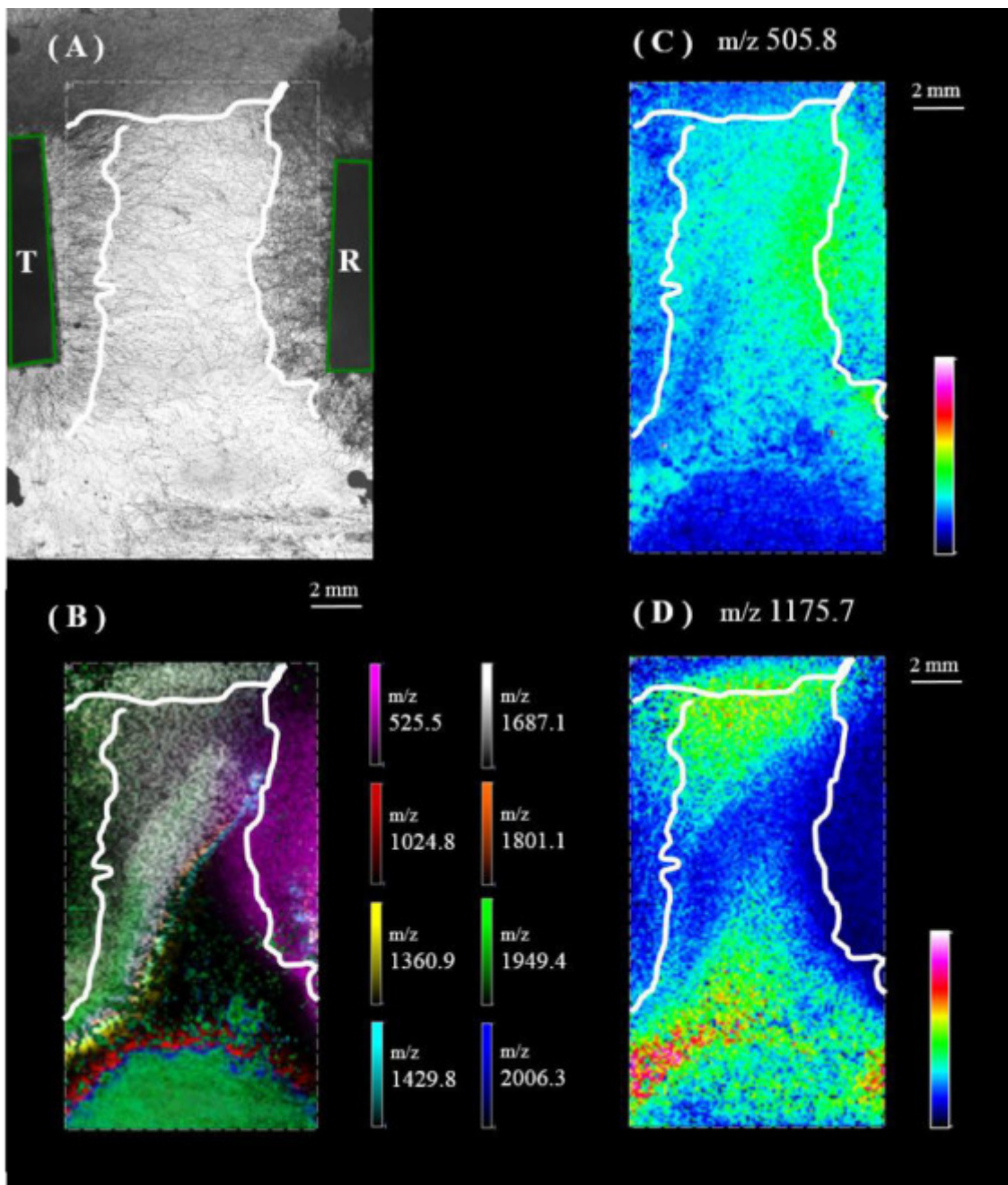
S4: Single ion images of *R.solani* (R) specific metabolites derived during interaction with *T.atroviride* (T). (A) Light microscopic image showing points of inoculation (green tetragons), the outer rim of dense hyphal growth for both species (white lines) and borders for features detected by MSI (blue lines). Spatial distributions of metabolites with (B) m/z 525.5, (C) m/z 1360.9, (D) m/z 1429.8 and (E) m/z 1801.1 are visualized. Images (F), (G), (H) and (I) highlight the respective ion intensity distributions.

Supplemental Figure 5 and 6

As suppression of ionization represents a significant issue in MALDI MSI, intensity distributions of ions in the hyphae free zone (non-interacting assay, S5) and in a particular area free of detected metabolites (interacting assay, S6) are shown.



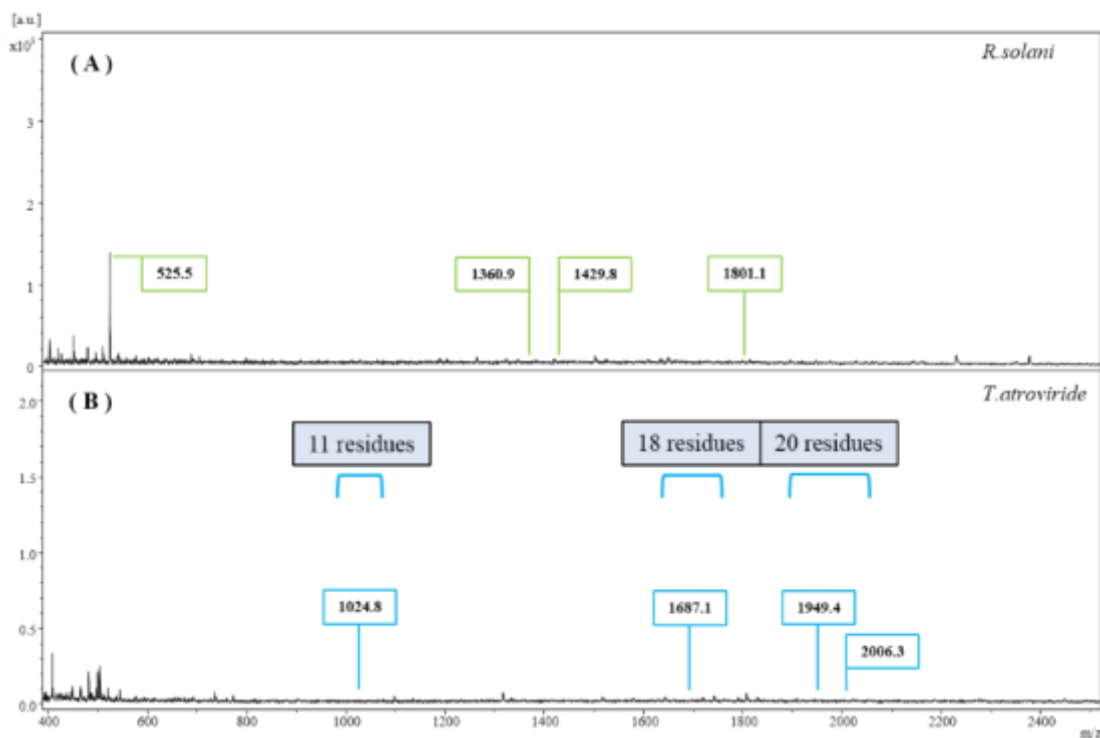
S5: MALDI MSI of physically non-interacting *T.atroviride* and *R.solani* hyphae. (A) Light microscopic image showing non-interacting hyphae of *T.atroviride* and *R. solani*. White lines mark the outer rim of hyphal growth. (B) Distribution of selected m/z values representing characteristics for *T. atroviride* (m/z 1949.4 and 2006.3) and *R. solani* (m/z 525.5). (C) Intensity distribution of a background ion (m/z 689.2) from the growth medium in the hyphae free zone indicating no potential ion suppression in the particular area.



S6: Disproval of ion suppression during MALDI MSI of interacting *T.atroviride* and *R.solani* hyphae. (A) Light microscopic image of interacting *T.atroviride* (T) and *R.solani* (R) hyphae. White lines mark the outer rim of hyphal growth for both species. Green tetragons show the points of inoculation. (B) Molecular distributions of selected secondary metabolites characteristic for *T.atroviride* and *R.solani* localized by MALDI MSI. Intensity distributions of (C) a minor abundant metabolite with m/z 505.8. and (D) a background ion derived from PDA with m/z 1175.7 disproving potential suppression of ionization in the particular area.

Supplemental Figure 7

Profile mass spectra of separately grown *R.solani* and *T.atroviride* were measured to exclude the detected secondary metabolites from being produced by non-interacting fungi but rather being stress-released during the mycoparasite-host interaction.



S7: Individual mass profiles of separately grown (A) *R.solani* and (B) *T.atroviride* (ROI 400-2600 Da). These mass spectra exhibit absence of characteristic signals of metabolites being released by (A) *R.solani* (1360.9/1429.8/1801.1; in green) and (B) *T.atroviride* (1024.8/1687.1/1949.4/2006.3; in blue) during mycoparasite-host interaction.

**6 IN SITU CHARACTERIZATION OF TISSUE-RESIDENT IMMUNE
CELLS BY MALDI MASS SPECTROMETRY IMAGING**

|article published in *Journal of Proteome Research* (2017), 16(1), 65-76 |

In Situ Characterization of Tissue-Resident Immune Cells by MALDI Mass Spectrometry Imaging

Matthias Holzlechner,^{†,⊥} Katharina Strasser,^{‡,§,⊥} Elitsa Zareva,[†] Luise Steinhäuser,[‡] Hanna Birnleitner,[‡] Andrea Beer,^{||} Michael Bergmann,[‡] Rudolf Oehler,[‡] and Martina Marchetti-Deschmann^{*,†}

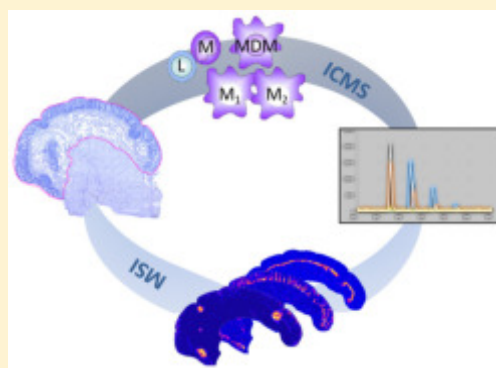
[†]Institute of Chemical Technologies and Analytics (CTA), TU Wien, 1060 Vienna, Austria

[‡]Department of Surgery and Comprehensive Cancer Center, ^{||}Clinical Institute for Pathology, Medical University of Vienna, 1090 Vienna, Austria

[§]CBmed GmbH—Center for Biomarker Research in Medicine, 8020 Graz, Austria

S Supporting Information

ABSTRACT: Tissue-resident immune cells differ from their corresponding blood cells in many functional aspects. Although the proteome of blood immune cells has been well-investigated, there are almost no data on tissue-resident immune cells. Here, we explored the potential of using MALDI-TOF-MS imaging (MSI) to investigate these cells in colon tissue, which exhibits a strong infiltration of immune cells. MSI identified several proteinaceous markers that colocalized with specific structures of the colon, such as mucosa or muscularis mucosae, in six patients. In addition, we showed that certain m/z values have the same spatial distribution as CD3⁺ T lymphocytes in the lymphoid follicular structures or as CD206⁺ macrophages in the lamina propria. For further corroboration, blood lymphocytes and monocytes from 10 healthy volunteers were analyzed by intact cell mass spectrometry (ICMS). Furthermore, we analyzed monocyte-derived macrophages that had been polarized in vitro into proinflammatory M₁ and anti-inflammatory M₂ phenotypes. The mass spectra differed clearly among all immune cell types. Additionally, it was found that distinct signals from ICMS analysis were identical to the m/z values found in the MSI experiment in lymphoid follicular structures. These data show for the first time that MSI is well-suited to visualize the spatial distribution of immune cells in human colon tissue. We consider MALDI mass spectrometry imaging to be a technique with high potential for use in rapid investigations of tissue-specific features of cells.



KEYWORDS: MALDI mass spectrometry imaging, immunohistochemistry, immune cells, monocytes, lymphocytes, macrophages, colon tissue

INTRODUCTION

The intestine contains the highest number of immune cells of any tissue in the body, which reflects the massive antigen load that these cells are exposed to in this environment.¹ A functional immune system is therefore essential for the homeostasis of the gastrointestinal (GI) tract. There are two major compartments of immune cells within the intestine, mucosa-associated lymphoid tissue (MALT) and diffuse mucosal lymphoid and myeloid cells.² MALT is a system of small follicular aggregates of lymphocytes. These follicles are scattered throughout the intestine, showing an increased frequency in the colon, which is linked to the abundant and diverse microbial flora in this part of the intestine. Diffuse mucosal immune cells are located in the mucosa and consist of various cells, such as lymphocytes, plasma cells, macrophages, and granulocytes. Intraepithelial lymphocytes are mainly CD8⁺ T cells, important for cytotoxicity and cytokine secretion, whereas CD4⁺ T cells and B cells are predominantly found in follicles.² Together with the innate branch of the gut immune

system, these effector lymphocytes form the first line of defense against invading pathogens and play a crucial role in maintaining barrier integrity.

Tissue-resident lymphocytes originate from the same precursor cells as their counterparts in the circulation; however, they differentiate into specialized cells depending on the stimuli they receive and the location into which they migrate.³ These cells differ in various parts of the body and provide regional immunity. Thus, the presence of T lymphocytes in the GI tract provides tissue-restricted priming to intestinal antigens.⁴ Lymphocytes also provide immunoglobulins for the direct quenching of bacterial virulence factors within the mucus.⁵

Blood monocytes originate from myeloid progenitor cells of the bone marrow. If blood monocytes migrate from the bloodstream into a tissue, they differentiate into macrophages

Special Issue: The Immune System and the Proteome 2016

Received: July 1, 2016

Published: October 18, 2016

that are polarized in a manner that depends on the stimuli received from the microenvironment. Reports have shown that macrophages of the lung, liver, central nervous system, and peritoneal cavity derive from embryonic precursors that can proliferate in situ. In contrast, intestinal macrophages are replenished by blood monocytes.⁶ When monocytes leave the blood and migrate into the GI tract, they lose CD14 expression and adopt an anti-inflammatory phenotype manifested by the expression of various cell surface markers, such as CD206, also called mannose receptor C type 1 (MRC1).^{6,7} Macrophages in the entire GI are mostly located in the lamina propria of the mucosa in close proximity to the epithelial cells of the crypts.⁸ They are also found in the smooth muscle layers, where they are important for the motility of the intestine.^{9,10} GI macrophages play also an essential role in the homeostasis of the intestine by interacting with other cells, producing cytokines and other soluble factors, scavenging dead cells and debris, and encapsulating and destroying material that enters the epithelial barrier such as bacteria.^{1,7}

Classically, immune cells are characterized by their expression of proteins mainly on their cell surface, such as cluster of differentiation (CD) molecules. These molecules can be identified using monoclonal antibodies against the appropriate marker and analyzed with flow cytometry. More than one marker is typically necessary to clearly identify a certain cell population or the activation and polarization status of these cells. With multicolor flow cytometers and sophisticated gating strategies, it is feasible to identify subpopulations of immune cells with differently labeled antibodies against several cell markers. The identification of immune cells in tissue sections also requires multicolor immunohistochemical staining.¹ Still, it is a challenge to reliably identify single immune cells and their activation or polarization status within one tissue section. Additionally, the differences between blood immune cells and tissue-resident immune cells include modifications of the epigenetic profile and transcriptome of these cells.¹¹ However, very little is known about the proteome of tissue-resident immune cells. Thus, mass spectrometry (MS) is a promising tool that can detect cell characteristics without being restricted to the use of specific antibodies. Intact cell mass spectrometry (ICMS), introduced in 2001 for bacterial differentiation, has made a significant impact not only in environmental but also in biotechnological and clinical research.¹² Despite this growing importance, to date only a few applications have been described for the analysis of mammalian cells and immune cells in particular.

Munteanu and co-workers showed that MALDI-MS can differentiate between different cell types and interindividual variations of cells in suspension.¹³ They also stated that this method is suitable for global analysis of differences in mass spectral signatures of intact polymorphonuclear neutrophils and monocytes obtained from blood samples.¹⁴ The research group of Textoris was able to assess a set of peaks that represent the MS signature of immune cells,¹⁵ and they also characterized different polarization levels of human macrophages.¹⁶ They differentiated monocyte-derived macrophages in vitro either into M₁ or M₂ type macrophages and identified specific protein patterns by ICMS. At the level of CD markers, in contrast, a differentiation between these two polarization types is nearly impossible. A very recent study used the same technique to distinguish human monocyte subpopulations.¹⁷

Mass spectrometric imaging (MSI) is a rapidly developing application. In MSI, both the intensities of m/z values and their respective x/y positions within a sample are recorded, allowing for the generation of images representing ion intensities at certain tissue localizations. This information is of special interest when analytes are not evenly distributed but compartmentalized, such as in a tissue. Consequently, this method provides a potential tool for the investigation of tissue-resident immune cells. A recently introduced technology, mass cytometry, combines MSI with metal-chelated antibodies as an alternative method to classical immunohistochemistry (IHC). IHC uses enzyme-linked antibodies to detect antigens on tissue slides. The enzyme catalyzes the reaction of a substrate to a colored product, which can be seen in a microscope. The new technology uses metal-chelated antibodies where images of metal distributions within the tissue are generated from respective isotopes measured by MS.^{18,19} This method is more sensitive than IHC, yet it is still a knowledge-driven approach. To date, no study has been published focusing on an unbiased approach to distinguish the proteomic profiles of immune cells in a tissue.

In the present study, we investigated whether MSI can be used to study immune cells in tissue samples without using antibodies. First, we analyzed human colon tissues sections and compared the results to classical IHC stainings of immune cells. Then, we used ICMS to characterize isolated peripheral blood lymphocytes and monocytes. We showed that MSI provides additional information on immune cells within the tissue, which allows the cross-talk between lymphocytes and their microenvironment to be visualized.

■ EXPERIMENTAL SECTION

Materials

All reagents were purchased from Sigma-Aldrich (St. Louis, MO, USA) with a purity of at least 99%, if not otherwise stated. Calibrants for mass spectrometry, insulin (bovine), cytochrome C (horse heart), and myoglobin (horse heart), were obtained from LaserBio Laboratories (Sophia-Antipolis, Cedex, FR). Ultra-high-quality water (ddH₂O) with a resistivity <18.2 MΩ·cm @ 25 °C was obtained from a Simplicity system (Millipore, Billerica, MA, USA). Conductive indium tin oxide (ITO)-coated microscope glass slides were purchased from Delta Technologies (Loveland, MN, USA). Buffy coats were bought from the Red Cross (Vienna, AT). CD14⁺ isolation was performed with MACS technology, and all reagents and equipment were bought from Miltenyi Biotec (Bergisch Gladbach, DE). Ethanol (96%, technical grade) was purchased from the pharmacy of the general hospital of Vienna (AT). All reagents used for immunohistochemical staining were purchased from Vector Laboratories (Burlingame, CA, USA), if not stated otherwise.

Collection and Processing of Human Colon Tissue

Pieces of normal colon tissue were taken from surgical specimens that were resected in the course of colon cancer surgery. The patients gave informed consent, and sample collection was approved by the ethical committee of the Medical University of Vienna. Tissues of seven patients were investigated. One of the samples did not show follicular lymphoid structures and was considered a control for our findings (markers in lymphoid structures). Fresh colon tissues were snap frozen and stored at -80 °C. The tissues were transferred on dry ice to a Leica CM3050 cryostat (Leica

Microsystems GmbH, Wetzlar, DE) and cryosectioned at a nominal thickness of 10 μm . Frozen tissue sections were thaw-mounted on ITO slides, vacuum-dried in a desiccator for ≥ 1 h at room temperature, and stored in a sealed slide holder at -80 $^{\circ}\text{C}$ until needed. Consecutive sections were collected for MSI and histological analyses.

Immunohistochemistry (IHC)

Every other section was immunostained to assess the histological accuracy of ion images. For IHC staining, cryosectioned tissues were fixed for 10 min in 96% ethanol and stained according to standard protocols with the Vectastain Universal ABC kit. Briefly, endogenous peroxidases were blocked with Bloxall for 10 min in the dark. After 5 min of washing in 0.1% Tween 20 in DPBS, nonspecific binding sites were blocked with horse serum for 20 min. The sections were incubated with primary anti-human CD3e (clone SP7, 1:150; Thermo-Fisher Scientific) or CD206 (clone 19.2, 1:500; Becton-Dickinson, Franklin Lakes, NJ, USA) antibody at room temperature for 1 h. Slides were then washed and incubated for 30 min with an anti-mouse/rabbit horse secondary antibody. After three washing steps, the ABC reagent was applied for 30 min followed by another washing step. The tissues were incubated briefly with 3,3-diaminobenzidine (DAB) substrate, and the nuclei were counterstained with hematoxylin (Merck, Darmstadt, Germany). Slides were scanned with a TissueFAXS (Zeiss Axio Imager.M1, TissueFAXS 4.2, TissueGnostics GmbH, Vienna, AT) slide scanning system.

MALDI MSI of Human Colon Tissue

All seven patient samples were analyzed at least in duplicate. Frozen tissue sections were allowed to equilibrate to room temperature in a desiccator prior to six washing steps.²⁰ Briefly, mounted tissue sections were consecutively submerged in 70% ethanol, 100% ethanol, Carnoy's solution (60% ethanol, 30% chloroform, 10% acetic acid), 100% ethanol, ddH₂O, and 100% ethanol for 30 s each, with the exception of the Carnoy's solution (2 min). Special care was taken not to agitate the mounted sample during incubation. Human colon tissue sections were then dried in a desiccator (≥ 15 min) prior to matrix application. Matrix deposition was performed using a home-built sublimation apparatus (TU Wien). In a vacuum-sealed and pressure-controlled deposition chamber, 25.5 mg of SA was vaporized and sublimed on the tissue at 165 $^{\circ}\text{C}$ and 35 mTorr. Subsequent recrystallization and hydration were performed according to Yang et al.²⁰ Briefly, the matrix-covered ITO slide was attached to a stainless steel plate on the bottom side of a Petri dish lid. After placing a filter paper soaked in 5% aqueous acetic acid in the Petri dish, the hydration chamber was reassembled and incubated at 85 $^{\circ}\text{C}$ for 4 min.

MSI data were acquired on a MALDI TOF/RTOF mass spectrometer (ultrafleXtreme) using a linear geometry and flexControl software v3.4 (Bruker Daltonics, Bremen, DE). The laser attenuator offset was adjusted to 65%, and the laser fluency was set to 60%. The mass range between 4 and 20 kDa was selected with ion suppression for analytes below 3.9 kDa. Pulsed ion extraction and the sampling rate were adjusted to 250 ns and 0.25 GS/s, respectively. The accelerating voltage was set to 20.0 kV, the extraction voltage, to 18.6 kV, and the lens voltage, to 6.5 kV. MSI data were acquired at a lateral resolution of 30 μm by summing 100 shots per array position (without intraspot rastering) within an array of 22 210 points

using a laser repetition rate of 1 kHz. Mass spectra were calibrated externally using the cubic enhanced algorithm. Data acquisition and image representation were carried out using flexImaging software v3.0 (Bruker Daltonics) and SCiLS Lab software v2015b (SCiLS, Bremen, DE). Acquired imaging data were normalized to the total ion current (TIC).

After data acquisition, the remaining matrix was removed from the sample by sonification in 96% ethanol for 10 s. The tissue section was fixed in 96% ethanol for 10 min and further used for hematoxylin staining.

Collection and Processing of Blood Samples for ICMS

Blood from 10 healthy volunteers was used. Peripheral blood mononuclear cells (PBMCs) were isolated from buffy coats by Ficoll-Paque Plus (GE Healthcare, Little Chalfont, GB) gradient centrifugation according to the manufacturer's instructions. In short, 10 mL of Ficoll-Paque Plus was layered underneath 5 mL of buffy coat mixed with 30 mL of Dubecco's phosphate-buffered saline (DPBS; Gibco, Thermo Fisher Scientific, Waltham, MA, USA). Tubes were centrifuged for 20 min at 400g at room temperature with deceleration set to off. PBMCs were further transferred from the interphase into new tubes and washed with 30 mL of DPBS. For further cell separation, CD14⁺ cells were isolated by magnetic cell sorting (MACS technology) according to the company's protocol. Briefly, cells were resuspended in MACS buffer and CD14 microbeads and incubated on ice for 15 min. After washing with MACS buffer, cells were resuspended in 4 mL of degassed MACS buffer and applied to LS columns on a MidiSeparator. CD14 negative cells were collected, and after two washing steps, the tube was replaced with a new one. Bound CD14 positive cells were flushed out of the column with MACS buffer. Isolated cells were aliquoted to 1×10^6 cells per tube and washed two times with 20 mL of sterile magnesium and calcium free DPBS. The suspension was centrifuged at 400g for 5 min at 4 $^{\circ}\text{C}$. DPBS was discarded, and the cell pellets were snap frozen in liquid nitrogen and stored at -80 $^{\circ}\text{C}$ until further use.

For differentiation, fresh monocytes were cultivated in RPMI-1640 (Gibco) supplemented with 10% fetal calf serum (FCS; Linaris, Dossenheim, DE) at 37 $^{\circ}\text{C}$ and 5% CO₂. They were differentiated with 100 ng/mL macrophage colony-stimulating factor (M-CSF; eBioscience, San Diego, USA) for 5 days and further polarized for 2 days with 20 ng/mL interferon gamma (IFN γ ; Imukin injection solution; Boehringer Ingelheim, Vienna, A) and 100 ng/mL lipopolysaccharide (LPS; M₁ or M_{IFN γ /LPS}) or with 20 ng/mL IL-4 (M₂ or M_{IL-4}; Miltenyi Biotec). The cells were aliquoted at 1×10^6 cells per tube, washed two times with sterile DPBS (as described above), snap frozen as a pellet, and stored at -80 $^{\circ}\text{C}$ until further analysis.

ICMS of Primary Human Peripheral Blood Cells and Differentiated Monocytes

Samples were analyzed at least in triplicate. Trifluoroacetic acid (TFA; 100 μL of 0.1%) in ddH₂O was added to a cell pellet, and cells were further disintegrated by sheering (multiple rounds of aspirating the solution into a pipet tip and quickly emptying the tip). One microliter of the cell lysate was applied on a stainless steel target and dried for 10 min at underambient conditions. One microliter of matrix solution (10 mg sinapic acid (SA)/mL in acetonitrile/0.1% aqueous TFA, 1/1 (v/v)) was carefully pipetted onto the dried cell layer and allowed to dry again for 10 min under ambient conditions followed by 5

min in vacuum. ICMS measurements were performed on the instrument described for the MSI experiment, using the same parameters as above, except for the sampling rate, which was set to 0.50 GS/s. Eighty spectra were accumulated for each sample spot (random walk; 100 shots per spot, 8000 laser shots per sample).

Statistical Analysis of ICMS

MS data were analyzed using ClinProTools v3.0 (Bruker Daltonics). The analysis included postprocessing, calculating peak statistics, unsupervised hierarchical cluster analysis (HCA), receiver operating characteristic (ROC) curves, and principal component analysis (PCA). Mass spectra were baseline subtracted (Top Hat; 10% minimal baseline width) and smoothed using the Savitzky–Golay algorithm (width: 3 Da; cycles: 1). Thereafter, spectra were recalibrated within a mass accuracy of 1000 ppm and a 30% match to calibrant peaks. Automatic peak picking was performed on total average spectra using a signal-to-noise (S/N) threshold of 7. A peak statistics report was generated including average peak intensities along with standard deviations derived from monocytes and lymphocytes. For further validation of the measurements, we included all spectra acquired from monocytes, lymphocytes, and polarized cells in the HCA (10 mass spectra per cell type from independent experiments; scaling method: unit variance; dimension reduction: 95% explained sum variance; distance method: Euclidean; linkage algorithm: Ward). The area-under-the-curve (AUC) value of a ROC analysis was used to assess the discriminative power of m/z values within the mass spectra acquired from these two immune cell populations. Additionally, the statistical significance of their differential expression was calculated using Student's t test. MS data were evaluated by PCA using the same data processing parameters to show the mass spectra and m/z values with the highest variance between the data sets.

RESULTS AND DISCUSSION

MALDI MSI of Tissue-Specific Structures in Human Colon

To investigate the potential of MALDI MSI for in-tissue cell detection in support of immunohistology, we analyzed human colon tissue samples and compared MSI data to classical hematoxylin and immunohistochemical stainings. Human colon tissues of seven patients were cryosectioned, mounted on ITO-covered glass slides, and washed. After covering the tissue section with MALDI matrix by sublimation, the matrix layer was recrystallized and the tissue section was hydrated to enhance analyte extraction. Figure 1A shows the hematoxylin staining of a colon tissue section after MSI analysis. The investigated region of interest (ROI) is indicated by the dotted line. The microscopic image and the color coding in the inset depict the different structures of the colon: (i) the mucosa consisting of epithelial crypts and lamina propria, (ii) the lamina muscularis mucosae, (iii) the submucosa, and (iv) the muscularis externa. In addition, the human colon sample was interspersed with nodular lymphoid structures. Figure 1B shows morphological details of selected tissue regions investigated by MSI: B1–B3 show nodular lymphoid structures and B4 and B5 display enlargements of the epithelial crypts (longitudinal and transversal, respectively). MSI at a lateral resolution of 30 μm allowed for the visualization of peptide and protein distributions according to the colon's morphology (Figure 1C–E and Supporting Information Figure S1). By comparing ion images of different m/z values with the

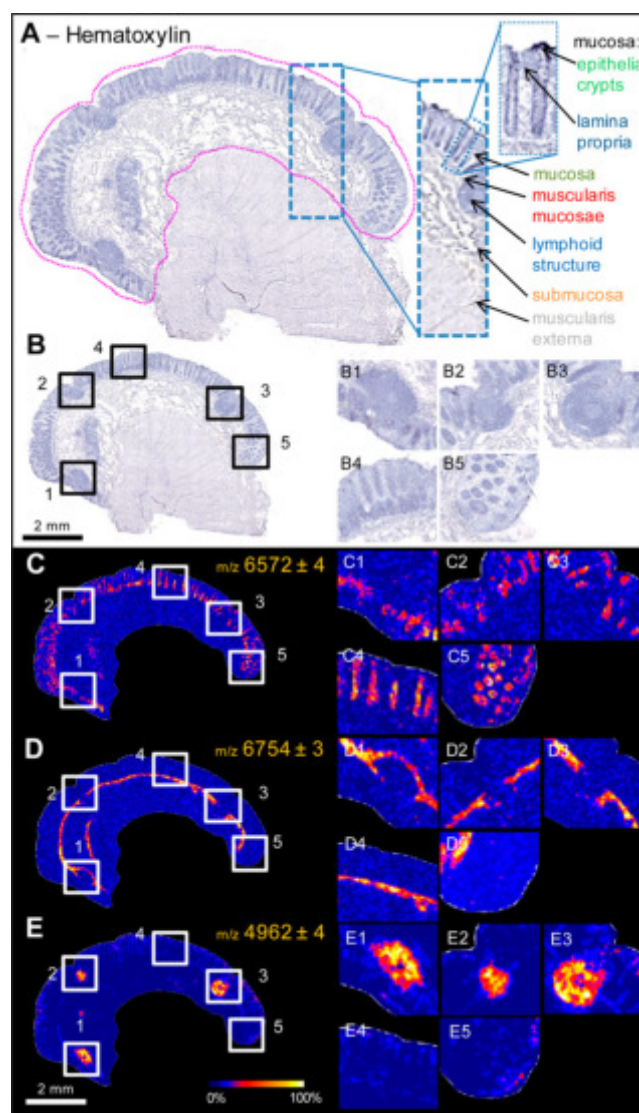


Figure 1. Correlation of IHC and MALDI MSI analyses to visualize human colon structures. (A) Hematoxylin staining of a 10 μm colon tissue section after MALDI MSI with details of the morphological structures indicated. (B) Location and magnifications of distinct ROIs studied by MSI. (C–E) Distribution of selected m/z values visualized by MALDI MSI: (C) m/z 6572 \pm 4, resembling the cryptic organization of the epithelial cells (longitudinal and transversal), (D) m/z 6754 \pm 3, showing the arrangement of the lamina muscularis mucosae, and (E) m/z 4962 \pm 4, visualizing nodular lymphoid structures. (Relative intensities are in accordance with the color scale.)

morphology after hematoxylin staining, several signals were observed to be unambiguously distributed in distinct colon tissue structures. As indicated in Table 1, some m/z values were uniquely located in the mucosa, resembling the cryptic organization of epithelial cells (longitudinal and transversal). As an example, the ion distribution of m/z 6572 \pm 4 in human colon tissue is shown in Figure 1C. Distributions of other mass values such as m/z 6754 \pm 3 form a small band and border the mucosa, revealing the arrangement of the lamina muscularis mucosae (Figure 1D). Additionally, some analyte distributions such as m/z 4962 \pm 4 were restricted to nodular lymphoid structures (Figure 1E). Yet, various m/z values were found to be distributed in more than one tissue structure, indicating commonly expressed markers (see Table 1). These allocations

Table 1. Mass Values Characteristic of Specific Regions in Colon Tissue^a

<i>n</i>	mucosa	muscularis mucosae	follicular lymphoid structures	commonly expressed markers
6/6	6239 ± 3	6754 ± 3	4744 ± 3	4609 ± 5
	6572 ± 4		4962 ± 4	4729 ± 3
	6690 ± 4		5169 ± 4	5657 ± 3
	7081 ± 4			6774 ± 5
	7763 ± 4			8560 ± 5
	8089 ± 5			
5/6	8955 ± 5	5622 ± 4		5737 ± 3
	9069 ± 5			6970 ± 5
	10 092 ± 5			
	7430 ± 4			
	9742 ± 5			
4/6	11 961 ± 5			
	7823 ± 5			
2/6				6171 ± 3

^aSupporting Information provides MALDI MSI images of all listed values for all patient samples (*n*, frequency of occurrence in the patient samples; *x*, *m/z* values ± peak width). One patient sample did not show follicular lymphoid structures and was therefore considered a control sample.

were observed in all colon samples from seven donors (see Table 1; ion images for all tissue samples can be found in Supporting Information Figures S4–S7).

Next, we looked for potential immune cell-specific *m/z* values in colon tissue. Therefore, we compared the acquired MALDI ion images with consecutive tissue sections that were immunohistochemically stained for the expression of either the T lymphocyte marker CD3 or the macrophage marker CD206 using specific antibodies. Figure 2 shows a colon section that was hematoxylin stained after MALDI MSI (Figure 2A) and the same area of a consecutive section stained for CD3 (Figure 2B; all other samples, see Supporting Information Figure S3). The two enlargements show regions containing a nodular lymphoid structure (region 1) and the mucosa (region 2). CD3⁺ cells were detected at a very high concentration in nodular lymphoid aggregates (Figure 2B1) and as dispersed single cells within the lamina propria (Figure 2B2). Figure 2C shows the spatial distribution of *m/z* 4744 ± 3, which colocalized nicely with CD3⁺ cells in the nodular lymphoid structures, as indicated by the high ion intensities (Figure 2C1). The two other ions that were found to be specific for these lymphoid structures (*m/z* 4962 ± 4 and 5169 ± 4) showed a similar colocalization (Table 1 and Supporting Information Figure S2). This was confirmed in colon tissues from all other donors (Supporting Information Figure S4). However, the interspersed single lymphocytes within the mucosa (Figure 2B2) were not detected (Figure 2C2).

Figure 2D,E shows IHC staining for the macrophage mannose receptor 1 (MRC1 or CD206) and the corresponding ion distribution of *m/z* 9069 ± 5. CD206⁺ macrophages were localized as single cells in all parts of the colon, but they were highly concentrated in the lamina propria, especially beneath the epithelial cell layer of the crypts, and were only sporadically found in nodular lymphoid aggregates. It was observed that the *m/z* values of 9742 ± 5 and 9069 ± 5 exhibited similar ion distributions, where the latter showed high intensities in structures beneath the epithelium but not in lymphoid structures (Figure 2E).

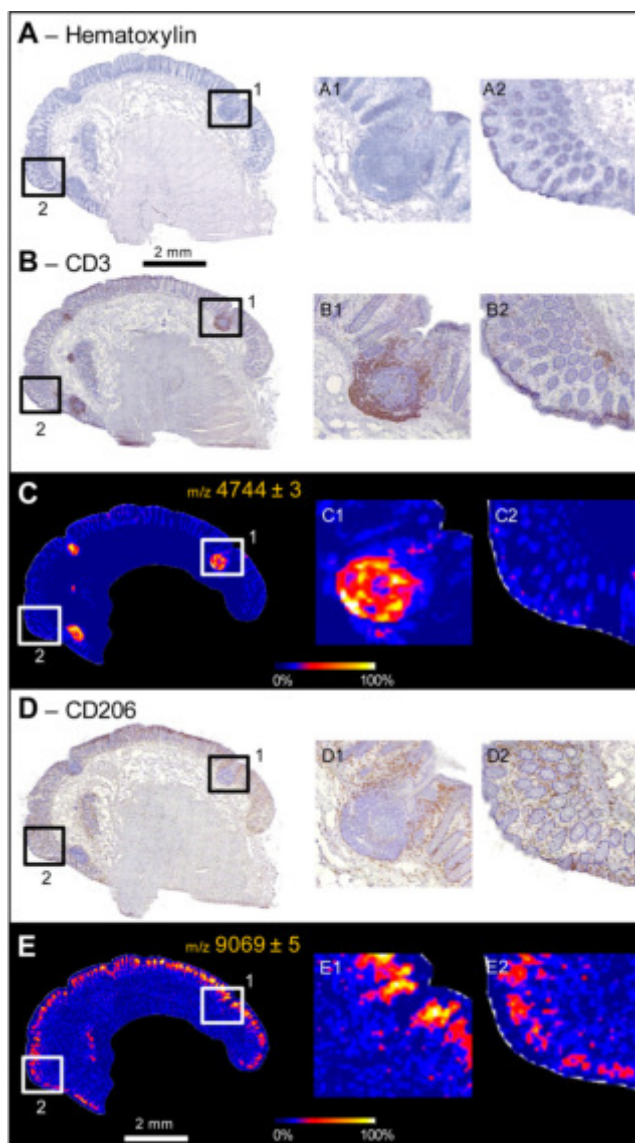


Figure 2. Tissue-resident lymphocytes and macrophages visualized by MALDI MSI. (A) Hematoxylin staining after MALDI MSI, (B) immunohistochemical stainings for lymphocytes (CD3) and (D) macrophages (CD206) of consecutive colon tissue sections (10 μm each). Regions of structural interest are highlighted. (C) *m/z* 4744 ± 3 distributions correlate to nodular lymphoid structures. (E) *m/z* 9069 ± 5 distributions represent macrophage presence underneath the epithelial layer of the mucosa. (Relative intensities are in accordance with the color scale.)

These MALDI MSI measurements of human colon tissue revealed a variety of *m/z* values that allowed specific structures in the tissue to be visualized. Epithelial cells of the crypts, muscle cells of the muscularis mucosae, and follicular immune cell structures were depicted clearly by *m/z* 6572 ± 4, 6754 ± 3, 4962 ± 4, respectively (Figure 1C–E). This might hint at a certain protein or peptide that is highly abundant in these cell types. Several studies confirmed that MALDI MSI is well-suited to visualize the spatial distribution of specific molecules in animal or human tissues (for review, see, ref 21). However, the number of reports on colon tissue is very limited. The group of Fernandez used MSI to investigate lipid distribution in human colon with a resolution of 10 μm.²² They found a similar tissue cell-specific pattern as observed here. The authors identified

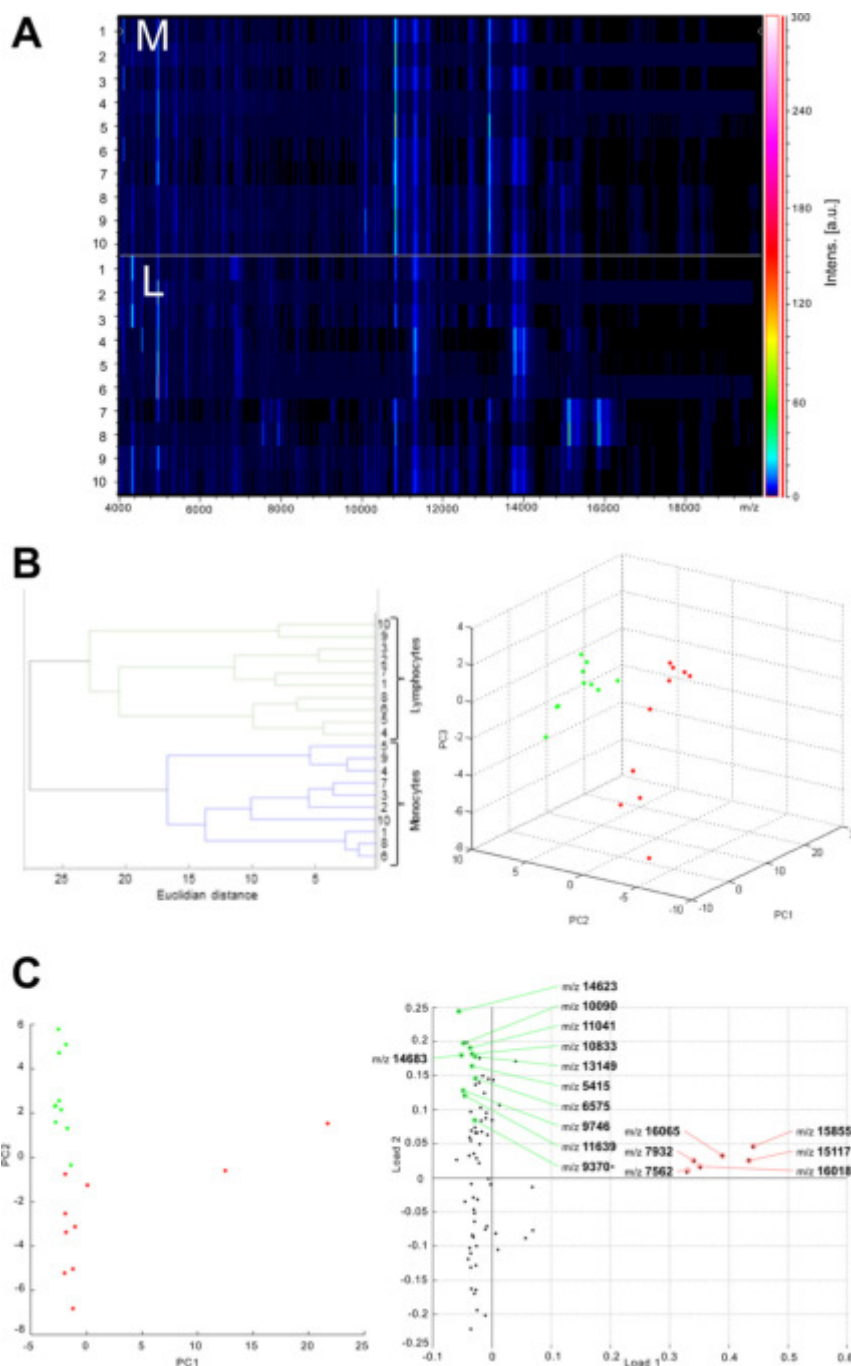


Figure 3. Statistical results for acquired ICMS data from isolated peripheral blood lymphocytes and monocytes. (A) Heatmap visualizing interindividual peak variations for mass spectra obtained from monocytes and lymphocytes isolated from 10 different blood donors. (B) Unsupervised HCA clearly differentiating cell types, and PCA showing a significant variance between the mass spectra of both groups, monocytes (green) and lymphocytes (red). (C) Scores plot showing that PC1 and PC2 successfully separate the different cell clusters, and loadings plot showing m/z values of characteristics for the cell types.

lipid molecules that were present only in the epithelial crypts or specific for the lamina propria. Unfortunately, the authors did not include follicular lymphoid structures in their analysis. The present study is, to our knowledge, the first that investigates the distribution of peptides and proteins in human colon. It provides proof that this experimental setting is able to identify specific cell layers in this tissue. Furthermore, it represents the first MALDI MSI study that focuses on tissue-infiltrating immune cells in situ. There are a few reports on the use of MSI for the analysis of immune cells. The group of Setou used

MALDI MSI for lipid analysis in plasma cells of patients suffering from multiple myeloma.²³ However, they isolated the plasma cells by fluorescence-activated cell sorting before analysis. Similarly, MSI was applied by the group of Schaller to study protein expression profiles of isolated granulocytes of the spider *Cupiennius salei*.²⁴ One study by Mas et al. investigated inflammatory mediators in situ in frozen carotid atheroma plaques using time-of-flight secondary ion mass spectrometry.²⁵ They found that the spatial distribution of nonesterified fatty acids correlates with the distribution of

Table 2. HCA and PCA Analyses of ICMS Spectra Identify Mass Values Characteristic of Lymphocytes and Monocytes Isolated from Blood^a

mass values ($m/z \pm$ peak width)	lymphocytes (mean intensity \pm SD)	monocytes (mean intensity \pm SD)	AUC	Student's <i>t</i> test (<i>p</i> -value)
5415 \pm 7	1.72 \pm 0.79	6.79 \pm 2.64	1	0.00113
6575 \pm 8	1.53 \pm 0.82	4.51 \pm 1.09	1	0.000069
9370 \pm 8	0.61 \pm 0.15	1.28 \pm 0.36	1	0.00113
9746 \pm 11	0.45 \pm 0.19	1.58 \pm 0.7	1	0.00328
10 090 \pm 11	2.54 \pm 1.38	13.62 \pm 5.04	1	0.000702
10 833 \pm 10	14.69 \pm 11.12	100.69 \pm 49.6	1	0.00237
11 041 \pm 11	1.62 \pm 0.99	8.2 \pm 2.23	1	0.0000584
11 639 \pm 13	3.27 \pm 1.47	9.92 \pm 2.15	1	0.0000398
13 149 \pm 15	7.28 \pm 6.19	33.03 \pm 10.41	1	0.00015
14 622 \pm 13	0.29 \pm 0.12	2.31 \pm 1.39	1	0.00719
14 683 \pm 13	0.39 \pm 0.12	2.24 \pm 2.46	1	0.0969
7562 \pm 10	4.4 \pm 6.83	0.64 \pm 0.27	0.93	0.173
15 117 \pm 12	23.76 \pm 44.25	0.82 \pm 1.1	0.9	0.196
7932 \pm 10	3.89 \pm 6.43	0.63 \pm 0.3	0.8	0.205
15 855 \pm 18	19.19 \pm 37.45	1.1 \pm 0.74	0.79	0.213
16 065 \pm 14	2.5 \pm 4.5	0.29 \pm 0.2	0.71	0.212
16 018 \pm 18	1.53 \pm 2.65	0.24 \pm 0.19	0.67	0.212

^aMass values most contributing to the differentiation observed in PCA analysis are listed with their respective intensities in isolated immune cells. HCA reveals that 13 m/z values are excellent predictors for monocytes (AUC 0.9–1). Three m/z values are of less significance (AUC < 0.8), yet they show a significant contribution in forming clusters in PCA (AUC, area under the receiver operating characteristic curve).

monocyte chemotactic protein 1 (MCP-1/CCl2), lipoprotein lipase (LPL), and activated nuclear factor (NF)-kappa B. The localization of these inflammatory mediators was assessed by IHC on consecutive tissue slices. We used a similar approach to address the question of whether immune cells can be detected by MSI. We performed IHC stainings for T lymphocytes (CD3) and macrophages (CD206) and compared them to MSI images, an approach well-accepted for MSI confirmation. Follicular structures revealed intense CD3 staining. These structures also had intense expression of several mass values listed in Table 1. However, interspersed CD3⁺ cells in the mucosa between the crypts were hardly visible in MSI. Although it has been shown that rare cells can be differentiated from large cell populations by MSI,²⁶ it is very unlikely that a single cell can be deciphered from its biological surroundings at a lateral resolution of 30 μ m, which is larger than the cells themselves. Therefore, a measured signal comprises information on a single CD3⁺ cell, but to a greater extent from neighboring cells. Additionally, one has to consider the possibility that sparsely scattered lymphocytes might not be hit by the laser beam. As CD14 was only weakly expressed in scattered cells within the mucosa, no matching MSI pictures were expected (data not shown). In this regard, we choose a macrophage marker, CD206 or MRC1, to stain anti-inflammatory macrophages that are known to be present at a high density within the mucosa close to the epithelial cell layer.^{6,7} Our CD206 IHC staining confirmed the presence of anti-inflammatory macrophages within the mucosa. They are abundantly dispersed throughout the lamina propria. In this case, scattered macrophages within the submucosa were again not detected with MSI, which might be caused by the limitations of lateral resolution mentioned above. IHC was confirmed by MSI, which moreover revealed several more mass values fitting the immunohistochemical staining, showing the benefit of an untargeted imaging approach.

Comparison of MALDI MSI with Intact-Cell MALDI MS of Blood Immune Cells

The comparison of MALDI MSI with IHC alone provided insufficient evidence that the colocalizing spectra are of immune cell origin. As the number of immune cells in the colon tissue was too low to be purified for confirmational experiments, we were restricted to using blood samples as a source of immune cells, which were analyzed by ICMS. Blood was taken from 10 healthy volunteers and subjected to density gradient centrifugation to separate peripheral blood mononuclear cells (PBMCs) from red blood cells, platelets, and granulocytes. PBMCs were further sorted by immunoaffinity chromatography for CD14⁺ cells (monocytes) and CD14⁻ cells (lymphocytes). Monocytes represent a homogeneous cell population, whereas lymphocytes consist of various subgroups such as CD3⁺ T cells (approximately 65%), B cells (approximately 25%), and NK cells (approximately 7%). After pelleting and freezing, cells were further lysed, applied to ITO-covered glass slides, covered with matrix solution, and analyzed by ICMS. This particular approach was chosen to mimic conditions of tissue sections on glass slides in MSI experiments. Cutting a tissue means that some cells are no longer intact, this was simulated by the cell lysis that was performed. Applying lysed cells directly on the slide imitates the situation of placing tissue sections on glass. Covering the cells with the matrix reproduces the situation of tissue covered with matrix (including the recrystallization and hydration step). The m/z values measured in isolated blood lymphocytes and monocytes by ICMS were compared with the m/z values measured in situ by MSI using two different approaches: (i) characterization of cell type-specific ions within the ICMS data set and comparing the results to the MSI data set and (ii) searching the ICMS data set for m/z values found in the MSI experiment to be tissue-specific.

Different statistical analyses were chosen to characterize lymphocyte- and monocyte-specific ICMS m/z values. The heat map in Figure 3A shows ion intensities of all detected m/z values in all measured samples already pointing out character-

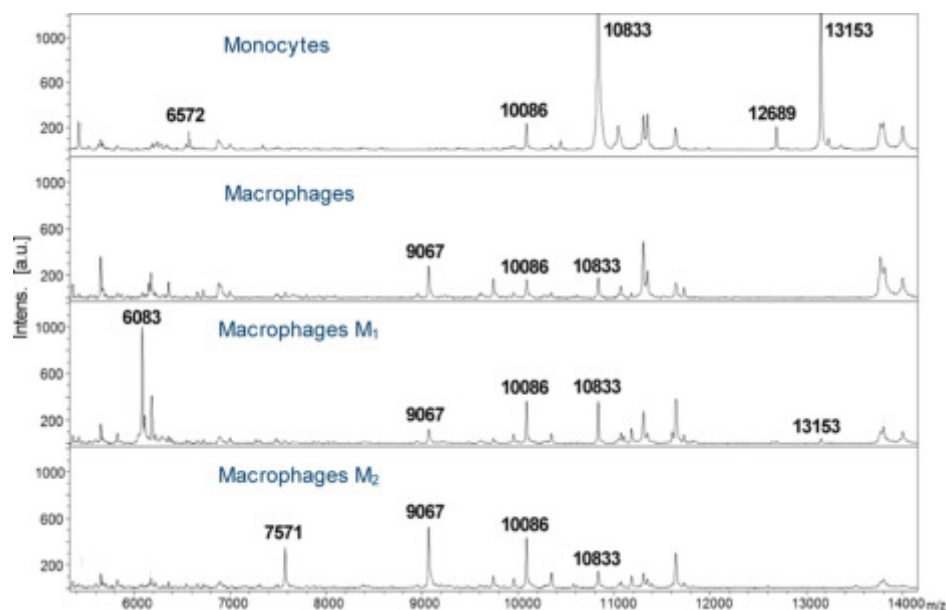


Figure 4. ICMS analysis of monocytes, unpolarized macrophages, and polarized macrophages. The upper panel shows a typical ICMS spectrum of monocytes before differentiation into macrophages. The ICMS spectrum of unpolarized macrophages shows significant differences when compared with spectra derived from IFN γ /LPS (Macrophages M₁) or IL-4 (Macrophages M₂) stimulated macrophages.

istic peaks for both cell types. Also, biological variations observed in the mass spectra of the different blood donors become visible. Despite interindividual variation, an unsupervised HCA with ICMS data of all 10 donor samples revealed that the two immune cell populations, monocytes and lymphocytes, can be perfectly differentiated (Figure 3B). The monocyte cluster exhibits a lower Euclidian distance (approximately 17) than the lymphocytes cluster (approximately 23), indicating a higher degree of similarity among this cell type. This is in agreement with the significantly lower number of monocyte subtypes (classical, intermediate, and nonclassical)¹⁷ compared to the numerous lymphocyte subtypes.²⁷ To classify m/z values responsible for this separation, we calculated the AUC of the ROC and determined the statistical significance of the differential expression. The most important m/z values are reported in Table 2, summarizing cell types, AUCs, and p -values. ROC analysis revealed 11 highly characteristic peaks for monocytes (AUC = 1) and no discriminant signal for lymphocytes. However, visual inspection of the ICMS spectra showed two signals with higher signal intensities in the case of lymphocytes. Their m/z values of 7562 ± 10 and 15117 ± 12 have AUCs of 0.93 and 0.9, respectively. No further peaks for lymphocytes with AUC > 0.9 could be identified. These two ions were therefore regarded as candidate markers for lymphocytes in the MSI experiments. However, neither m/z value could be found in the MSI data set. All other ions shown in Table 2 were more intensive in monocytes. The monocyte-specific m/z values of 5415, 6575, and 10833 were also found by Ouedraogo et al.,¹⁶ corroborating the data in the present study. Figure 3B shows that the clear differentiation of the subgroups is also observed by PCA, an analysis identifying the patterns encoding the highest variance in the data set (Figure 3B). PC1 and PC2 mainly contribute to this successful separation of cell clusters (Figure 3C). Moreover, the loadings plot in Figure 3C shows that 9 out of 11 m/z values responsible for subgroup differentiation in the HCA (AUC = 1) contribute to PC2, whereas two mainly contribute to PC1. The additional ICMS features that give a distinction between monocytes and

lymphocytes are m/z 7932 ± 10 , 15855 ± 18 , 16065 ± 14 , and 16018 ± 18 , showing AUCs of lower significance (≤ 0.8). Here again, none of the monocyte markers listed in Table 2 were found in MSI experiments.

Monocytes differentiate into macrophages when they migrate into a tissue. To take this into account, we simulated this step in vitro and analyzed the differentiated cells by ICMS. Therefore, we cultivated CD14⁺ monocytes in the presence of M-CSF, resulting in monocyte-derived macrophages (MDM), which were then polarized either into proinflammatory M₁ macrophages or into anti-inflammatory M₂ macrophages by adding IFN γ /LPS or IL-4, respectively. Our preliminary results show significant spectral differences for these cell types (Figure 4). Without further statistical analysis, characteristic m/z values for monocytes can be observed (m/z 6572 ± 15 and 12689 ± 21), and one such value was observed only in macrophages (m/z 9067 ± 18). Some m/z values exhibited significant intensity differences, e.g., monocytes show 10-fold higher intensities for m/z 10833 ± 30 and 13153 ± 26 ; both signals correlate to features identified in the previously discussed ICMS experiment as being highly monocyte specific (Table 2, AUC = 1). We found characteristic signals for M_{IFN γ /LPS} (M₁; m/z 6083 ± 14) and M_{IL-4} (M₂; m/z 7571 ± 11) polarized macrophages, which were not found for undifferentiated and unpolarized monocytes. Although we herewith present data lacking a significant number of repeats for reliable statistical analysis, HCA revealed higher similarity for all macrophage subtypes compared to monocytes (data not shown). Work published by Ouedraogo et al.¹⁶ confirms our first findings for M₁ and M₂ polarized macrophages, yet varying experimental conditions make a direct comparison of m/z values difficult because the authors showed that the polarization of macrophages with different stimuli does not necessarily result in the same peak pattern.

A reverse comparison of the MSI data with the ICMS data set also identified overlapping results. Three m/z values (m/z 4744 ± 3 , 4962 ± 4 , and 5169 ± 4) showed a clear differentiation of nodular lymphoid structures in colon tissue (Figure 5). m/z 4744 ± 3 was detected solely by MALDI MSI

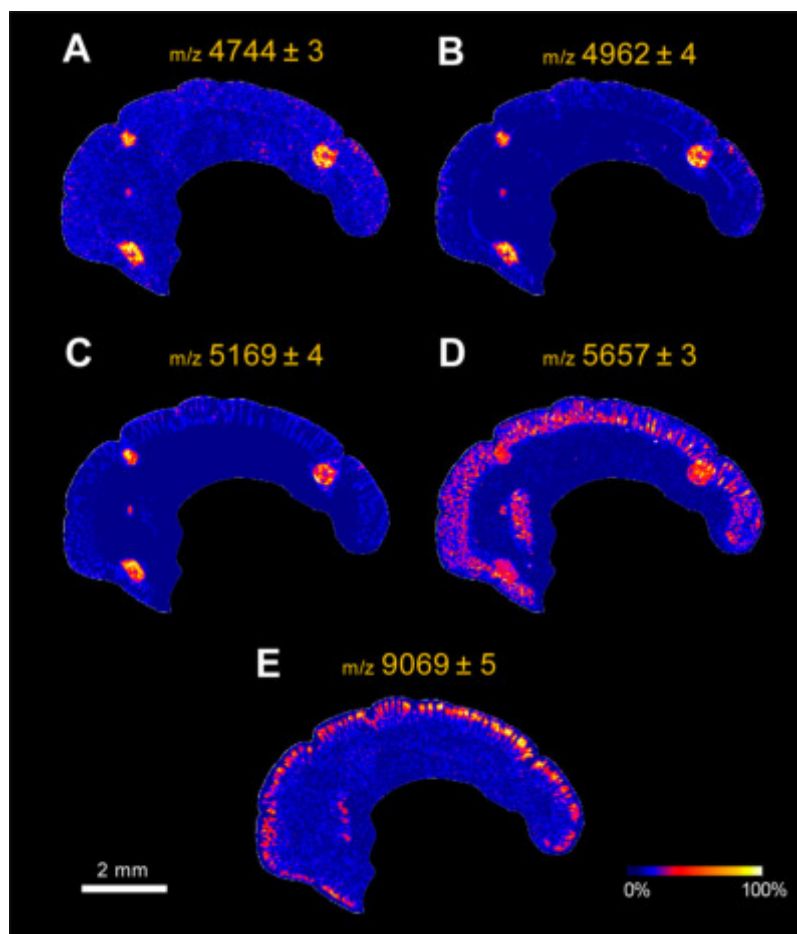


Figure 5. MALDI MSI images of m/z values also detected by ICMS of isolated immune cells. (A–C) m/z 4744 \pm 3, 4962 \pm 4, and 5169 \pm 4 are expressed in the lymphoid structures of the colon tissue, but they are also detected in lymphocytes and monocytes by ICMS. (D) m/z 5657 \pm 3 was found to be distributed in the nodular lymphoid structures and in the epithelial cells of the crypts, but it was also detected in blood-isolated lymphocytes and monocytes. (E) m/z 9069 \pm 5 is located underneath the epithelial cells of the crypts and is not detected in isolated monocytes and lymphocytes, whereas ICMS analysis of macrophages polarized with IL-4 showed the expression of this marker. (Relative intensities are in accordance with the color scale.)

(Figure 5A), but m/z 4962 \pm 4 and 5169 \pm 4 (Figure 5B,C) were found not only by MSI but also in the majority of ICMS spectra of isolated lymphocytes (in 10 of 10 and 7 of 10, respectively) and monocytes (in 10 of 10 and 5 of 10, respectively). This confirms our findings from the experiments described above; these m/z values are specific for immune cells. However, they are not specific for one of the two immune cell populations. From our findings, we conclude that the presence of these molecular markers is limited to nodular lymphoid structures where no monocytic immunohistochemical staining was detectable. Therefore, we can assume that the detected mass values are of lymphocytic origin.

Additionally, MALDI MSI revealed seven m/z values (4609 \pm 5, 4729 \pm 3, 5657 \pm 3, 5737 \pm 3, 6774 \pm 5, 6970 \pm 5, and 8560 \pm 5; Table 1) that are simultaneously distributed in nodular lymphoid structures and the mucosa of the colon tissue (Supporting Information Figure S1B). Of these, only m/z 5657 \pm 3 (Figure 5D) was also present in isolated lymphocytes (in 10 of 10) and monocytes (in 9 of 10), thus not allowing them to be differentiated. These discrepancies between the ICMS and MSI results may be explained by ion suppression effects, a method-inherent problem in untargeted MALDI approaches. In the early days of MALDI, it was already recognized that molecular ions have different detection responses under certain

conditions (presence or absence of coanalytes).^{28–31} Yet, by taking a closer look at the ion image of m/z 9069 \pm 5 (Figure 5E), we observed that the distribution correlates nicely with CD206⁺ cells in the tissue (Figure 2D,E). A corresponding m/z value was found in macrophages, irrespective of their polarization status (see Figure 4), suggesting that the MSI image is related to tissue-resident macrophages. By this, the first link between ICMS analysis and MSI is given, indicating that MSI is able to detect proteome rearrangements of blood monocytes that migrate into a tissue and thereby differentiate into macrophages. Interestingly, only a limited number of mass values were identical when comparing isolated peripheral lymphocytes and tissue-resident lymphocytes (4 m/z values) or in vitro polarized macrophages and tissue macrophages (M_1 : 15 m/z values, M_2 : 12 m/z values). This divergence might be due to the microenvironment of tissue immune cells. The microenvironment offers cell–cell contact and various soluble factors that can influence protein expression in the cells. The impact of the microenvironment on immune cells in diseases is getting more and more attention in research. Many reviews have been published about the tumor microenvironment and the influence on or of immune cells.^{32–34}

Although our scope was not the identification of certain mass values, we found that m/z 4962 \pm 4, highly expressed in

lymphoid aggregates (Supporting Information Figure S2A) and present in all ICMS spectra of isolated cells, matched perfectly with thymosin beta 4,^{14,35} a protein broadly expressed in lymphoid cells.³⁶ Moreover, the thymosin beta 4 gene is highly conserved in mammals and widely expressed in various tissues. Although there is no link between the expression of this gene and the differentiation of T cells, the protein is involved in various biological processes and was even described as playing a role in colon carcinogenesis³⁷ and breast cancer.³⁸ Today, the identification of peptides and proteins directly from a tissue is challenging. First, unambiguous sequencing of molecular structures by MALDI-TOF/TOF instrumentation is possible only for isolated substances, which allows for good detection of fragment ions in the MS/MS experiment. In any other case, background ions with similar m/z are fragmented together with the ion of interest, and MS/MS spectra with mixed sequence information are generated. Thus, sequence identification is extremely difficult. Additionally, top-down sequencing of molecules beyond 3 kDa in a MALDI-TOF/TOF approach is successful only for reasonable analyte concentrations (pmol) because only then are the intensities and accuracies of the generated fragment ions good enough for sequence tag annotations. In the case of MALDI MSI experiments, both challenges are met. The most critical issue is the fact that analyte concentrations per MALDI MSI pixel are extremely low. The analyzed tissue volume is only $\sim 4 \text{ mm}^3$ (laser diameter: $25 \mu\text{m}$; tissue: $10 \mu\text{m}$), giving fragment ion spectra of low quality (S/N, mass accuracy). In addition, from each measured spot, not only is the most abundant signal desorbed and ionized but also a number of isobaric components of low abundance increase the number of background signals, which ultimately results in MS/MS spectra with mixed information. Although we have strong indications that m/z 4962 is thymosin beta 4, future work will focus on efforts to unequivocally identify thymosin in follicular lymphoid structures, e.g., by a peptidomics approach after laser microdissection, and to verify its presence and distribution in cancerous colon tissue.

CONCLUSIONS

Immune cells maintain the homeostasis of the intestinal tract, and lymphocytes and macrophages are of special interest as they have been shown to be involved in various diseases of the colon such as cancer. Since these cells are still insufficiently described in this tissue, we evaluated the potential of MS to address this challenge. Our data demonstrate that MSI is a suitable tool for the characterization and in situ localization of immune cell accumulations without using antibodies, which is based on protein expression in these cells. MSI also offers a method to detect m/z values specific for tissue structures. Furthermore, we provide mass values allowing for identification and discrimination of lymphocytes, monocytes, and polarized macrophages by ICMS. Finally, we showed that a combination of both MS approaches reveals mass values that are conserved between peripheral and tissue-resident immune cells, whereas others are found only within the tissue. We assume the latter to be derived from the adaption of these cells to their microenvironment.

ASSOCIATED CONTENT

Supporting Information

The Supporting Information is available free of charge on the ACS Publications website at DOI: 10.1021/acs.jproteome.6b00610.

MALDI MS images of m/z values characteristic of specific regions in colon tissue (Figure S1); MALDI MS images of m/z 4962 \pm 4 and 5169 \pm 4 revealing high signal intensities in nodular lymphoid aggregates (Figure S2); light microscopy images and CD3 IHC staining of consecutive colon tissue sections of seven patients (Figure S3); MALDI MS images of m/z values characteristic of follicular lymphoid structures in colon tissue of seven patients (Figure S4); MALDI MS images of m/z values characteristic of muscularis mucosae in colon tissue of seven patients (Figure S5); MALDI MS images of m/z values characteristic of mucosa in colon tissue of seven patients (Figure S6); and MALDI MS images of m/z values commonly expressed in colon tissue of seven patients (Figure S7) (PDF)

AUTHOR INFORMATION

Corresponding Author

*E-mail: martina.marchetti-deschmann@tuwien.ac.at. Phone: +43-1-58801-15162. Fax: +43-1-58801-15199.

Author Contributions

¹M.H. and K.S. contributed equally to this work.

Notes

The authors declare no competing financial interest.

ACKNOWLEDGMENTS

This study was funded by the Austrian Federal Government within the COMET K1 Centre Program of the Österreichische Forschungsförderungsgesellschaft (FFG), Land Steiermark, and Land Wien. Parts of this project were supported by TU Wien (Innovative Projects 2011). The authors further acknowledge COST Action BM1104 (Mass Spectrometry Imaging: New Tools for Healthcare Research) for valuable discussions, and the authors highly appreciate the support of Prof. Günter Allmaier (TU Wien) for sharing his expertise and granting access to instrumentation.

ABBREVIATIONS

AUC, area under the curve; CD, cluster of differentiation; DAB, 3,3-diaminobenzidine; DPBS, Dubecco's phosphate-buffered saline; FCS, fetal calf serum; GI, gastrointestinal tract; HCA, hierarchical cluster analysis; ICMS, intact cell mass spectrometry; IELs, intraepithelial lymphocytes; IFN γ , interferon gamma; IHC, immunohistochemistry; IL4, interleukin 4; ITO, indium tin oxide; LPS, lipopolysaccharide; MACS, magnetic cell sorting; MALDI, matrix-assisted laser desorption/ionization; MALT, mucosa-associated lymphoid tissue; M-CSF, macrophage colony-stimulating factor; MDM, monocyte-derived macrophages; MRC1, mannose receptor C type 1, CD206; MS, mass spectrometry; MSI, mass spectrometry imaging; NK cells, natural killer cells; PBMCs, peripheral blood mononuclear cells; PCA, principal component analysis; ROC, receiver operation characteristic; ROI, region of interest; RTOF, reflector time-of-flight; SA, sinapic acid; SIMS,

secondary ion mass spectrometer; TIC, total ion current; TFA, trifluoroacetic acid; TOF, time-of-flight

REFERENCES

- (1) Bain, C. C.; Mowat, A. M. Macrophages in intestinal homeostasis and inflammation. *Immunol. Rev.* **2014**, *260* (1), 102–117.
- (2) Chang, F.; Mahadeva, U.; Deere, H. Pathological and clinical significance of increased intraepithelial lymphocytes (IELs) in small bowel mucosa. *APMIS* **2005**, *113* (6), 385–99.
- (3) MacKay, L. K.; Rahimpour, A.; Ma, J. Z.; Collins, N.; Stock, A. T.; Hafon, M.-L.; Vega-Ramos, J.; Lauzurica, P.; Mueller, S. N.; Stefanovic, T.; Tschärke, D. C.; Heath, W. R.; Inouye, M.; Carbone, F. R.; Gebhardt, T. The developmental pathway for CD103+CD8+ tissue-resident memory T cells of skin. *Nat. Immunol.* **2013**, *14* (12), 1294–1301.
- (4) van Wijk, F.; Cheroutre, H. Mucosal T cells in gut homeostasis and inflammation. *Expert Rev. Clin. Immunol.* **2010**, *6* (4), 559–566.
- (5) Mantis, N. J.; Rol, N.; Corthesy, B. Secretory IgA's complex roles in immunity and mucosal homeostasis in the gut. *Mucosal Immunol.* **2011**, *4* (6), 603–611.
- (6) Bain, C. C.; Scott, C. L.; Uronen-Hansson, H.; Gudjonsson, S.; Jansson, O.; Grip, O.; Williams, M.; Malissen, B.; Agace, W. W.; Mowat, A. M. Resident and pro-inflammatory macrophages in the colon represent alternative context-dependent fates of the same Ly6Chi monocyte precursors. *Mucosal Immunol.* **2013**, *6* (3), 498–510.
- (7) Smith, P. D.; Smythies, L. E.; Shen, R.; Greenwell-Wild, T.; Gliozzi, M.; Wahl, S. M. Intestinal macrophages and response to microbial encroachment. *Mucosal Immunol.* **2011**, *4* (1), 31–42.
- (8) Hume, D. A.; Robinson, A. P.; MacPherson, G. G.; Gordon, S. The mononuclear phagocyte system of the mouse defined by immunohistochemical localization of antigen F4/80. Relationship between macrophages, Langerhans cells, reticular cells, and dendritic cells in lymphoid and hematopoietic organs. *J. Exp. Med.* **1983**, *158* (5), 1522–1536.
- (9) Mikkelsen, H. B.; Rumessen, J. J. Characterization of macrophage-like cells in the external layers of human small and large intestine. *Cell Tissue Res.* **1992**, *270* (2), 273–9.
- (10) Muller, P. A.; Kosco, B.; Rajani, G. M.; Stevanovic, K.; Berres, M.-L.; Hashimoto, D.; Mortha, A.; Leboeuf, M.; Li, X.-M.; Mucida, D.; Stanley, E. R.; Dahan, S.; Margolis, K. G.; Gershon, M. D.; Merad, M.; Bogunovic, M. Crosstalk between Muscularis Macrophages and Enteric Neurons Regulates Gastrointestinal Motility. *Cell (Cambridge, MA, U. S.)* **2014**, *158* (2), 300–313.
- (11) Huang, E.; Wells, C. A. The Ground State of Innate Immune Responsiveness Is Determined at the Interface of Genetic, Epigenetic, and Environmental Influences. *J. Immunol.* **2014**, *193* (1), 13–19.
- (12) Fenselau, C.; Demirev, P. A. Characterization of intact microorganisms by MALDI mass spectrometry. *Mass Spectrom. Rev.* **2001**, *20* (4), 157–171.
- (13) Munteanu, B.; Hopf, C. Emergence of whole-cell MALDI-MS biotyping for high-throughput bioanalysis of mammalian cells? *Bioanalysis* **2013**, *5* (8), 885–893.
- (14) Munteanu, B.; von Reitzenstein, C.; Haensch, G. M.; Meyer, B.; Hopf, C. Sensitive, robust and automated protein analysis of cell differentiation and of primary human blood cells by intact cell MALDI mass spectrometry biotyping. *Anal. Bioanal. Chem.* **2012**, *404* (8), 2277–2286.
- (15) Ouedraogo, R.; Flaudrops, C.; Ben Amara, A.; Capo, C.; Raoult, D.; Mege, J.-L. Global analysis of circulating immune cells by matrix-assisted laser desorption ionization time-of-flight mass spectrometry. *PLoS One* **2010**, *5* (10), e13691.
- (16) Ouedraogo, R.; Daumas, A.; Ghigo, E.; Capo, C.; Mege, J.-L.; Textoris, J. Whole-cell MALDI-TOF MS: A new tool to assess the multifaceted activation of macrophages. *J. Proteomics* **2012**, *75* (18), 5523–5532.
- (17) Portevin, D.; Pflüger, V.; Otieno, P.; Brunisholz, R.; Vogel, G.; Daubenberger, C. Quantitative whole-cell MALDI-TOF MS fingerprints distinguishes human monocyte sub-populations activated by distinct microbial ligands. *BMC Biotechnol.* **2015**, *15*, 24.
- (18) Bodenmiller, B.; Zunder, E. R.; Finck, R.; Chen, T. J.; Savig, E. S.; Bruggner, R. V.; Simonds, E. F.; Bendall, S. C.; Sachs, K.; Krutzik, P. O.; Nolan, G. P. Multiplexed mass cytometry profiling of cellular states perturbed by small-molecule regulators. *Nat. Biotechnol.* **2012**, *30* (9), 858–867.
- (19) Bendall, S. C.; Nolan, G. P.; Roederer, M.; Chattopadhyay, P. K. A deep profiler's guide to cytometry. *Trends Immunol.* **2012**, *33* (7), 323–332.
- (20) Yang, J.; Caprioli, R. M. Matrix Sublimation/Recrystallization for Imaging Proteins by Mass Spectrometry at High Spatial Resolution. *Anal. Chem. (Washington, DC, U. S.)* **2011**, *83* (14), 5728–5734.
- (21) Schwamborn, K.; Caprioli, R. M. Molecular imaging by mass spectrometry - looking beyond classical histology. *Nat. Rev. Cancer* **2010**, *10* (9), 639–646.
- (22) Garate, J.; Fernandez, R.; Lage, S.; Bestard-Escalas, J.; Lopez, D. H.; Reigada, R.; Khorrami, S.; Ginard, D.; Reyes, J.; Amengual, I.; Barcelo-Coblijn, G.; Fernandez, J. A. Imaging mass spectrometry increased resolution using 2-mercaptobenzothiazole and 2,5-diaminonaphthalene matrices: application to lipid distribution in human colon. *Anal. Bioanal. Chem.* **2015**, *407* (16), 4697–4708.
- (23) Hossen, M. A.; Nagata, Y.; Waki, M.; Ide, Y.; Takei, S.; Fukano, H.; Romero-Perez, G. A.; Tajima, S.; Yao, I.; Ohnishi, K.; Setou, M. Decreased level of phosphatidylcholine (16:0/20:4) in multiple myeloma cells compared to plasma cells: a single-cell MALDI-IMS approach. *Anal. Bioanal. Chem.* **2015**, *407* (18), 5273–5280.
- (24) Kuhn-Nentwig, L.; Kopp, L. S.; Nentwig, W.; Haenni, B.; Streitberger, K.; Schurch, S.; Schaller, J. Functional differentiation of spider hemocytes by light and transmission electron microscopy, and MALDI-MS-imaging. *Dev. Comp. Immunol.* **2014**, *43* (1), 59–67.
- (25) Mas, S.; Martinez-Pinna, R.; Martin-Ventura, J. L.; Perez, R.; Gomez-Garre, D.; Ortiz, A.; Fernandez-Cruz, A.; Vivanco, F.; Egido, J. Local non-esterified fatty acids correlate with inflammation in atheroma plaques of patients with type 2 diabetes. *Diabetes* **2010**, *59* (6), 1292–1301.
- (26) Ong, T.-H.; Kissick, D. J.; Jansson, E. T.; Comi, T. J.; Romanova, E. V.; Rubakhin, S. S.; Sweedler, J. V. Classification of Large Cellular Populations and Discovery of Rare Cells Using Single Cell Matrix-Assisted Laser Desorption/Ionization Time-of-Flight Mass Spectrometry. *Anal. Chem. (Washington, DC, U. S.)* **2015**, *87* (14), 7036–7042.
- (27) MacIver, N. J.; Michalek, R. D.; Rathmell, J. C. Metabolic Regulation of T Lymphocytes. *Annu. Rev. Immunol.* **2013**, *31* (1), 259–283.
- (28) Knochenmuss, R. A Quantitative Model of Ultraviolet Matrix-Assisted Laser Desorption/Ionization Including Analyte Ion Generation. *Anal. Chem.* **2003**, *75* (10), 2199–2207.
- (29) Karas, M.; Krueger, R. Ion formation in MALDI: The cluster ionization mechanism. *Chem. Rev. (Washington, DC, U. S.)* **2003**, *103* (2), 427–439.
- (30) Dreisewerd, K. The desorption process in MALDI. *Chem. Rev. (Washington, DC, U. S.)* **2003**, *103* (2), 395–425.
- (31) Zenobi, R.; Knochenmuss, R. Ion formation in MALDI mass spectrometry. *Mass Spectrom. Rev.* **1998**, *17* (5), 337–366.
- (32) Gajewski, T. F.; Schreiber, H.; Fu, Y.-X. Innate and adaptive immune cells in the tumor microenvironment. *Nat. Immunol.* **2013**, *14* (10), 1014–1022.
- (33) Whiteside, T. L. The tumor microenvironment and its role in promoting tumor growth. *Oncogene* **2008**, *27* (45), 5904–5912.
- (34) Galon, J.; Fridman, W.-H.; Pages, F. The Adaptive Immunologic Microenvironment in Colorectal Cancer: A Novel Perspective. *Cancer Res.* **2007**, *67* (5), 1883–1886.
- (35) Hanrieder, J.; Wicher, G.; Bergquist, J.; Andersson, M.; Fex-Svenningsen, A. MALDI mass spectrometry based molecular phenotyping of CNS glial cells for prediction in mammalian brain tissue. *Anal. Bioanal. Chem.* **2011**, *401* (1), 135–147.
- (36) Gomez-Marquez, J.; Dosal, M.; Segade, F.; Bustelo, X. R.; Pichel, J. G.; Dominguez, F.; Freire, M. Thymosin-β4 gene. Preliminary

characterization and expression in tissues, thymic cells, and lymphocytes. *J. Immunol.* **1989**, *143* (8), 2740–2744.

(37) Nemolato, S.; Cabras, T.; Restivo, A.; Zorcolo, L.; Felice, E. D.; Fanni, D.; Gerosa, C.; Messina, I.; Castagnola, M.; Faa, G.; Casula, G. Thymosin $\alpha 4$ expression in colorectal polyps and adenomas. *Clinics (Sao Paulo)* **2013**, *68* (9), 1220–1224.

(38) Yoon, S. Y.; Lee, H. R.; Park, Y.; Kim, J. H.; Kim, S. Y.; Yoon, S. R.; Lee, W. J.; Cho, B. J.; Min, H.; Bang, J.-W.; Park, H.; Bang, S. L.; Cho, D. Thymosin $\beta 4$ expression correlates with lymph node metastasis through hypoxia inducible factor- α induction in breast cancer. *Oncol. Rep.* **2011**, *25* (1), 23–31.

IN SITU CHARACTERIZATION OF TISSUE-RESIDENT IMMUNE CELLS BY MALDI MASS SPECTROMETRY IMAGING

Matthias Holzlechner^{1}, Katharina Strasser^{2,3*}, Elitsa Zareva¹, Luise Steinhäuser²,
Hanna Birnleitner², Andrea Beer⁴, Michael Bergmann², Rudolf Oehler², Martina
Marchetti-Deschmann^{1#}*

*equal contributions

¹Institute of Chemical Technologies and Analytics (CTA), TU Wien, Vienna, Austria

²Department of Surgery and Comprehensive Cancer Center, Medical University of Vienna, Vienna, Austria

³CBmed GmbH – Center for biomarker Research in Medicine, Graz, Austria

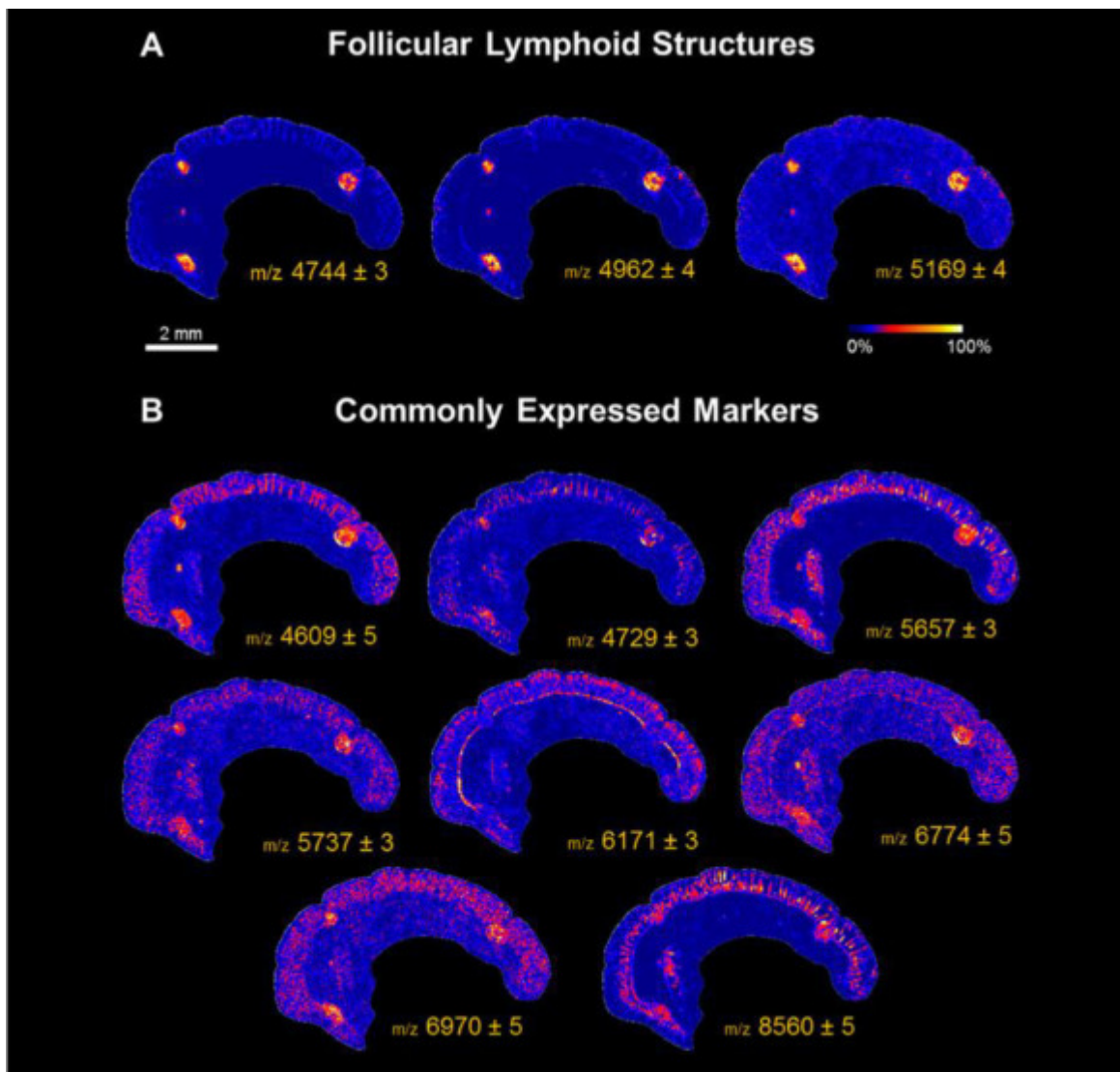
⁴Clinical Institute for Pathology, Medical University of Vienna, Vienna, Austria

Corresponding Author

Assoc.-Prof. Dr. Martina Marchetti-Deschmann; TU Wien, Institute of Chemical Technologies and Analytics, Getreidemarkt 9/164-IAC, 1060 Vienna, E: martina.marchetti-deschmann@tuwien.ac.at, T: +43-1-58801-15162, F: +43-1-58801-15199

KEYWORDS: *MALDI mass spectrometry imaging, immunohistochemistry, immune cells, monocytes, lymphocytes, macrophages, colon tissue*

Figure S-1 MALDI MS images of m/z values characteristic for specific regions in colon tissue. (A) m/z values specific for follicular lymphoid structures and (B) m/z values that occur in more than one region. (C) Mucosa, (D) muscularis mucosae specific mass values. (Relative intensities according to color scale).



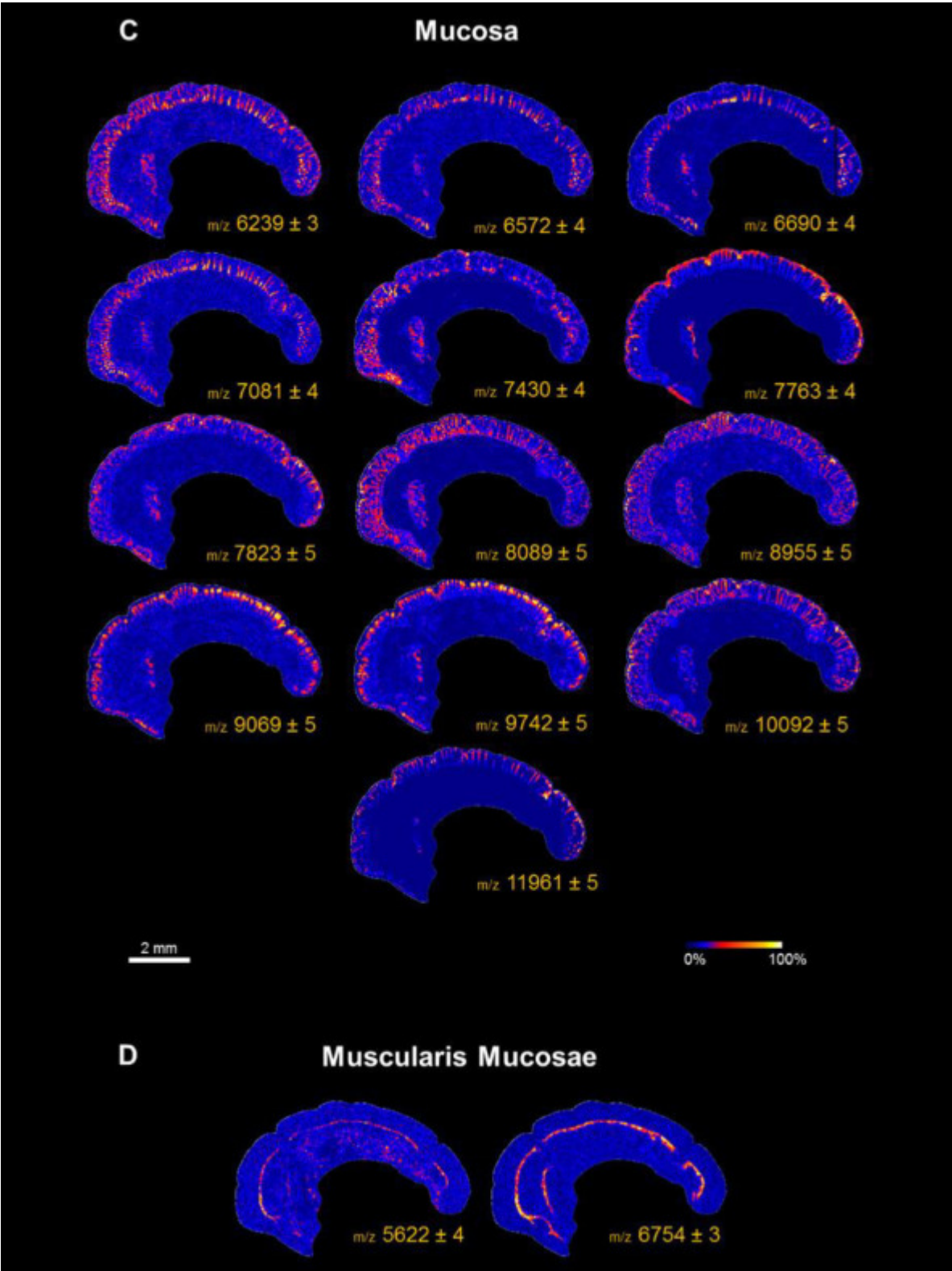


Figure S-2 MALDI MS images of m/z 4962 \pm 4 and 5169 \pm 4 revealing high signal intensities in nodular lymphoid aggregates.

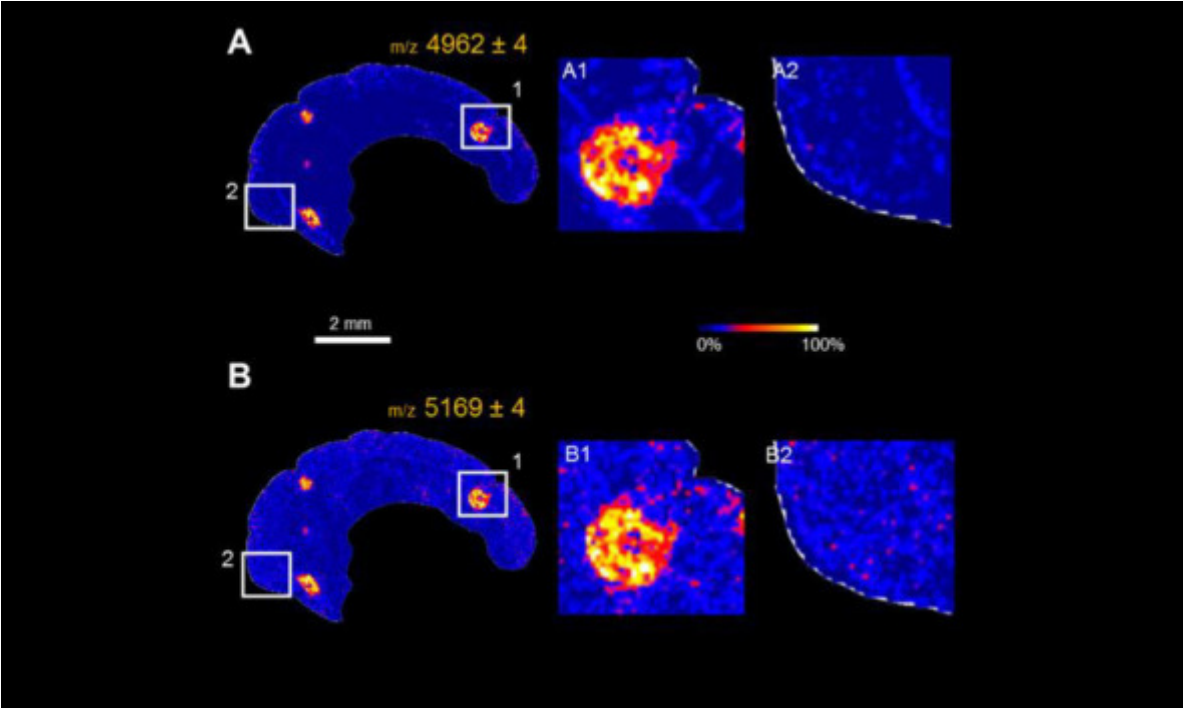


Figure S-3 Light microscopy images and CD3 IHC staining of consecutive colon tissue sections of seven patients. Patient sample 1 is discussed in detail in the main manuscript. Patient sample 2-6 were measured at least in duplicates to confirm all findings discussed for sample 1. One sample did not show follicular structures and was used as negative control.

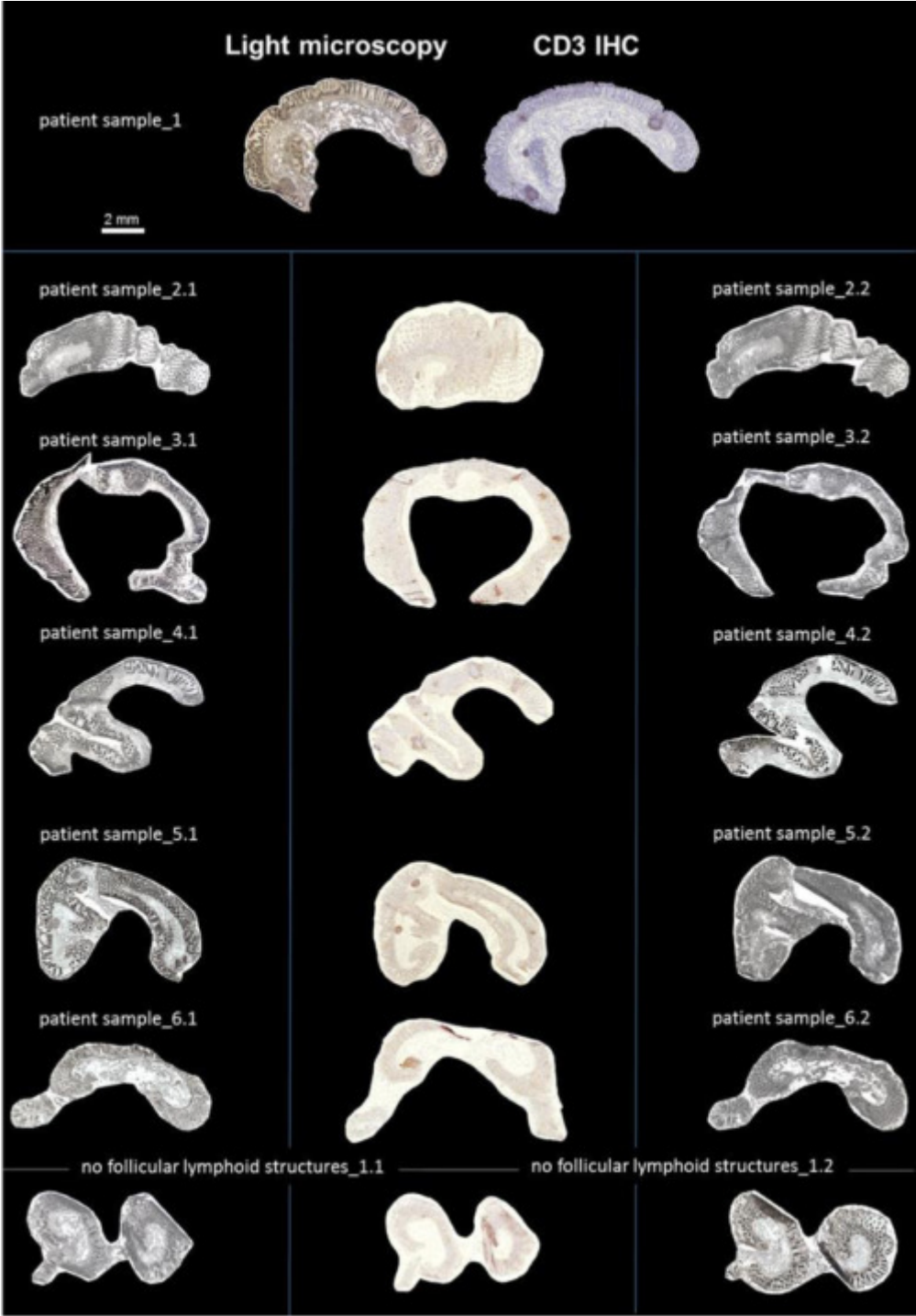
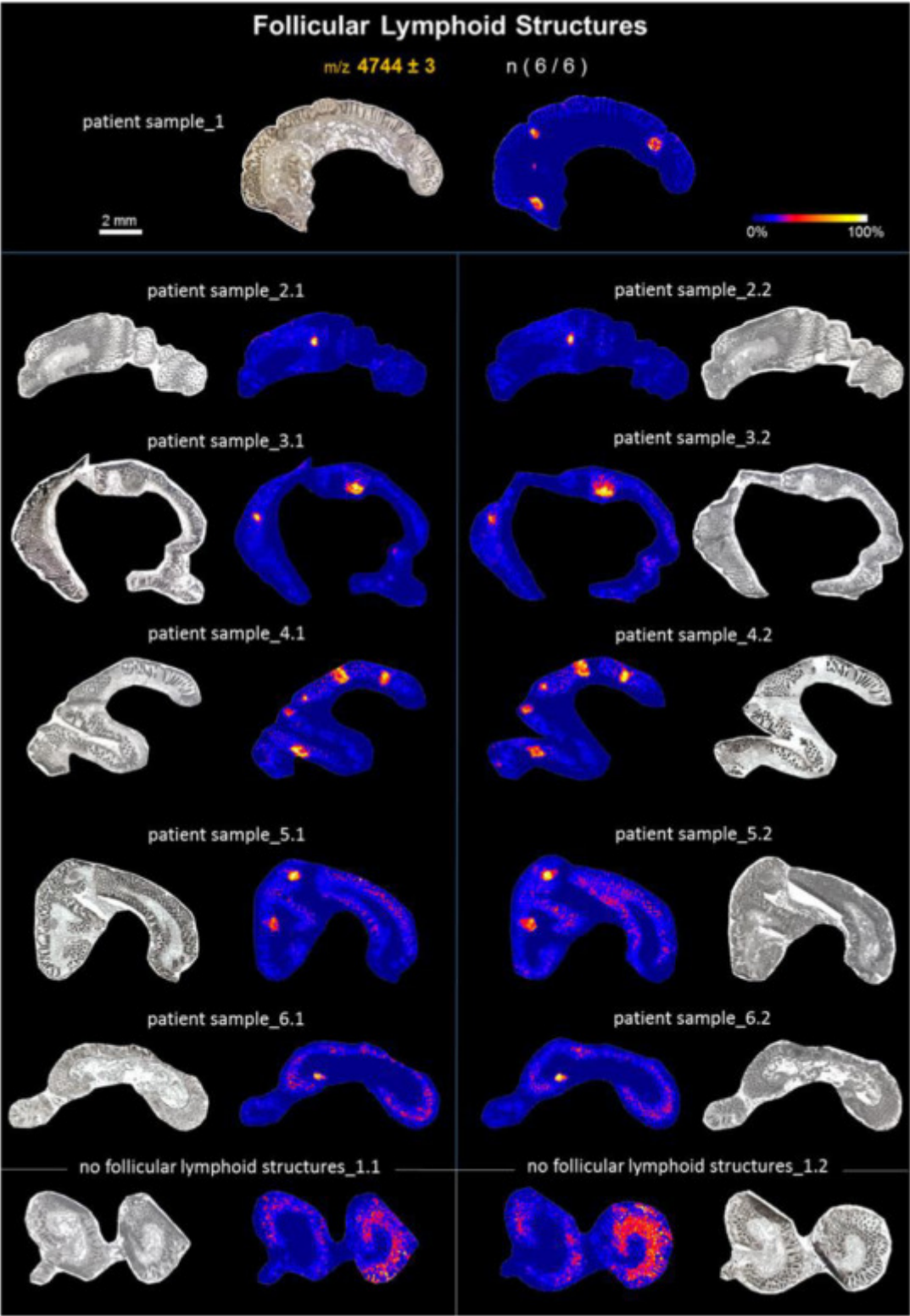


Figure S-4 MALDI MS images of m/z values characteristic for follicular lymphoid structures in colon tissue of seven patients.

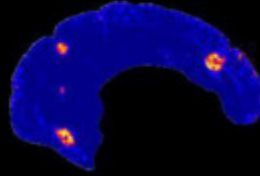


Follicular Lymphoid Structures

m/z 4962 ± 4

n (6 / 6)

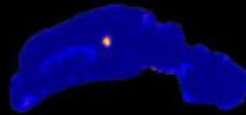
patient sample_1



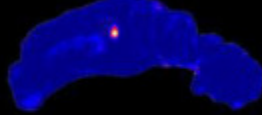
2 mm



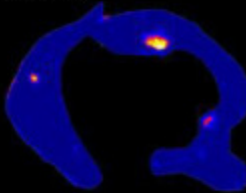
patient sample_2.1



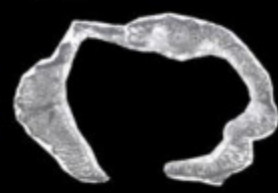
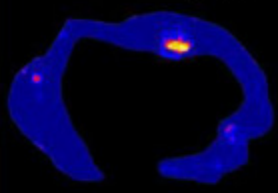
patient sample_2.2



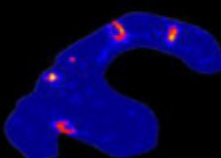
patient sample_3.1



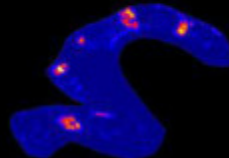
patient sample_3.2



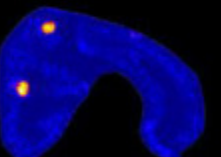
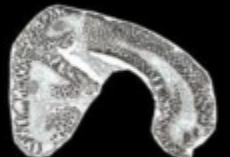
patient sample_4.1



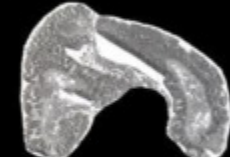
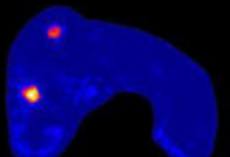
patient sample_4.2



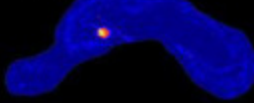
patient sample_5.1



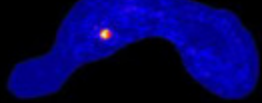
patient sample_5.2



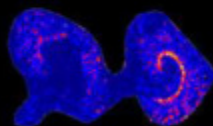
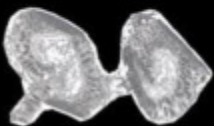
patient sample_6.1



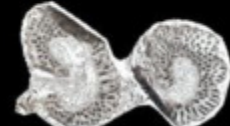
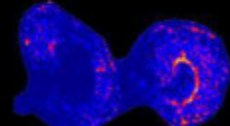
patient sample_6.2



no follicular lymphoid structures_1.1



no follicular lymphoid structures_1.2



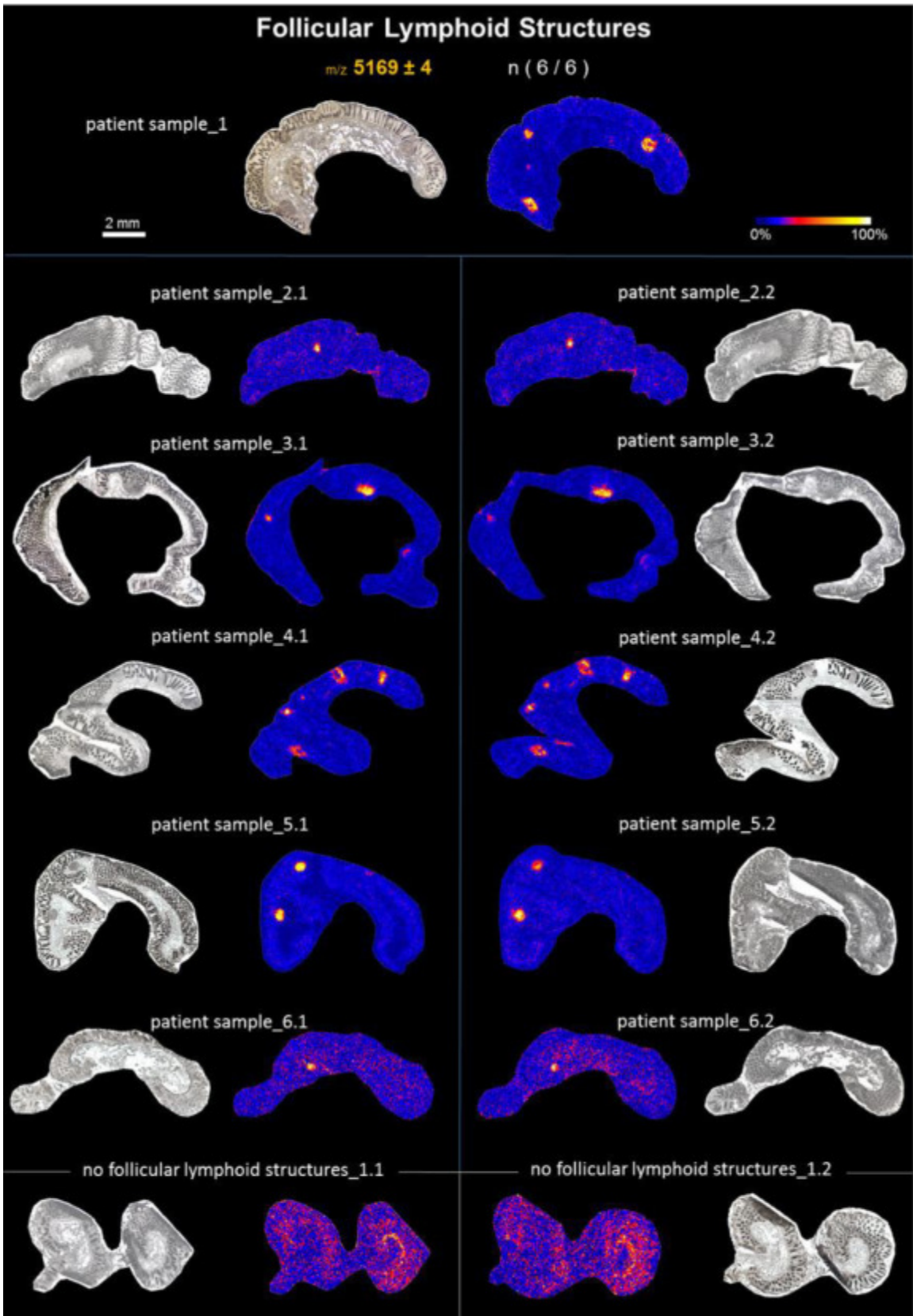
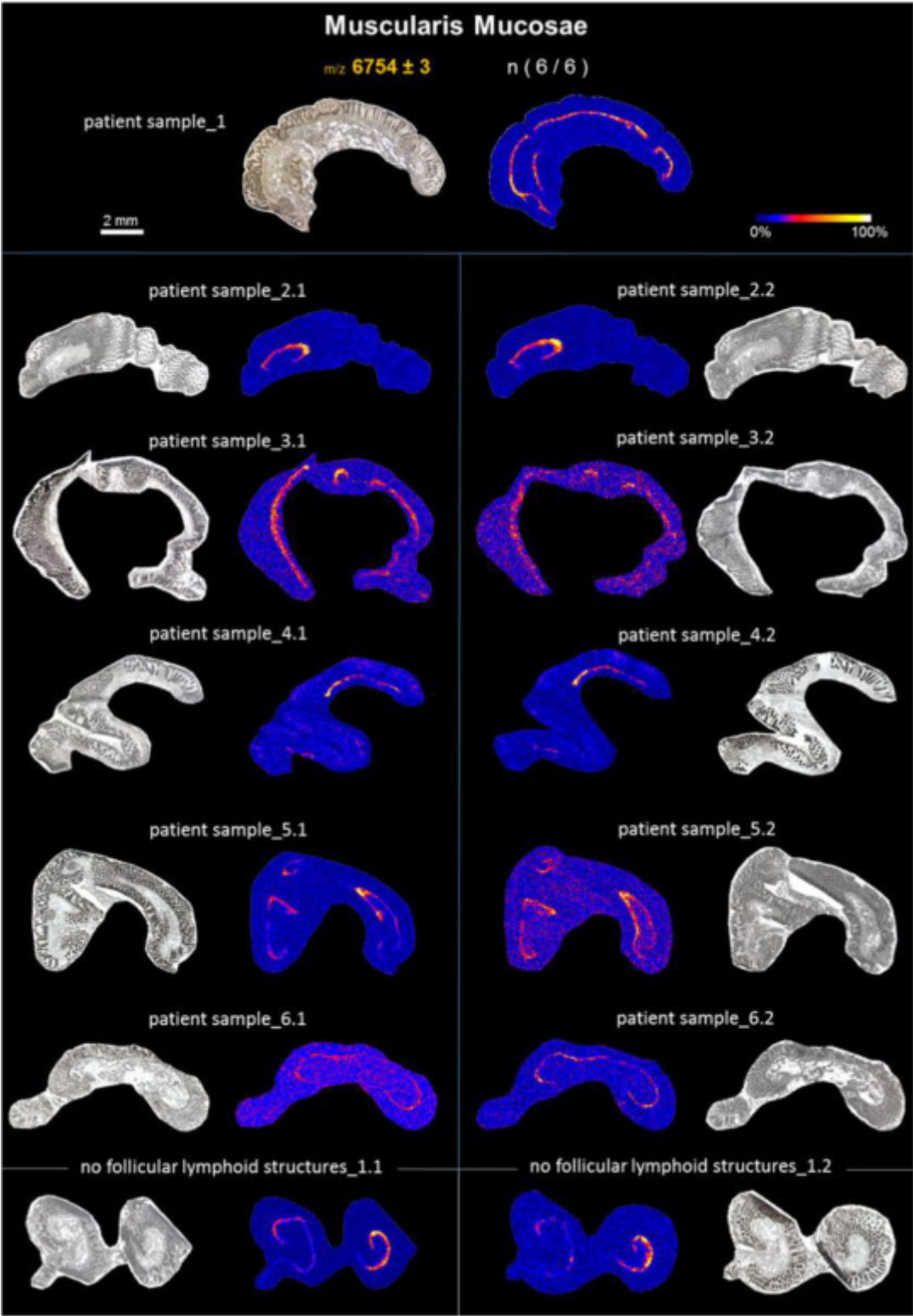


Figure S-5 MALDI MS images of m/z values characteristic for muscularis mucosae in colon tissue of seven patients (sample outliers are indicated in red).



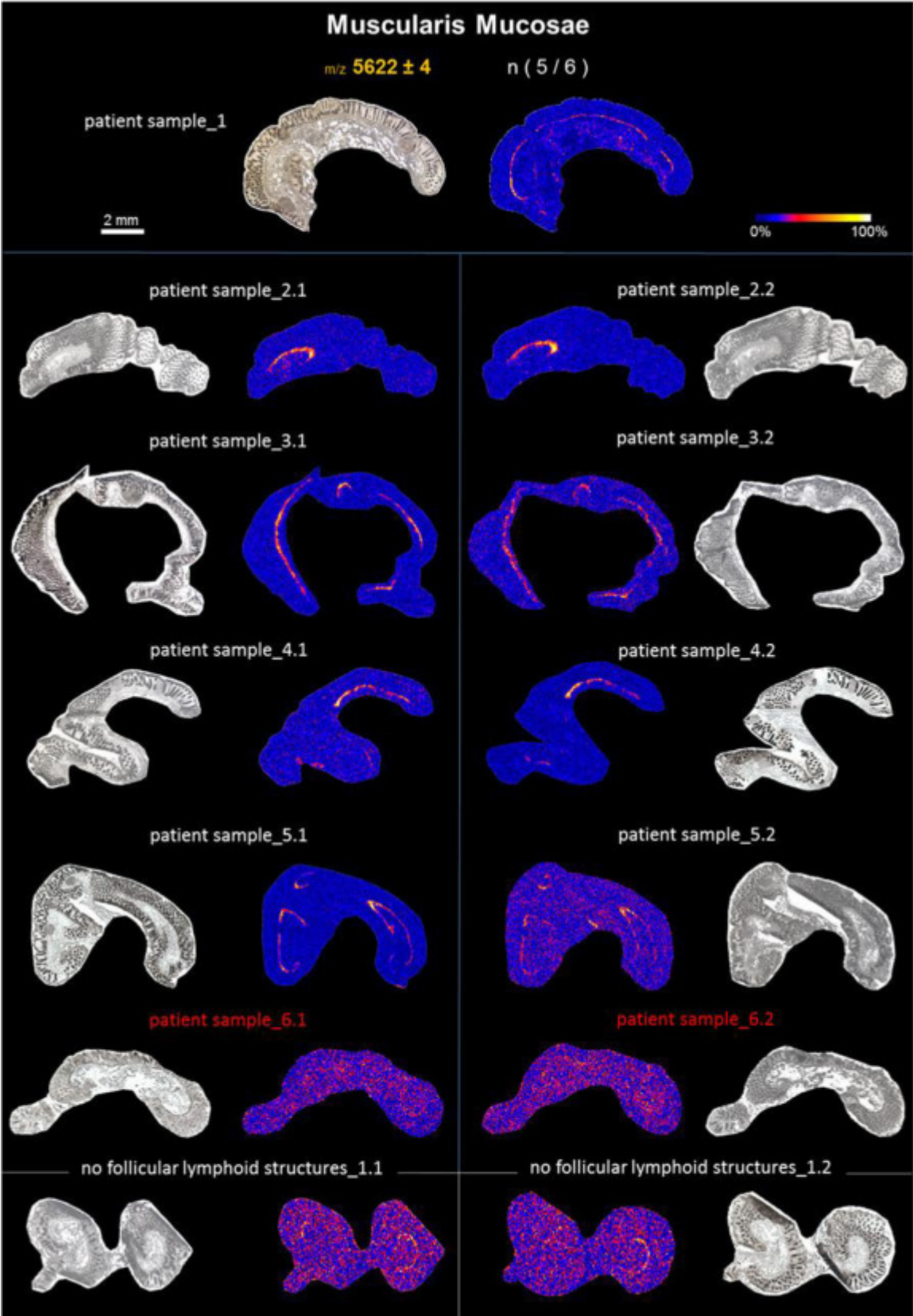
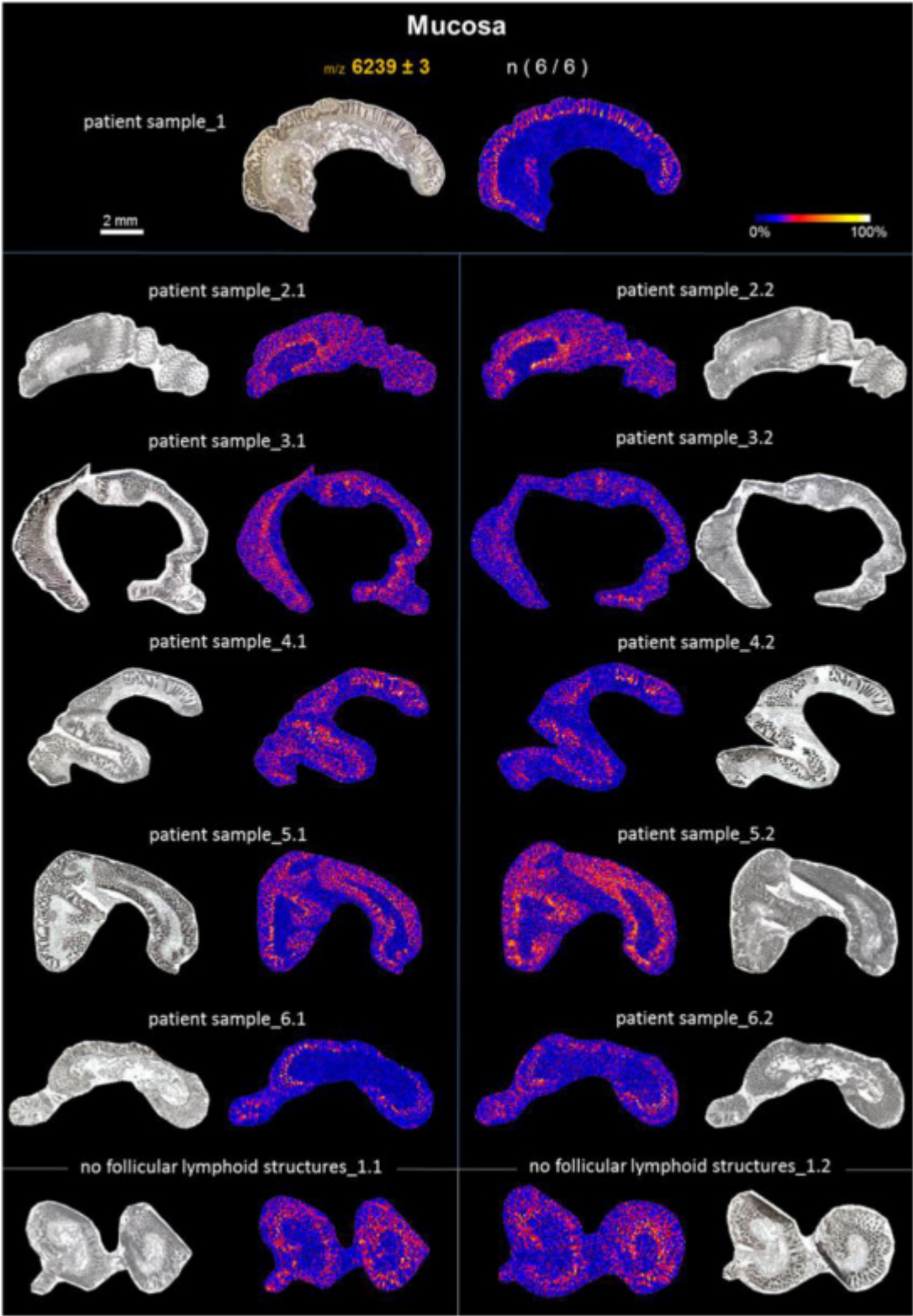
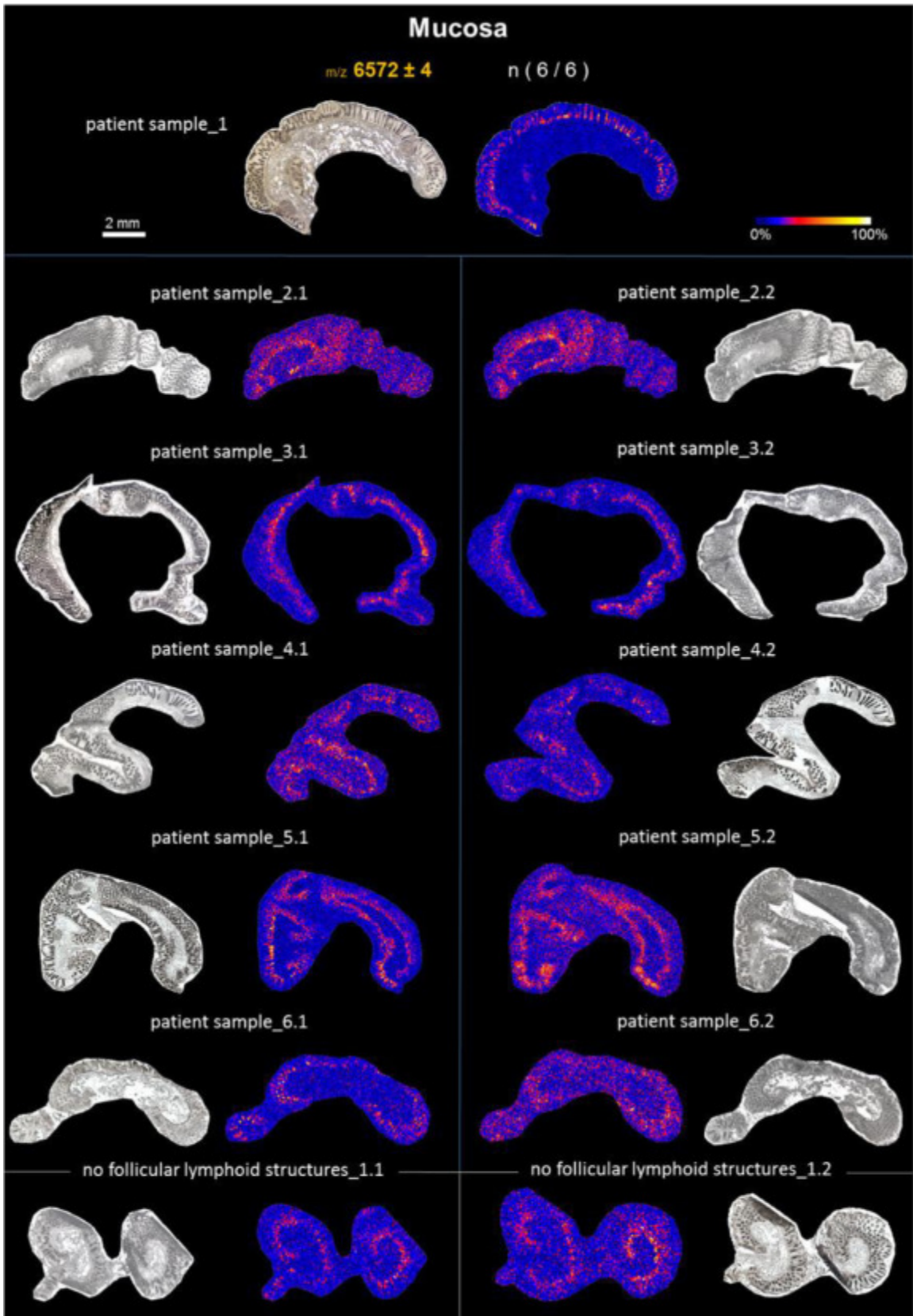
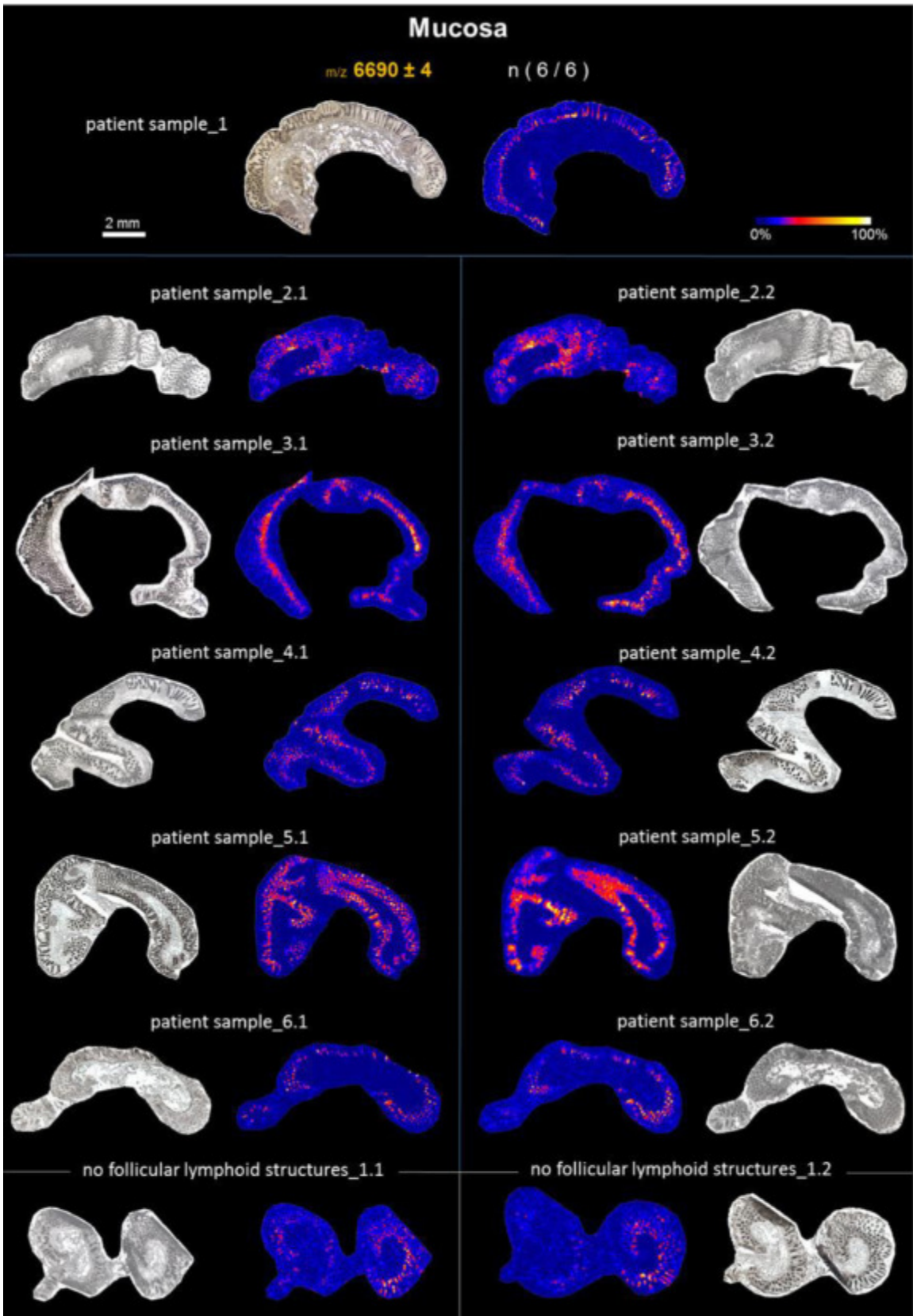
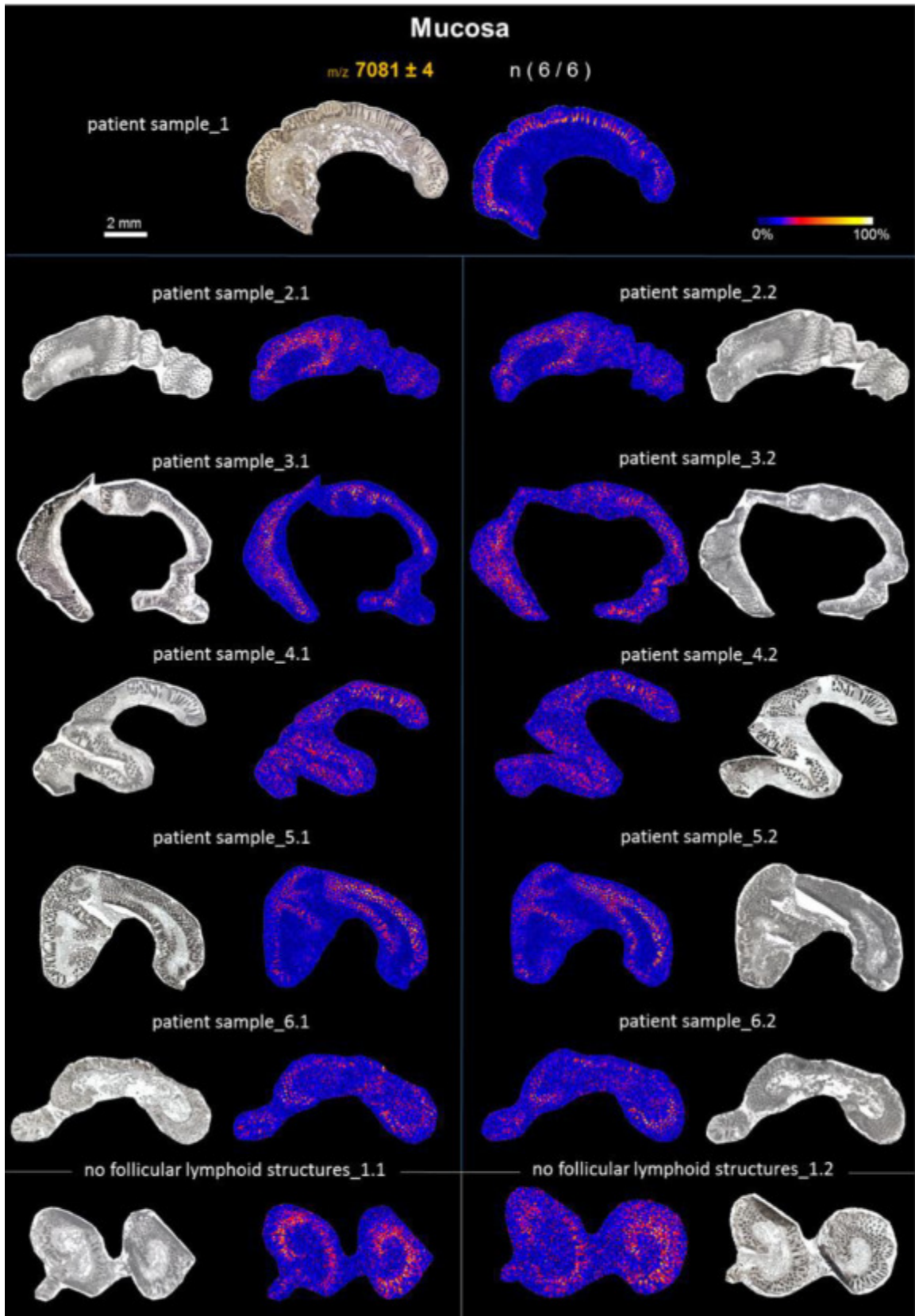


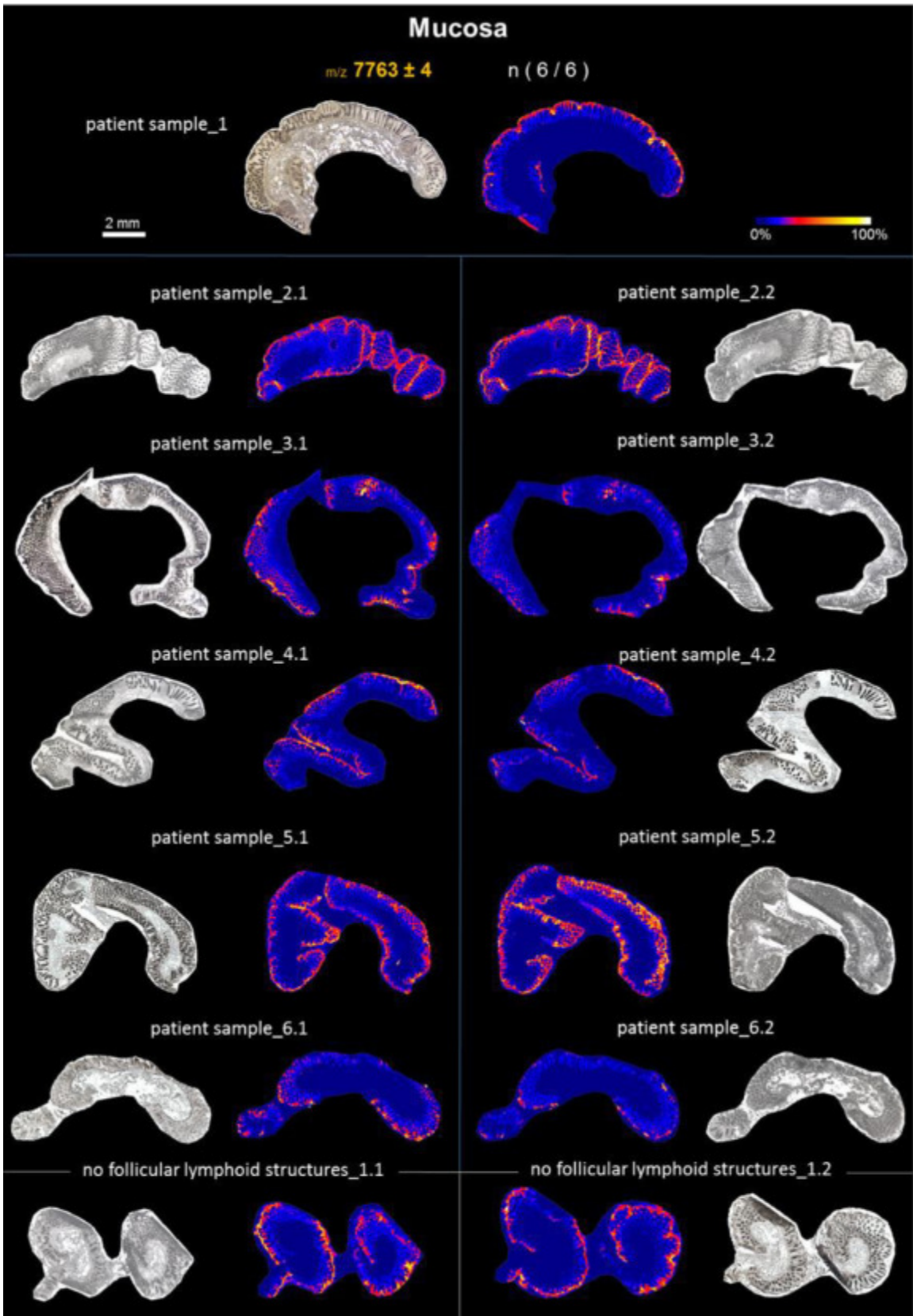
Figure S-6 MALDI MS images of m/z values characteristic for mucosa in colon tissue of seven patients (sample outliers are indicated in red).

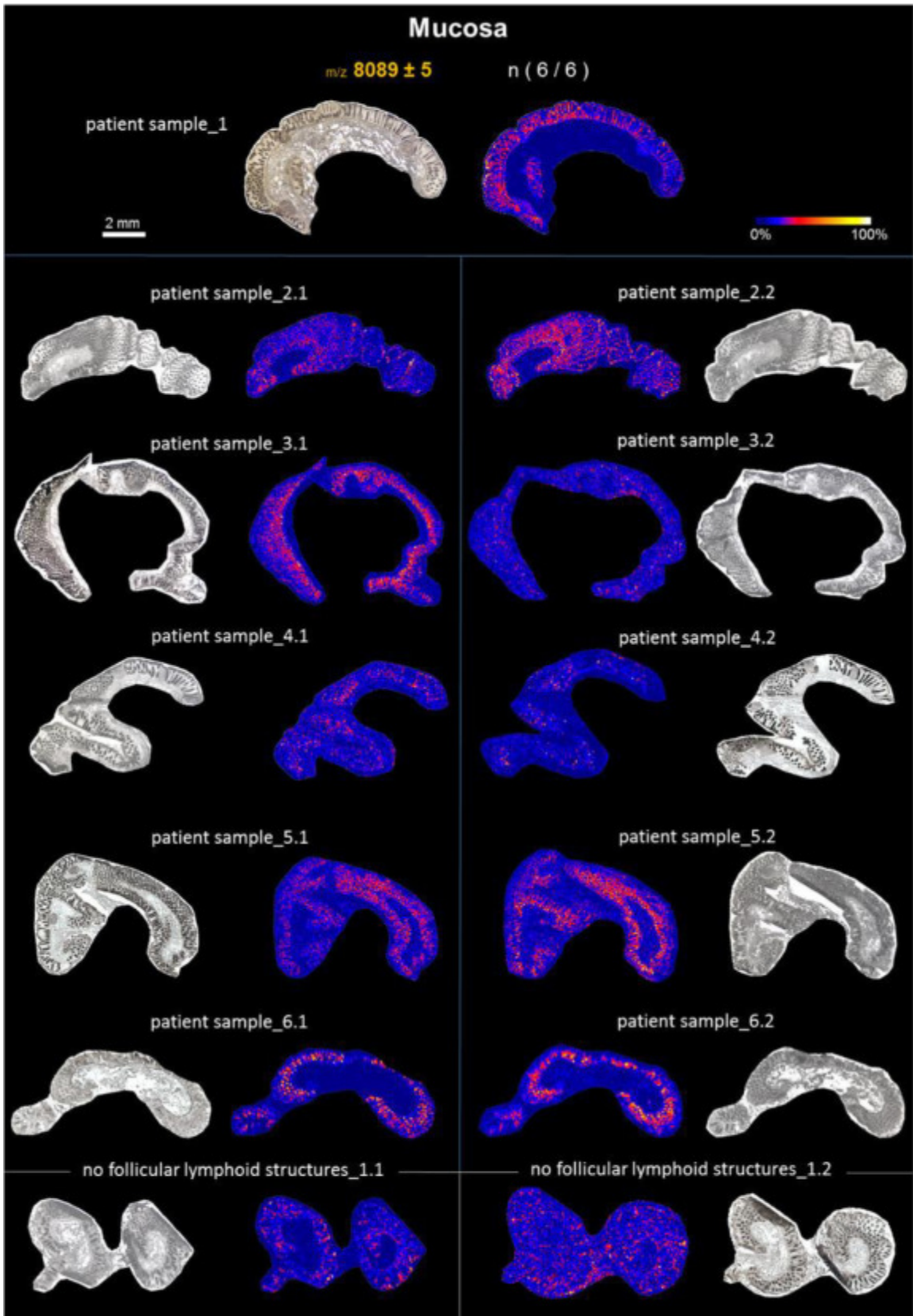


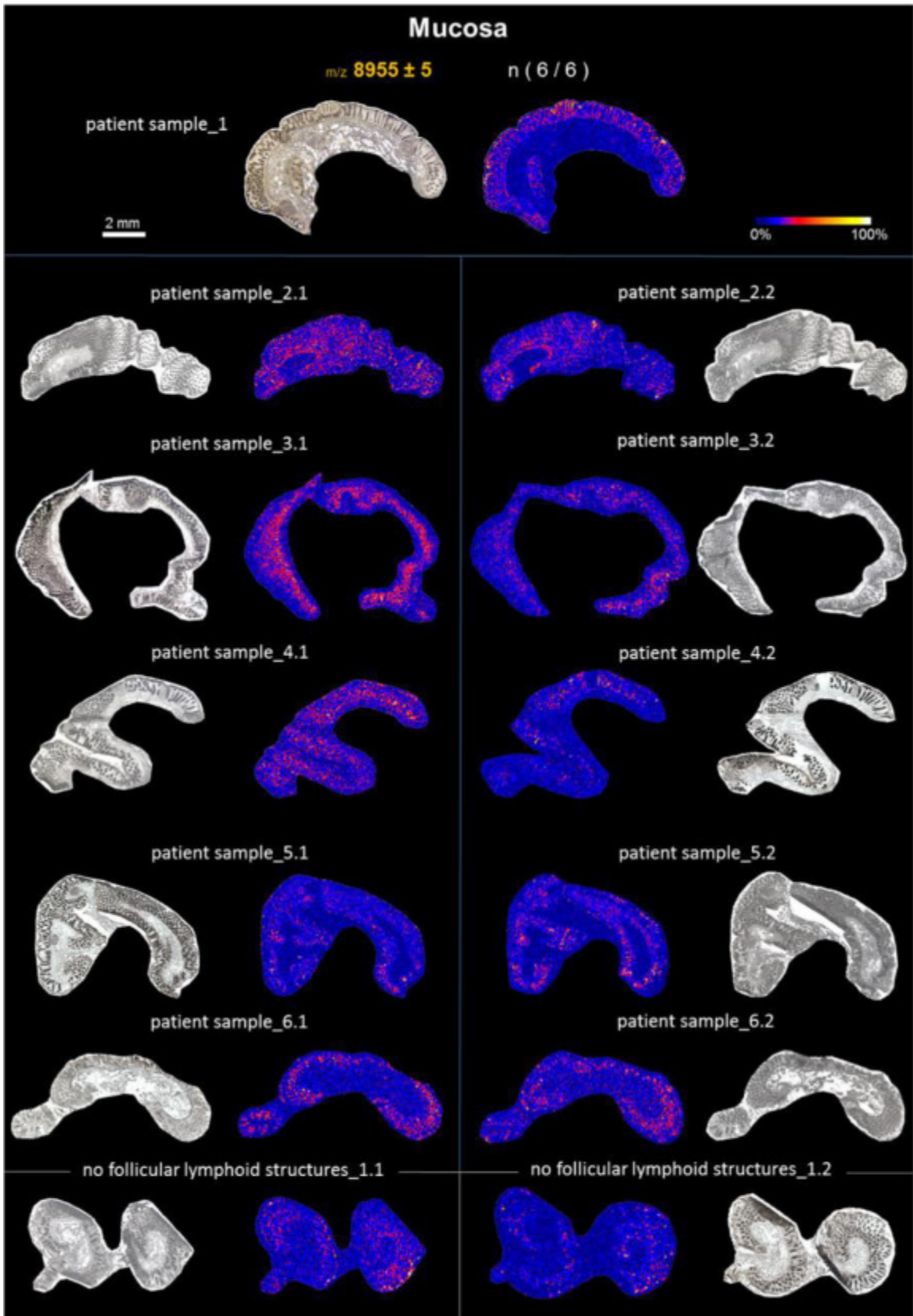


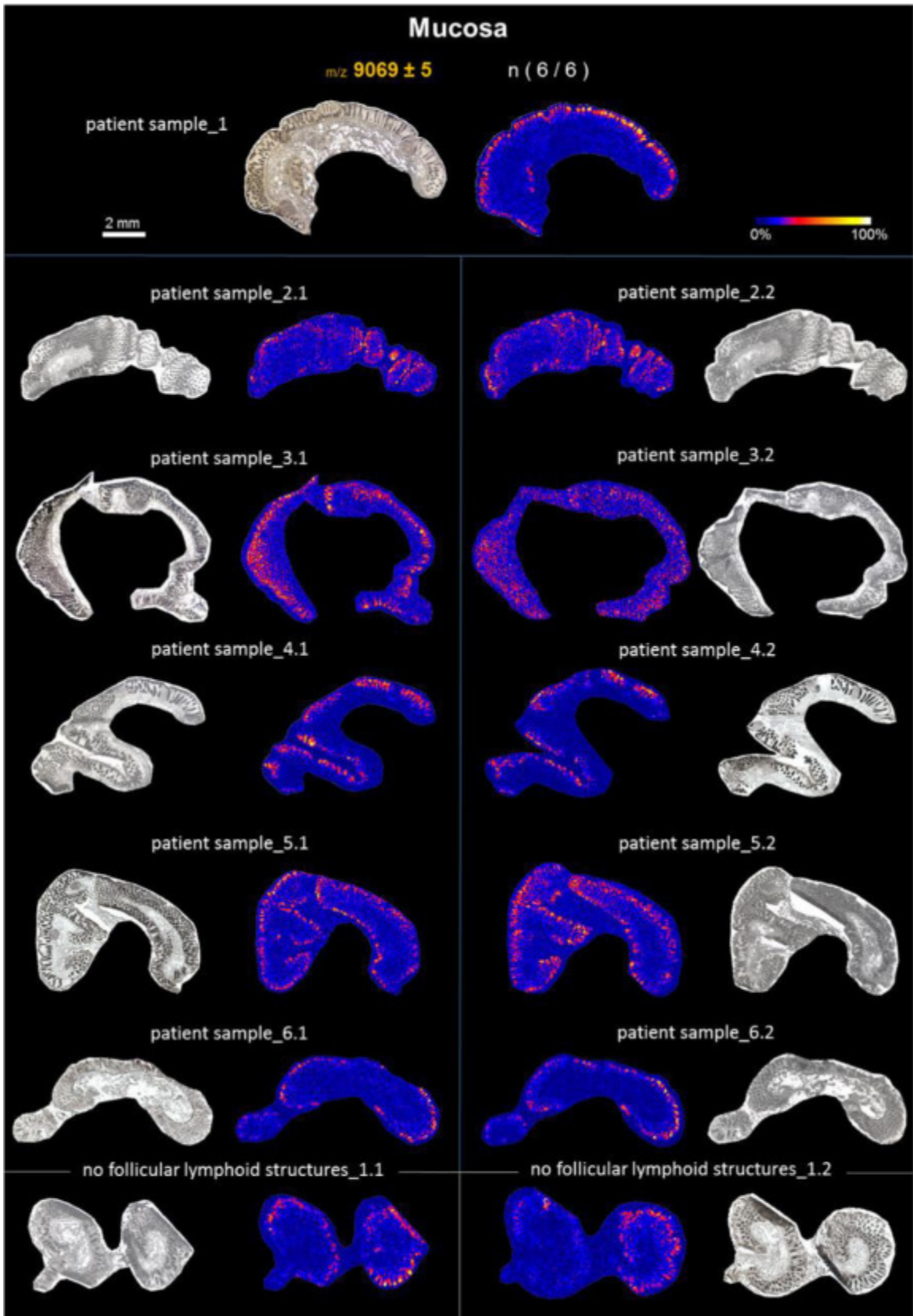


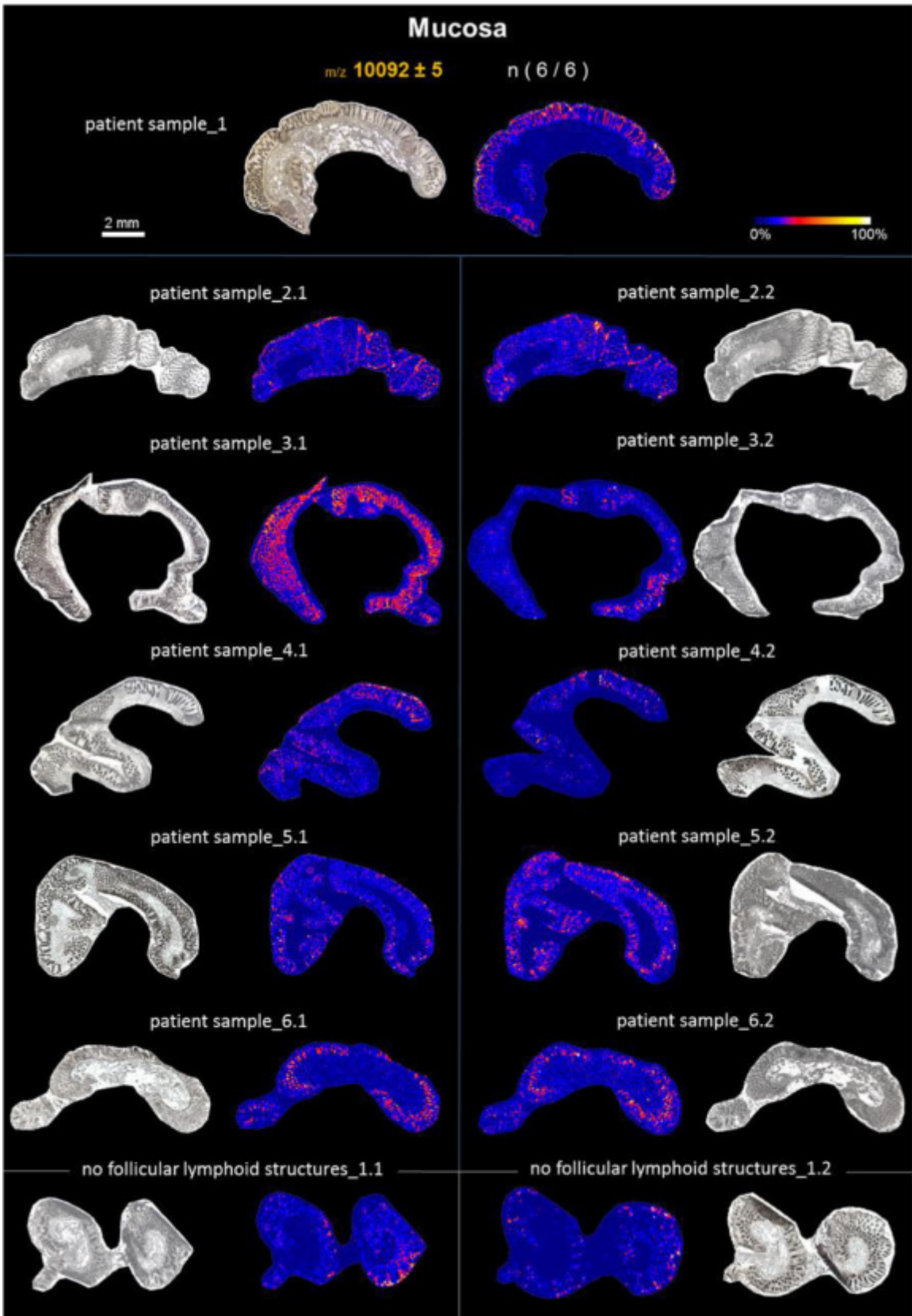


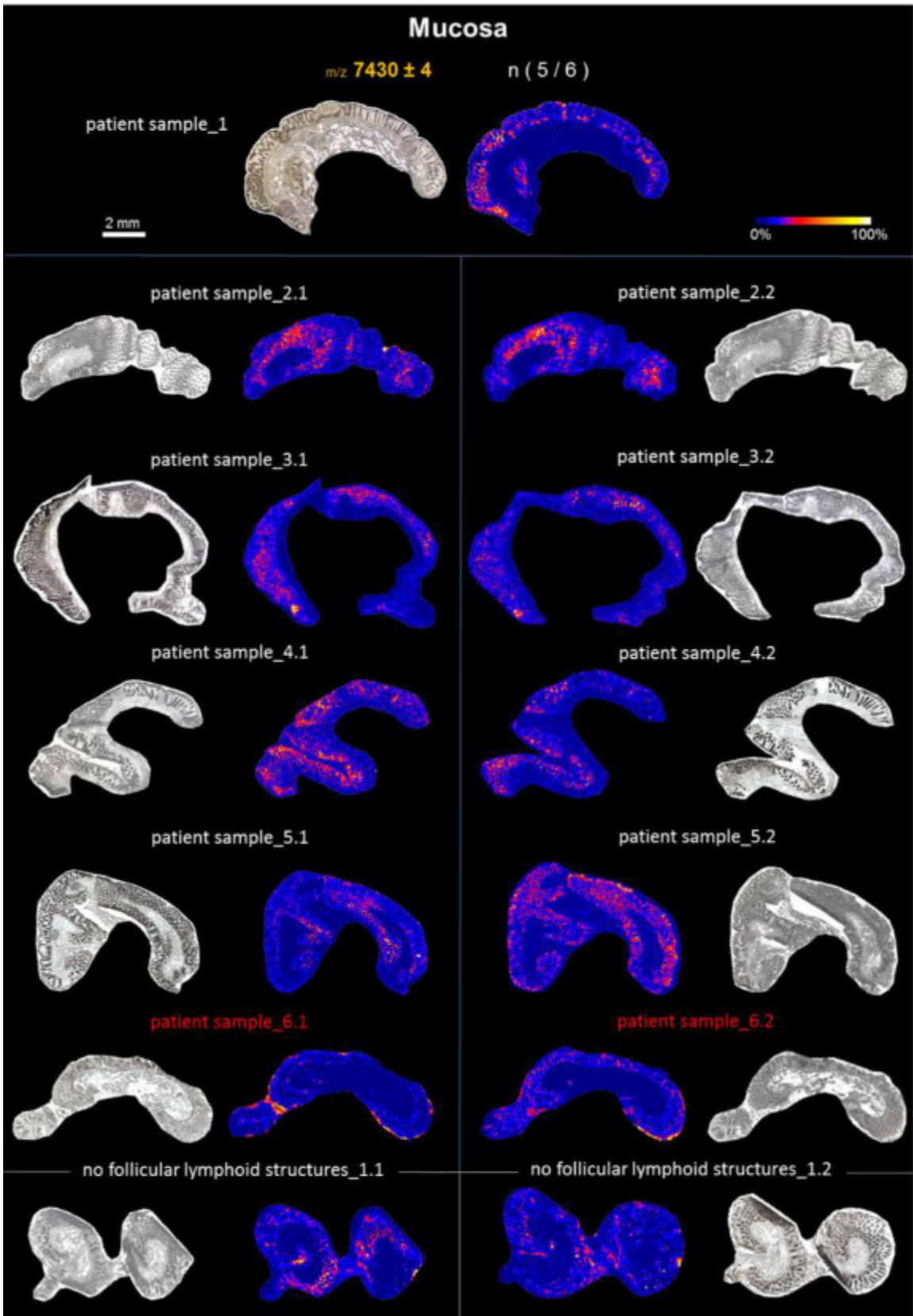


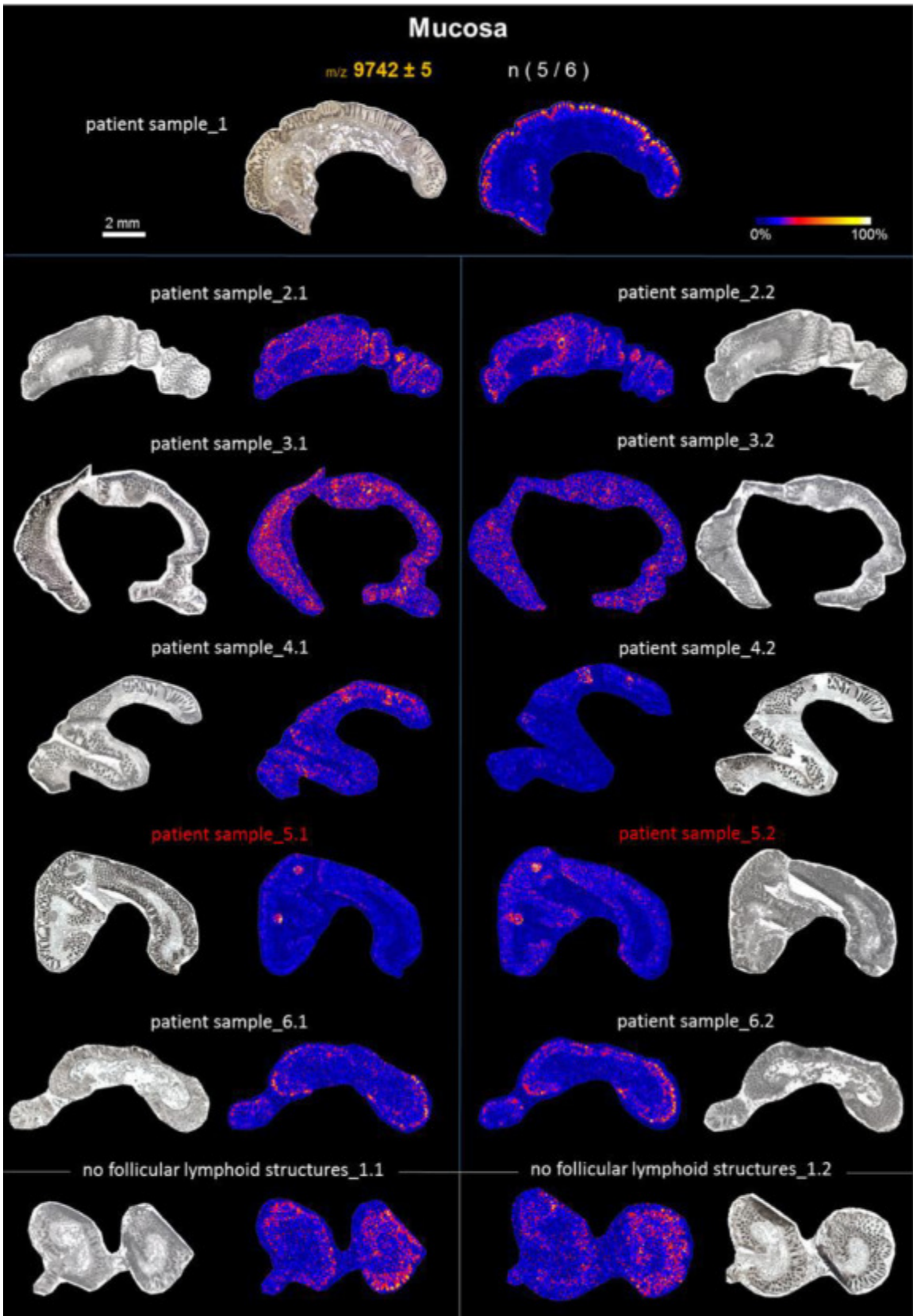


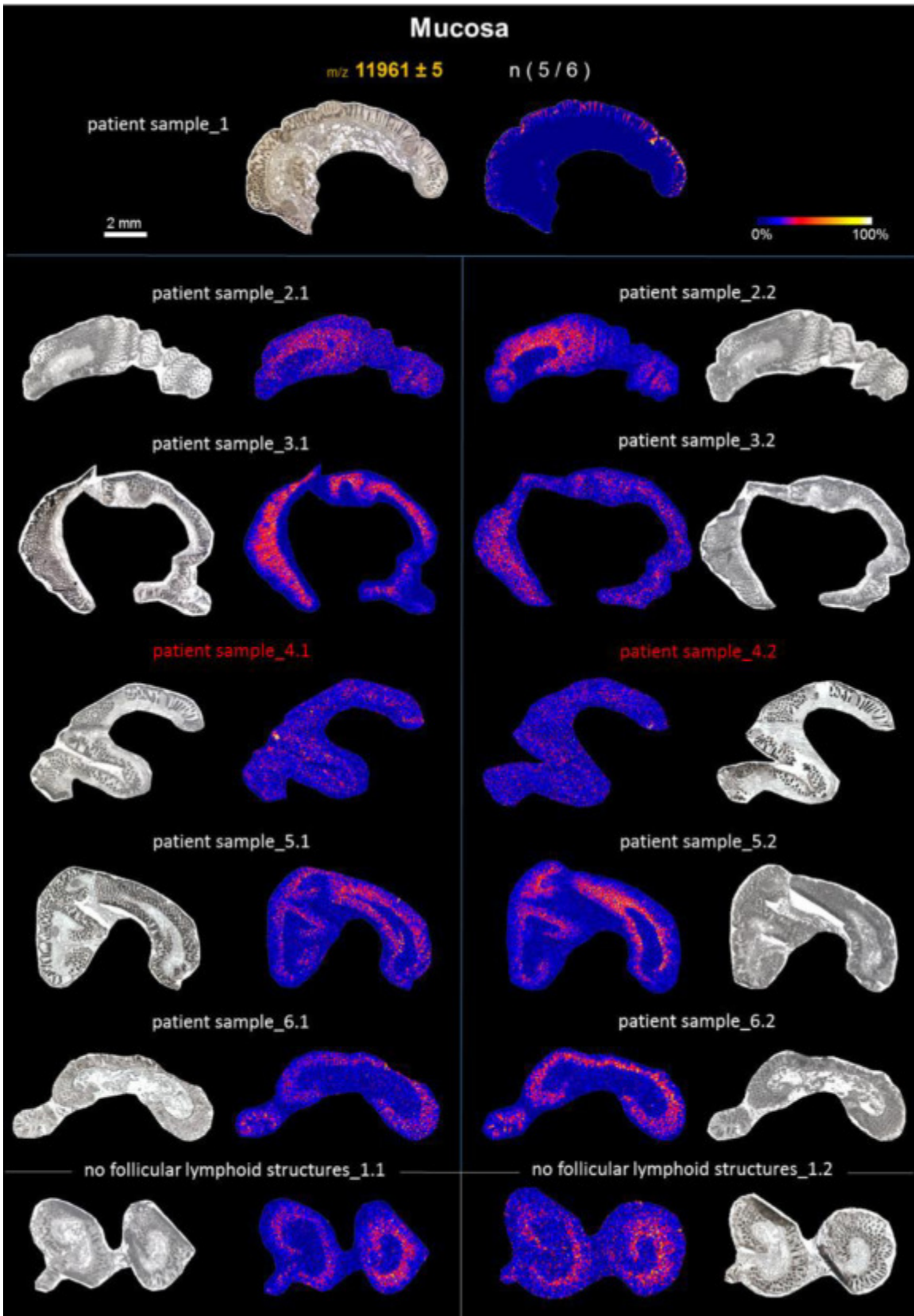












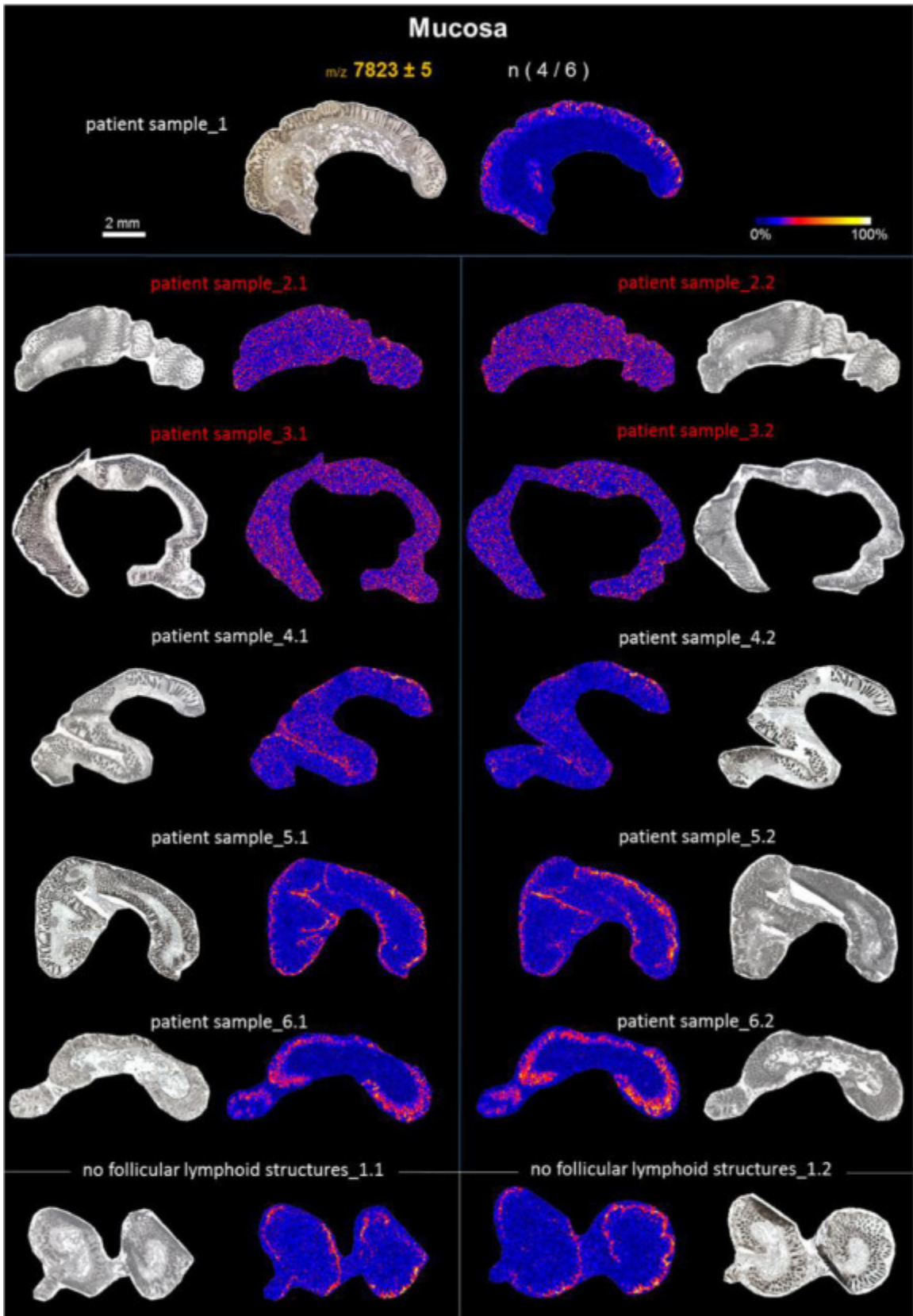
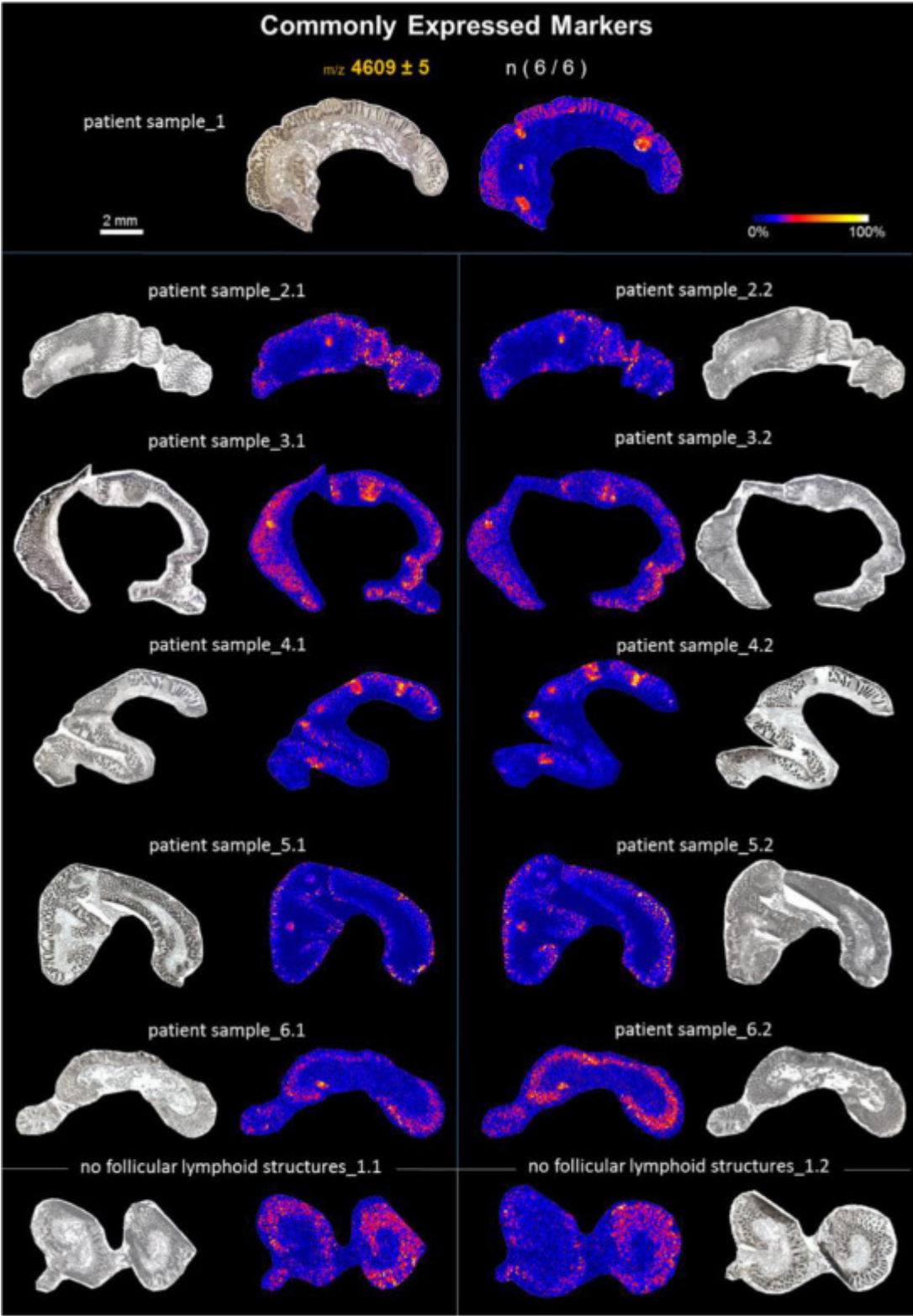


Figure S-7 MALDI MS images of m/z values commonly expressed in colon tissue of seven patients (sample outliers are indicated in red).

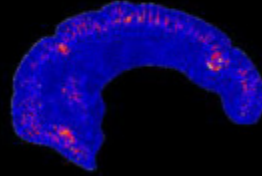


Commonly Expressed Markers

m/z 4729 ± 3

n (6 / 6)

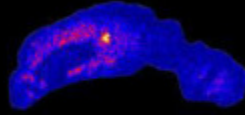
patient sample_1



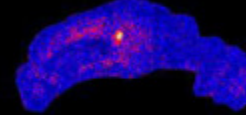
2 mm



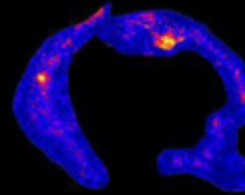
patient sample_2.1



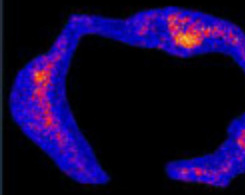
patient sample_2.2



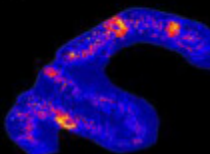
patient sample_3.1



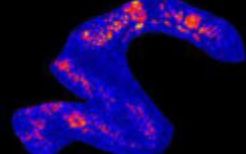
patient sample_3.2



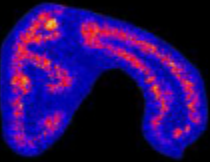
patient sample_4.1



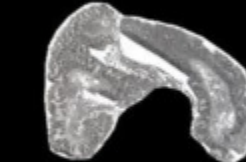
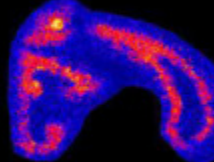
patient sample_4.2



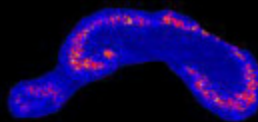
patient sample_5.1



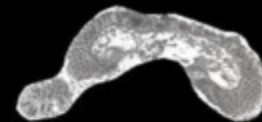
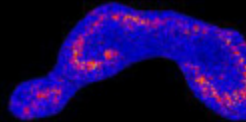
patient sample_5.2



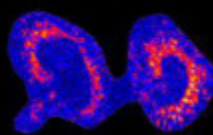
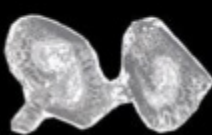
patient sample_6.1



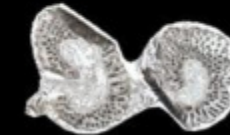
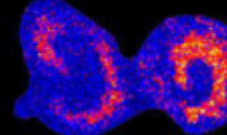
patient sample_6.2



no follicular lymphoid structures_1.1



no follicular lymphoid structures_1.2

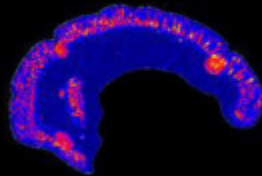


Commonly Expressed Markers

m/z 5657 ± 3

n (6 / 6)

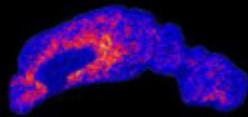
patient sample_1



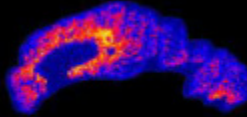
2 mm



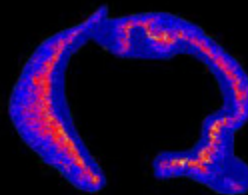
patient sample_2.1



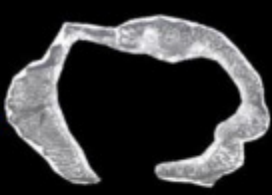
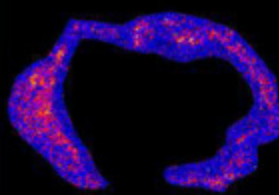
patient sample_2.2



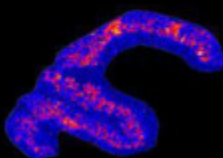
patient sample_3.1



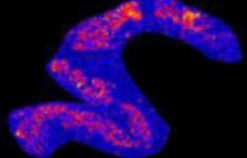
patient sample_3.2



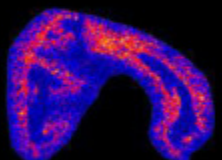
patient sample_4.1



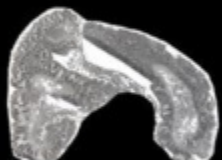
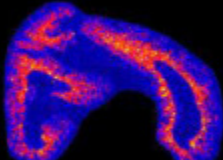
patient sample_4.2



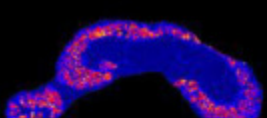
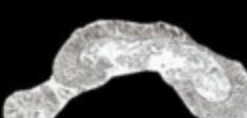
patient sample_5.1



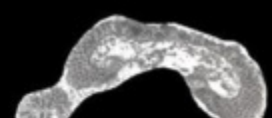
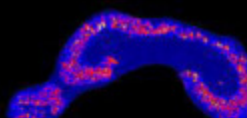
patient sample_5.2



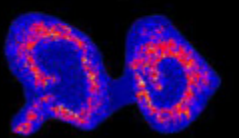
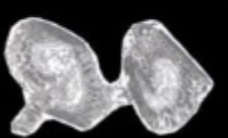
patient sample_6.1



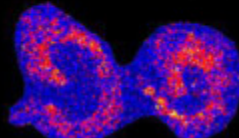
patient sample_6.2

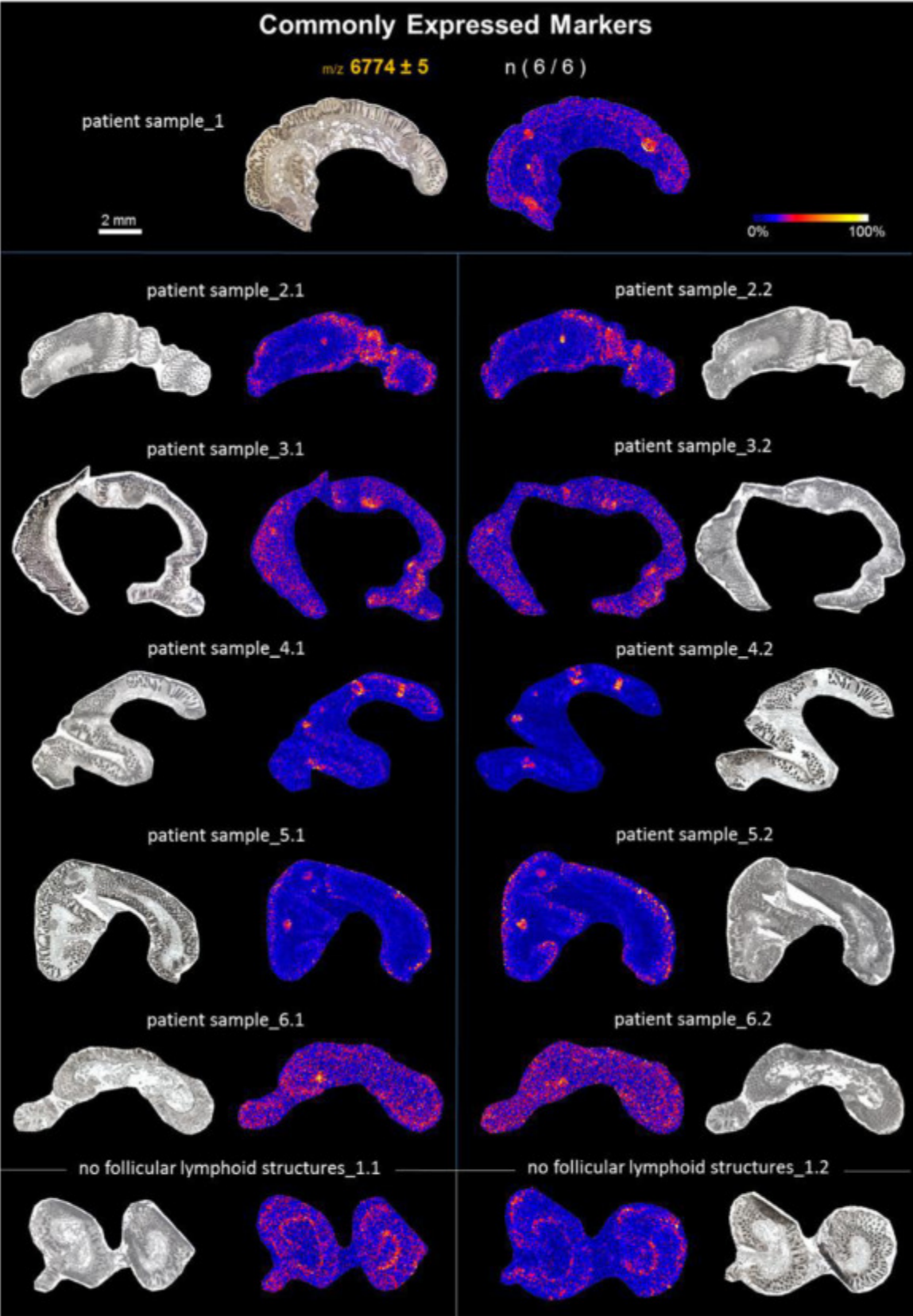


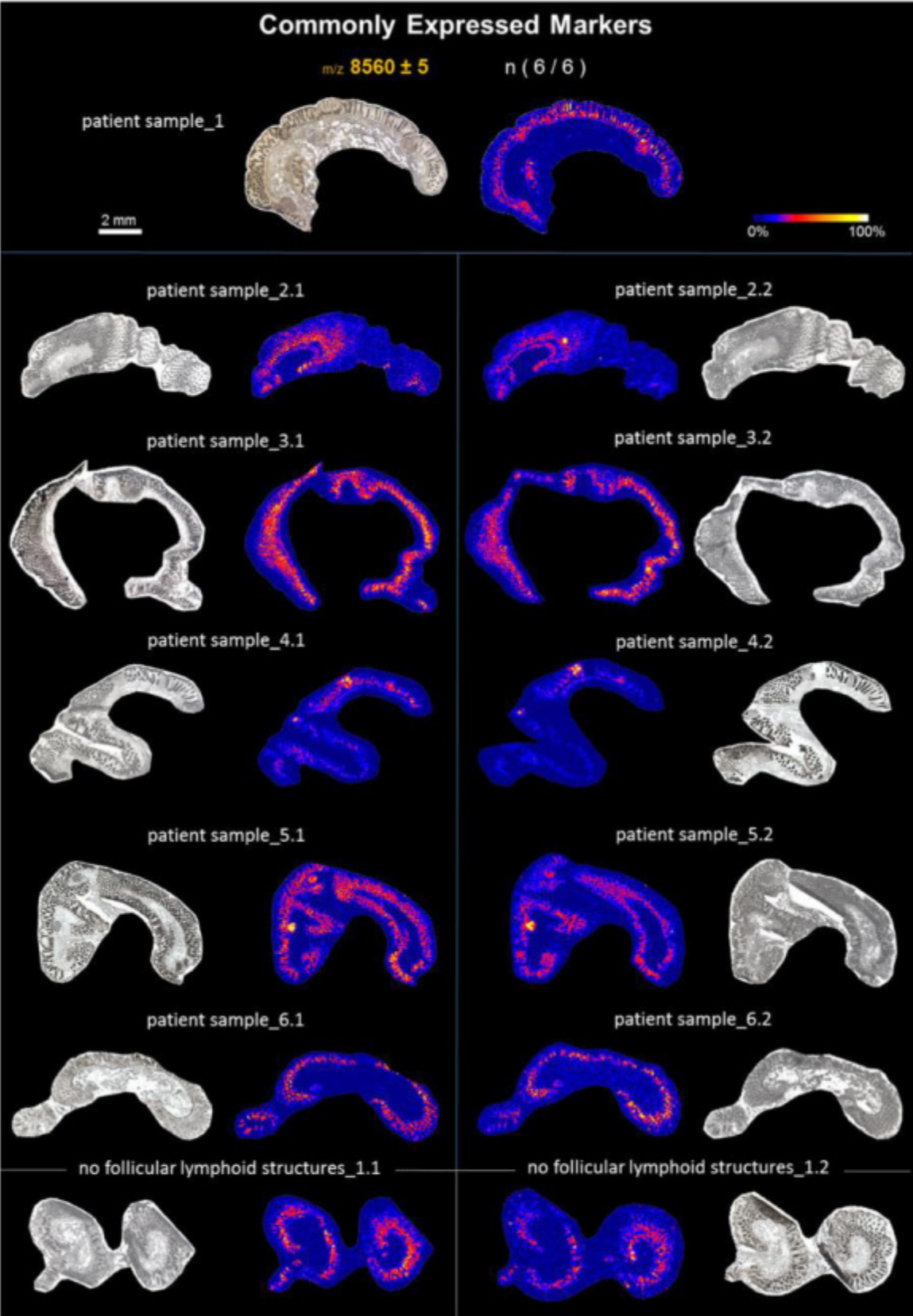
no follicular lymphoid structures_1.1

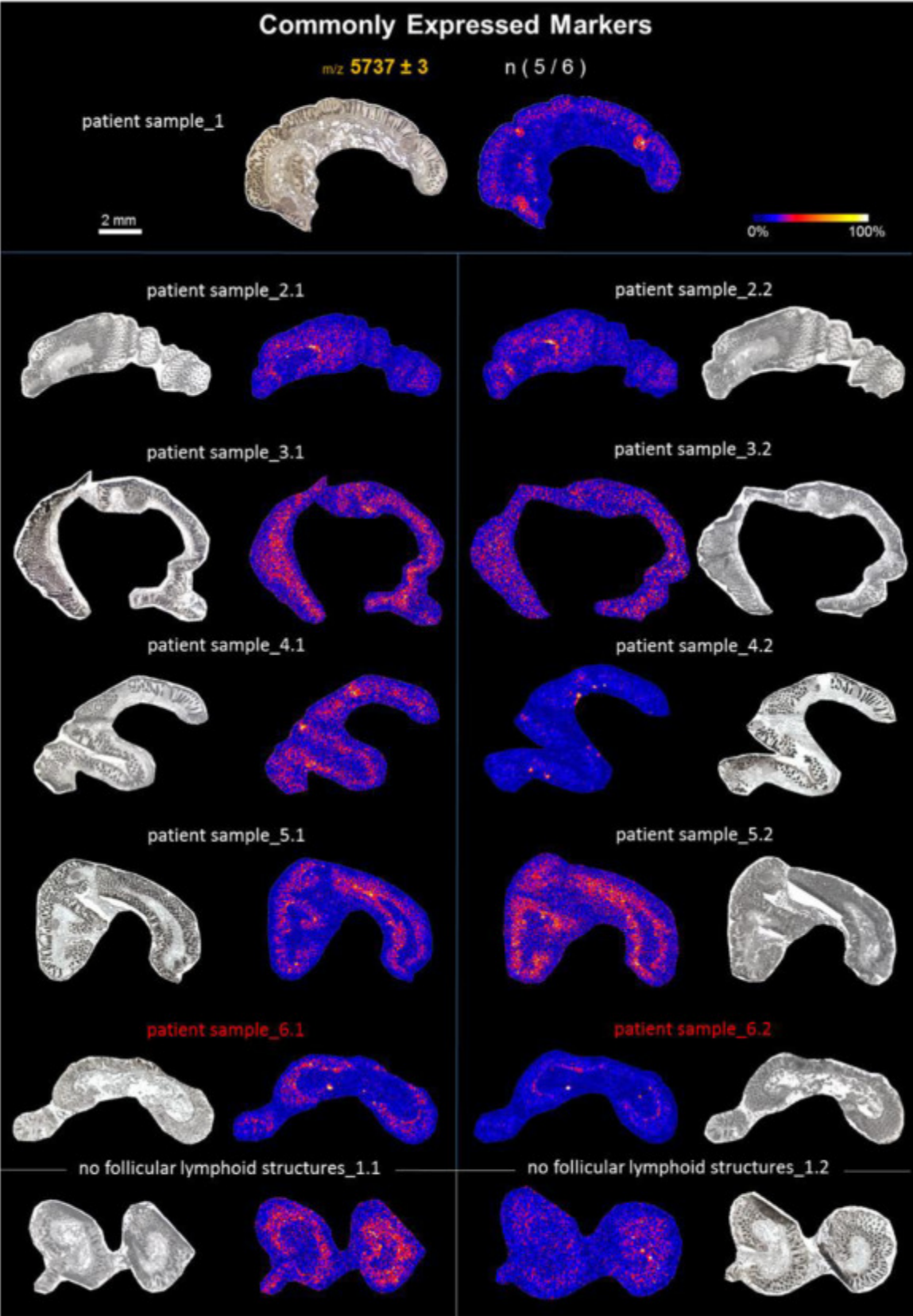


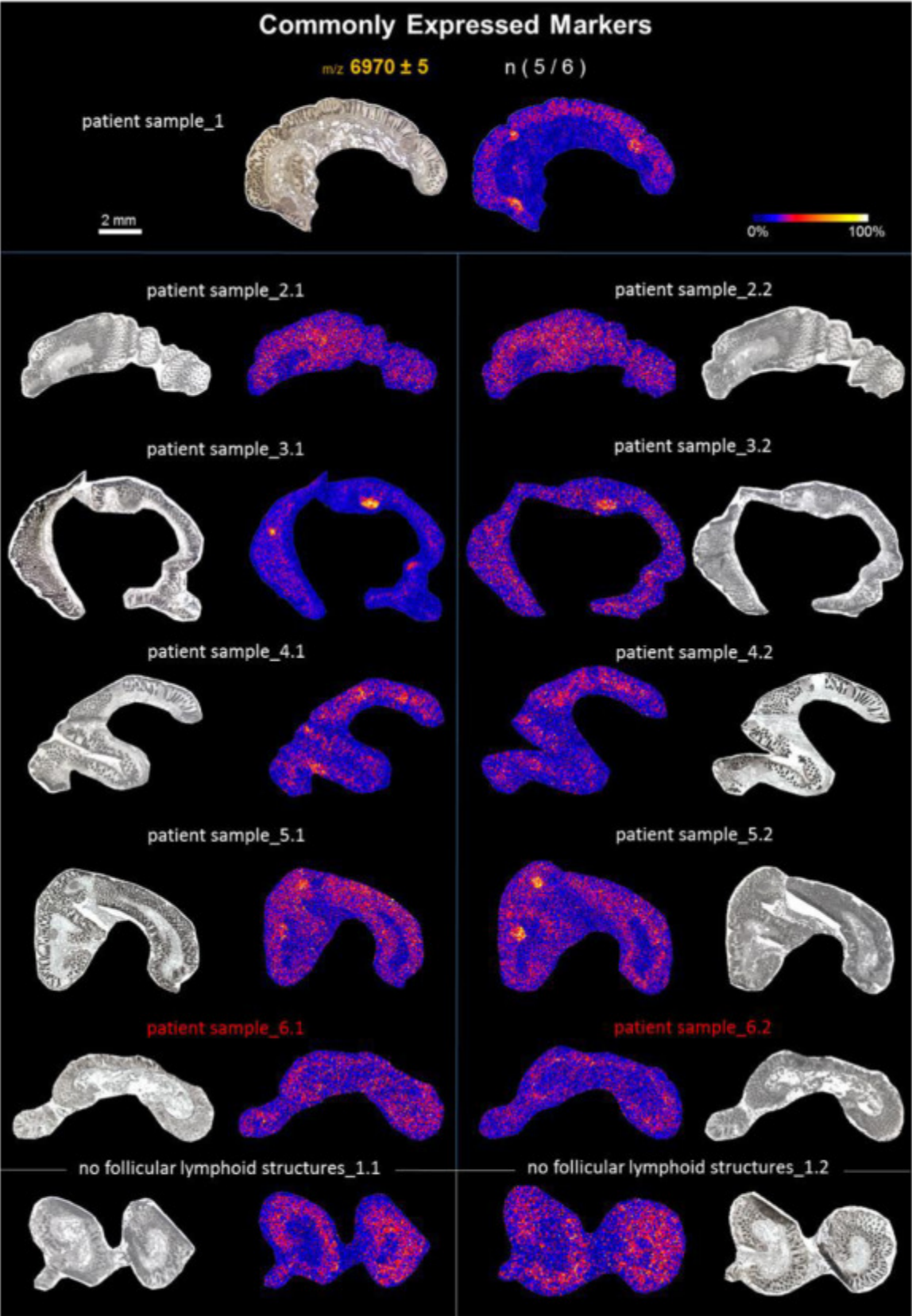
no follicular lymphoid structures_1.2

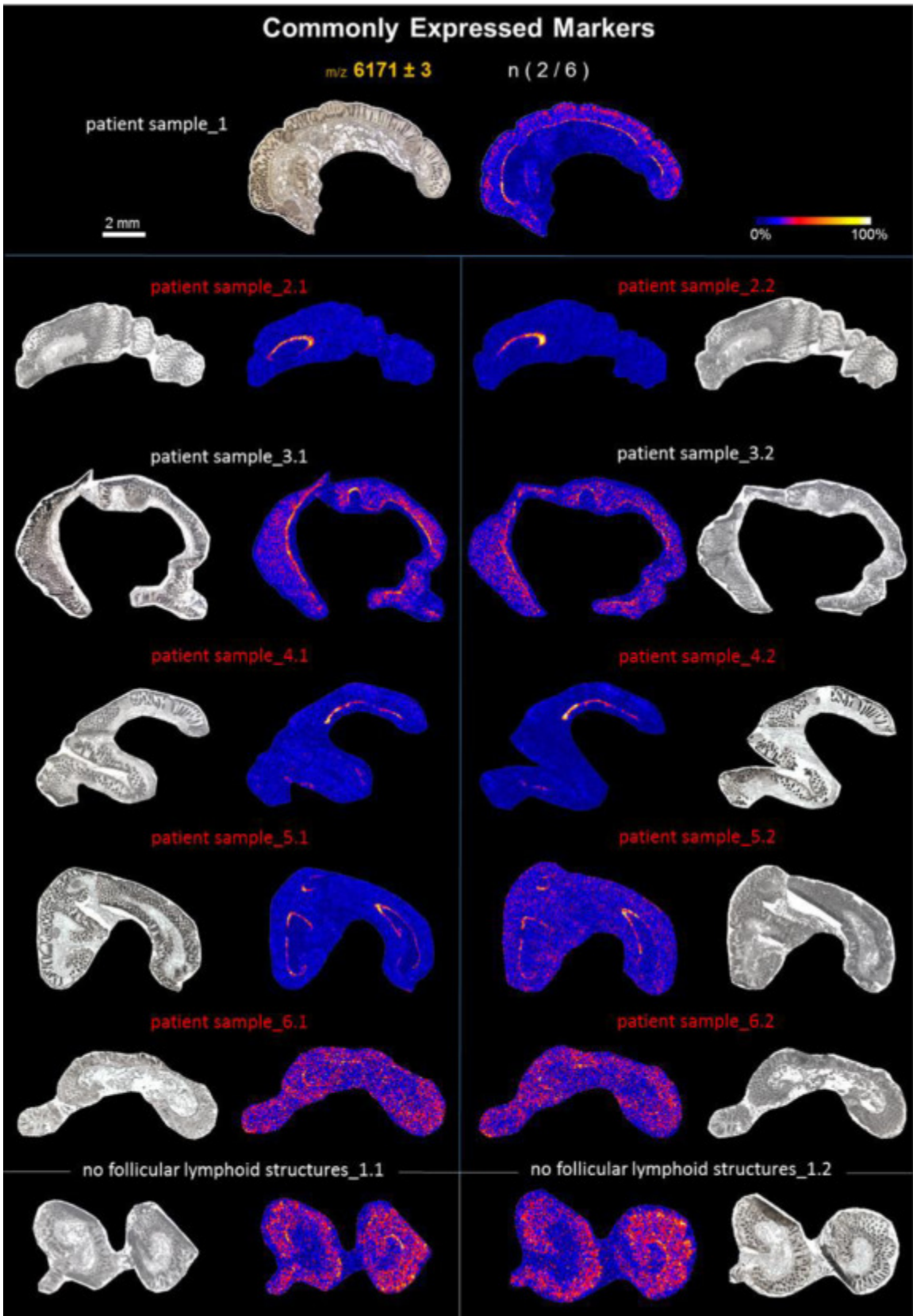












**7 MULTI-SENSOR IMAGING— FROM SAMPLE PREPARATION TO
INTEGRATED MULTI-MODAL INTERPRETATION OF LA-ICP-MS
AND MALDI MS IMAGING DATA**

| manuscript submitted to *Analytical Chemistry* |

Multi-sensor Imaging— from sample preparation to integrated multi-modal interpretation of LA-ICP-MS and MALDI MS imaging data

Matthias Holzlechner[†], Maximilian Bonta[†], Hans Lohninger[†], Andreas Limbeck[†], Martina Marchetti-Deschmann^{†*}

[†]Institute of Chemical Technologies and Analytics, TU Wien, Getreidemarkt 9, 1060 Vienna, Austria.

ABSTRACT: Laterally resolved chemical analysis (chemical imaging) has increasingly attracted attention in the Life Sciences during the past years. While some developments have provided improvements in lateral resolution and speed of analysis, there is a trend towards the combination of two or more analysis techniques, so-called multi-sensor imaging, for providing deeper information into the biochemical processes within one sample. In this work, a human malignant pleural mesothelioma sample from a patient treated with cisplatin as cytostatic agent has been analyzed using LA-ICP-MS and MALDI MS. Whilst LA-ICP-MS was able to provide quantitative information on the platinum distribution along with the distribution of other elemental analytes in the tissue sample, MALDI MS could reveal full information on lipid distributions as both modes of polarity, negative and positive, were used for measurements. Tandem MS experiments verified the occurrence of distinct lipid classes. All imaging analyses were performed using a lateral resolution of 40 μm , providing information with excellent depth of details. By analyzing the very same tissue section, it was possible to perfectly correlate the obtained analyte distribution information in an evaluation approach comprising LA-ICP-MS and MALDI MS data. Correlations between platinum, phosphorus and lipid distributions were found by the use of advanced statistics. The present proof-of-principle study demonstrates the benefit of data combination for outcomes beyond one method imaging modality and highlights the value of advanced chemical imaging in the Life Sciences.

Modern clinical studies often rely on chemical analysis for in-depth investigation. Abundances of proteins, lipids, metabolites, or trace elements may for example be excellent indicators for the success of a therapy. Besides the knowledge of average analyte contents in tissue, gaining insight into the lateral distribution within a sample has attracted increased interest during the past years. Using solid sampling techniques, it is possible to analyze tissue sections generally with only minor sample preparation whilst maintaining the spatial integrity of the analytes of interest. Subsequently, obtained

lateral distribution information can be compared with results from classical histological or immunohistochemical staining techniques.

Laser ablation inductively coupled plasma mass spectrometry (LA-ICP-MS) is a widely-accepted method for elemental analysis of solid samples ^{1 2}. Due to its exceptional limits of detection (below the $\mu\text{g g}^{-1}$ -range for most elements), achievable lateral resolutions down to the single-digit μm -scale and a quite extensive range of available possibilities for quantification, this technique has found its way into many disciplines of science. [References Among them, Life Sciences have become a wide application range, with LA-ICP-MS offering the possibility of depicting lateral distribution of trace elements in various types of biological samples.

But also matrix-assisted laser desorption/ionization mass spectrometry (MALDI MS) is a potent analytical technique for investigating larger intact molecules, such as proteins, peptides, lipids and metabolites, features which are especially appealing for biological samples ^{3 4}. As being a solid sampling technique as well, the direct analysis of tissue samples is feasible, providing lateral distribution information of analytes. Thereby, matrix application to enable the analyte desorption and ionization process is a crucial step. If lateral resolution information is desired, special care has to be taken as not to corrupt the natural analyte distribution in the sample. In the past years, methods such as matrix sublimation have been developed for this purpose ^{5 6 7}.

Since LA-ICP-MS and MALDI MS offer complementary analyte information, excellent insight into the chemical nature of a sample can be gained by combination of these two techniques in a multi-sensor (different MS instrumentation), multi-modal (different ionization modes) imaging (MSMMI) approach. Of course, using consecutive tissue thin-cuts might seem most straight-forward for this purpose, especially when the methods' requirements for sample preparation are different. However, even two consecutive tissue sections, cut at only some tens of μm distance can show variation in analyte distributions. These may originate from the sample itself (cell size and shape) or from the sample preparation process (cutting accuracy). Therefore, analyzing the same sample using two different methods would be highly desirable to exclude the possibility of inter-sample variations but also to guarantee appropriate data quality for MSMMI approaches.

Multi-sensor imaging combining LA-ICP-MS and MALDI MS on a single tissue sample has already been demonstrated in literature ^{8 9} and some issues are also outlined in these publications like sample preparation. MALDI MSI requires matrix application which can delocalize elements targeted by LA-ICP-MS. But performing LA-ICP-MS before MALDI MSI is not possible because the sample is usually completely consumed.

To our knowledge, until today no publication is available providing information on an integrated data evaluation strategy taking every gathered information into account. We present data from different instruments (LA-ICP-MS and MALDI MS), different types of analyte (elements and molecules) and

different modes of ionization (ICP, MALDI in negative and positive ion mode), all measured from the same tissue section, and combine this information for a more comprehensive analysis.

So, the main goal of the study is to present a universal MSMMI approach for LA-ICP-MS and MALDI MS imaging from one single tissue section. A human malignant pleural mesothelioma (MPM) sample from an individual being treated with cisplatin as cytostatic drug has been used. The sample preparation strategy has been adjusted to fit the needs of each imaging method, LA-ICP-MS and MALDI MSI, whilst providing the possibility of species identification by MALDI MS and quantification of elements, especially platinum, by LA-ICP-MS. Ultimately, an integrated data evaluation strategy has been developed combining LA-ICP-MS and negative and positive ion mode MALDI MS data. Advanced statistical analysis finally allowed the correlation of platinum distribution with certain lipids. Results of the study prove the surplus of combining multiple instruments and measurement modes and underpins the importance of an integrated data analysis approach for valid findings.

MATERIALS AND METHODS

Materials. All reagents were purchased from Sigma-Aldrich (St. Louis, MO, US) with a purity of at least 99%, if not otherwise stated. Sections of a human MPM tissue were provided by the Department of Surgery and Comprehensive Cancer Center (Medical University of Vienna, AT). The tissue sections were sliced at a 10 μ m thickness using a CM3050 cryostat from Leica Microsystems GmbH (Wetzlar, DE) and stored at -70 $^{\circ}$ C until further analysis. Ultra-high quality water (ddH₂O) with a resistivity < 18.2 M Ω ×cm @ 25 $^{\circ}$ C was obtained from a Simplicity system (Millipore, Billerica, MA, US). Conductive indium tin oxide (ITO) coated microscope glass slides were purchased from Delta Technologies (Loveland, MN, US). Ar used as collision gas in MALDI tandem MS (MS²) experiments as well as He and Ar used for LA-ICP-MS measurements were purchased from Messer Austria GmbH (Gumpoldskirchen, AT) and were of grade 5.0 purity.

Tissue Preparation. Prior to MALDI mass spectrometry-based imaging (MSI), the frozen tissue sections were allowed to equilibrate to room temperature in a desiccator for \geq 2 h and subsequently washed by submerging the slides in 50 mM ammonium acetate (pH 6.7, 4 $^{\circ}$ C) 4 times, 5 s each. After each incubation step the tissue was dried in a gentle stream of N₂ and finally stored in a desiccator for min. 15 min before analyses.

Matrix Application for MALDI MS. Matrix deposition was performed using a home-built sublimation apparatus ¹⁰. In a vacuum-sealed and pressure-controlled deposition chamber 25.5 mg of 1,5-diaminonaphthalene (1,5-DAN) were quantitatively vaporized and sublimed onto the tissue sections at 145 $^{\circ}$ C and 4.7 Pa forming a homogenous layer (0.23 mg cm⁻²) of crystals.

Molecular Imaging by MALDI MS. MSI data were acquired on a MALDI TOF/RTOF mass spectrometer (ultrafleXtreme™) using reflectron geometry and flexControl software v3.4 (Bruker Daltonics, Bremen, DE). The attenuator offset of the laser (smartbeam-II, wavelength 355 nm) was adjusted to 65% and the laser fluence was set to 45%. The mass range between 440 to 1700 Da was selected with ion suppression for analytes smaller than 340 Da. Imaging data was collected by analyzing at 40 μm lateral resolution in the negative mode, followed by positive ion mode after offsetting x and y positions by 20 μm . By using a laser repetition rate of 1kHz, 100 shots per array position were summed up (no intra-spot rastering). Mass spectra were calibrated externally using the cubic enhanced algorithm on singly charged ions of 1,5-DAN, bovine cardiolipin disodium salt and castor oil. Data acquisition and image representation were carried out using flexImaging software v3.0 (Bruker Daltonics) and ImageLab software (Epina GmbH, Retz, Austria). Acquired imaging data were normalized to the total ion current (TIC). MS/MS experiments in LIFT mode were performed for selected mass values for analyte identification, which was based on fragment information and comparison of parent ion information with theoretical m/z values according to LIPID MAPS Structure Database (The LIPID MAPS Lipidomics Gateway, <http://www.lipidmaps.org/>) and [Metabolomics Workbench Metabolite Database](http://www.metabolomicsworkbench.org/) (<http://www.metabolomicsworkbench.org/>, both University of California, San Diego, USA).

Elemental Imaging by LA-ICP-MS. ICP-MS data were obtained using a NWR213 laser ablation system (ESI, Fremont, CA, US) equipped with a frequency quintupled Nd:YAG laser (213 nm) in connection with a Thermo iCAP Qc (ThermoFisher Scientific, Bremen, DE). Experimental parameters were optimized in preliminary experiments to obtain the best possible tradeoff between low analysis time and high data quality. All imaging analyses were performed using consecutive line scans at 40 μm laser beam diameter, 120 $\mu\text{m s}^{-1}$ stage scan speed, 7.56 J cm^{-2} laser fluence and 20 Hz repetition rate. Helium gas at a flow rate of 1 L min^{-1} was used as carrier gas. Using the ICP-MS, signals of ^{31}P , ^{34}S , and ^{195}Pt were monitored at a quadrupole dwell time of 10 ms per isotope and a mass resolution of 300 $\text{m}/\Delta\text{m}$.

Prior to LA-ICP-MS analysis, samples were coated with a thin layer of gold using a sputter coater (Agar B7340, Agar Scientific Ltd, Essex, UK). The gold layer is ablated simultaneously with the sample and serves as a pseudo-internal standard. Such use has been reported earlier elsewhere ¹¹. The pseudo-internal standard can be employed to mitigate matrix effects and allows the quantification of platinum after external calibration using printed patterns on paper ¹².

The combined workflow of the MSMMI experiment is shown in Figure 1.

Data Fusion, Spectral Descriptors and Multivariate Analysis. MALDI MS and LA-ICP-MS imaging datasets were combined into a MSMMI dataset using the software package ImageLab (Epina GmbH, Retz, Austria) as previously described ¹³. The multivariate analysis of the hyperspectral datacube is based on spectral descriptors (SPDCs) as earlier introduced in the context of mass spectrometry ¹⁴. Thereby, each SPDC corresponds to a feature in the obtained mass spectra. For the MALDI MS data cubes with negative and positive polarities, SPDCs were created algorithmically using the Spectral Descriptor Generator (peak width: 1 Da). SPDCs for the individual elements from the LA-ICP-MS data cube were simply defined by applying single intensity descriptors of the signals.

Random Decision Forest (RDF)-based classifiers are often used models for classification. Besides SPDCs, a set of training data must be defined to create a classifier. Therefore, 20 individual image pixels were selected and assigned to the elemental distributions of both ³¹P and ¹⁹⁵Pt within tissue using the Dataset Editor. The set of SPDCs along with the training data were loaded in the Decision Forest Training Engine for classification (R: 0.5, no. of trees: 75).

SPDC-based principal component analysis (PCA), hierarchical cluster analysis (HCA) and k-Means cluster analysis were applied to verify the RDF-based results. Further details on the definition of SPDCs, standardization and application of multivariate statistics to the MSMMI datasets, as well as introductions to the different statistical methods can be found elsewhere ^{13 15}.

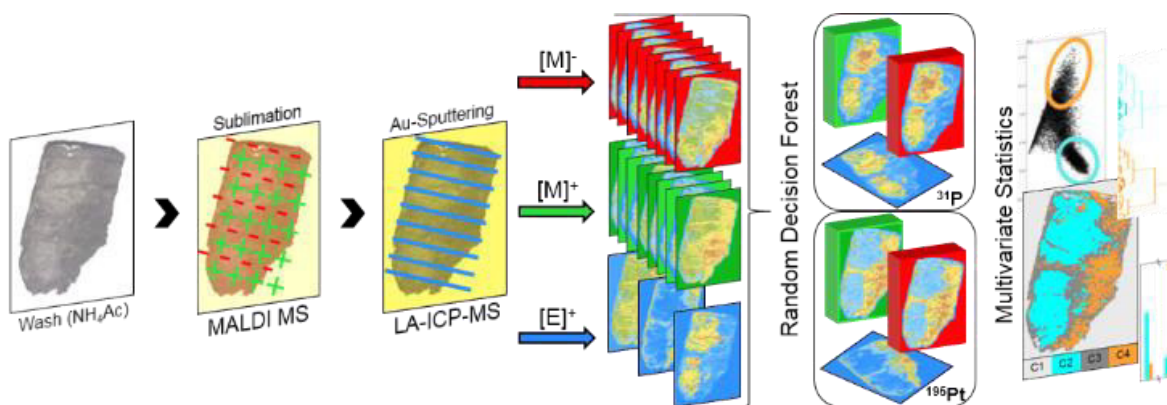


Figure 1: Scheme of a MSMMI workflow.

RESULTS AND DISCUSSION

Evaluation of Sample Carrier and MALDI Matrix. For MSI, tissue thin-cuts are usually mounted on sample carriers providing conductive surfaces essential for sufficient analyte ionization. Thus, in the present case, ITO - coated glass slides were sought to be employed having the desired surface resistivity obligatory for MALDI. However, due to the high sensitivity of LA-ICP-MS, background signals originating from these specific glass slides for the analytes of interest (i.e., phosphorus and platinum) had to be investigated to ensure suitability for elemental analysis. In contrast, usually employed sample carriers for LA-ICP-MS are ordinary microscope glass slides or high-purity silicon wafers, which do not have the desired electric conductivity or transparency. Additionally, the absence of elements of interest in the MALDI matrix (usually polar substances with conjugated π systems required for effective UV light absorption) had to be proven to avoid contamination of the sample from this route. For the purpose of this study, a blank ITO - coated glass slide underwent the matrix sublimation protocol described in the experimental section. Single linescans with the same experimental conditions as used for the following LA-ICP-MS imaging experiments were applied and the resulting analyte signals for ^{31}P , ^{34}S , and ^{195}Pt were collected. None of the isotopes showed signals which were significantly different for the gas blank of the respective measurement series (data not shown). Therefore, it could be concluded that neither ITO - coated target surfaces nor 1,5-DAN as the MALDI matrix of choice influence the analyte signals detected during LA-ICP MS imaging.

Elemental Bioimaging. Platinum is the active moiety of the administered drug cisplatin and thus, its distribution within the malignant pleural mesothelioma (MPM) samples needed to be determined to obtain insights into the uptake mechanism of the drug. Applying a lateral resolution of 40 μm provided a good tradeoff between minimal measurement time and good information content for medical interpretation. Only three elements of interest were investigated using this technique, namely sulphur (^{34}S), phosphorus (^{31}P), and platinum (^{195}Pt). While platinum served as the drug marker, sulphur and phosphorus were used as indicators for the presence of biological material. Derived elemental distribution images are shown in Figure 2.

For the sake of simplicity of the illustration, only qualitative elemental distribution images are shown in the figures; quantification of the respective elements would not essentially influence the visual appearance of the distribution images. In the used color scale, black color represents the lowest relative values while yellow/white color represents the highest relative values. In between, colors blue (medium-low), red/purple (medium) and orange (medium-high) along with linear mixtures of these colors are used.

While the distribution of sulphur (Figure 2b) is rather homogeneous, phosphorus (Figure 2c) and platinum (Figure 2d) show distinct distribution patterns indicating different histological sub-structures

of the tissue sample. This assumption is confirmed when comparing the elemental distributions with the hematoxylin stain of a consecutive thin-cut (Figure 2e).

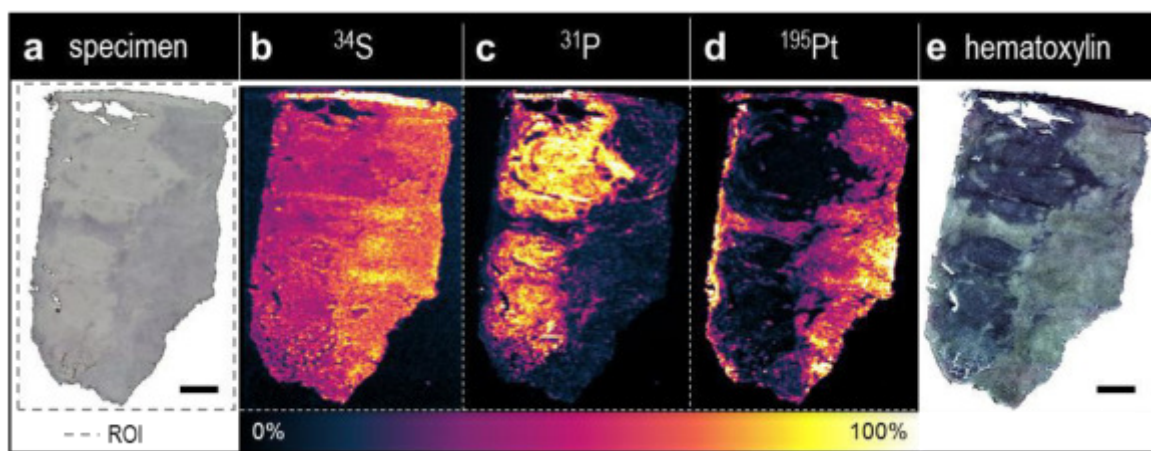


Figure 2: Microscopic image of the investigated sample (a), elemental distributions of sulphur (b), phosphorus (c), and platinum (d), and a consecutive tissue section of the same tumor after hematoxylin staining (e). Scale bar is 1mm.

Blue areas indicate viable tumor areas within the tissue while unstained regions presumably correspond to already recovered tissue. Distributions of phosphorus and platinum correlate well with this staining, where phosphorus is enriched in the viable tumor areas and platinum shows higher concentrations in the remaining areas of the sample. While the origin of the platinum signal is clear, no further information on the nature of phosphorus can be obtained using elemental bioimaging. Thus, molecular bioimaging capable of detecting larger intact molecules was required to answer this open question.

Molecular Bioimaging. Phospholipids are preferentially detected as either positive or negative ions depending on the headgroup of the different classes. Phosphatidylcholine (PC) and sphingomyelin (SM) lipids contain positively charged headgroups, whereas phosphatidylethanolamine (PE) and phosphatidylinositol (PI) are present in permanently neutral or negative charge states. Thus, for comprehensive analyses, MALDI MSI studies have to be performed in both, negative- and positive-ion mode to gain maximum information depth of phospholipid distributions within a single tissue section. For accurate analyte correlation ablation from the same tissue section is highly favorable, therefore the tissue section was ablated by LA-ICP-MS after MALDI MS analyses. The overall workflow is depicted in Figure 1 and examples of acquired analyte ion distributions are shown in Figure 3.

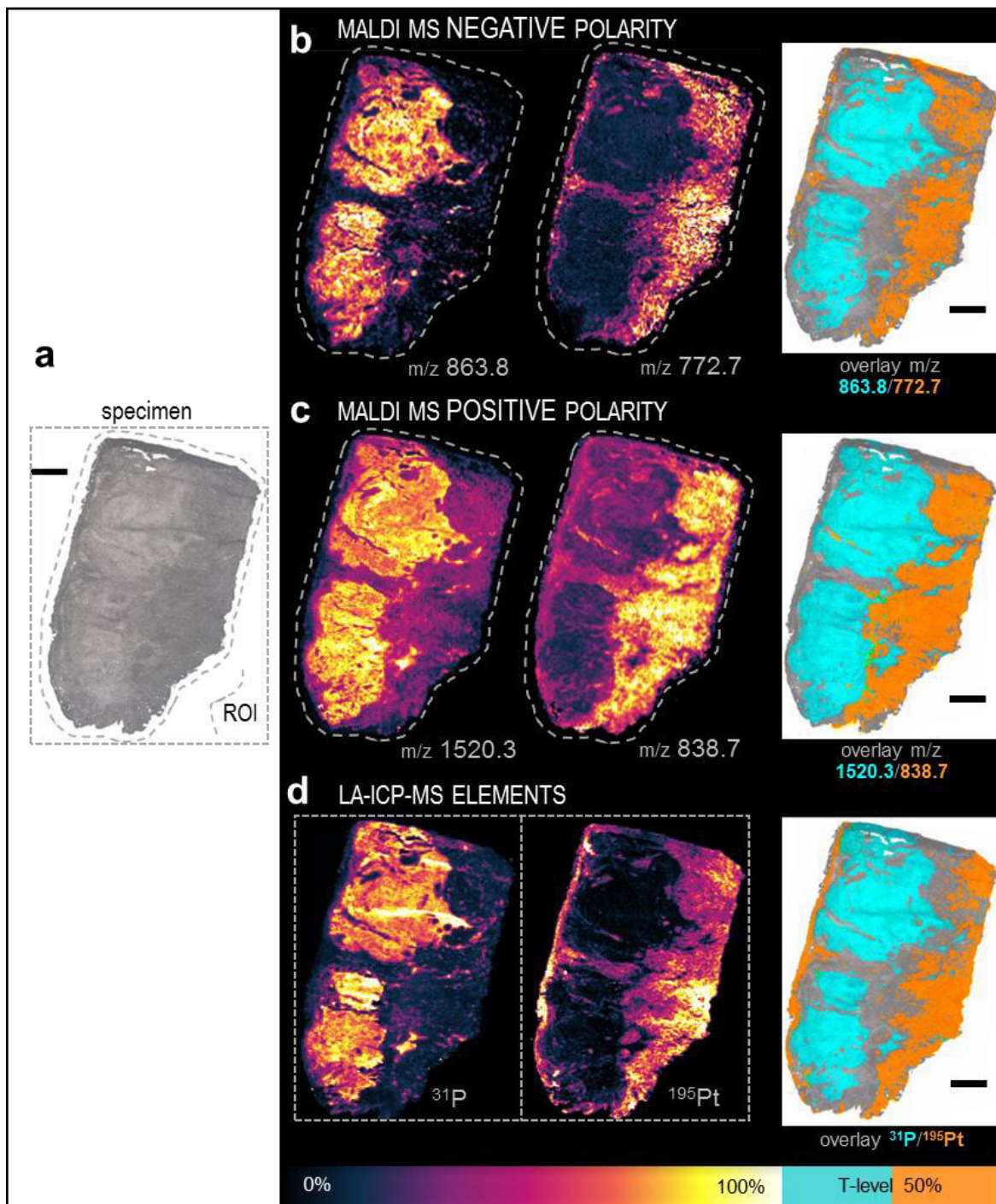


Figure 3: Microscopic image of a consecutive thin-cut showing rectangular and polygonal regions of interest (ROI) for LA-ICP-MS and MALDI MS imaging experiments, respectively (a), negative ion intensity distributions of m/z 772.7 and 863.8 (b), positively charged ions of m/z 838.7 and 1520.3 (c) as well as elemental distributions of phosphorus and platinum (d), all data collected from one tissue sample. Overlays of ion distributions are represented at an intensity threshold level of 50%, scale bar is 1 mm.

As two different samples have been used for obtaining the elemental distribution images shown in Figs. 2 and 3, the respective distribution images differ slightly. Even though thin-cuts from the very same tumor sample have been used, variations may occur due to the cryo-cutting process, which lead to negligible differences even between two consecutive samples.

Interestingly, many of the detected molecular ions quite well resemble phosphorus and platinum distributions already revealed by LA-ICP-MS imaging and hematoxylin staining. This holds true for both negative and positive MALDI MSI (see Supporting Information Figure S1 and S2 for profile spectra). Especially masses acquired with negative polarity correlate well with distributions of phosphorus and platinum. Contrarily, in the positive ion mode, ion distributions correlating with the elemental distribution of phosphorus are exclusively found in the higher mass range (1400 – 1650 Da). Due to the nature of their ionization it can be certainly assumed that these m/z values represent phospholipid dimers which are usually formed at higher concentrations of the species in the sample during the MALDI process. Also, the corresponding monomers can be identified in the respective mass spectra.

MALDI Tandem MS (MS^2) Analysis. Analyte identification in the viable tumor area is of special interest to confirm the supposed presence of phospholipids. One of the most critical issues in MALDI TOF-based MSI is the fact, that analyte concentrations per pixel are extremely low usually resulting in fragment ion spectra of poor quality (S/N, mass accuracy). In addition, not only the most abundant analyte is desorbed and ionized from each measured spot but numerous components of low abundance in the given ion selection window (± 2 Da) increase the number of background signals which ultimately results in MS^2 spectra exhibiting mixed structural information. A workaround is high-resolution mass spectrometry (HRMS) or tissue lysis in combination with LC- MS^2 to isolate and identify analytes. Yet, HRMS was not available and LC-MS is an inadequate approach if lateral distribution information is needed. Therefore, MALDI MS^2 was performed directly from tissue for selected mass values with high abundances giving insight into the structural nature of the detected lipids. Examples are shown in Figure S3, where MS^2 spectra of m/z 861.8 and 863.8 (negative ion mode) exhibit fragments corresponding to phosphatidylinositols (PIs). An exemplary MS^2 spectrum of m/z 1520.3 in Figure S4 proofs the presence of lipid dimers in the higher mass range ($m/z > 1000$).

Multi-Sensor Multi-Modal Imaging (MSMMI) of MPM tissue. Imaging by LA-ICP-MS and MALDI MS delivered valuable insights in the morphological nature of the present tumor sample and the respective platinum interaction. To further increase information depth, an integrated data evaluation approach was prospected. For this task, the very same tissue sample already analyzed by MALDI MSI was also measured using LA-ICP-MS.

As some tissue material is assumed to be ablated during the MALDI MS analysis, quantification of the platinum content in this sample seemed to be doubtful. Additionally, the washing step of the sample prior to MALDI-MSI analysis might lead a wash-out of metals which are only loosely bound to the biological matrix. Such effect has already been reported in an earlier study and was observed especially for alkaline metals ¹⁶.

Validity of the used quantification approach for platinum in tissue thin-cuts has already been demonstrated earlier by a comparison of values obtained by this approach with bulk platinum concentrations determined by liquid ICP-MS after acid digestion of samples ¹².

To obtain an estimate for the validity of the quantification, the average platinum content found in this sample was compared to the one found in the sample which had only been analyzed using LA-ICP-MS.

For this, all pixels from the respective sample area were averaged to obtain a mean value for the platinum concentration. While the MPM section analyzed by LA-ICP-MS alone only yielded 1.75 µg platinum/g tissue, the MPM section analyzed by MALDI MS prior to LA-ICP-MS showed an average of 1.91 µg/g. Given the fact that consecutive sections potentially differ in cell content, tumor morphology and section thickness due to cryo-sectioning, the relative deviation of less than 10% between the two averages can be considered to be negligible. Thus, it can be stated that MALDI MSI analysis does not ablate significant amounts of platinum from the tissue sample allowing to obtain reliable quantitative distribution maps of elements even from a sample already analyzed by MALDI MSI. Furthermore, the results indicate that the washing step prior to MALDI-MS analysis does not lead to a significant decrease of the average platinum concentration in the tissue.

Data Evaluation of Multi-Modal Distribution Images. In total, 94 SPDCs have been created based on the MSMMI data set comprising LA-ICP-MS data and MALDI MS data from both polarities. Of these, RDF-based classification exhibited 59 m/z values from MALDI MSI showing a correspondence to either the phosphorus or the platinum distribution pattern within the tissue. The list of SPDCs with their spectrometric background information is given in Figure S5 along with their ion distributions within the MPM tissue section (Figure S6). The list comprises 61 SPDCs, 2 of elemental and 59 of molecular origin.

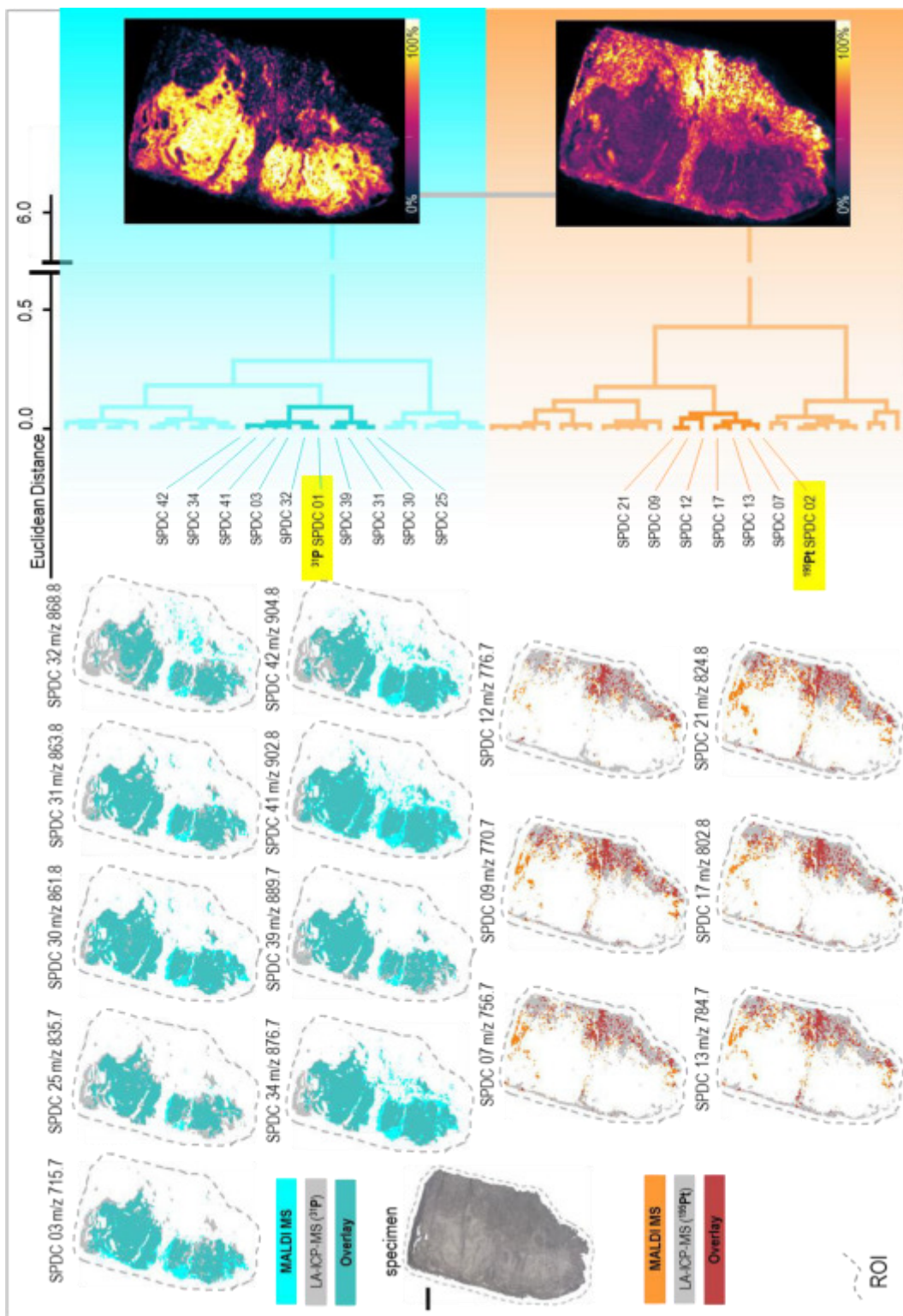


Figure 4: Cluster analysis of the loadings of the first 2 principal components reveals two sub-clusters (right side), elemental and molecular ion overlays are shown representing an intensity threshold level of 50% (cyan: phosphorus related m/z, orange: platinum related m/z, grey: ^{195}Pt and ^{31}P), scale bar length corresponds to 1mm

Of the 59 used m/z values derived from MALDI MSI, 30 corresponded to the phosphorus distribution pattern (all detected in the negative ion mode) and 29 corresponded to the platinum distribution pattern (22 detected in the negative and 7 in the positive ion mode). It has to be pointed out here, that in order not to bias the information content of the data set by duplication of information, signals of lipid dimers were excluded from analysis.

To verify the RDF-based classification approach, further chemometric analysis was applied to the MSMMI dataset. Results of the PCA are shown in Figure S7. The plotted loadings of PCs 1 and 2 clearly distinguish the analyte distributions related to phosphorus and platinum (encircled in cyan and orange, respectively).

After defining the most significant contributors to the variance of the combined dataset, hierarchical cluster analysis (HCA) of the loadings of the PCA could be performed. In Figure 4, the two resulting sub-clusters of the HCA show a distinction between the viable tumor region (phosphorus related, cyan sub-cluster) and the assumingly recovered tissue (platinum related, orange sub-cluster).

Thus, HCA was able to confirm the correlation of analytes detected by MALDI MSI with the elemental distributions of phosphorus and platinum. In Figure 4, those m/z values directly clustering with the two elements are shown as overlays with the respective elemental distribution of phosphorus and platinum. Complete information is given in Figure S8 of the Supporting Information.

When performing k-Means Clustering, a number of clusters has to be assumed prior to the calculations. Here, 4 clusters were selected as the target number. This number is based on visual examination of the Score-Plots shown in Figure S9, which suggests the occurrence of 4 major clusters. Results of k-Means Clustering are shown in Figure S10. Accordingly, results from the k-Means cluster analysis could be combined with the results from PCA and HCA of the PCA, as shown in Figure 5. Clusters 2 and 4 from the k-Means Clustering are shown in Figure 5c. They clearly resemble the elemental distributions of phosphorus and platinum as shown in Figure 5a in cyan and orange, respectively. Further comparability is given with the sub-cluster of the HCA of the PCA loadings (Figure 5b). k-Means Clustering also allowed extracting component spectra of the viable tumor areas and the assumingly recovered tissue. The corresponding results are shown in Figure 5 (lower part). Notably, areas with viable tumor tissue (cyan) show higher abundances of phospholipid dimers in positive ion mode (Figure 5f), a finding that correlates well with the higher phosphorus signals detected in the same areas (Figure 5d). This finding supports the assumption that the higher amounts of phosphorus detected in the viable tumor areas indeed correspond to the presence of phospholipids.

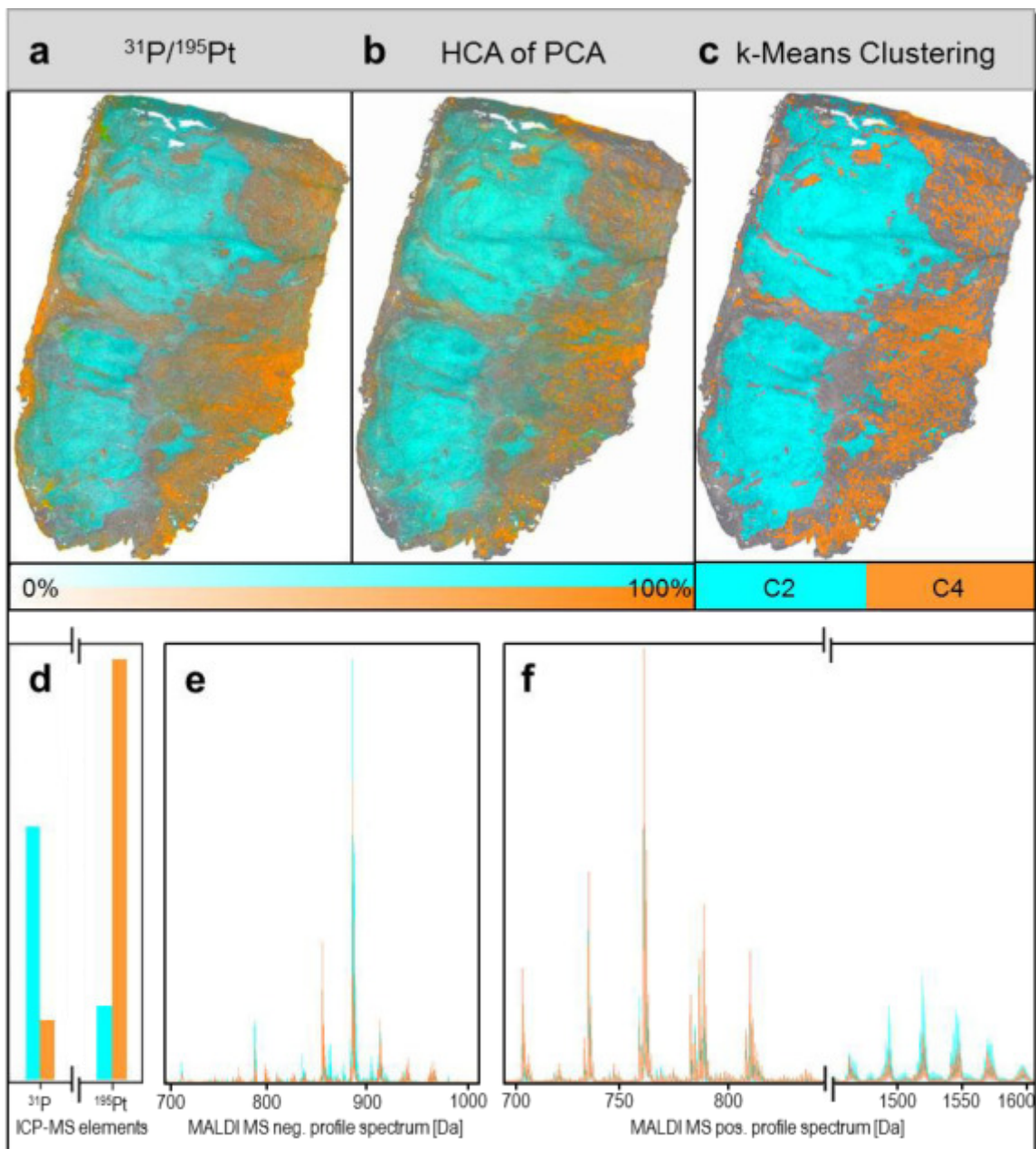


Figure 5: Superpositions of a light-microscopic image of the MPM sample and elemental distribution of $^{31}\text{P}/^{195}\text{Pt}$ (a), results from the HCA of the PCA loadings (b), and clusters 2 and 4 from k-Means Clustering; extracted cluster spectra from k-Means Clustering of the MSMMI dataset (d-f).

In contrast, the negative ion spectra (Figure 5e) do not exhibit any obvious structural differences between the two clusters. It is assumed that high phospholipid abundance in the viable tumor areas corresponds to the higher metabolic activity in these regions. However, we present a proof-of-principle study and biologically valid hypotheses can only be proposed after further studies.

CONCLUSION AND OUTLOOK

Results from this study show that the combination of multiple analysis techniques is able to enhance the information depth obtained from one sample to a great extent. Especially the combination of elemental and molecular analysis techniques offers advantages as the results are truly complementary, more accurate because biological variations from different tissue sections are eliminated and the obtained information is not overlapping.

We showed for the first time that it is possible to use one tissue section for both, negative and positive mode MALDI MS and subsequently measure quantitatively elemental distributions by LA-ICP-MS. This approach allowed maximum correlation of data sets in contrast to the usually performed analysis of consecutive thin cuts.

Furthermore, we present for the first time that RDF-based calculations identify numerous lipid distributions in the MALDI dataset correlating either to the phosphorus or the platinum distribution pattern. In future studies we aim at the application of our innovative methodology in medical studies providing larger sample stocks to obtain biologically relevant information. Using the presented approach, it will be possible to correlate elemental features not only with lipids but any other type of analyte, i.e. proteins, peptides, metabolites, drugs, leading to an enhanced understanding of biological processes such as tumor genesis or the mechanism of action of anti-tumor drugs.

AUTHOR INFORMATION

Corresponding Author

* Martina Marchetti-Deschmann. Address: TU Wien, Institute of Chemical Technologies and Analytics, Getreidemarkt 9/164, A-1060 Vienna. Tel.: +43-1-58801- 15162. Fax: +43-1-58801-915162.

E-mail: martina.marchetti-deschmann@tuwien.ac.at

Author Contributions

· These authors contributed equally. All authors have given approval to the final version of the manuscript.

ACKNOWLEDGMENT

The authors acknowledge COST Action 1104 and the PhD program MEIBio (supported by TU Wien) for scientific exchange, personnel funding and valuable discussions. The authors further acknowledge B. Hegedus (University of Duisburg-Essen) for providing MPM sections, and highly appreciate the support of G. Allmaier (TU Wien) for granting access to instrumentation.

REFERENCE

1. J. S. Becker, M. Zoriy, A. Matusch, B. Wu, D. Salber, C. Palm, J. S. Becker, *Mass Spectrom. Rev.* 2009, *29*. 156-175, DOI: 10.1002/mas.20239.
2. D. Drescher, C. Giesen, H. Traub, U. Panne, J. Kneipp, N. Jakubowski, *Anal. Chem. (Washington, DC, U. S.)* 2012, *84*. 9684-9688, DOI: 10.1021/ac302639c.
3. K. Dreisewerd, *Anal. Bioanal. Chem.* 2014, *406*. 2261-2278, DOI: 10.1007/s00216-014-7646-6.
4. B. Spengler, *Anal. Chem. (Washington, DC, U. S.)* 2015, *87*. 64-82, DOI: 10.1021/ac504543v.
5. J. A. Hankin, R. M. Barkley, R. C. Murphy, *J. Am. Soc. Mass Spectrom.* 2007, *18*. 1646-1652, DOI: 10.1016/j.jasms.2007.06.010.
6. W. Bouschen, O. Schulz, D. Eikel, B. Spengler, *Rapid Commun. Mass Spectrom.* 2010, *24*. 355-364, DOI: 10.1002/rcm.4401.
7. J. Yang, R. M. Caprioli, *Anal. Chem. (Washington, DC, U. S.)* 2011, *83*. 5728-5734, DOI: 10.1021/ac200998a.
8. A.-C. Niehoff, J. Schulz, J. Soltwisch, S. Meyer, H. Kettling, M. Sperling, A. Jeibmann, K. Dreisewerd, K. A. Francesconi, T. Schwerdtle, U. Karst, *Anal. Chem. (Washington, DC, U. S.)* 2016, *88*. 5258-5263, DOI: 10.1021/acs.analchem.6b00333.
9. R. Gonzalez de Vega, M. L. F. Sanchez, N. Eiro, F. J. Vizoso, M. Sperling, U. Karst, A. S. Medel, *Anal. Bioanal. Chem.* 2017. Ahead of Print, DOI: 10.1007/s00216-017-0537-x.
10. M. Holzlechner, in *Mass Spec Forum Vienna*, 2016.
11. M. Bonta, H. Lohninger, M. Marchetti-Deschmann, A. Limbeck, *Analyst (Cambridge, U. K.)* 2014, *139*. 1521-1531, DOI: 10.1039/c3an01511d.
12. M. Bonta, H. Lohninger, V. Laszlo, B. Hegedus, A. Limbeck, *J. Anal. At. Spectrom.* 2014, *29*. 2159-2167, DOI: 10.1039/C4JA00245H.
13. H. Lohninger, J. Ofner, *Spectrosc. Eur.* 2014, *26*. 6-10.
14. H. Lohninger, K. Varmuza, *Anal. Chem.* 1987, *59*. 236-44, DOI: 10.1021/ac00129a005.
15. J. Ofner, K. A. Kamilli, E. Eitenberger, G. Friedbacher, B. Lendl, A. Held, H. Lohninger, *Anal. Chem. (Washington, DC, U. S.)* 2015, *87*. 9413-9420, DOI: 10.1021/acs.analchem.5b02272.
16. M. Bonta, S. Toeroek, B. Hegedus, B. Doeme, A. Limbeck, *Anal. Bioanal. Chem.* 2017, *409*. 1805-1814, DOI: 10.1007/s00216-016-0124-6.

Supporting Information

Multi-sensor Imaging– from sample preparation to integrated multi-modal interpretation of LA-ICP-MS and MALDI MS imaging data

Matthias Holzlechner[†], Maximilian Bonta[†], Hans Lohningert[†], Andreas Limbeck[†], Martina Marchetti-Deschmann^{†*}

[†]Institute of Chemical Technologies and Analytics, TU Wien, Getreidemarkt 9, 1060 Vienna, Austria.

MALDI MSI profile spectra

Figure S1

- MALDI negative profile spectrum

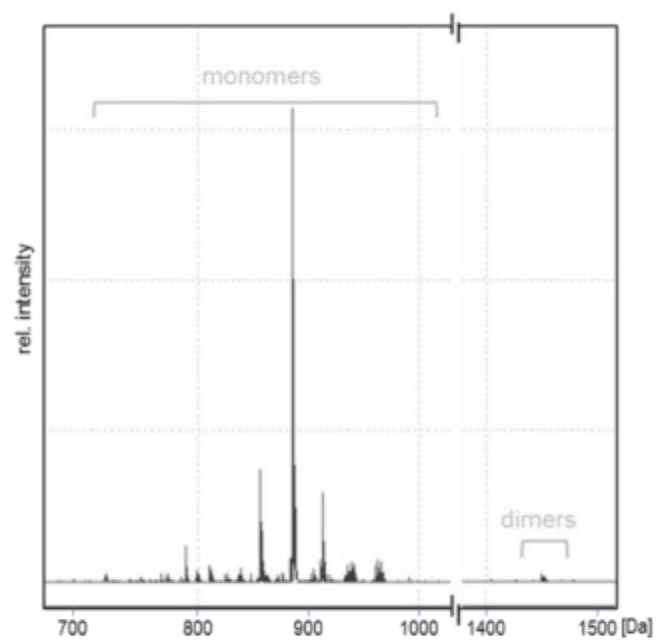


Figure S2

- MALDI positive profile spectrum

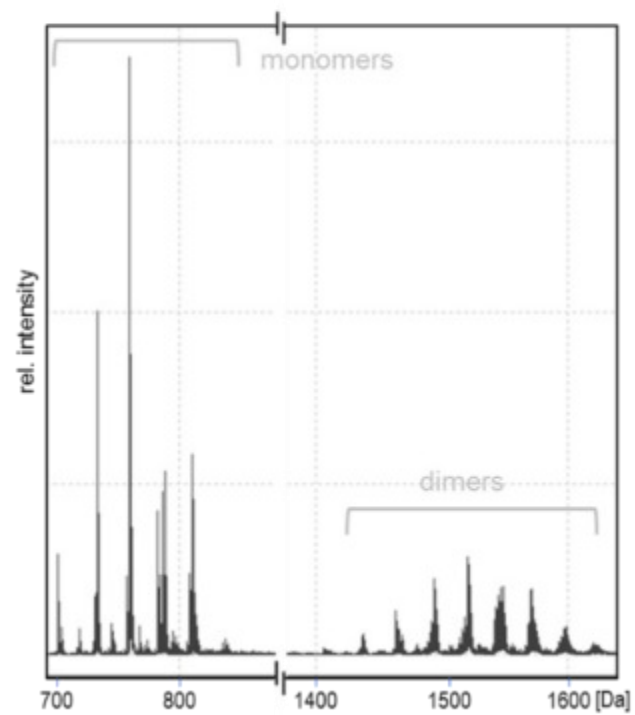


Figure S3 MALDI MS² of Lipid Monomers m/z 861.8, 863.8

m/z 861.8 PI (36:1)
PI (18:0/18:1)

m/z 863.8 PI (36:2)
PI (18:0/18:2)
(18:1/18:1)

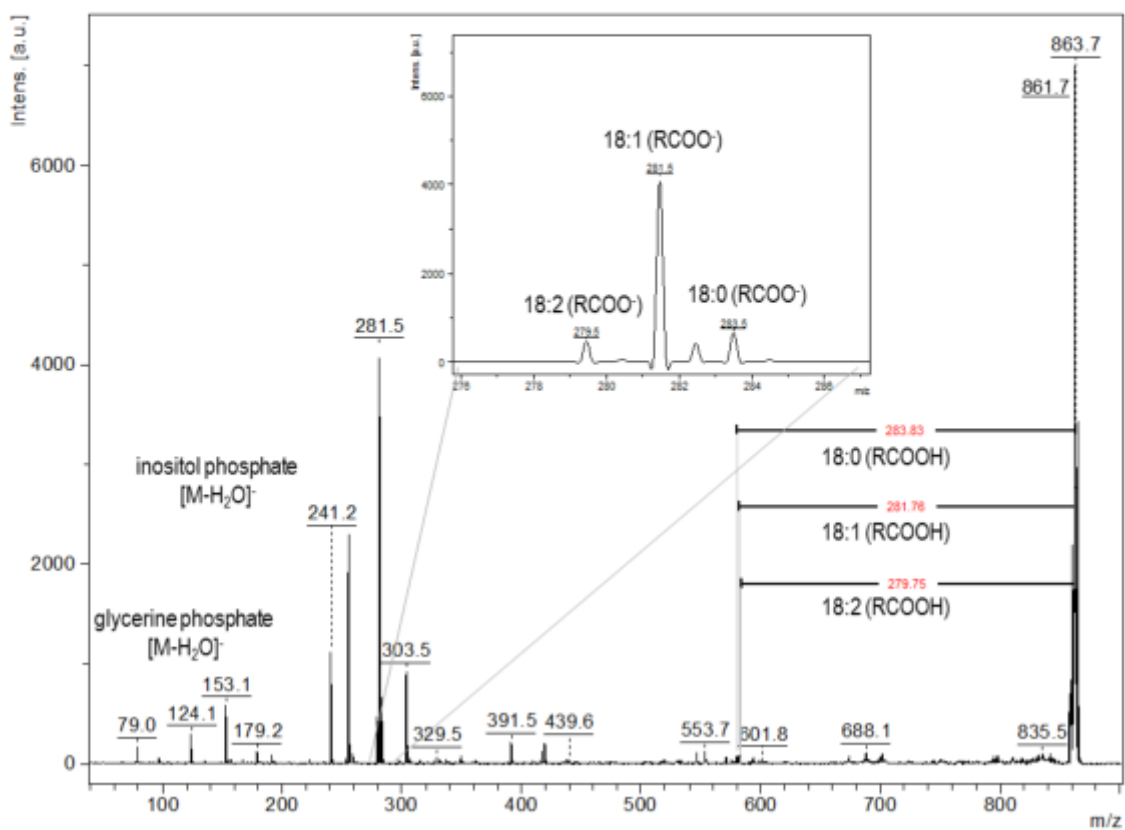


Figure S4 MALDI MS² of Lipid Dimer m/z 1520.3

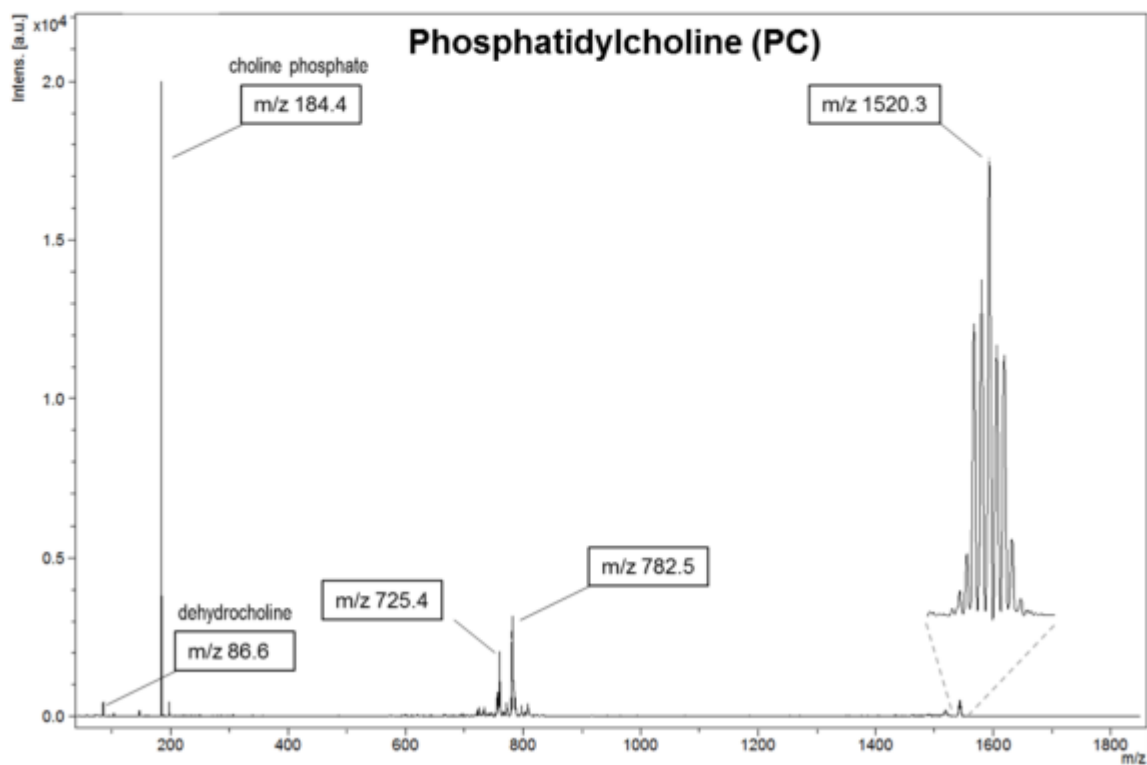


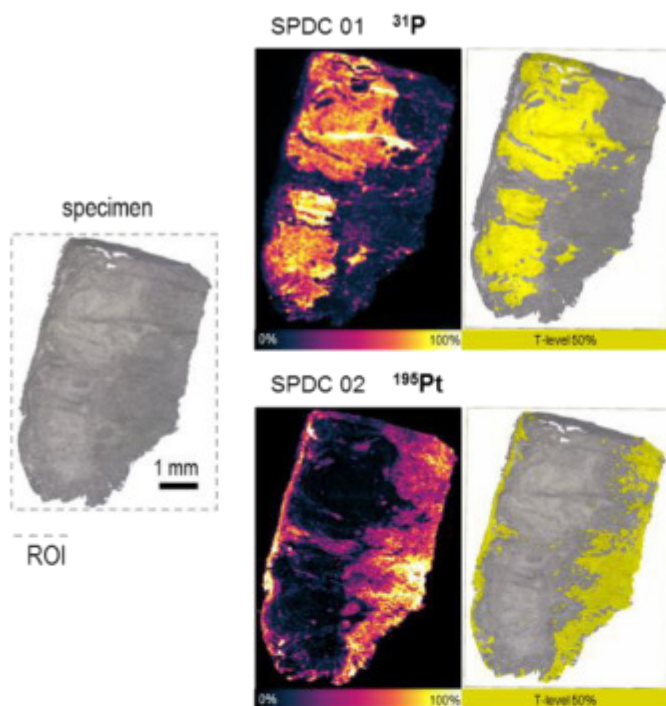
Figure S5

List of Spectral Descriptors (SPDCs)

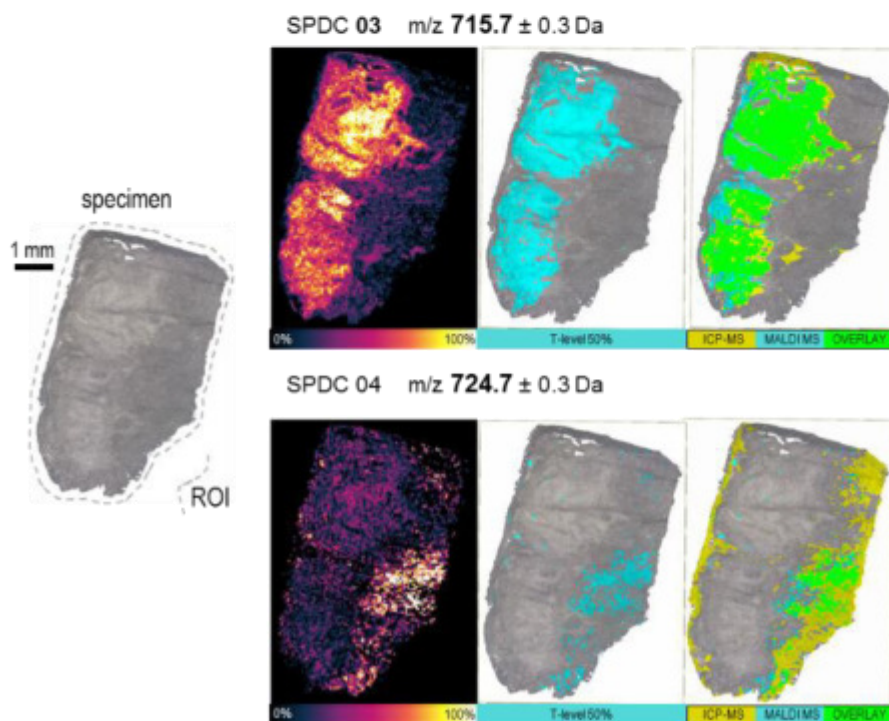
SPDCs	MS spectral type	cube
SPDC 01 ²¹ P	Single ions	ICPMS
SPDC 02 ¹⁹⁹ Pt	Single ions	ICPMS
SPDC 03 m/z 715.7 ± 0.3 Da	Neg. Data	MALDI
SPDC 04 m/z 724.7 ± 0.3 Da	Neg. Data	MALDI
SPDC 05 m/z 747.7 ± 0.3 Da	Neg. Data	MALDI
SPDC 06 m/z 748.8 ± 0.3 Da	Neg. Data	MALDI
SPDC 07 m/z 756.7 ± 0.3 Da	Neg. Data	MALDI
SPDC 08 m/z 760.7 ± 0.3 Da	Neg. Data	MALDI
SPDC 09 m/z 770.7 ± 0.3 Da	Neg. Data	MALDI
SPDC 10 m/z 772.7 ± 0.3 Da	Neg. Data	MALDI
SPDC 11 m/z 774.7 ± 0.3 Da	Neg. Data	MALDI
SPDC 12 m/z 776.7 ± 0.3 Da	Neg. Data	MALDI
SPDC 13 m/z 784.7 ± 0.3 Da	Neg. Data	MALDI
SPDC 14 m/z 785.7 ± 0.3 Da	Neg. Data	MALDI
SPDC 15 m/z 788.8 ± 0.3 Da	Neg. Data	MALDI
SPDC 16 m/z 800.8 ± 0.3 Da	Neg. Data	MALDI
SPDC 17 m/z 802.8 ± 0.3 Da	Neg. Data	MALDI
SPDC 18 m/z 809.7 ± 0.3 Da	Neg. Data	MALDI
SPDC 19 m/z 816.8 ± 0.3 Da	Neg. Data	MALDI
SPDC 20 m/z 820.8 ± 0.3 Da	Neg. Data	MALDI
SPDC 21 m/z 824.8 ± 0.3 Da	Neg. Data	MALDI
SPDC 22 m/z 826.8 ± 0.3 Da	Neg. Data	MALDI
SPDC 23 m/z 828.7 ± 0.3 Da	Neg. Data	MALDI
SPDC 24 m/z 833.7 ± 0.3 Da	Neg. Data	MALDI
SPDC 25 m/z 835.7 ± 0.3 Da	Neg. Data	MALDI
SPDC 26 m/z 837.7 ± 0.3 Da	Neg. Data	MALDI
SPDC 27 m/z 846.9 ± 0.3 Da	Neg. Data	MALDI
SPDC 28 m/z 855.7 ± 0.3 Da	Neg. Data	MALDI
SPDC 29 m/z 857.8 ± 0.3 Da	Neg. Data	MALDI
SPDC 30 m/z 861.8 ± 0.3 Da	Neg. Data	MALDI
SPDC 31 m/z 863.8 ± 0.3 Da	Neg. Data	MALDI
SPDC 32 m/z 868.8 ± 0.3 Da	Neg. Data	MALDI
SPDC 33 m/z 870.8 ± 0.3 Da	Neg. Data	MALDI
SPDC 34 m/z 876.7 ± 0.3 Da	Neg. Data	MALDI
SPDC 35 m/z 880.7 ± 0.3 Da	Neg. Data	MALDI
SPDC 36 m/z 881.7 ± 0.3 Da	Neg. Data	MALDI
SPDC 37 m/z 883.7 ± 0.3 Da	Neg. Data	MALDI
SPDC 38 m/z 887.7 ± 0.3 Da	Neg. Data	MALDI
SPDC 39 m/z 889.7 ± 0.3 Da	Neg. Data	MALDI
SPDC 40 m/z 896.7 ± 0.3 Da	Neg. Data	MALDI
SPDC 41 m/z 902.8 ± 0.3 Da	Neg. Data	MALDI
SPDC 42 m/z 904.8 ± 0.3 Da	Neg. Data	MALDI
SPDC 43 m/z 915.8 ± 0.3 Da	Neg. Data	MALDI
SPDC 44 m/z 918.8 ± 0.3 Da	Neg. Data	MALDI
SPDC 45 m/z 934.8 ± 0.3 Da	Neg. Data	MALDI
SPDC 46 m/z 940.9 ± 0.3 Da	Neg. Data	MALDI
SPDC 47 m/z 942.8 ± 0.3 Da	Neg. Data	MALDI
SPDC 48 m/z 960.8 ± 0.3 Da	Neg. Data	MALDI
SPDC 49 m/z 962.8 ± 0.3 Da	Neg. Data	MALDI
SPDC 50 m/z 967.9 ± 0.3 Da	Neg. Data	MALDI
SPDC 51 m/z 980.8 ± 0.3 Da	Neg. Data	MALDI
SPDC 52 m/z 1068.7 ± 0.3 Da	Neg. Data	MALDI
SPDC 53 m/z 1096.7 ± 0.3 Da	Neg. Data	MALDI
SPDC 54 m/z 1261.9 ± 0.3 Da	Neg. Data	MALDI
SPDC 55 m/z 782.8 ± 0.3 Da	Pos. Data	MALDI
SPDC 56 m/z 788.8 ± 0.3 Da	Pos. Data	MALDI
SPDC 57 m/z 808.7 ± 0.3 Da	Pos. Data	MALDI
SPDC 58 m/z 810.7 ± 0.3 Da	Pos. Data	MALDI
SPDC 59 m/z 812.7 ± 0.3 Da	Pos. Data	MALDI
SPDC 60 m/z 836.7 ± 0.3 Da	Pos. Data	MALDI
SPDC 61 m/z 838.7 ± 0.3 Da	Pos. Data	MALDI

Figure S6

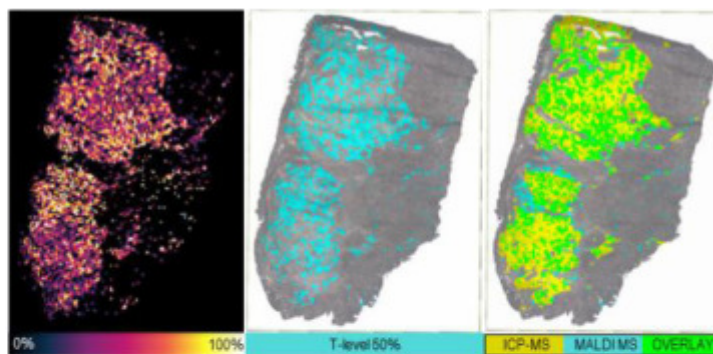
LA-ICP-MS single ions



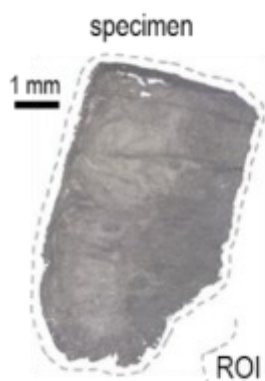
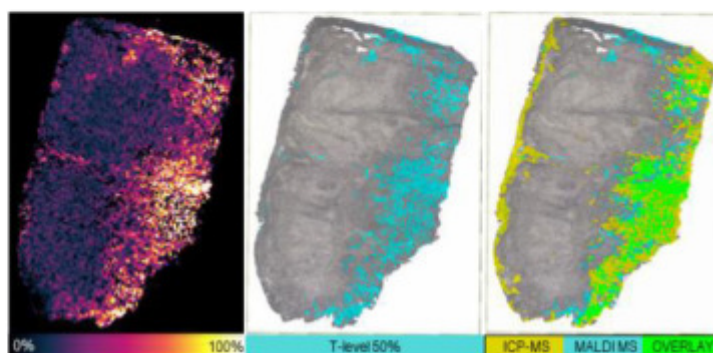
MALDI MS m/z values – negative polarity



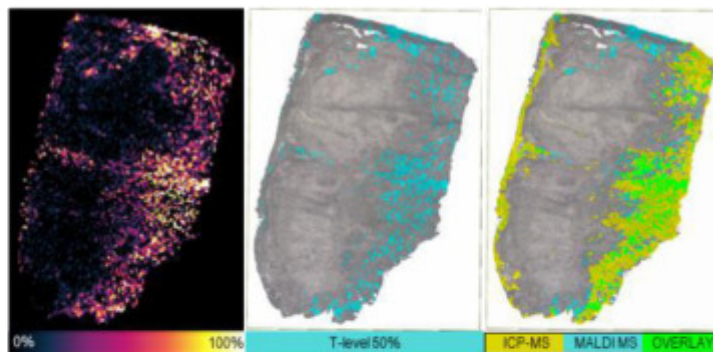
SPDC 05 m/z 747.7 \pm 0.3 Da



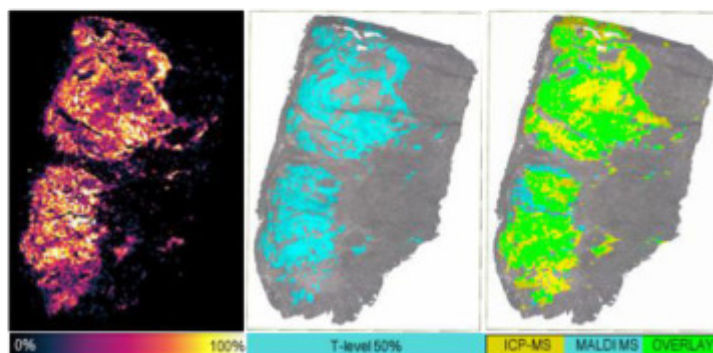
SPDC 06 m/z 748.8 \pm 0.3 Da



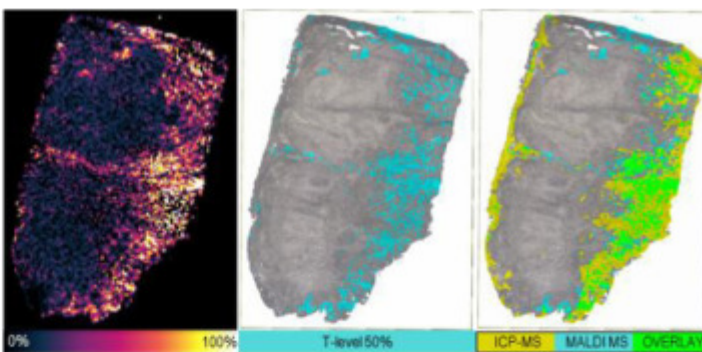
SPDC 07 m/z 756.7 \pm 0.3 Da



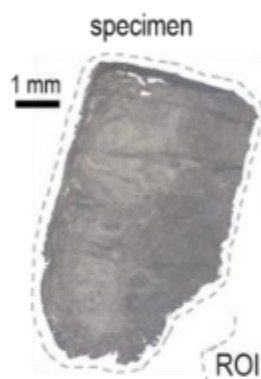
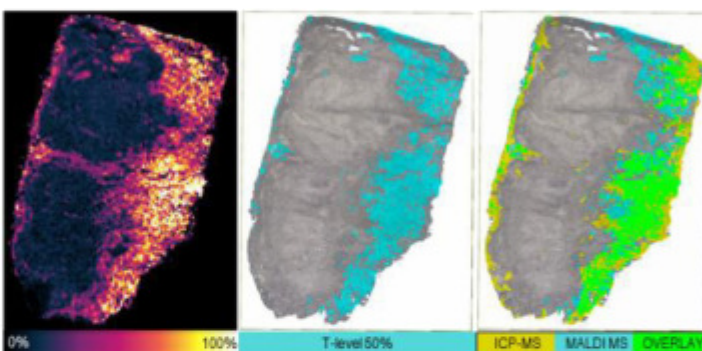
SPDC 08 m/z 760.7 \pm 0.3 Da



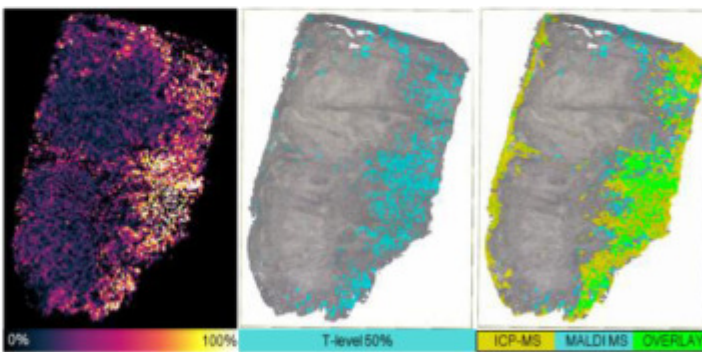
SPDC 09 m/z 770.7 \pm 0.3 Da



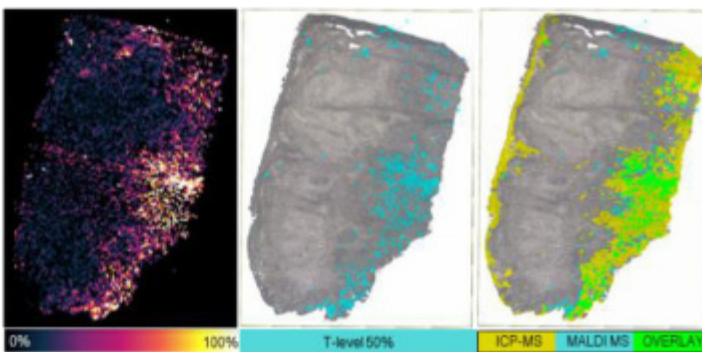
SPDC 10 m/z 772.7 \pm 0.3 Da



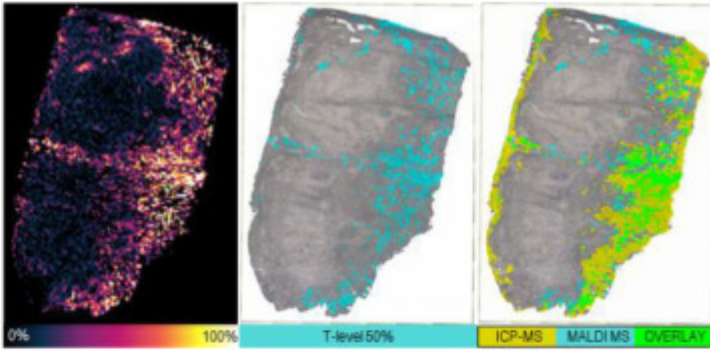
SPDC 11 m/z 774.7 \pm 0.3 Da



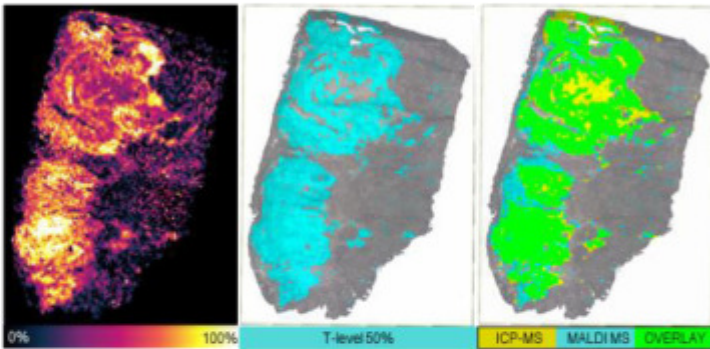
SPDC 12 m/z 776.7 \pm 0.3 Da



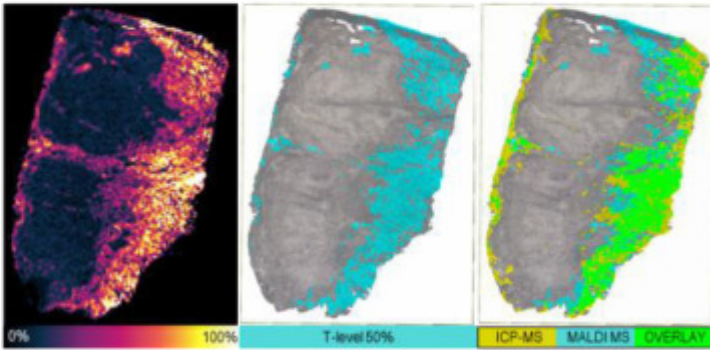
SPDC 13 m/z 784.7 \pm 0.3 Da



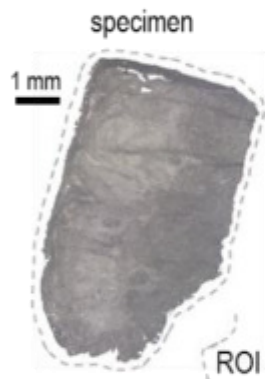
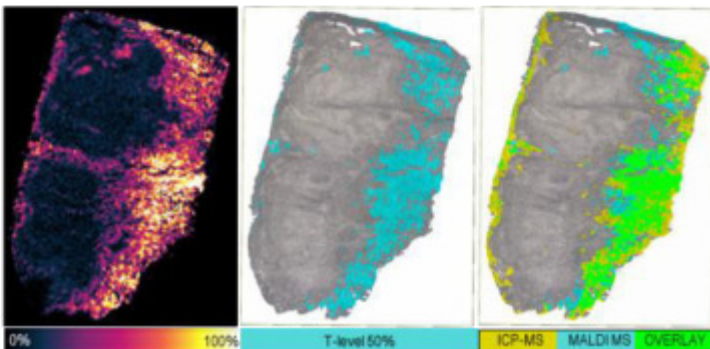
SPDC 14 m/z 786.7 \pm 0.3 Da



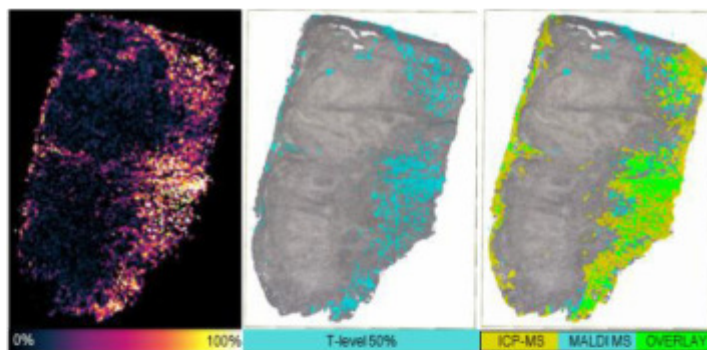
SPDC 15 m/z 798.8 \pm 0.3 Da



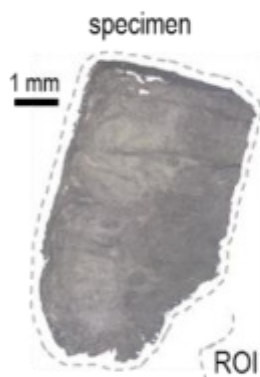
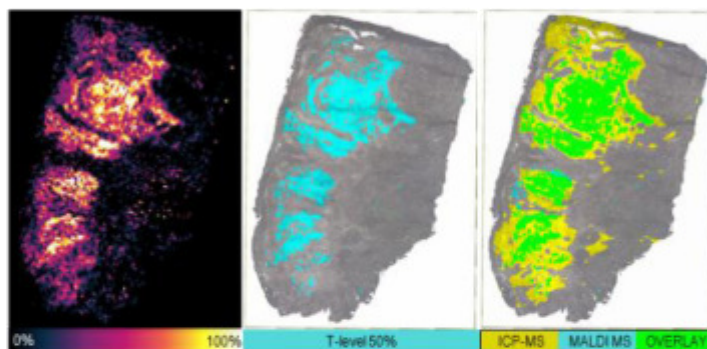
SPDC 16 m/z 800.8 \pm 0.3 Da



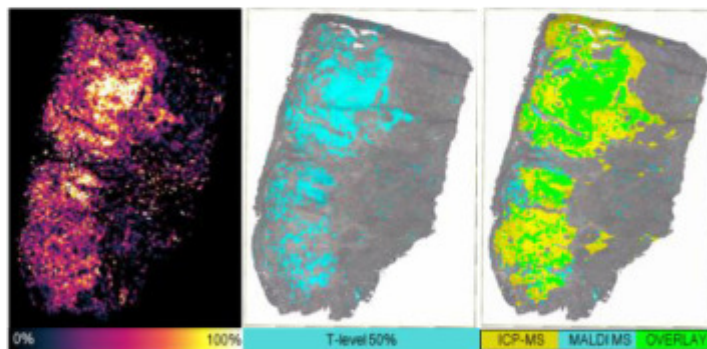
SPDC 17 m/z 802.8 \pm 0.3 Da



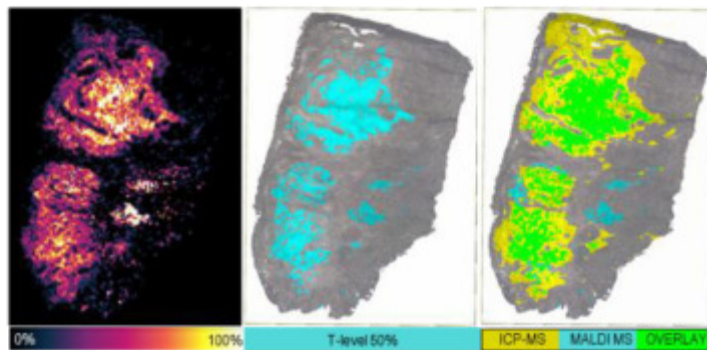
SPDC 18 m/z 809.7 \pm 0.3 Da



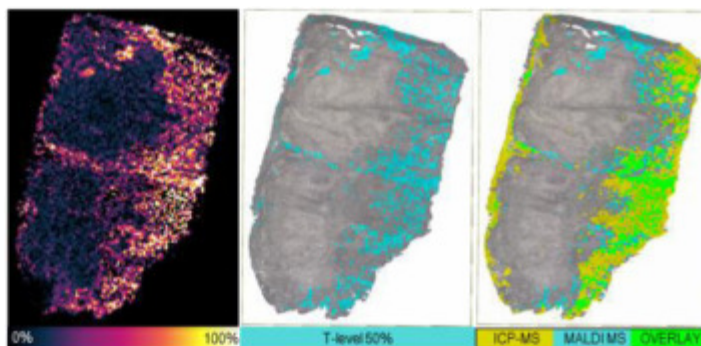
SPDC 19 m/z 816.8 \pm 0.3 Da



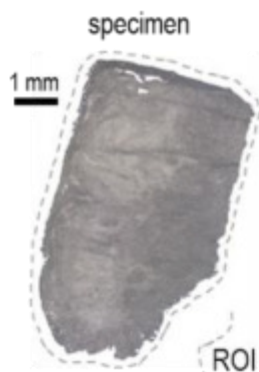
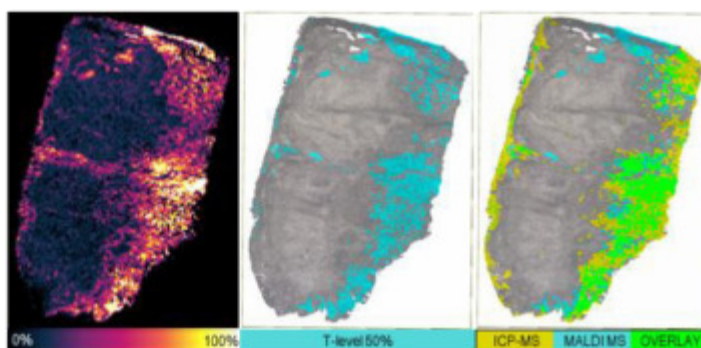
SPDC 20 m/z 820.8 \pm 0.3 Da



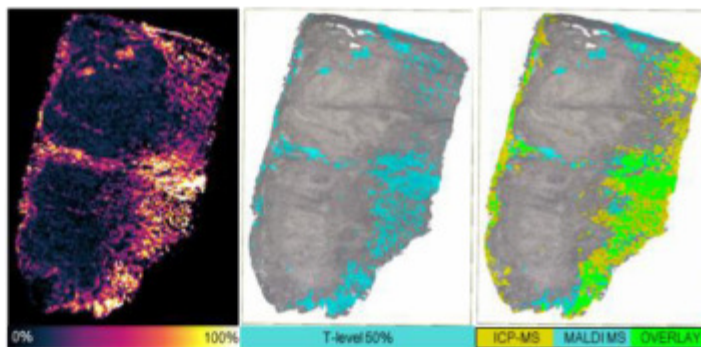
SPDC 21 m/z 824.8 ± 0.3 Da



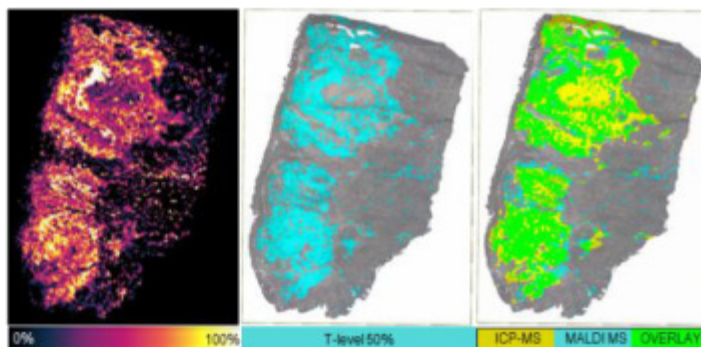
SPDC 22 m/z 826.8 ± 0.3 Da



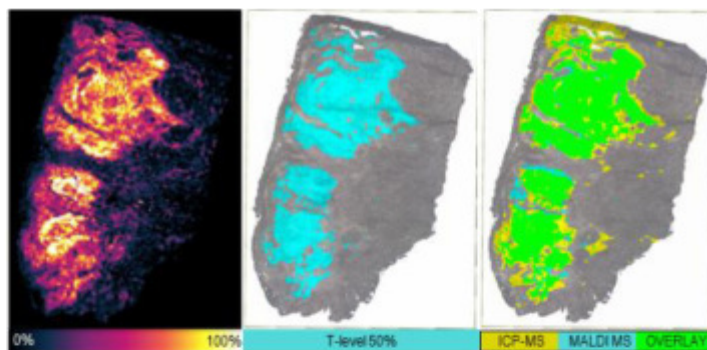
SPDC 23 m/z 828.7 ± 0.3 Da



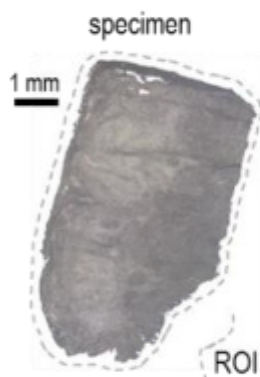
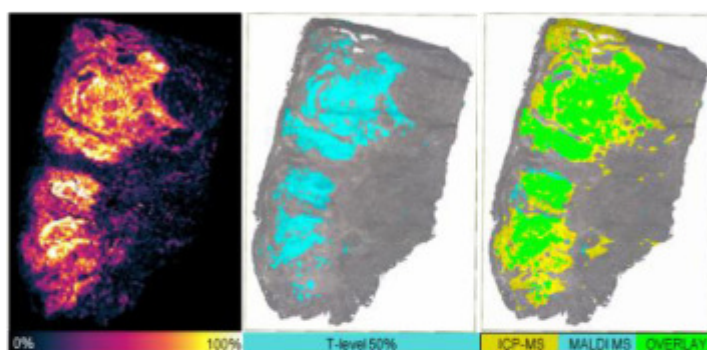
SPDC 24 m/z 833.7 ± 0.3 Da



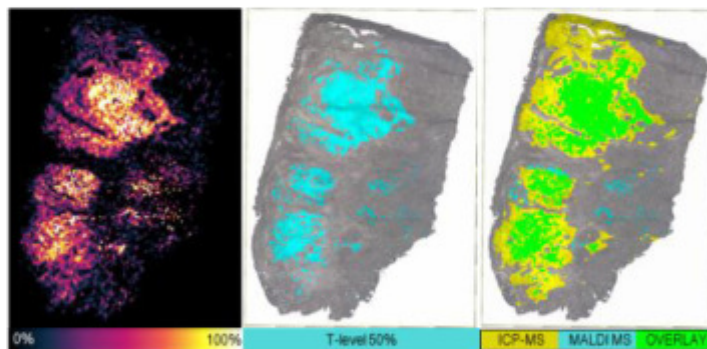
SPDC 25 m/z 835.7 ± 0.3 Da



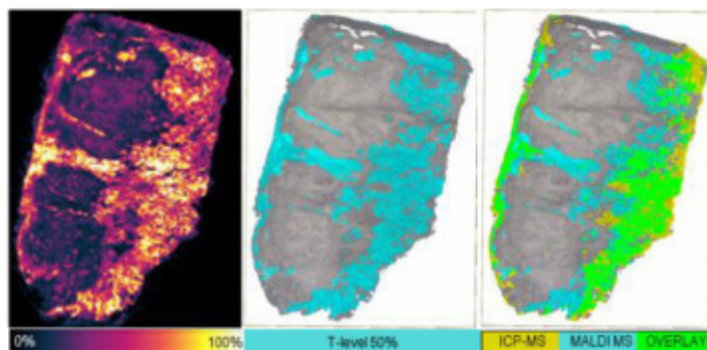
SPDC 26 m/z 837.7 ± 0.3 Da



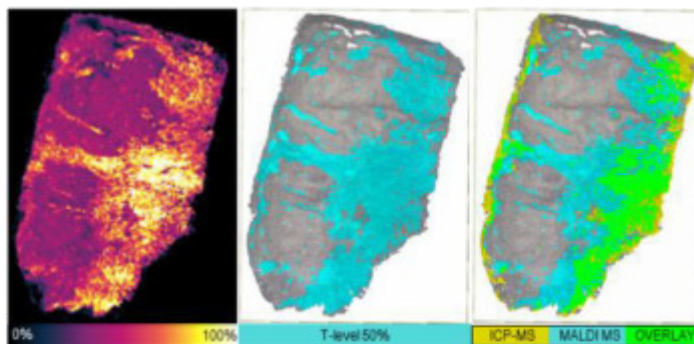
SPDC 27 m/z 846.9 ± 0.3 Da



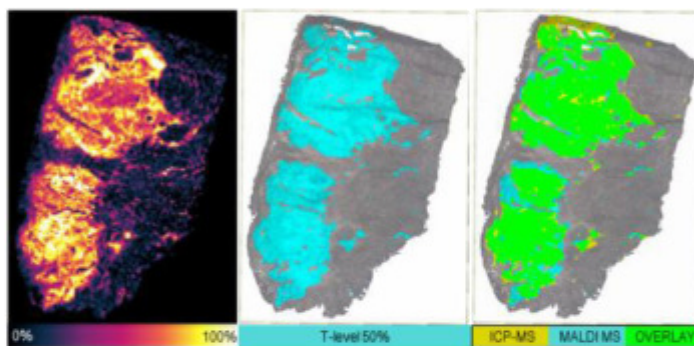
SPDC 28 m/z 855.7 ± 0.3 Da



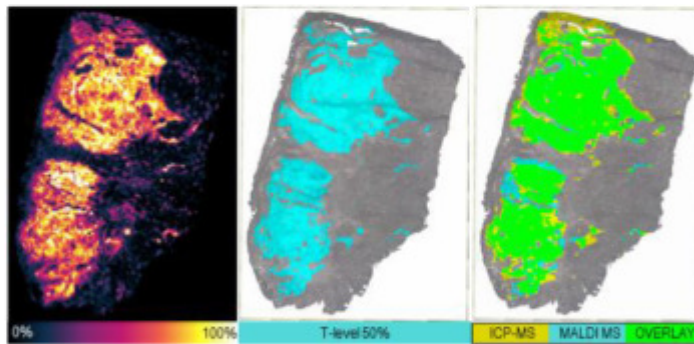
SPDC 29 m/z 857.8 ± 0.3 Da



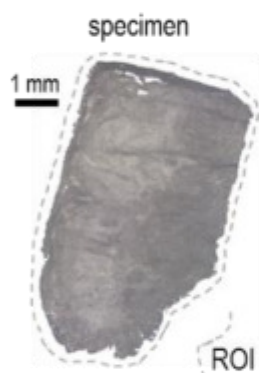
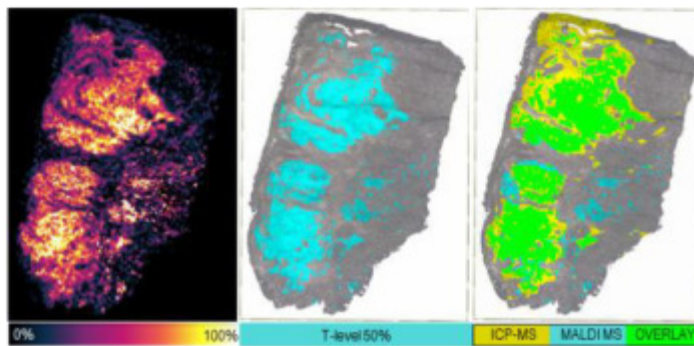
SPDC 30 m/z 861.8 ± 0.3 Da



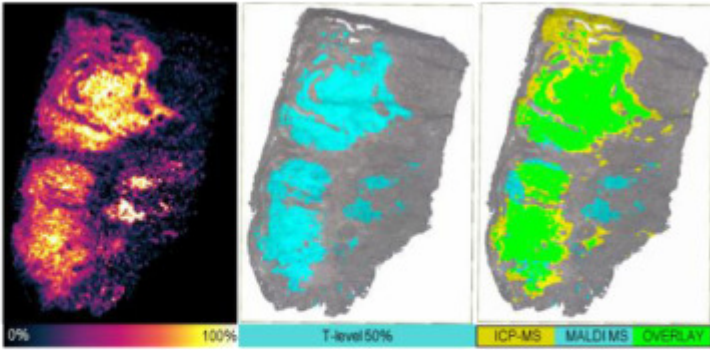
SPDC 31 m/z 863.8 ± 0.3 Da



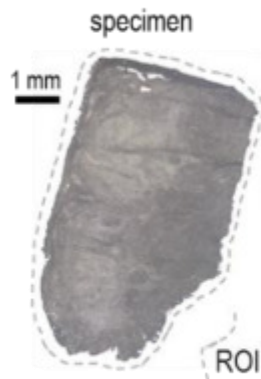
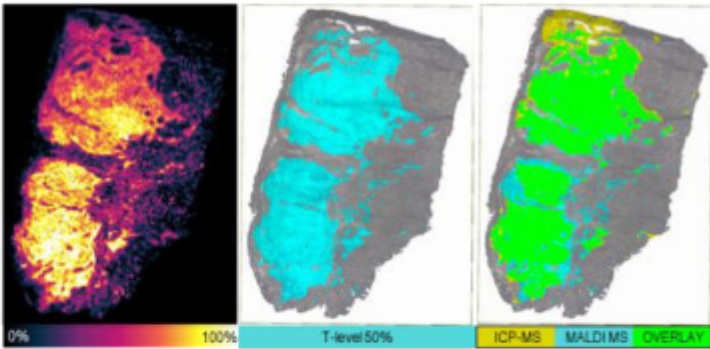
SPDC 32 m/z 868.8 ± 0.3 Da



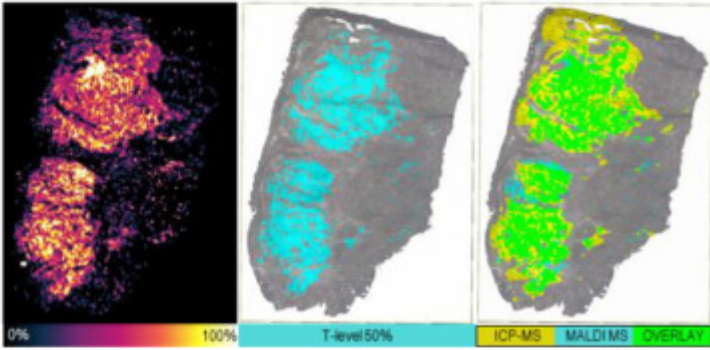
SPDC 33 m/z 870.8 ± 0.3 Da



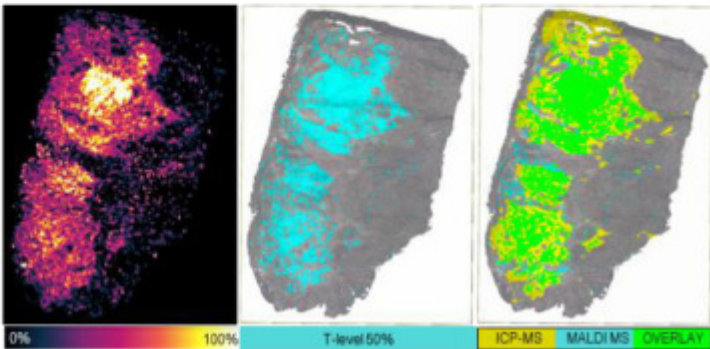
SPDC 34 m/z 876.7 ± 0.3 Da



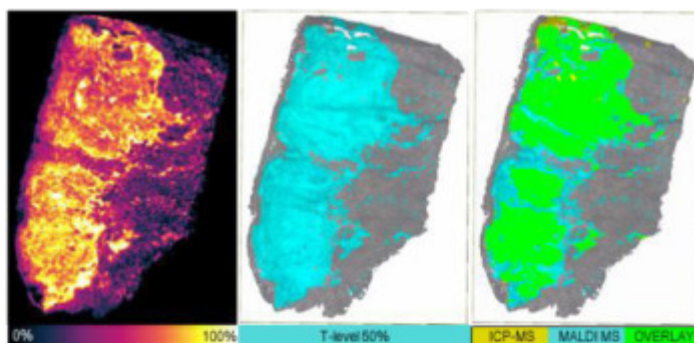
SPDC 35 m/z 880.7 ± 0.3 Da



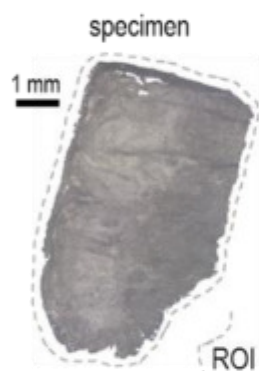
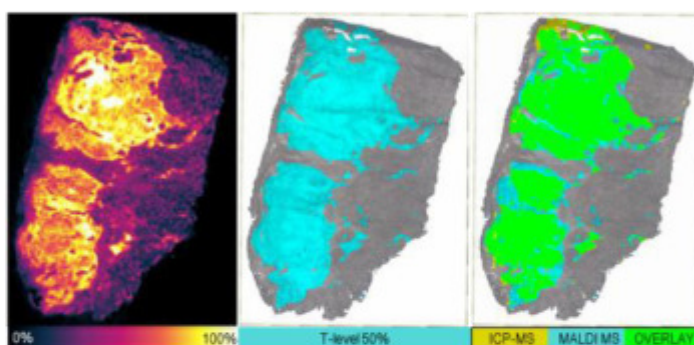
SPDC 36 m/z 881.7 ± 0.3 Da



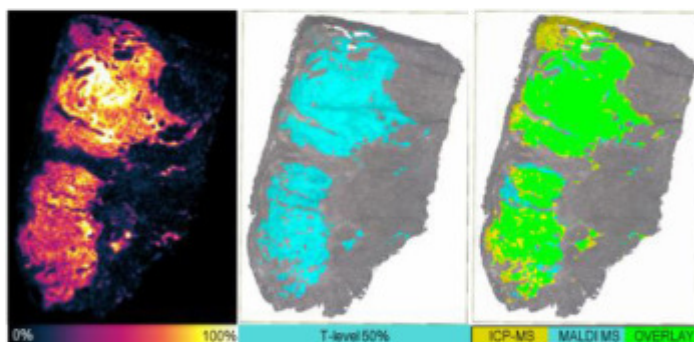
SPDC 37 m/z 883.7 ± 0.3 Da



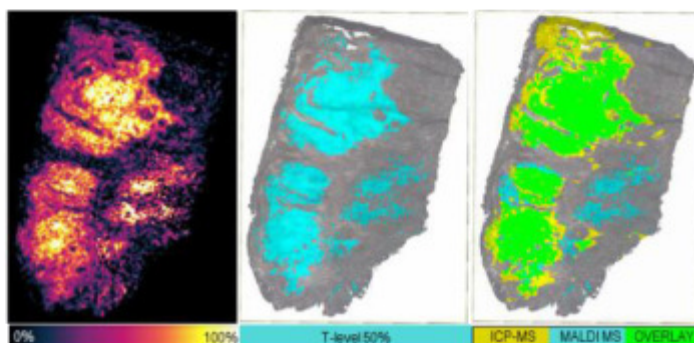
SPDC 38 m/z 887.7 ± 0.3 Da



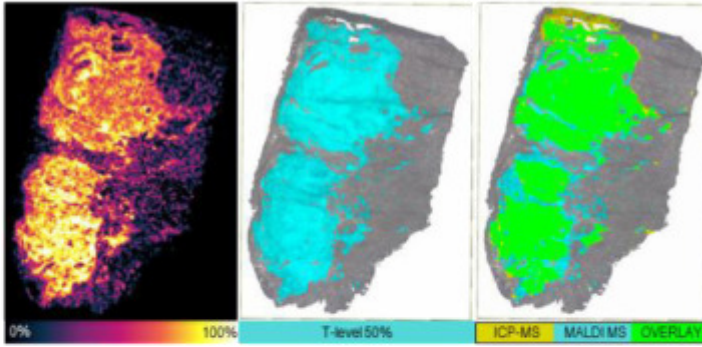
SPDC 39 m/z 889.7 ± 0.3 Da



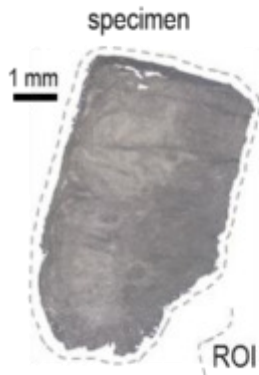
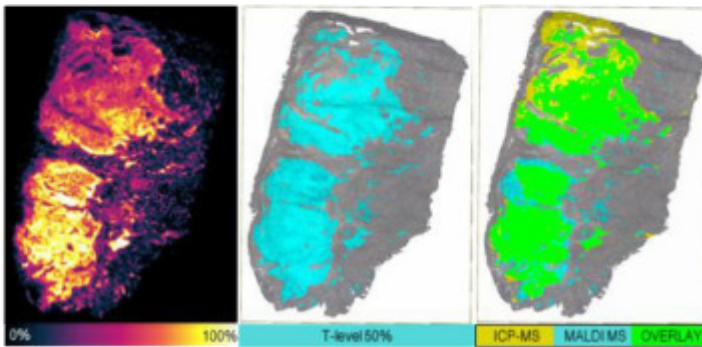
SPDC 40 m/z 896.7 ± 0.3 Da



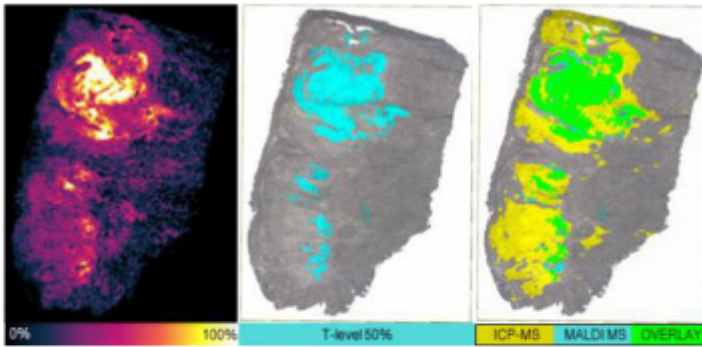
SPDC 41 m/z 902.8 ± 0.3 Da



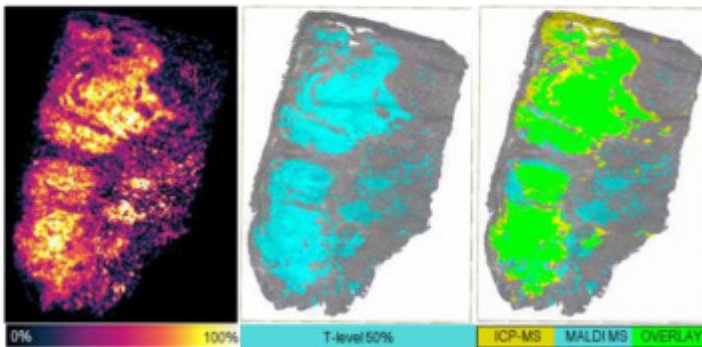
SPDC 42 m/z 904.8 ± 0.3 Da



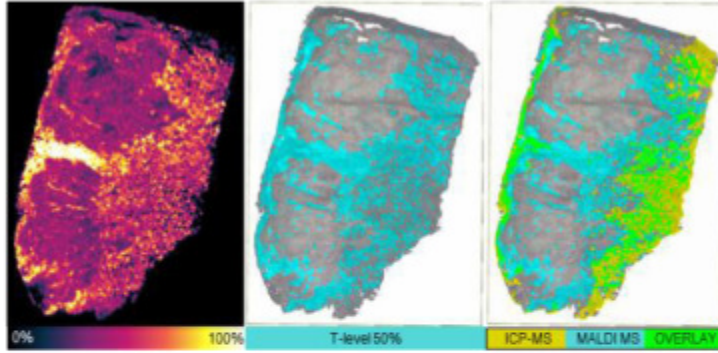
SPDC 43 m/z 915.8 ± 0.3 Da



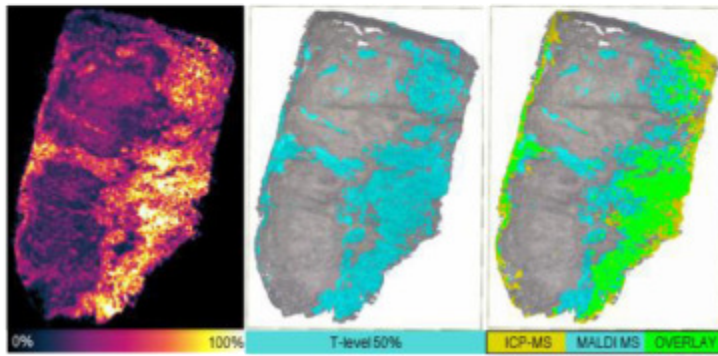
SPDC 44 m/z 918.8 ± 0.3 Da



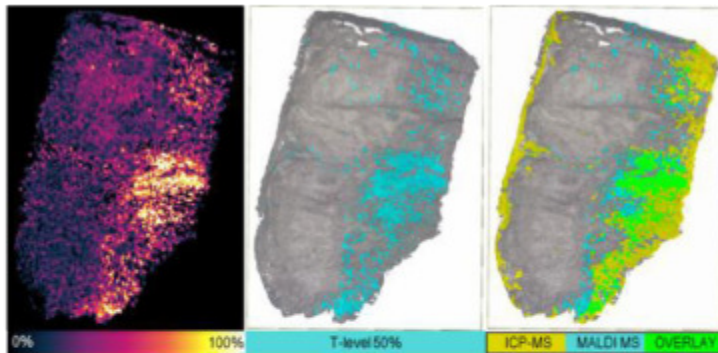
SPDC 45 m/z 934.8 ± 0.3 Da



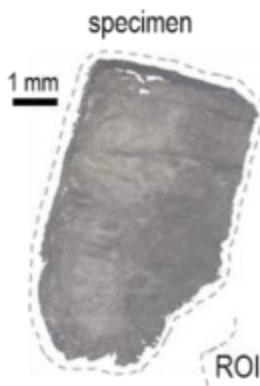
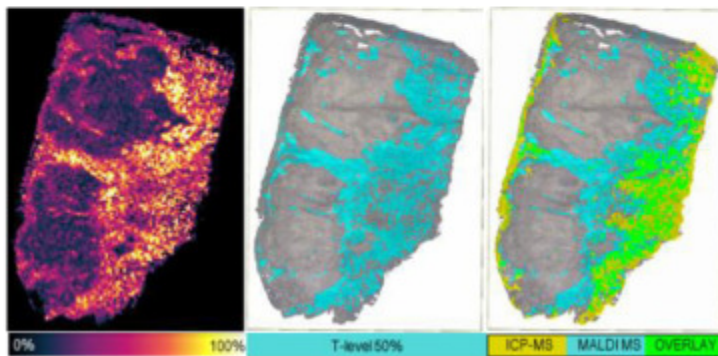
SPDC 46 m/z 940.9 ± 0.3 Da



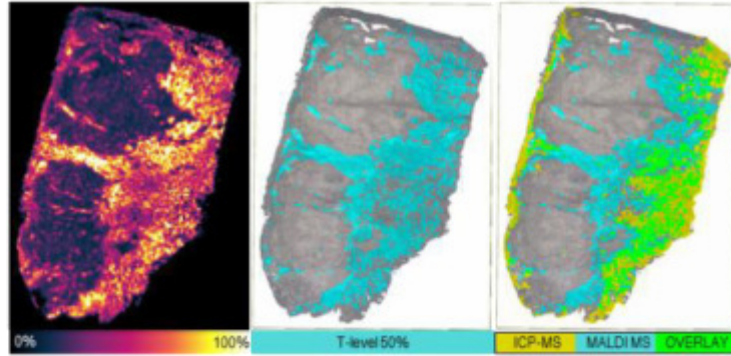
SPDC 47 m/z 942.8 ± 0.3 Da



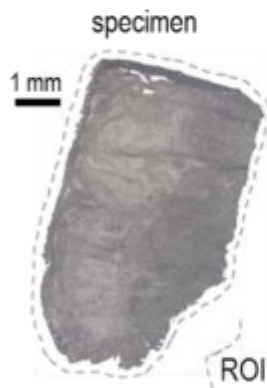
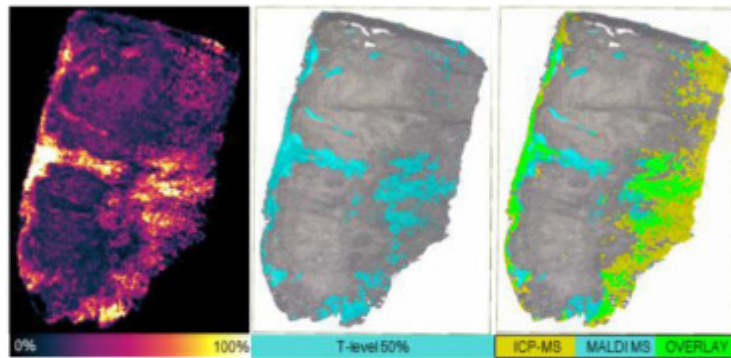
SPDC 48 m/z 960.8 ± 0.3 Da



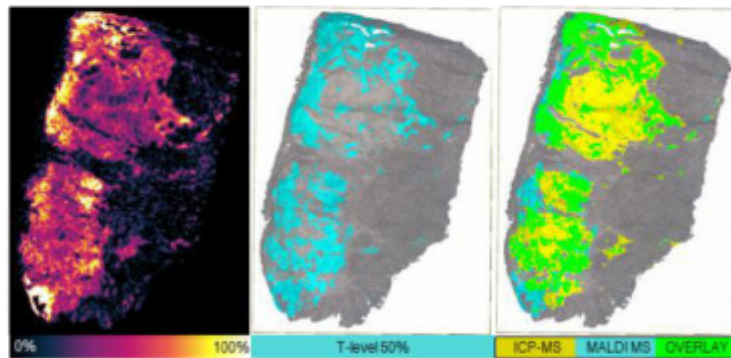
SPDC 49 m/z **962.8** \pm 0.3 Da



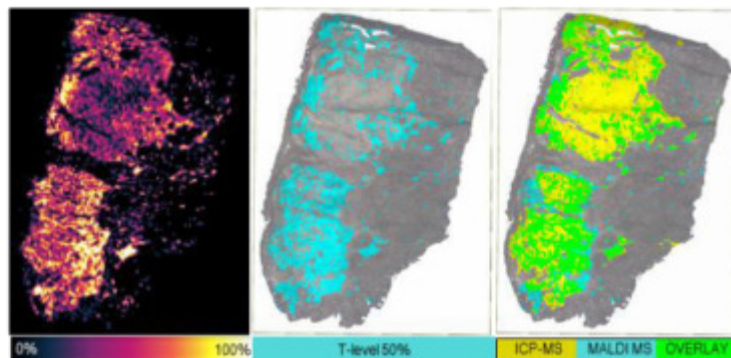
SPDC 50 m/z **967.9** \pm 0.3 Da



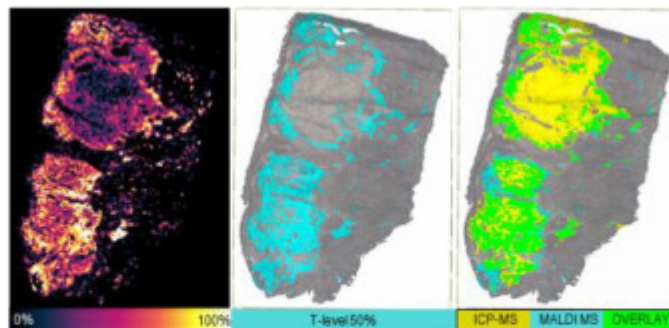
SPDC 51 m/z **980.8** \pm 0.3 Da



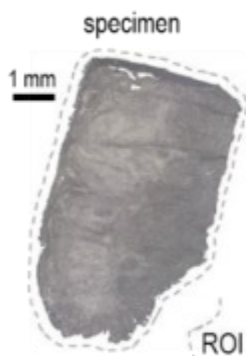
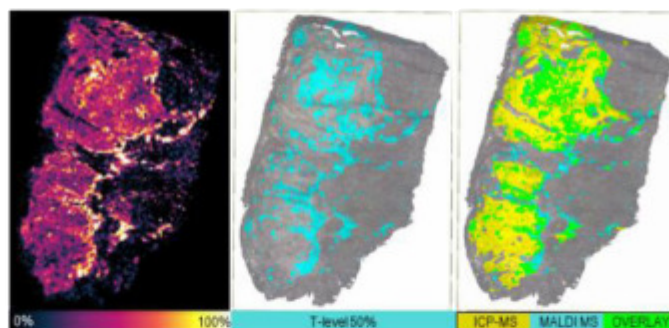
SPDC 52 m/z **1068.7** \pm 0.3 Da



SPDC 53 m/z 1096.7 ± 0.3 Da

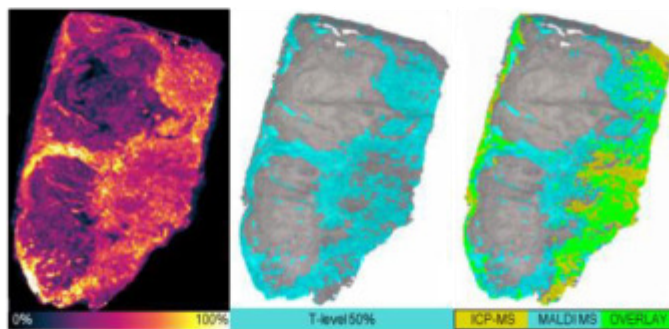


SPDC 54 m/z 1261.9 ± 0.3 Da

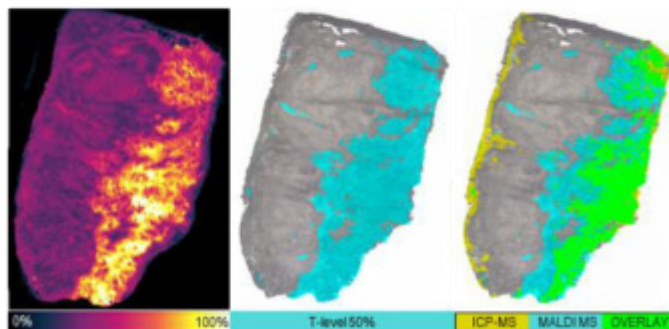


MALDI-MS m/z values – positive polarity

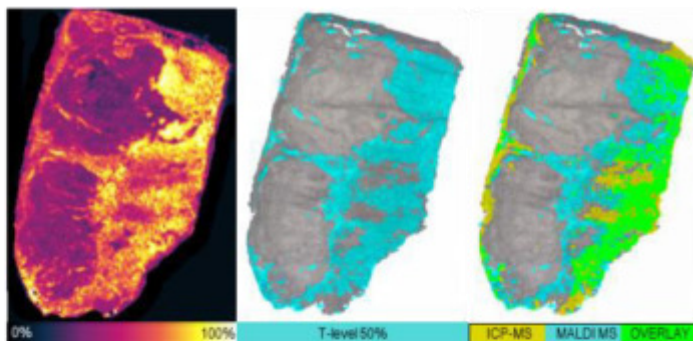
SPDC 55 m/z 782.8 ± 0.3 Da



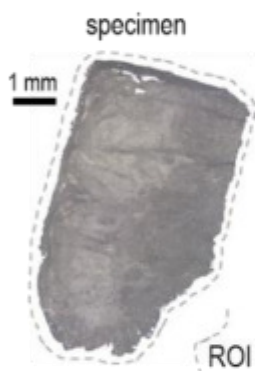
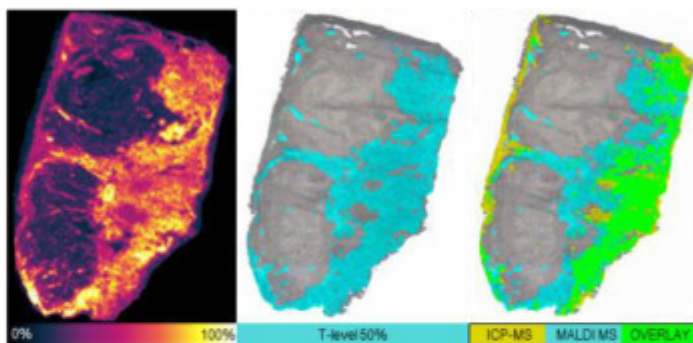
SPDC 56 m/z 788.8 ± 0.3 Da



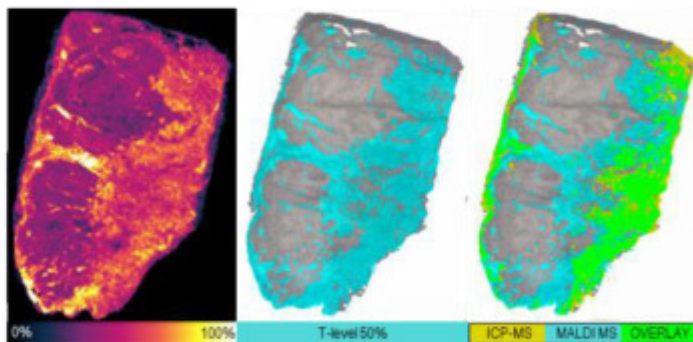
SPDC 57 m/z 808.7 ± 0.3 Da



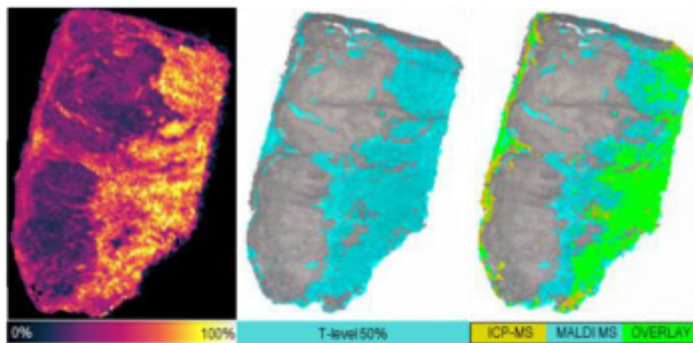
SPDC 58 m/z 810.7 ± 0.3 Da



SPDC 59 m/z 812.7 ± 0.3 Da



SPDC 60 m/z 836.7 ± 0.3 Da



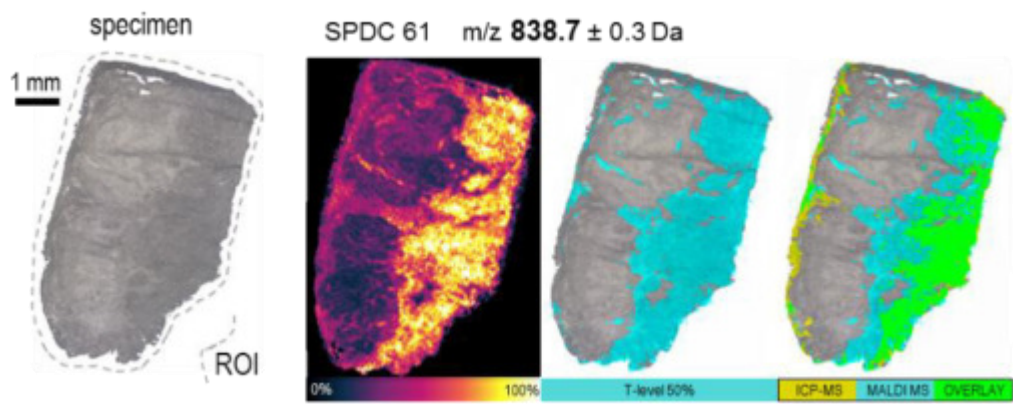


Figure S7 PCA of 61 SPDCs (mean centered)

- Loadings/Score-Plot PC1/PC2

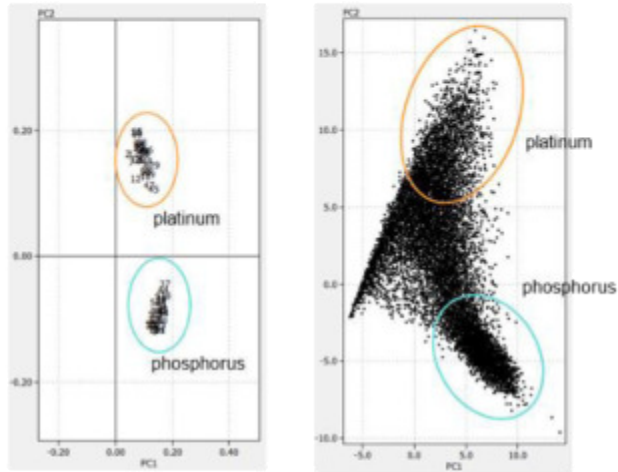


Figure S8 HCA on the loadings of the PCA (61 SPDCs)

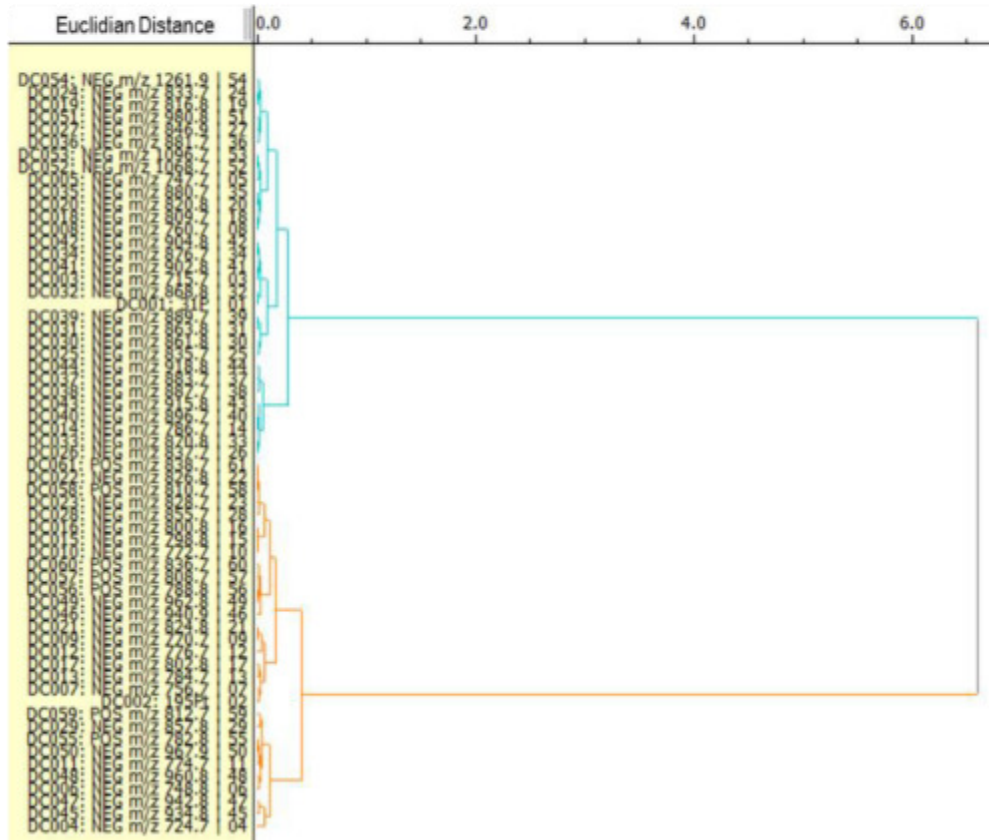


Figure S9

PCA (61 SPDCs)

- Examination of Score-Plots

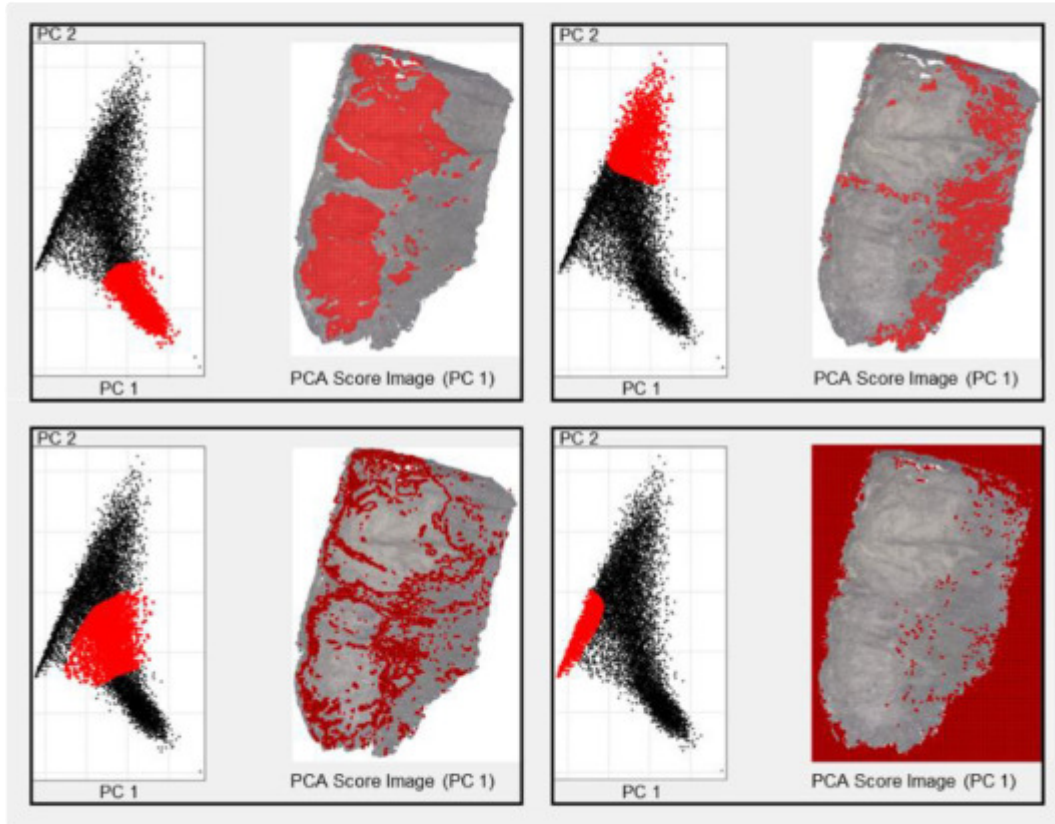
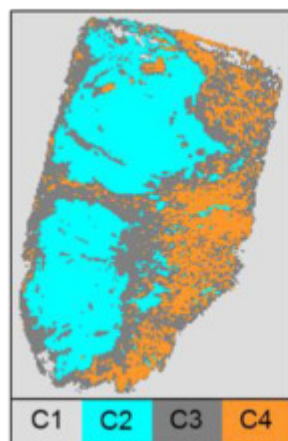


Figure S10

k-Means Clustering (61 SPDCs)

- Cluster image and table



cluster	no. (pixels)
C1	11889
C2	8528
C3	7135
C4	3856

**8 PHOSPHONATE COATING OF SiO₂ NANOPARTICLES
ABROGATES INFLAMMATORY EFFECTS AND LOCAL CHANGES
OF THE LIPID COMPOSITION IN THE RAT LUNG: A
COMPLEMENTARY BIOIMAGING STUDY**

| manuscript submitted to *Particle and Fibre Toxicology* |

Phosphonate Coating of SiO₂ Nanoparticles Abrogates Inflammatory Effects and Local Changes of the Lipid Composition in the Rat Lung: A Complementary Bioimaging Study

Mandy Großgarten,¹ Matthias Holzlechner,² Antje Vennemann,³ Anna Balbekova,² Karin Wieland,²
Michael Sperling,¹ Bernhard Lendl,² Martina Marchetti-Deschmann,²
Uwe Karst,¹ and Martin Wiemann³

¹ University of Münster, Institute of Inorganic and Analytical Chemistry, Corrensstraße 28/30, 48149 Münster, Germany

² TU Wien, Institute of Chemical Technologies and Analytics, Getreidemarkt 9, 1060 Vienna, Austria

³ IBE R&D Institute for Lung Health GmbH, Mendelstraße 11, 48149 Münster, Germany

Corresponding Author: martin.wiemann@ibe-ms.de
Phone: ++49 251 9802340
Fax: ++49 251 9802349

ABSTRACT

Background: The well-known inflammatory and fibrogenic changes of the lung upon crystalline silica are accompanied by early changes of the phospholipid composition (PLC) as detected in broncho-alveolar lavage fluid (BALF). Silica (SiO₂) nanoparticles (NPs) evoke transient lung inflammation, but their effect on PLC is unknown. Here, we compared effects of unmodified and phosphonated SiO₂ NP and describe, for the first time, local changes of the PLC with innovative bio-imaging tools.

Methods: Unmodified (SiO₂), phosphonated (SiO₂-P), and fluorescent surrogate NP (SiO₂-FITC) (all sized 15 nm) were used in this study. In vitro toxicity was tested with NR8383 alveolar macrophages. Rats were intratracheally instilled with either NP and effects on lungs were analysed after 3 days. BALF from the right lung was analysed for inflammatory markers. Cryo-sections of the left lung were subjected to fluorescence microscopy and PLC analyses by matrix-assisted laser desorption/ionization mass spectrometry imaging (MALDI-MS), Fourier transform infrared microspectroscopy (FT-IR), and MS/MS experiments.

Results: Unmodified SiO₂ NPs were more cytotoxic to macrophages in vitro and more inflammatory in the rat lung, as reflected by increased concentration of neutrophils and protein in BALF. Fluorescence microscopy revealed a typical patchy distribution of SiO₂-FITC located within the lung parenchyma and alveolar macrophages. Superimposable to this pattern SiO₂ and SiO₂-FITC, but not by SiO₂-P, elicited local increases of phosphatidylglycerol (PG) and phosphatidylinositol (PI), both of which are important lipids of the lung surfactant. In contrast, phosphatidylserine (PS) and signals from triacylglyceride (TAG) were decreased in the same areas.

Conclusions: Phosphonate coating mitigates effects of SiO₂ NP in the lung and abolishes their locally induced changes in PLC pattern. Bioimaging methods based on MALDI-MS may become a useful tool to investigate the mode of action of NPs in tissues.

Keywords: Lung surfactant, Silica nanoparticles, in vitro and in vivo lung toxicity, MALDI-MS Imaging, Phospholipids, Phosphonate coating, PI/PG ratio, Fourier transform infrared microspectroscopy imaging.

BACKGROUND

Nanoparticles (NP) consisting of SiO₂ are among the most common materials of everyday life. Besides other applications, SiO₂ NP acts as bulking agent in car wheels, as drug delivery system in cancer therapy or as food additive (E551) to prevent pulverulent foodstuffs from agglutinating. Moreover, SiO₂ particles are highly abundant in the environment. Respirable airborne SiO₂ particles may enter the lungs and it is known for crystalline silica particles (quartz, cristobalite) that they elicit strong adverse health effects such as neoplastic transformation, progressive fibrosis or even cancer [1]. Amorphous nanosized SiO₂ particles are of less concern. They are produced by different production processes such that precipitated, fumed, or colloidal silica qualities are to be distinguished. From a toxicological point of view, most amorphous nanosized SiO₂ particles, at least above a certain dose, have been shown to cause acute pulmonary inflammation but no progressive lung fibrosis [2–4]. Also genotoxic or mutagenic effects, which had been described for cells *in vitro* mostly at high concentrations, have not been identified in the lung or secondary target organs [5]. This holds true also for comparatively high dose rates and even under conditions which increase the population of neutrophilic granulocytes inside the lung to extreme values [3].

The mechanisms underlying the cytotoxic, membrane disrupting or haemolytic potential of amorphous SiO₂ seem to involve silanol groups which are present at the particles' surface and may interact with biological molecules such as proteins [6–9]. Accordingly, the biologic activity of amorphous SiO₂ NPs correlates largely with the overall size of the SiO₂ surface [10,11] and modification of the chemical surface structures of SiO₂ NPs alters their bioactivity. Effects of the colloidal SiO₂, SiO₂-FITC and SiO₂-P used in this study have been investigated previously: In the lung, the coating of SiO₂ (diameter: 15 nm, BET surface: 200 m²·g⁻¹) with 3-(trihydroxysilyl)propyl methylphosphonate (TPMP) largely abrogated the typical signs of inflammation elicited by the unmodified SiO₂ NPs [12][13]. The effect was not attributable to altered particle properties in general, as the TPMP coating had no or only minor effects on particle properties or agglomeration of SiO₂-P in biological media [12]. Interestingly, the *in vitro* binding of phospholipids from lung surfactant to SiO₂ and SiO₂-P (both negatively charged) was similarly low, but increased in the presence of surfactant proteins A and D [14]. However, the binding of lung surfactant components to SiO₂ and SiO₂ under *in vivo* conditions remains an unsolved issue. Lung surfactant is produced by alveolar type II cells and released in the form of lamellar bodies which consist of 90% phospholipids and 10% surfactant proteins [15]. The unfolded lipid layer covers the inner surface of the lung and decreases the surface tension of the air-liquid interface [16]. The surfactant proteins A and D (so called collectins) are immunologically relevant as they can bind to microorganisms or foreign material such as (nano)particles, thus, augmenting their uptake by alveolar macrophages [17–19]. For micron-sized crystalline silica and also for other particles it is known that they change the phospholipid composition (PLC) in the bronchoalveolar lavage fluid (BALF) is a time-

and dose-dependent manner [20–22]. Thereby, the overall concentration of the major constituent phosphatidylcholine increases, and fractions of phosphatidylglycerol (PG) and phosphatidylinositol (PI) decrease and increase, respectively [20]. Accordingly, the ratio PI/PG has been used as a sensitive tool to describe an impaired lung function, as observed during bleomycin- or quartz-induced lung fibrosis [20,23]. Importantly, the ratio PI/PG is also subject to change in humans suffering from the acute respiratory distress syndrome or other lung diseases such as cystic fibrosis [24,25]. As outlined above an impact of SiO₂ NP on the lung surfactant or PLC of the lung is unknown.

In contrast to previous studies on the composition of phospholipids in BALF, here we apply bioimaging methods to cryo-sections of the rat lung to demonstrate local lipid changes upon intratracheal instillation caused by SiO₂ NPs in a laterally resolved manner. It is to be expected that allocation of changes in PI and PG to the presence of particles in the lung will improve our understanding of biological processes elicited by nanoparticles. To this aim, matrix-assisted laser desorption/ionization mass spectrometry imaging (MALDI-MS) and Fourier transform infrared (FT-IR) microspectroscopy imaging were applied to cryo-conserved lung sections to localize changes in the phospholipid composition secondary to the application of SiO₂ NPs and TPMP-coated, i.e. phosphonated SiO₂ nanoparticles (SiO₂-P). With these methods, we found typical changes of distinct phospholipids to be co-localized with the distribution pattern of SiO₂ but not with SiO₂-P nanoparticles.

RESULTS

In vitro and in vivo toxicity study

To demonstrate the differential toxicity of three SiO₂ nanoparticle varieties, *in vitro* testing with a rat alveolar macrophage cell line was carried out with increasing concentrations of the particles (22.5, 45, 90, and 180 µg·mL⁻¹). Exposure to the pristine material for 16 h (Figure 1a-d) led to dose-dependent increases in the cell culture supernatant of lactate dehydrogenase (LDH, a), glucuronidase (Glu, b), and TNF-α (d), mostly beginning at 22.5 µg·mL⁻¹. These cytotoxic and inflammatory effects were reduced upon SiO₂-P, while the release of H₂O₂ from NR8383 cells, as measured during a 90 min incubation period, was augmented (c).

In vivo tests were carried out with SiO₂, and SiO₂-P. The fluorescence surrogate SiO₂-FITC was used to demonstrate particle distribution in the left lung lobe secondary to intratracheal instillation which was carried out with a micro-sprayer device. In all tests, a concentration of 0.36 mg per rat lung was used to match the lung burden achieved in a previous inhalation study [13]. BALF analysis was conducted 3 days after intratracheal instillation of the NPs in order to examine their effect on cell counts and total protein content. SiO₂ and SiO₂-FITC both increased the numbers of alveolar macrophages (AM) and polymorphonuclear leukocytes (PMN) as well as the concentration of total protein in BALF compared to the vehicle control (Figure 1e-f). Based on these biological effects, no difference was

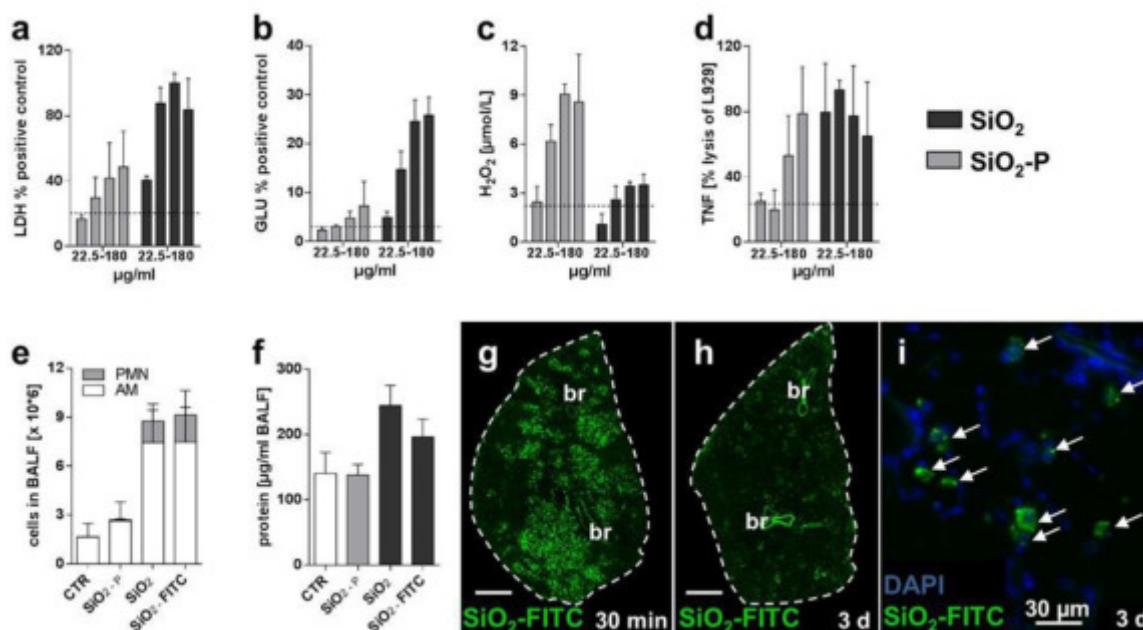


Figure 1. Differential effects of SiO₂, SiO₂-FITC, and SiO₂-P NPs in vitro and in vivo. (a-d). Dose dependent in vitro effects of SiO₂ and SiO₂-P NPs (22.5, 45, 90, and 180 µg·mL⁻¹) on NR8383 cells, showing cytotoxicity by increased release into medium of (a) LDH, (b) Glu, (c) H₂O₂ and (d) TNF-α (in vitro data taken from [54]). LDH and Glu activities were measured relative to positive control (Triton X-100) after 16 h. The H₂O₂ concentration was measured in µmol·L⁻¹ after 90 min, and bioactive TNF-α was measured after 16 h as lysis of TNF-α responsive L-929 cells. Data are depicted as mean values ± standard deviation of 3 independent experiments. Untreated cells served as controls (n=3, dashed lines indicate mean values). (e-i) In vivo effects of SiO₂, SiO₂-P and SiO₂-FITC NPs (0.36 mg) intratracheally instilled into rat lungs (n=5) and compared to vehicle control (CTR). e-f) Analysis of bronchoalveolar lavage fluid for differential cell counts (e) and total protein (f) 3 d post instillation. AM: Alveolar macrophages. PMN: polymorphonuclear leukocytes. (g-h) Fluorescence micrographs of transversal cryosections of the left lung 30 min (g) and 3 d (h) after intratracheal instillation of SiO₂-FITC NPs. Dashed lines demarcate the outer rim of each section. Scale bars represent 200 µm. Large bronchi (br) appear as strongly autofluorescent structures. (i) Detail of the section shown in (h); the fluorescent signal is confined to phagocytic cells (arrows) which were identified as alveolar macrophages in preceding studies. Nuclei of lung cells are stained with 4',6-diamidin-2-phenylindol (DAPI).

found between SiO₂-FITC and the pristine SiO₂ NPs. Spray application of particles resulted in a patchy distribution pattern of particles inside the lung typically found upon intratracheal instillation (Figure 1g-i) [26]. Higher magnification revealed many condensed fluorescent NP agglomerates alongside the alveolar septa after 30 min. After 3 d, the majority of this material had disappeared from alveolar walls but occurred within alveolar macrophages (Figure 1i), whose overall distribution was still detectable by fluorescent microscopy and reflected the original sites of particle deposition. On hematoxylin-eosin stained lung cryo-sections either type of SiO₂ nanoparticles or agglomerates were

not detectable with bright field optics. However, SiO₂- or SiO₂-FITC-treated lungs showed regions with increased macrophage numbers, slightly deteriorated structure and beginning hypercellularity. These changes were absent in lung treated with vehicle control or SiO₂-P (Figure S1).

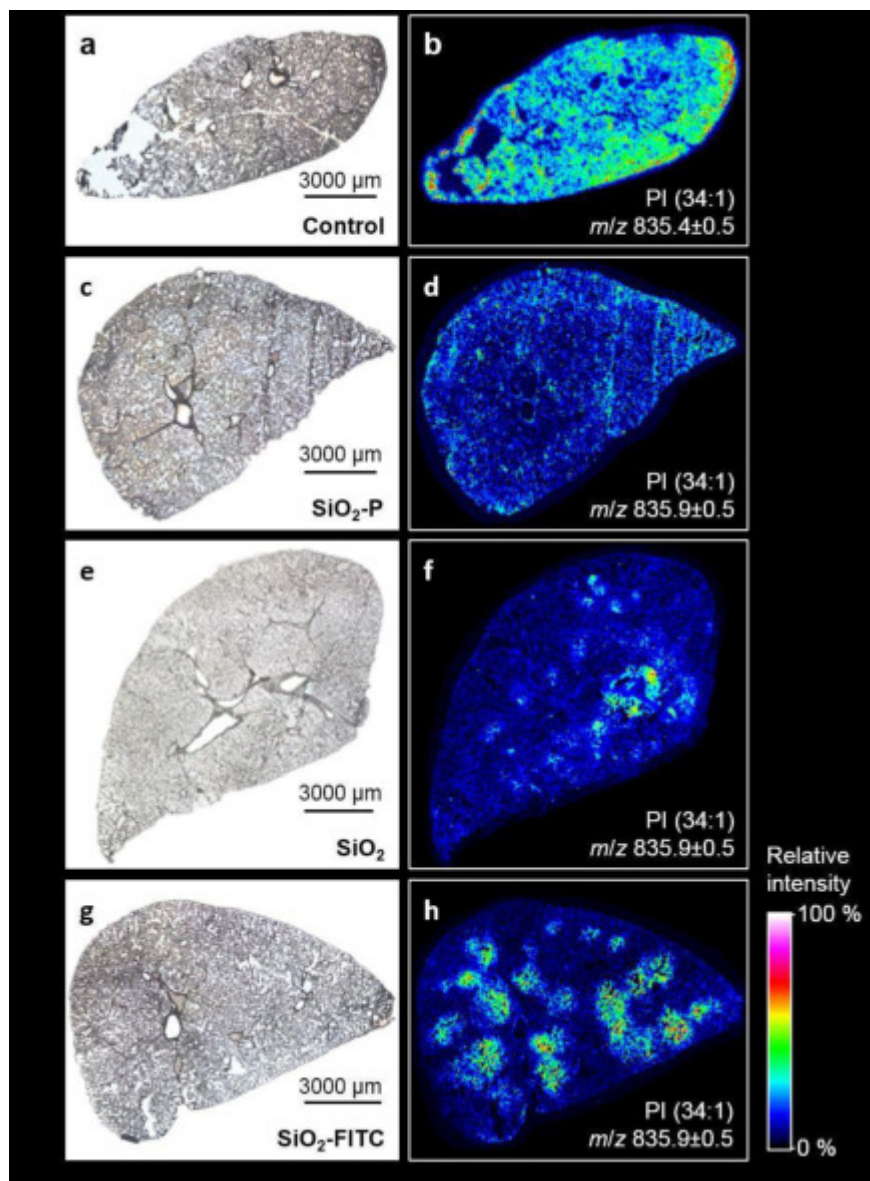


Figure 2. Local increases of PI concentration in the rat lung upon SiO₂ NP treatment are abrogated by phosphonate coating. Distribution of phosphatidylinositol PI (34:1) 3 d after instillation of SiO₂ NPs (0.36 mg/lung) with different surface modification: Microscopic images of the investigated cryosections (left) and corresponding MALDI-MS ion images of *m/z* 835.9 (right, detected as [M-H]⁻ in negative ion mode) of rat lung treated with (a-b) SiO₂-P NPs, (c-d), SiO₂ NPs (e-f), or SiO₂-FITC NPs (g-h). Note the patchy occurrence of PI upon SiO₂ and SiO₂-FITC but not upon SiO₂-P. The seemingly high signal of the control section results from automated scaling of the relative signal intensity.

Identification of phospholipid species with MALDI-MS

To get information about particle-related changes of PLC we analyzed cryo-sections of the lung for phospholipid distribution by MALDI-MS in control animals, and secondary to the application of inflammatory SiO₂ or SiO₂-FITC, as well as non-inflammatory SiO₂-P NPs. Figure n2 shows low power micrographs of the sections and respective MALDI-MS ion images for mass-to-charge ratio (m/z) of 835.9 assigned to PI (34:1). This molecule gave a sufficient contrast in the negative ion mode and was therefore selected as a starting point to highlight the distributional disparities between the three surveyed nanoparticle species. The lateral resolution (50 μm) of the method allowed to visualize major tissue components such as large and medium-sized bronchi.

Vehicle-treated rat lung sections (Figure 2a, b) showed a largely homogeneous distribution of PI (34:1) and all other detected m/z . Signal inhomogeneity in this case was artificial and attributable to compression (lower right margin) or loss of the tissue (left hand side), as was evident from the low-power micrograph (Figure 2a). Of note, as the pseudocolor scale reflects relative intensity values and spreads the complete set of data from 0 to 100 %, a comparison of absolute values cannot be made for different treatments, i.e., between different tissue sections. Yet, absolute intensity values within one tissue section can be compared.

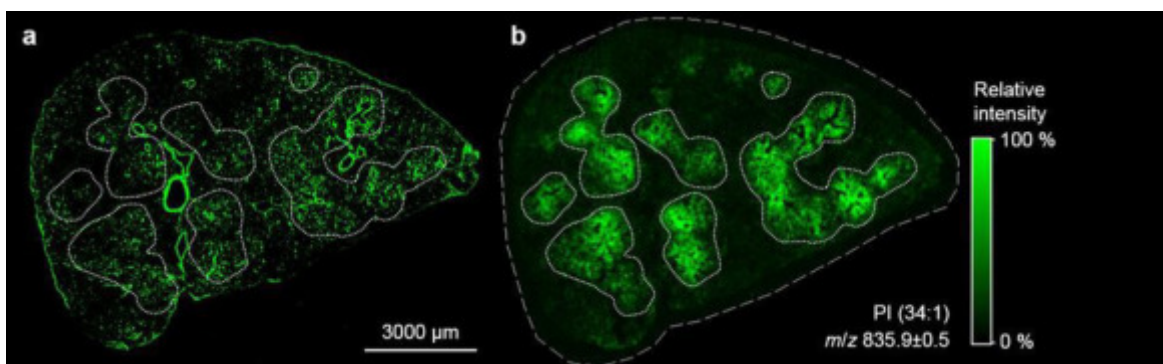


Figure 3. Correlation of nanoparticle distribution and local PI overexpression 3 d post instillation of SiO₂-FITC NPs. (a) Fluorescence overview image visualizing the principal distribution of NPs mainly located in alveolar macrophages. (b) MALDI-MS ion image of PI (34:1) ([M-H]⁻) in a parallel tissue section (bordered by a dashed line). The fine dotted lines demarcate seven areas of PI overexpression. These areas were transferred to the fluorescence image in (a) to show the co-localization with FITC fluorescence. Large blood vessels and bronchioli show strong autofluorescence but no PI signal.

However, particle treatment changed the homogeneous lipid distribution pattern in a striking manner: While SiO₂-P had no influence on the lipid distribution (Figure 2 d), SiO₂-FITC NPs induced round-shaped patchy regions within which PI (34:1) signal was strongly increased (Figure 1h). Similarly, but with larger heterogeneity, SiO₂ induced several regions with increased PI (34:1) (Figure 2 f).

To analyze whether there is a congruency of particle distribution and the pattern of increased PI (34:1) intensity, we compared serial sections of the same lung for their distribution patterns of FITC fluorescence and PI (34:1). Figure 3 shows the overview distribution of FITC fluorescence and the PI (34:1) signal: Hand-drawn regions demarcating PI (34:1)-enriched regions were transferred from Figure 3b to the fluorescent image of Figure 3a. Although connective tissue around bronchiolar structures and blood vessels stands out clearly due to considerable autofluorescence, fluorescent dots in PI (34:1)-enriched regions are far more numerous. At higher magnification these fluorescent signals represent SiO₂-FITC-laden cells (compare Figure 1i) which have the fluorescent material.

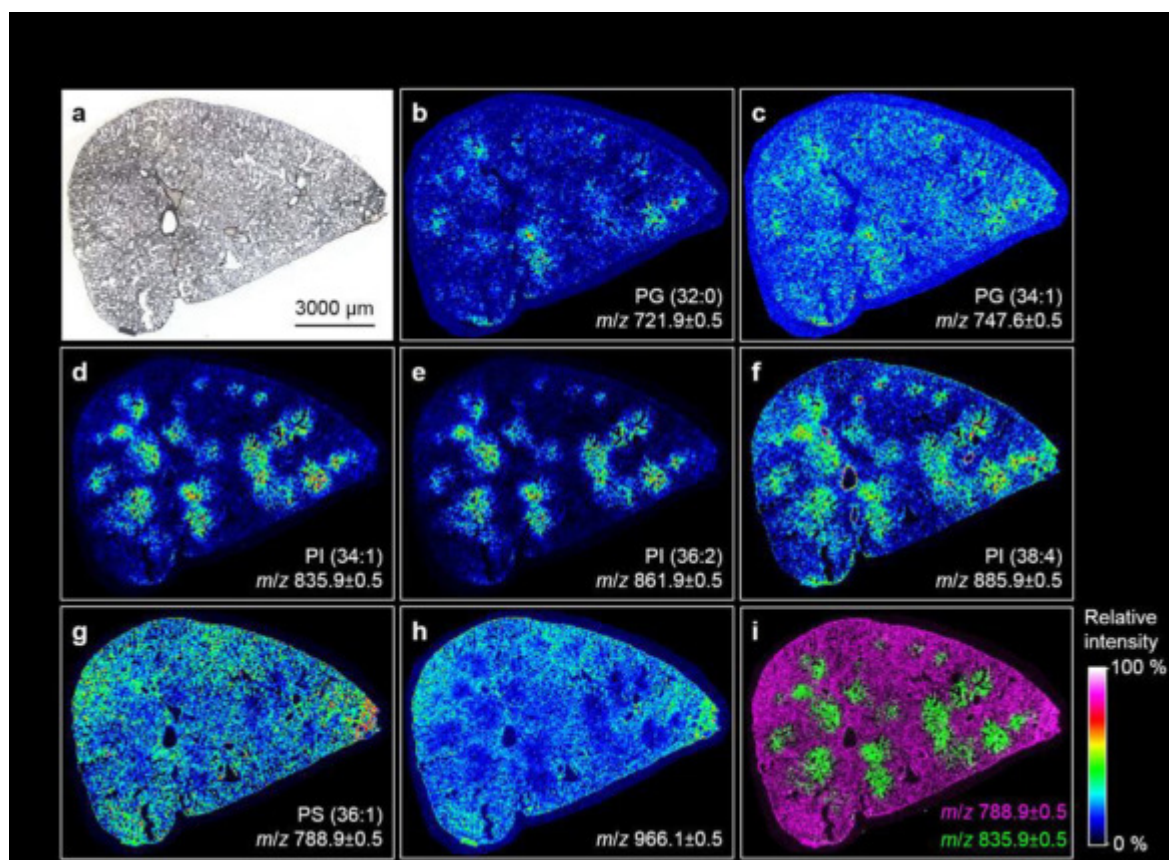


Figure 4. MALDI-MS ion images of local changes of lipid concentration in the SiO₂-FITC laden rat lung. Cryo-section from an animal 3 d after intratracheal instillation of 0.36 mg SiO₂-FITC NPs. (a) Microscopic image of investigated cryosection. (b-c) Ion images indicating a minor local overexpression of PGs. (d-f) Ion images pronounced local overexpression of PIs. (g-h) Ion images of m/z 788.0 \pm 0.5 and 966.1 \pm 0.5 revealing an inversely correlating distribution of PS and TAG compared to the PIs shown in d, e and f. (i) Overlay of MS ion images shown in d and g; m/z are assigned to ion [M-H].

Figure 4 displays further MALDI-MS ion images of distinct m/z representing a variety of phospholipids detected in negative ion mode in the lung section originating from a rat instilled with SiO₂-FITC NPs. Detected m/z were classified as phosphatidylglycerol (Figures 4b,e), phosphatidylinositol (Figures 4d-f) and phosphatidylserine (PS) (Figure 4i), each featuring two fatty acyl residues. The assignment of m/z 966.1 (Figure 4h) will be discussed below. Shorthand designations, which will be used in the next section, represent the length of the carbon chains summarizing all fatty acyl residues and the degree of unsaturation, i.e. the number of double bonds within fatty acid chains. Most striking, the round-shaped regional overexpression of the previously mentioned PI (34:1) with a m/z of 835.9 (Figure 4d) was largely colocalized with m/z which can be assigned to [M-H]⁻ ions of PI (36:2) (m/z 861.9) and PI (38:4) (m/z 885.9, Figure 4e-f). Interestingly, highest concentration of PI (38:4) apparently lined the larger bronchi. The pattern of round-shaped regional increases was found, to a lesser extent, also for m/z corresponding to phospholipids of the phosphatidylglycerol (PG) class (b-c), such that overexpression of both PIs and PGs were highly co-located.

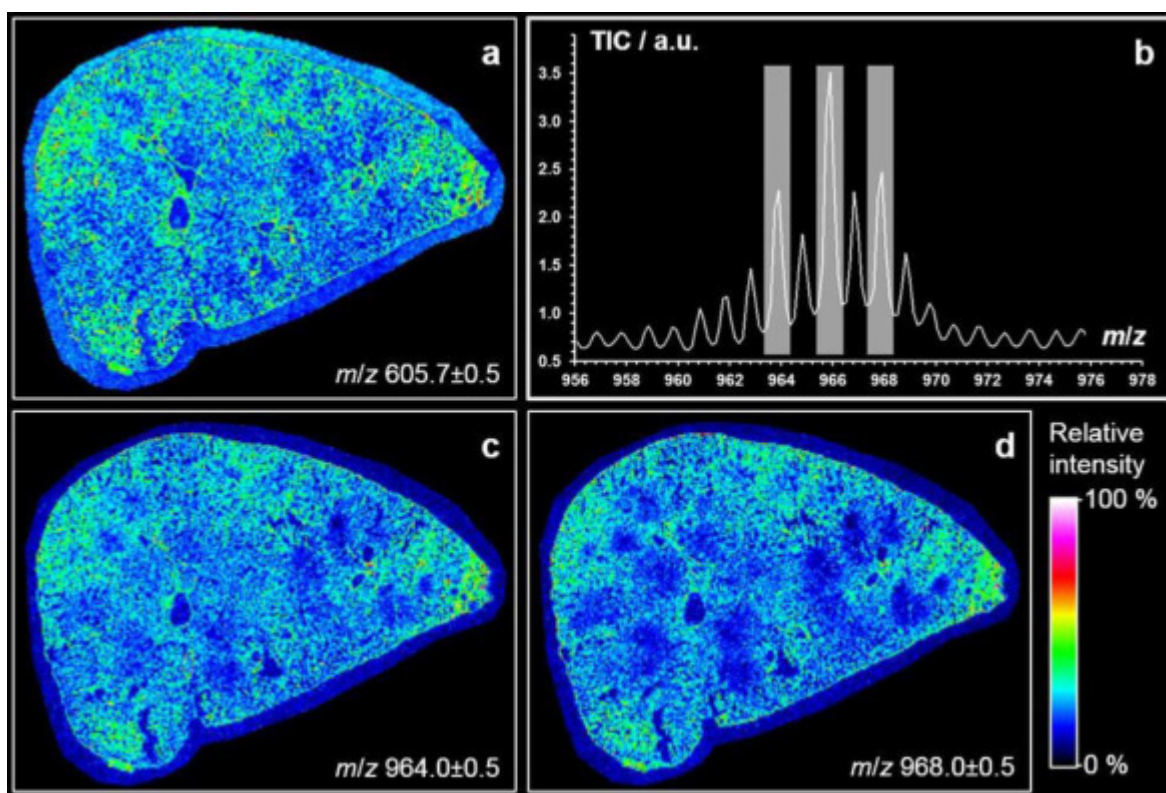


Figure 5. MALDI-MS ion images showing the local distribution of TAG and DAG-like molecules in a SiO₂-FITC laden rat lung. Cryo-section from an animal 3 d after intratracheal instillation of 0.36 mg SiO₂-FITC NPs. Ion images of (a) m/z 605.7 from DAG-like fragment (36:1) as [M-H₂O+H]⁺ detected in the positive ion mode, (c) m/z 964.0 assumed to be TAG (60:5), d) m/z (968.0) assumingly from TAG (60:3). (b) Relevant section of the average MALDI-MS spectrum (negative ion mode) of the analysis of the rat lung tissue shown in c and d.

Compared to PIs and PGs, a mild inversely correlating distribution was found for m/z 788.9 assigned to PS (36:1) (Figure 4g), and in a more pronounced manner as for m/z 966.1 (Figure 4h). This contrastive distribution of different phospholipids is further shown in an overlay image of m/z 788.9 and 835.9 in Figure 4i.

For verification purposes, two exemplary m/z , namely, m/z 721.4 assigned to PG (32:0) and m/z 861.5 assumed to be PI (36:2) were selected as precursor ions for MS/MS experiments. Mass spectra of their characteristic fragments (Figures S2 and S3) confirm the abundance of PIs and PGs as the major phospholipid classes detected in the negative ion mode. They further indicate that PG (32:0) consists of two (16:0) chains (Figure S2), while for PI (36:2) both fatty acyl compositions, PI (18:1|18:1) and PI (18:0|18:2), are deduced (Figure S3).

Since especially the ratio PI/PG is a long-known marker of lung affection in BALF, we calculated a *local* PI/PG on the basis of absolute intensity data. Regions of interest (ROIs) were defined on sections of SiO₂-FITC-treated and vehicle-treated lungs, within which the signal intensities of PI (34:1) (m/z 835.9) and PG (34:1) (m/z 747.6) were integrated from 600 spectra. On an untreated lung tissue section, where phospholipids appeared evenly distributed, a control ROI was chosen randomly. Its absolute intensity values were 0.67 a.u. (arbitrary units) for PI (34:1) and 0.36 a.u. for PG (34:1), resulting in a PI/PG of 1.9. On a lung section from a SiO₂-FITC NP instilled animal, a ROI with an apparent local PI overexpression was chosen. The absolute intensities therein were calculated as to be 2.15 a.u. for PI (34:1) and 0.38 a.u. for PG (34:1) resulting in a high local PI/PG ratio of 5.7. Together with the localization of SiO₂-FITC the result shows that PI/PG was locally increased in SiO₂ NP laden regions.

In contrast to PI and PG, we found m/z 966.1 and other closely related masses to be lowered in particle-laden regions (Figures 4h). Results obtained by MALDI-MS suggest that m/z 966.1 represents a triacylglyceride TAG (60:4). Interestingly, the signal was co-distributed with closely related molecules whose peaks showed mass differences of two mass units (m/z 964.0, 966.0 and 968.0, see Figure 5) and, therefore, might correspond to related TAGs whose number of double bonds ranged from 3 to 5. Further evidence for the correct detection of TAG comes from the co-distribution of a DAG-like derivative m/z 605.7 (Figure 5a) because this fragment is derived from TAG in tissue by cleavage of a fatty acyl residue [27].

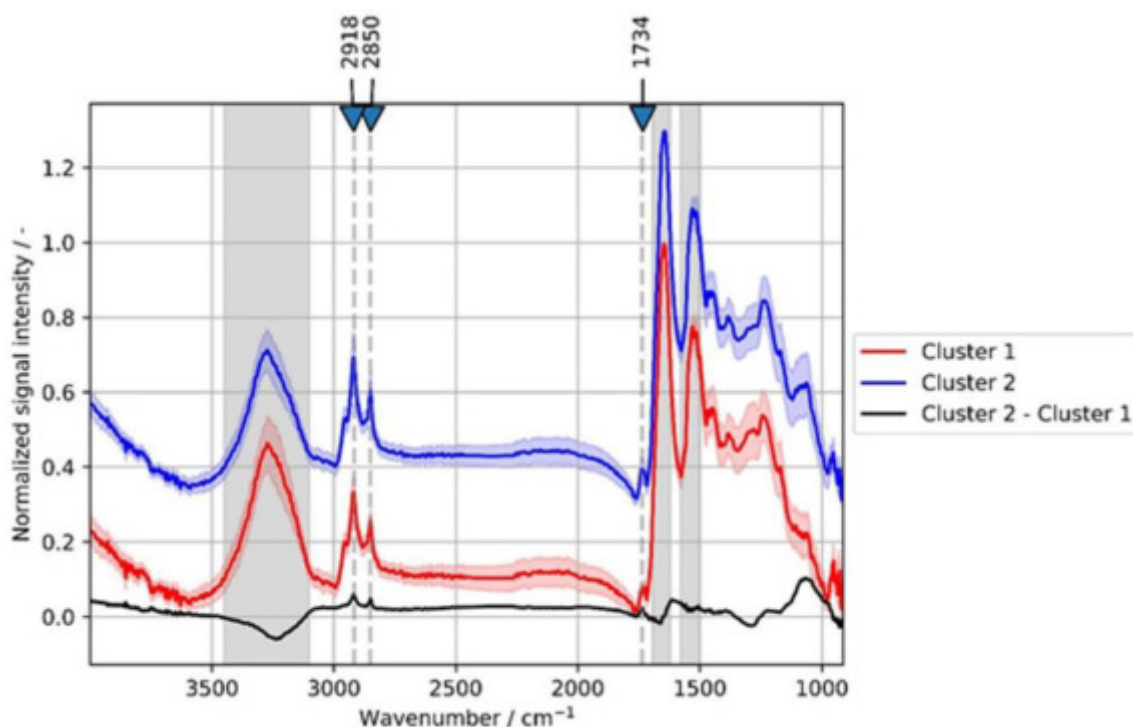


Figure 6. FT-IR microspectroscopy of a SiO₂-FITC laden rat lung cryo-section. Average spectra and standard deviation from hierarchical cluster analysis. Red curve: cluster 1; blue curve: cluster 2 (an offset was added to cluster 2 for better visualization); black curve: difference spectrum (cluster 2 - cluster 1). Dashed lines mark wavenumbers identifying lipids. Protein bands are indicated by grey background.

Fourier transform infrared microspectroscopy and hierarchical cluster analysis

Unlike MALDI-MS Fourier transform infrared (FT-IR) microspectroscopy generates molecular information through the determination of spectral fingerprints, which can be assigned to particular functional groups in the building blocks of biological tissues, such as lipids, proteins, carbohydrates, and nucleic acids. To test whether lipid-enriched areas seen with MALDI-MS could be verified with another independent technique, FT-IR microspectroscopy was carried out on parallel sections of the SiO₂-FITC laden rat lung tissue, i.e. adjacent to the sections investigated with MALDI-MS. The pre-processed spectral data generated by means of FT-IR imaging were subjected to a hierarchical cluster analysis (HCA), which is a powerful tool to statistically validate the spectral disparities between the pixels within an image. Average spectra of two ascertained clusters (cluster 1: red line; cluster 2: blue line) along with their difference spectrum (cluster 2 - cluster 1: black line) are shown in Figure 6. Three positive deviations at defined position of this difference spectrum (arrows in Figure 6) indicate that the blue cluster pixels have more intense vibrations resulting from lipids (CH₂ asymmetric stretching vibration at 2918 cm⁻¹ and CH₂ symmetric stretching vibration at 2850 cm⁻¹) and esters of free fatty acids (C=O stretching vibration at 1734 cm⁻¹). In contrast, the red cluster pixels show increased

signal intensities for bands in the spectral ranges of 1695–1620 cm^{-1} , 1580–1480 cm^{-1} , and 3290 cm^{-1} (grey areas in Figure 6) which can be assigned to peptide groups termed Amide I, Amide II and Amide A, respectively. Thus, while the red cluster 1 contains more protein, the blue cluster 2 contains more lipids.

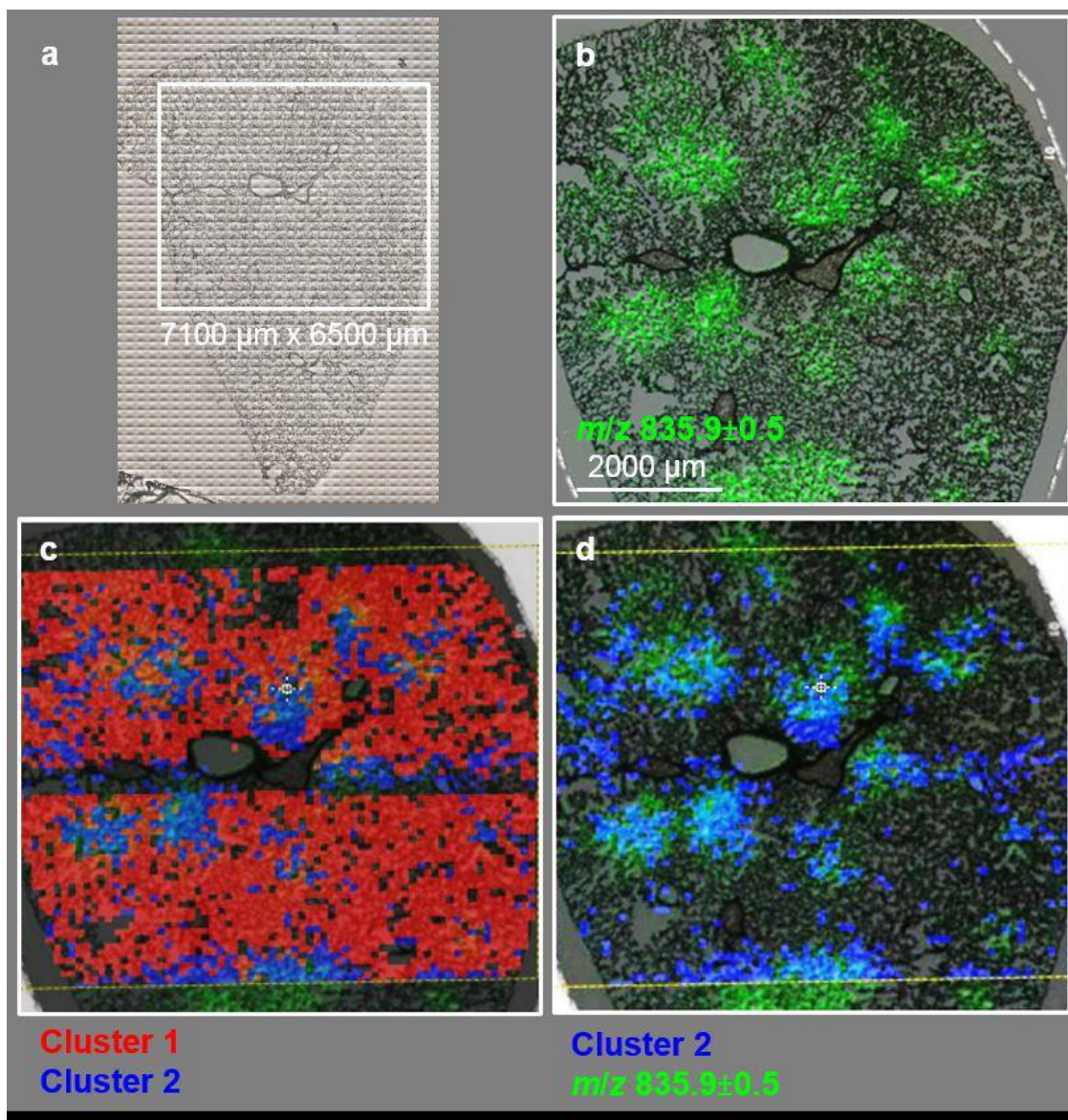


Figure 7. Comparison of MALDI-MS imaging with FT-IR spectroscopy followed by add-on hierarchical cluster analysis. (a) Optical image of lung cryosection. Region inside the white box was analyzed by means of FT-IR imaging. (b) Overlay of optical image with MALDI-MS ion image of PI 34:1 of the marked area. (c) Overlay of (b) with cluster 1 (red) and cluster 2 pixels (blue), as derived from HCA of FT-IR analysis data (Figure 6). (d) Overlay of (b) with cluster 2 pixels (blue), indicating that their positions are largely co-located with regions of PI overexpression.

Figures 7a-d show the superposition of the spatially resolved images of clusters 1 and 2 to the MALDI-MS image of PI (34:1, m/z 835.9), and the optical image of the SiO₂-FITC laden lung tissue section from Figure 7b. Comparing the color-coded regions it can be seen that the lipid-enriched cluster 2 pixels (blue) were largely co-localized with PI (34:1) (Figure 7d), whereas protein-enriched cluster 2 pixels (red) were evenly distributed throughout the lung parenchyma but were lowered in PI (34:1) enriched region (Figure 7c). Thus, the detection of lipid enrichment by FT-IR microspectroscopy confirms results from MALDI-MS studies on adjacent sections.

DISCUSSION

This study has shown that the cytotoxicity and acute inflammation typically induced by SiO₂ NP is strongly diminished by phosphonate residues using TPMP as a coating agent. The primary distribution of SiO₂-FITC administered to the lung was mirrored by local changes of PI, PG, PS and TAG as measured for the first time by MALDI-MS and confirmed by FT-IR spectroscopy. Importantly, phosphonate coated SiO₂-P evoked no such changes in local PLC pattern. Together the findings suggest that changes in the (phospho)lipid composition were secondary to local inflammatory processes.

Effects of phosphonate coating on bioactivity of SiO₂

The cytotoxic, membrane disrupting and/or haemolytic potential of amorphous SiO₂ has been attributed to silanol groups at the particle surface [7–9,28]. Pandurangi *et al.* observed a correlation between the concentration of surface silanol groups determined by means of FT-IR spectroscopy and the hemolytic activity of silica particles expressed as enhanced cell lysis of sheep blood erythrocytes [8]. Adverse effects of SiO₂ may therefore be reduced by modifying surface silanol groups, as shown for cristobalite, which lost its cytotoxicity upon heating to 1300 °C, a treatment which condenses silanol groups to siloxane bridges [9]. Cytotoxic and inflammatory effects of silica may also be suppressed by coating with hydrophobic substances [29], poly(vinylpyridine N-oxide) [30], or amino groups [12]. As TPMP coating largely reduced cytotoxic and inflammatory properties, phosphonate residues appear well suited to protect cell and tissue components against effects of silanol groups or other types of surface reactivity. Interestingly, a reduction of particle reactivity *in vitro* and *in vivo* has also been achieved for NP composed of rare earth elements [32] or of partially soluble metals such as Ni, Co, and Cu [31] using ethylenediamine tetra(methylene phosphonic acid) (EDTMP) as a coating agent. However, EDTMP can chelate metal ions released from NP surface [31] and this mode of action may underlie the beneficiary effect of EDTMP, which therefore differs from that of TPMP. Nevertheless, the outwardly directed phosphonate residues of both, EDTMP and TPMP, seem to confer a high degree of biocompatibility to NPs.

In contrast to the lowering of cytotoxicity of SiO₂ NP upon phosphonate coating, SiO₂-P increased the H₂O₂ release from alveolar macrophages if compared to unmodified SiO₂. This finding may be interpreted as an augmentation of hazardous bioactivity and a non-specific stimulation of H₂O₂ generating processes in alveolar macrophages upon exposure to phosphonate residues cannot be excluded (e.g. via NADPH oxidase). However, the effect may rather be due to the lower cytotoxicity of SiO₂-P which permits an undisturbed metabolism and ongoing H₂O₂ production upon SiO₂ NP treatment.

Methodological considerations of MALDI-MS

MALDI-MS is most commonly used for the spatially resolved determination of biomolecules such as lipids and proteins as well as drugs and their metabolites [32–34]. Due to fast laser scan speed and high sensitivity, while covering a broad mass range, MALDI-MS provides high potential for the determination of lipids and has successfully been applied to study the composition of bronchoalveolar lavage fluid [35,36]. In the lung a fairly even distribution of phospholipids has been shown for the lung parenchyma by MALDI-MS, whereas there was a differential overexpression of arachidonate/docosahexaenoate phospholipids and sphingomyelin molecular species lining the profiles of larger bronchioli and blood vessels, respectively [34].

Surprisingly, no information is available on the influence of nanoparticles on the spatial distribution of phospholipids in lung tissue [34]. By weight, ~90% of the lung surfactant consists of lipids, from which phosphatidylcholine (PC) is the major component (70–80%). In addition, variable amounts of phosphatidylglycerols (7–18%), phosphatidylinositols (2–4%), and phosphatidylethanolamines (2–3%) are contained [37]. As the MALDI-MS analyses presented here were conducted in the negative ion mode, acidic phospholipids such as the low abundance PIs and PGs are preferably detected and this is in contrast to PCs, which are rather ionized in positive mode. To properly assign the detected *m/z* to corresponding (phospho)lipid species we first analyzed published MALDI-MS analyses of rat BALF for respective phospholipid classes [34,38,39]. Next, we compared experimental and theoretical *m/z* values from the Metabolomics Workbench Metabolite Database and the LIPID MAPS Structure Database to assign the *m/z* detected during MALDI-MS to distinct phospholipid species. To finally confirm the assignments and deduce the composition of the individual fatty acyl residues, MS/MS experiments were conducted regarding distinct *m/z*. Phospholipid species were identified via characteristic fragment ions. With this strategy phosphatidylglycerols PG (32:0) and PG (34:1) as well as the phosphatidylinositols PI (34:1), PI (36:2), and PI (38:4) were confirmed in the rat lung. It could also be shown by MS/MS experiments (Figure S2) that PG (32:0) is composed of PG (16:0|16:0). This finding is in accord with a previous study on the composition of BALF phospholipids [39], which also suggests that PG (34:1) is composed of a 16:0 and an 18:1 fatty acyl residue. With respect to PI species the same study on BALF composition showed that PI (34:1) is PI (16:0|18:1), and PI (38:4) is PI (18:0|20:4). For PI (36:2) it was found [39] that it is build up from two 18:1 chains. This finding was

also confirmed by MS/MS experiments (Figure S3), which furthermore identified PI as to be composed of (18:0|18:2). In general, PI species with highly unsaturated acyl residues are highly abundant in BALF and, therefore, seem to be characteristic components of the rodent lung surfactant [39].

Although MALDI-MS is a highly reliable technique one should keep in mind that the detection of distinct phospholipid species is not only concentration-dependent, but also a matter of accessibility to ionization. Intensity differences observed for specific ions likely show differences in amounts of lipids within the sample, however, the final estimation is subject to some limitations [40]. More specifically, experimental and theoretical m/z ratios showed a systematic bias ($\Delta = -0.3$ Da) possibly caused by the topographical structure of the cryosection and/or the small height difference of the calibration standard, which had to be pipetted onto the sample target as a small droplet. Notably different starting locations of desorbed ions at the time of acceleration lead to a deviation in the drift time, thus negatively affecting mass resolution. We are aware that all these restrictions make MALDI-MS a semi-quantitative method. Nevertheless, the changes of PI and PG in SiO₂ NP laden areas, which were imaged with MALDI-MS and confirmed by MALDI MS/MS for the first time, are highly plausible and especially the locally observed increases in PI/PG ratio are in accordance with previous particle-elicited changes of PI and PG in BALF of animals treated with crystalline silica [20].

Specific changes of phospholipids in the lung

As outlined above, many amorphous SiO₂ particles and especially crystalline quartz elicit strong inflammation which, in case of quartz, progressively develops into lung fibrosis, accompanied or preceded by an increased PI/PG ratio [20–22,41]. However, the mechanism underlying these changes in lipid composition are not yet clear. It may be assumed that a switchover in the biosynthesis of both phospholipids may occur in alveolar type 2 cells in response to silica which enhances PI synthesis, but suppresses PG synthesis [21]. Further mechanisms may involve an ATP stimulated secretion by type 2 epithelial cells [42] and/or changes of the activity of specific cleaving enzymes such as phospholipase A2 or phospholipase C [25]. Furthermore, phospholipids are differentially taken up by alveolar type 2 cells and/or macrophages with PI being ingested to a lesser extent both *in vitro* and *in vivo* [43,44]. The biological significance of a PI/PG increase for particle-affected lung tissue is still incompletely understood. An increased PI/PG increases the rigidity and lowers the surface activity of the surfactant [24] which might be beneficial e.g. for the repair of local tissue damage. Concerning a possible dampening impact on local inflammation, *in vitro* experiments suggest that elevated concentrations of PI attenuate the non-specific inflammatory reaction via a reduced production of nitric oxide and tumour necrosis factor alpha (TNF- α) from alveolar macrophages [45]. Considering these findings and the fact that SiO₂-FITC NPs were localized in alveolar macrophages but not within alveolar type-2 cells led us to suggest that the locally increased ratio PI/PG originates, at least in part, originates from the population of NP-affected alveolar macrophages. These cells, when sufficiently loaded

with particles, have been shown to release mediators or signalling molecules, which might act on alveolar type-2 cells via specific pathways. This interpretation appears in line with the striking reduction of cytotoxic SiO₂-NP effects on NR8383 macrophages *in vitro* and the abrogation of inflammation *in vivo* upon phosphonate coating (see Figure 1). On the other hand, a local accumulation, e.g. by a binding of lipids and/or surfactant proteins to the large surface of SiO₂ NPs (BET: 200 m²/g) hardly contributes to this effect, because phosphonate coating had neither a major effect on polarity or surface charge of SiO₂ NP, nor had it an influence on the binding of native surfactant, at least under *in vitro* conditions [14]. A role of macrophages or other inflammatory cells such as neutrophilic granulocytes may also be suspected from a work describing dose-dependent changes of PI/PG in BALF from rat lung upon quartz DQ12: In that study PI/PG developed along with the numbers of cells in BALF, the majority of which were macrophages [20,46]. In the present study we found that SiO₂ and SiO₂-FITC but not SiO₂-P led to focal assemblies of macrophages in the lung parenchyma, intermingled with regions of beginning hypercellularity and some structural loss of alveolar septa, as far as this can be stated from hematoxylin-eosin stained cryo-sections (Figure S1). Although the accumulation of SiO₂ NP at these sites cannot clearly be stated and demands further study, it appears likely that these regions are structural correlates of the patchy areas with increased PI/PG ratio in SiO₂ and SiO₂-FITC treated lungs. Irrespective of the mechanism, it appears clearly from the present study that increases in PI/PG are local events at the site of particle deposition and that they are related to cytotoxic and/or activating effects of NP on alveolar macrophages. The detection of changes in PI/PG with imaging methods is therefore highly useful to detect early changes of lung tissue caused by NP. Apart from the changes in phospholipids there was a decrease in TAG in regions where SiO₂-FITC was accumulated. Although the final identification of these TAG species awaits further experiments (e.g. tandem MS and high-energy collision induced dissociation and/or high-resolution mass analysis), their presence is highly likely due to the congruent distribution of the DAG-like derivative *m/z* 605.7 (Figure 5) which are derived from TAG in tissue by cleavage of a fatty acyl residue [27]. The local diminution of TAG concentration may involve its consumption for phospholipid production: TAG is utilized for the formation of dipalmitoyl lecithin, which is the principal lipid in the lung surfactant [47] and which dose-dependently increases in BALF e.g. upon application of quartz to the lung [46]. A lowering of TAG might, therefore, mirror e.g. the new formation of lung surfactant. A decrease of TAG was also found for homogenates of quartz-treated silicotic rat lungs, if values were normalized to the treatment-increased lung weights [47]. As MALDI-MS reports on the concentration of a metabolite in tissue, local decreases of TAG in SiO₂-FITC laden regions are in line with these findings.

Unlike MALDI-MS, with FT-IR imaging methods molecular information is not generated instantaneously, but through the determination of spectral fingerprints, which can be assigned to particular functional groups in the building blocks of biological tissues, such as lipids, proteins, carbohydrates, and nucleic acids. Besides these building blocks, characteristic biochemical markers of disease are

detected and identified. Thus, although FT-IR imaging enables the distinction between healthy and initial-to-advanced states of disease [48], the method has not yet been applied for the examination of nanoparticle-affected lung tissues. Results obtained here appear, however, highly plausible as they showed accumulated lipids, which were confirmed by MALDI-MS as to be mainly related to PI and PG. Furthermore FT-IR spectroscopy revealed a local decrease in protein. Other infrared spectroscopic studies similarly demonstrated an increase in the overall lipid concentration accompanied by a decrease in protein concentration and suggested these changes as suitable markers for cytotoxic [49] or apoptotic changes in cells [50,51]. With respect to the whole lung, an increase in total phospholipid lung content was observed several days after administration of SiO₂ [52], and this effect may involve a transport of *de novo* formed lipids from liver to lung [47]. As a whole, the locally enhanced lung lipid content in SiO₂-NP laden areas observed here by means of FT-IR analysis appears to be in line with older results. Application of FT-IR spectroscopy therefore may become important in the field of lung toxicology and histology [53].

CONCLUSIONS

In this study, laterally resolved information on changes in phospholipid and distribution upon SiO₂ nanoparticles instilled into the rat lung were demonstrated for the first time by utilizing two powerful bioimaging techniques. MALDI-MS analysis of rat lung tissue sections revealed a local overexpression of PIs and, to a lesser extent, PGs. The pattern of changes was largely congruent with the distribution pattern of SiO₂-FITC in the lung tissue. FT-IR analyses of a neighboring cryosections combined with a subsequent hierarchical cluster analysis revealed regions representing enhanced lipid content, which corresponded invariably with the PI pattern. Notably, these observations were true only for FITC-coated and pristine nanoparticles, but not for phosphonated, i.e. TPMP-coated, NPs. This disparity was in excellent accordance with *in vitro* and *in vivo* toxicity studies confirming a TPMP-mediated abrogation in SiO₂ NP induced cytotoxicity and lung inflammation. As the binding of major surfactant lipids to SiO₂ and SiO₂-P is virtually equal [14,54], we conclude that the locally increased PI/PG ratio is primarily due to early cytotoxic effects of instilled SiO₂ NPs, which are successfully masked in the phosphonated form.

In sum, bioimaging revealed spatially resolved tissue remodeling of nanoparticle-affected tissue. The results show that changes in phospholipid composition depend on particle surface coating and are related to the particle distribution in the tissue. Therefore, the complementary use of MALDI-MS and FT-IR imaging is assumed to hold a great potential for the examination of health and disease states in biological tissue samples.

MATERIALS AND METHODS

Nanoparticle characterization

Colloidal SiO₂ NPs, the TPMP-treated modification thereof, and fluorescein isothiocyanate-labeled SiO₂ NPs were provided by project partners of the NanoGEM project and have been extensively characterized before [13,54]. Additionally, particle suspensions were investigated with a NanoSight instrument (LM-10, Malvern Instruments Ltd, Worcestershire, UK), equipped with a LM14 laser device (535 nm) and NTA software 2.1 to 2.3. All data are summarized in Table 1. The particles showed a similar size under conditions of *in vitro* (serum-free F-12K medium and KRPG buffer) and *in vivo* testing.

Table 1. Particle characterization and properties under study conditions.

	SiO ₂	SiO ₂ -FITC	SiO ₂ -P
Primary particle size (TEM)	5–50 nm	23–30 nm	5–50 nm
Average size (AUC)	19 nm	25 nm	19 nm
Zeta potential, pH 7.4	–39 mV	–39 mV	–42.9 mV
BET surface	200 m ² ·g ⁻¹	178 m ² ·g ⁻¹	200 m ² ·g ⁻¹
Crystallinity (XRD)	amorphous	amorphous	amorphous
Morphology	mostly spherical	mostly spherical	mostly spherical
Surface chemistry in XPS	O: 66 at.% Si: 29 at.% C: 4 at.% Na: 1 at.%	O: 63 at.% Si: 29 at.% C: 8 at.%	O: 66 at.% Si: 29 at.% C: 5 at.% Na: 0.5 at.% PO ₂ , PO ₃ : 0.5 at.%
pH of stock suspension	10.2	8.7	10.8
d ₅₀ in H ₂ O (NTA)	47.5±0.7 nm	n.m.	64.5±10.6 nm
d ₅₀ in KRPG buffer (NTA)	65.3±7.5 nm	n.m.	60.7±7.8 nm
d ₅₀ in F-12K medium (NTA)	73.3±14 nm	n.m.	59.3±8.1 nm
d ₅₀ in instillation fluid (NTA)	61.5±7.8 nm	51.0±4.2 nm	50.0±17.0 nm

TEM: Transmission electron microscopy; AUC: analytical ultracentrifugation; XRD: X-ray diffraction, XPS: X-ray photoelectron spectroscopy; NTA: NanoSight tracking analysis, KRPG= Krebs-Ringer phosphate glucose, d₅₀: median diameter, n.m.: not measured

In vitro toxicity study

The rat alveolar macrophage cell line NR8383 was cultured in 175 cm² culture flasks in F-12K medium (Biochrom GmbH, Berlin, Germany) supplemented with 15% heat inactivated standardized fetal calf serum at 37°C and 5% CO₂. Cell culture testing of SiO₂ NPs was carried out as described by Wiemann *et al.*[55]. In brief, NR8383 alveolar macrophages were incubated with ascending concentrations of particles in F-12K medium under serum-free conditions. Assays were run in triplicates in 96-well plates (with 3x10⁵ cells per well) and 3 independent experiments were conducted. Untreated cells were used as negative controls. Macrophage supernatants were analysed for typical signs of inflammation indicated by the release of lactate dehydrogenase, glucuronidase, and TNF- α 16 h after addition of the particles. LDH and Glu activities were expressed as % of the positive control value, which was obtained by adding 0.1% Triton X-100. The concentration of TNF- α was measured using 50 μ L of the supernatant from each well for inducing apoptosis in L-929 fibroblasts in the presence of actinomycin D and expressed as % killing activity. To measure the release of H₂O₂, cells and particles were prepared in Krebs-Ringer phosphate glucose (KRPBG) buffer. Quantitative measurements were carried out in the presence of horseradish peroxidase using resorufin as a detection reagent, which was added for 90 min during application of the particles. In all assays cell-free controls were run in parallel to test for particle interferences with the assays.

Animal study

Female rats (Wistar strain WU, 200–250 g, Charles River Laboratories, Sulzfeld, Germany) were maintained with a 12 h lights-on lights-off cycle with food and water being provided *ad libitum*. Animals were housed at least 14 d before the experiments were commenced. All animal experiments were ethically approved by local authorities (LANUV, Dortmund, Germany) and were carried out in the animal facility at the University Clinics of Essen, Germany.

Instillation fluid was prepared using a sterile mixture of 0.9% NaCl (9 parts by volume) and sodium buffered phosphate buffer, pH 7.3 (one part by volume). Phosphate concentration was 1 mmol·L⁻¹ and maintained a pH of the instillation fluid in the physiologic range. SiO₂, SiO₂-P and SiO₂-FITC particles were diluted from respective stock solutions to a final concentration of 0.72 mg·mL⁻¹. Particle-free instillation fluid was used as a vehicle control. For intratracheal instillation, rats were briefly anaesthetized with isoflurane. A total amount of 0.36 mg in 500 μ L instillation fluid was intratracheally instilled per animal using a Penn Century Microsprayer inserted into the trachea under visual control. This mass of particles was considered equivalent to the lung burden obtained for SiO₂ upon short term inhalation conditions[13]. After 3 d rats were deeply anaesthetized with a mixture of ketamine and xylazine and sacrificed by bleeding from the *Aorta descendens*. A cannula was inserted into the trachea and, while the left bronchus was transiently closed with a Diefenbach clamp, the right lung was lavaged five times with 3 mL, yielding a total of approx. 14 mL BALF per animal for further

analyses. Then the right bronchus was clamped and the left lung was inflated with 3 mL Cryomatrix (Thermo Shandon Ltd., Runcorn, UK). The left lung was then resected, snap frozen in liquid nitrogen, and stored at -80°C until further processing.

BALF analysis

Cells from pooled BALF preparations were collected at the bottom of a centrifuge vial (200 x g, 4 C, 10 min). The supernatant was centrifuged again and the final supernatant was used for protein determination according to the Lowry method[56]. Final numbers of cells were determined with a coulter counter (model Z2, Beckman Coulter GmbH, Krefeld, Germany) and the proportion of dead cells was determined by trypan blue testing. Differential cell counting was carried out with cytopspin preparations stained with May-Grünwald or Giemsa dyes. At least 400 cells per animal were evaluated under the light microscope.

Preparation of lung tissue for fluorescence microscopy

Transverse sections were cut from the hilar region of the left lung with a cryomicrotome (Microtome Cryostatsat HM 500, MICROM International GmbH, Walldorf, Germany). 7 μm thick sections were dried onto glass slides and stored under a nitrogen atmosphere at -20°C until further processing. To visualize the distribution of fluorescent SiO_2 -FITC NPs, sections were taken from the freezer, fixed with 4% buffered formaldehyde, rinsed thoroughly in phosphate buffered saline (PBS), and covered with a coverslip using Roti-Mount FluorCare (Carl Roth, Karlsruhe, Germany) to stain cell nuclei with the contained 4',6-diamidin-2-phenylindol (DAPI). Sections were viewed with an inverted fluorescence microscope (Olympus IX51, Olympus Deutschland GmbH, Hamburg, Germany), equipped with a 20x objective and conventional filter sets for DAPI and FITC. In some cases, an antibody labeling of CD68-positive alveolar macrophages was performed as described by Silge *et al.*[57]. Images were taken with a charge-coupled device camera connected to a Nikon Lucia system.

Sample preparation for bioimaging

Cryosections (8 and 10 μm thick) were prepared as described above. The sections were thaw-mounted on indium tin oxide coated glass slides (for MALDI-MSI) and calcium fluoride targets (for FT-IR imaging), respectively. Prior to MALDI-MSI analysis, frozen tissue sections were allowed to equilibrate to room temperature in a desiccator for ≥ 2 h. Samples were subsequently washed by submerging the glass slides in 50 mM ammonium acetate buffer (pH 6.7, 4 C) 4 times, 5 s each, without agitation, to remove the cryo-compound. After each washing step, tissues were dried in a gentle stream of N_2 . After drying the tissues for ≥ 15 min under vacuum, matrix deposition was performed using a home-built sublimation apparatus. In a vacuum-sealed and pressure-controlled deposition chamber, 25.5 mg of 2,5-dihydroxybenzoic acid (2,5-DHB, Sigma-Aldrich, St. Louis, MO, USA) were quantitatively vaporized and sublimed onto the tissue at 155°C and 4.7 Pa forming a

homogenous layer ($0.23 \text{ mg} \cdot \text{cm}^{-2}$) of crystals. Before FT-IR imaging the cryosections were thawed in a darkened desiccator for 1 h and subsequently washed three times, 5 s each, in *aqua dest.*, followed by a second drying step in a desiccator. As FT-IR imaging provides direct molecular specific information in a non-destructive way, no application of a special matrix is needed.

MALDI-MS

MALDI-MS measurements were performed using a MALDI-TOF/TOF mass spectrometer (ultrafleX-treme, Bruker Daltonics, Bremen, Germany) operated in reflectron mode. MSI data were acquired using flexControl software v3.4 (Bruker Daltonics). The attenuator offset of the laser (smartbeam-II, wavelength 355 nm) was adjusted to 65% and the laser fluence was set to 45%. For lipid analysis, the mass range was set from 440 to 1700 Da with ion suppression for analytes below 340 Da. Imaging data were acquired in the negative ion mode with a lateral resolution of $50 \mu\text{m}$ by summing up 100 shots per array position (without intra-spot rastering) using a laser repetition rate of 1 kHz. The sample originating from the rat instilled with SiO_2 -FITC NPs was subsequently rastered in the positive ion mode. Extraction voltage was set to 17.95 kV and lens voltage to 7.50 kV. Mass spectra were calibrated externally using the cubic enhanced algorithm on singly charged ions of bovine cardiolipin disodium salt (Sigma-Aldrich, St. Louis, MO, USA). Data acquisition and image representation were carried out with flexImaging software v3.0 (Bruker Daltonics). Acquired imaging data were normalized to the total ion current (TIC). Lipid identification was based on the comparison of the experimental with the theoretical m/z values according to the Metabolomics Workbench Metabolite Database and the LIPID MAPS Structure Database (www.metabolomicsworkbench.org and <http://www.lipidmaps.org>, both provided by the University of California, USA).

MS/MS experiments in LIFT mode were performed for selected mass values to confirm structural assignments.

FT-IR imaging and hierarchical cluster analysis

An infrared hyperspectral image of the lung tissue sample after intratracheal instillation of SiO_2 -FITC NPs was acquired using a Bruker Hyperion 3000 FT-IR microscope system equipped with a liquid nitrogen cooled single point mercury cadmium telluride (MCT) detector. Spectra were collected in transmission mode using 15x Cassegrain objectives. The sample was analyzed by automated raster scanning as a tile mosaic image with a spatial resolution of $100 \mu\text{m}$, defined by the aperture and the step size. At every measurement position (area of $100 \times 100 \mu\text{m}^2$), an infrared spectrum consisting of 4 accumulations (scans) was collected. The total measured area was $7.1 \times 6.6 \text{ mm}^2$. All spectra were recorded in the range of 400 to 4000 cm^{-1} with 4 cm^{-1} spectral resolution. A background spectrum was measured on the CaF_2 slide outside the tissue sample. Collected spectra were divided over background and automatically converted into absorbance by OPUS 7.0 software. Further spectral

pre-processing (baseline correction, scaling, and standardization) and multivariate data analysis were performed with ImageLab software (v.1.94, Epina GmbH, Pressbaum, Austria). Baseline correction applied to spectra was based on the Lieber algorithm in 30 iterations through a 3rd order polynomial. Spectral data was scaled between 0 and 1 and standardized (mean=0.0, standard deviation=1.0). Prior to hierarchical cluster analysis, spectra with poor signal-to-noise ratio (areas outside the sample) or those which were expected to exhibit properties significantly differing from the lung tissue under investigation (bronchus, bronchioles and blood vessels) were eliminated. These so-called “bad pixels” were excluded from further statistical evaluation. HCA was performed using Ward’s method, Euclidean distance measure and 13 spectral descriptors consisting of important spectral features (proteins, lipids) for identifying tissue remodeling due to nanoparticle instillation.

Abbreviations

AM: alveolar macrophage

BALF: broncho-alveolar lavage fluid

DAG: diacylglyceride

DAPI: 4',6-diamidin-2-phenylindol

EDTMP: ethylenediamine tetra(methylene phosphonic acid)

FT-IR: Fourier transform infrared (microspectroscopy)

HCA: hierarchical cluster analysis

m/z: mass-to-charge ratio

MALDI-MS: matrix-assisted laser desorption/ionization mass spectrometry

NP: nanoparticle

PG: phosphatidylglycerol

PI: phosphatidylinositol

PLC: phospholipid composition

PMN: polymorphonuclear leukocytes

PS: phosphatidylserine

SiO₂: Silica

SiO₂-FITC: fluorescent SiO₂ (core labelled with fluorescein isothiocyanate)

SiO₂-P: TPMP coated (phosphonated) SiO₂

TAG: triacylglyceride

TPMP: 3-(tri-hydroxysilyl)propyl methyl phosphonate

Declarations

Ethics approval. All animal experiments were ethically approved by local authorities (LANUV, Dortmund, Germany, Accession No. 84-02.04.2022.A157) and were carried out in the animal facility at the University Clinics of Essen, Germany.

Consent for publication. Not applicable

Availability of data and materials. The mass spectrometric datasets generated and/or analyzed during the current study are not publicly available due to high complexity but are available from the corresponding author on reasonable request. Data from the animal study are shown as mean values and individual data are available from the corresponding author on reasonable request.

Competing interests. Authors declare that there are no competing interests.

Funding. This study was sponsored by a grant given to MW and UK by the German Federal Ministry of Education and Research (BMBF, NanoBioDetect, Project No. 03X0146). Parts of this study were supported by the Cells in Motion Cluster of Excellence (CiM – EXC 1003), Münster, Germany (Project No. FF-2013-17) and a train-gain fellowship for a research internship of M.G. at the Technical University of Vienna.

Authors' contributions. M.G. evaluated and interpreted the data and wrote major parts of the manuscript. M.H. performed the MALDI-MS studies evaluated the data, and contributed to the manuscript, A.V. performed the in vitro and vivo studies. A. B. performed FT-IR imaging measurements, K. W. evaluated the FT-IR imaging data. M. S. and B. L. supervised the measurements and contributed to the manuscript, M. M.-D. planned the MALDI-MS experiments and interpreted the data, U. K contributed to the design of the analytical parts of the study and evaluated the data. M. W. initiated and performed the study, conducted the in vivo experiments and wrote parts the manuscript. All authors discussed the results and contributed to the manuscript.

Acknowledgements. The contribution of Andreas Schnapp to evaluation of mass spectral data is gratefully acknowledged.

Additional files:

A single file provides supplementary information and contains Figures S1, S2, and S3:

Figure S1: Effect of different SiO₂ NP on lung histology

Figure S2: MALDI-MS/MS spectrum resulting from the fragmentation of precursor *m/z* 721.4.

Figure S3: MALDI-MS/MS spectrum resulting from the fragmentation of precursor *m/z* 861.5.

REFERENCES

1. Napierska D, Thomassen LC, Lison D, Martens JA, Hoet PH. The nanosilica hazard: another variable entity. Part Fibre Toxicol. BioMed Central; 2010;7:39.
2. Arts JHE, Muijser H, Duistermaat E, Junker K, Kuper CF. Five-day inhalation toxicity study of three types of synthetic amorphous silicas in Wistar rats and post-exposure evaluations for up to 3months. Food Chem Toxicol. 2007;45:1856–67.
3. Johnston CJ, Driscoll KE, Finkelstein JN, Baggs R, O'Reilly MA, Carter J, et al. Pulmonary chemokine and mutagenic responses in rats after subchronic inhalation of amorphous and crystalline silica. Toxicol Sci Off J Soc Toxicol. Oxford University Press; 2000;56:405–13.
4. Reuzel PGJ, Bruijntjes JP, Feron VJ, Woutersen RA. Subchronic inhalation toxicity of amorphous silicas and quartz dust in rats. Food Chem Toxicol. Pergamon; 1991;29:341–54.
5. Maser E, Schulz M, Sauer UG, Wiemann M, Ma-Hock L, Wohlleben W, et al. In vitro and in vivo genotoxicity investigations of differently sized amorphous SiO₂ nanomaterials. Mutat Res Toxicol Environ Mutagen. 2015;794:57–74.
6. Fenoglio I, Martra G, Coluccia S, Fubini B. Possible Role of Ascorbic Acid in the Oxidative Damage Induced by Inhaled Crystalline Silica Particles. Chem Res Toxicol. American Chemical Society; 2000;13:971–5.
7. Hemenway DR, Absher MP, Fubini B, Bolis V. What is the Relationship between Hemolytic Potential and Fibrogenicity of Mineral Dusts? Arch Environ Health Int J. Taylor & Francis Group ; 1993;48:343–7.
8. Pandurangi RS, Seehra MS, Razzaboni BL, Bolsaitis P. Surface and bulk infrared modes of crystalline and amorphous silica particles: A study of the relation of surface structure to cytotoxicity of respirable silica. Environ Health Perspect. National Institute of Environmental Health Science; 1990;86:327–36.
9. Fubini B, Zanetti G, Altilia S, Tiozzo R, Lison D, Saffiotti U. Relationship between surface properties and cellular responses to crystalline silica: studies with heat-treated cristobalite. Chem Res Toxicol. 1999;12:737–45.
10. Panas A, Marquardt C, Nalcaci O, Bockhorn H, Baumann W, Paur H-R, et al. Screening of different metal oxide nanoparticles reveals selective toxicity and inflammatory potential of silica nanoparticles in lung epithelial cells and macrophages. Nanotoxicology. Taylor & Francis; 2012;7:259–73.
11. Waters KM, Masiello LM, Zangar RC, Tarasevich BJ, Karin NJ, Quesenberry RD, et al. Macrophage responses to silica nanoparticles are highly conserved across particle sizes. Toxicol Sci Off J Soc Toxicol. Oxford University Press; 2009;107:553–69.
12. Marzaioli V, Aguilar-Pimentel JA, Weichenmeier I, Luxenhofer G, Wiemann M, Landsiedel R, et al. Surface modifications of silica nanoparticles are crucial for their inert versus proinflammatory and immunomodulatory properties. Int J Nanomedicine. 2014;9:2815–32.
13. Landsiedel R, Sauer UG, Ma-Hock L, Schnekenburger J, Wiemann M. Pulmonary toxicity of nanomaterials: a critical comparison of published *in vitro* assays and *in vivo* inhalation or instillation studies. Nanomed. Future Medicine Ltd London, UK ; 2014;9:2557–85.

14. Wohlleben W, Driessen MD, Raesch S, Schaefer UF, Schulze C, Vacano B von, et al. Influence of agglomeration and specific lung lining lipid/protein interaction on short-term inhalation toxicity. *Nanotoxicology*. Taylor & Francis; 2016;10:970–80.
15. Pattle RE. Properties, Function, and Origin of the Alveolar Lining Layer. *Proc R Soc Lond B Biol Sci*. 1958;148.
16. Clements JA. Surface tension of lung extracts. *Exp Biol Med*. SAGE Publications; 1957;95:170–2.
17. Ruge CA, Kirch J, Cañadas O, Schneider M, Perez-Gil J, Schaefer UF, et al. Uptake of nanoparticles by alveolar macrophages is triggered by surfactant protein A. *Nanomedicine Nanotechnol Biol Med*. Elsevier; 2011;7:690–3.
18. Kapralov AA, Feng WH, Amoscato AA, Yanamala N, Balasubramanian K, Winnica DE, et al. Adsorption of Surfactant Lipids by Single-Walled Carbon Nanotubes in Mouse Lung upon Pharyngeal Aspiration. *ACS Nano*. American Chemical Society; 2012;6:4147–56.
19. Stringer B, Kobzik L. Alveolar macrophage uptake of the environmental particulate titanium dioxide: role of surfactant components. *Am J Respir Cell Mol Biol*. American Public Health Association; 1996;14:155–60.
20. Seiler F, Rehn B, Rehn S, Bruch J. Evidence of a no-effect level in silica-induced rat lung mutagenicity but not in fibrogenicity. *Arch Toxicol*. Springer-Verlag; 2001;74:716–9.
21. Adachi H, Hayashi H, Sato H, Dempo K, Akino T. Characterization of phospholipids accumulated in pulmonary-surfactant compartments of rats intratracheally exposed to silica. *Biochem J*. 1989;262:781–6.
22. Rehn B, Seiler F, Rehn S, Bruch J, Maier M. Investigations on the inflammatory and genotoxic lung effects of two types of titanium dioxide: Untreated and surface treated. *Toxicol Appl Pharmacol*. 2003;189:84–95.
23. Thrall RS, Swendsen CL, Shannon TH, Kennedy CA, Frederick DS, Grunze MF, et al. Correlation of Changes in Pulmonary Surfactant Phospholipids with Compliance in Bleomycin-Induced Pulmonary Fibrosis in the Rat. *Am Rev Respir Dis*. American Lung Association; 1987;136:113–8.
24. Girod S, Galabert C, Lecuire A, Zahm JM, Puchelle E. Phospholipid composition and surface-active properties of tracheobronchial secretions from patients with cystic fibrosis and chronic obstructive pulmonary diseases. *Pediatr Pulmonol*. Wiley Subscription Services, Inc., A Wiley Company; 1992;13:22–7.
25. Spyridakis S, Leondaritis G, Nakos G. A specific phospholipase C activity regulates phosphatidylinositol levels in lung surfactant of patients with acute respiratory distress syndrome. *Am J Of*. 2010;42:357–62.
26. Bivas-Benita M, Zwier R, Junginger HE, Borchard G. Non-invasive pulmonary aerosol delivery in mice by the endotracheal route. *Eur J Pharm Biopharm*. 2005;61:214–8.
27. Gidden J, Liyanage R, Durham B, Lay JO. Reducing fragmentation observed in the matrix-assisted laser desorption/ionization time-of-flight mass spectrometric analysis of triacylglycerols in vegetable oils. *Rapid Commun Mass Spectrom*. John Wiley & Sons, Ltd.; 2007;21:1951–7.

28. Fenoglio I, Martra G, Coluccia S, Fubini B. Possible role of ascorbic acid in the oxidative damage induced by inhaled crystalline silica particles. *Chem Res Toxicol*. 2000;13:971–5.
29. Horbett TA, Ratner BD, Schakenraad JM, Schoen FJ. Some background concepts. In: Ratner BD, Hoffmann AS, Schoen FJ, Lemons JE, editors. *Biomater Sci*. New York: Academic Press; 1996.
30. Albrecht C, Knaapen AM, Becker A, Höhr D, Haberzettl P, van Schooten FJ, et al. The crucial role of particle surface reactivity in respirable quartz-induced reactive oxygen/nitrogen species formation and APE/Ref-1 induction in rat lung. *Respir Res*. BioMed Central; 2005;6:129.
31. Cai X, Lee A, Ji Z, Huang C, Chang CH, Wang X, et al. Reduction of pulmonary toxicity of metal oxide nanoparticles by phosphonate-based surface passivation. *Part Fibre Toxicol*. 2017;14:13.
32. Dreisewerd K. Recent methodological advances in MALDI mass spectrometry. *Anal Bioanal Chem*. 2014;406:2261–78.
33. Spengler B. Mass spectrometry imaging of biomolecular information. *Anal Chem*. ACS Publications; 2014;87:64–82.
34. Berry KAZ, Li B, Reynolds SD, Barkley RM, Gijón MA, Hankin JA, et al. MALDI imaging MS of phospholipids in the mouse lung. *J Lipid Res*. 2011;52:1551–60.
35. Schiller J, Hammerschmidt S, Wirtz H, Arnhold J, Arnold K. Lipid analysis of bronchoalveolar lavage fluid (BAL) by MALDI-TOF mass spectrometry and ³¹P NMR spectroscopy. *Chem Phys Lipids*. 2001;112:67–79.
36. Sommerer D, Süß R, Hammerschmidt S, Wirtz H, Arnold K, Schiller J. Analysis of the phospholipid composition of bronchoalveolar lavage (BAL) fluid from man and minipig by MALDI-TOF mass spectrometry in combination with TLC. *J Pharm Biomed Anal*. 2004;35:199–206.
37. Veldhuizen R, Nag K, Orgeig S, Possmayer F. The role of lipids in pulmonary surfactant. *Biochim Biophys Acta*. 1998;1408:90–108.
38. Schiller J, Süß R, Arnhold J, Fuchs B, Leßig J, Müller M, et al. Matrix-assisted laser desorption and ionization time-of-flight (MALDI-TOF) mass spectrometry in lipid and phospholipid research. *Prog Lipid Res*. 2004;43:449–88.
39. Postle AD, Heeley EL, Wilton DC. A comparison of the molecular species compositions of mammalian lung surfactant phospholipids. *Comp Biochem Physiol - Mol Integr Physiol*. 2001;129:65–73.
40. Zemski Berry KA, Hankin JA, Barkley RM, Spraggins JM, Caprioli RM, Murphy RC. MALDI Imaging of Lipid Biochemistry in Tissues by Mass Spectrometry. *Chem Rev*. American Chemical Society; 2011;111:6491–512.
41. Kawada H, Horiuchi T, Shannon JM, Kuroki Y, Voelker DR, Mason RJ. Alveolar Type II Cells, Surfactant Protein A (SP-A), and the Phospholipid Components of Surfactant in Acute Silicosis in the Rat. *Am Rev Respir Dis*. American Lung Association; 1989;140:460–70.
42. Griese M, Gobran LI, Rooney SA. ATP-stimulated inositol phospholipid metabolism and surfactant secretion in rat type II pneumocytes. *Am J Physiol - Lung Cell Mol Physiol*. 1991;260.

43. Hallman M, Epstein BL, Gluck L. Analysis of labeling and clearance of lung surfactant phospholipids in rabbit. Evidence of bidirectional surfactant flux between lamellar bodies and alveolar lavage. *J Clin Invest. American Society for Clinical Investigation*; 1981;68:742–51.
44. Poelma DL, Ju MR, Bakker SC, Zimmermann LJ, Lachmann BF, van Iwaarden JF. A Common Pathway for the Uptake of Surfactant Lipids by Alveolar Cells. *Am J Respir Cell Mol Biol. American Thoracic Society*; 2004;30:751–8.
45. Kuronuma K, Mitsuzawa H, Takeda K, Nishitani C, Chan ED, Kuroki Y, et al. Anionic pulmonary surfactant phospholipids inhibit inflammatory responses from alveolar macrophages and U937 cells by binding the lipopolysaccharide-interacting proteins CD14 and MD-2. *J Biol Chem. American Society for Biochemistry and Molecular Biology*; 2009;284:25488–500.
46. Seiler F, Rehn B, Rehn S, Bruch J. Different toxic, fibrogenic and mutagenic effects of four commercial quartz flours in the rat lung. *Int J Hyg Environ Health*. 2004;207:115–24.
47. Eskelson CD, Stiffel V, Owen JA, Chvapil M. The importance of the liver in normal and silicotic lung-lipid homeostasis. 2. Cholesterol. *Environ Res*. 1979;19:432–41.
48. Naumann D. FT-INFRARED AND FT-RAMAN SPECTROSCOPY IN BIOMEDICAL RESEARCH. *Appl Spectrosc Rev*. 2001;36:239–98.
49. Dakhakhni TH, Raouf GA, Qusti SY. Evaluation of the toxic effect of the herbicide 2, 4-D on rat hepatocytes: an FT-IR spectroscopic study. *Eur Biophys J. Springer Berlin Heidelberg*; 2016;45:311–20.
50. Zelig U, Kapelushnik J, Moreh R, Mordechai S, Nathan I. Diagnosis of Cell Death by Means of Infrared Spectroscopy. *Biophys J*. 2009;97:2107–14.
51. Lamberti A, Sanges C, Arcari P. FT-IR spectromicroscopy of mammalian cell cultures during necrosis and apoptosis induced by drugs. *J Spectrosc*. 2010;24:535–46.
52. Eskelson CD, Stiffel V, Owen JA, Chvapil M. The importance of liver in normal and silicotic lung-lipid homeostasis. 1. Phospholipids. *J Environ Pathol Toxicol Oncol Off Organ Int Soc Environ Toxicol Cancer*. 1985;6:37–46.
53. Lin H, Luo Y, Sun Q, Zhang J, Tuo Y, Zhang Z, et al. Identification of Pulmonary Edema in Forensic Autopsy Cases of Sudden Cardiac Death Using Fourier Transform Infrared Microspectroscopy: A Pilot Study. *Anal Chem*. 2018;90:2708–15.
54. Izak-Nau E, Voetz M. As-produced: intrinsic physico-chemical properties and appropriate characterization tools. In: Wohlleben W, Kuhlbusch TAJ, Schnekenburger J, Lehr C-M, editors. *Saf Nanomater Their Lifecycle Release Expo Hum Hazards*. CRC Press; 2014. p. 3–24.
55. Wiemann M, Vennemann A, Sauer UG, Wiench K, Ma-Hock L, Landsiedel R. Particles causing lung disease. *J Nanobiotechnology. BioMed Central*; 2016;14:16.
56. Lowry OH, Rosenbrough NJ, Farr AL, Randall RJ. Protein measurement with the folin. *J Biol Chem*. 1951;193:265–75.
57. Silge A, Bräutigam K, Bocklitz T, Rösch P. ZrO₂ nanoparticles labeled via a native protein corona: detection by fluorescence microscopy and Raman microspectroscopy in rat lungs. *Analyst*. 2015;140:5120–8.

Supporting information

Phosphonate Coating of SiO₂ Nanoparticles Abrogates Inflammatory Effects and Local Changes of the Lipid Composition in the Rat Lung: A Complementary Bioimaging Study

Mandy Großgarten,¹ Matthias Holzlechner,² Antje Vennemann,³ Anna Balbekova,² Karin Wieland,² Michael Sperling,¹ Bernhard Lendl,² Martina Marchetti-Deschmann,² Uwe Karst,¹ and Martin Wiemann³

¹ University of Münster, Institute of Inorganic and Analytical Chemistry, Corrensstraße 28/30, 48149 Münster, Germany

² TU Wien, Institute of Chemical Technologies and Analytics, Getreidemarkt 9, 1060 Vienna, Austria

³ IBE R&D Institute for Lung Health gGmbH, Mendelstraße 11, 48149 Münster, Germany

Corresponding Author: martin.wiemann@ibe-ms.de

Phone: ++49 251 9802340

Fax: ++49 251 9802349

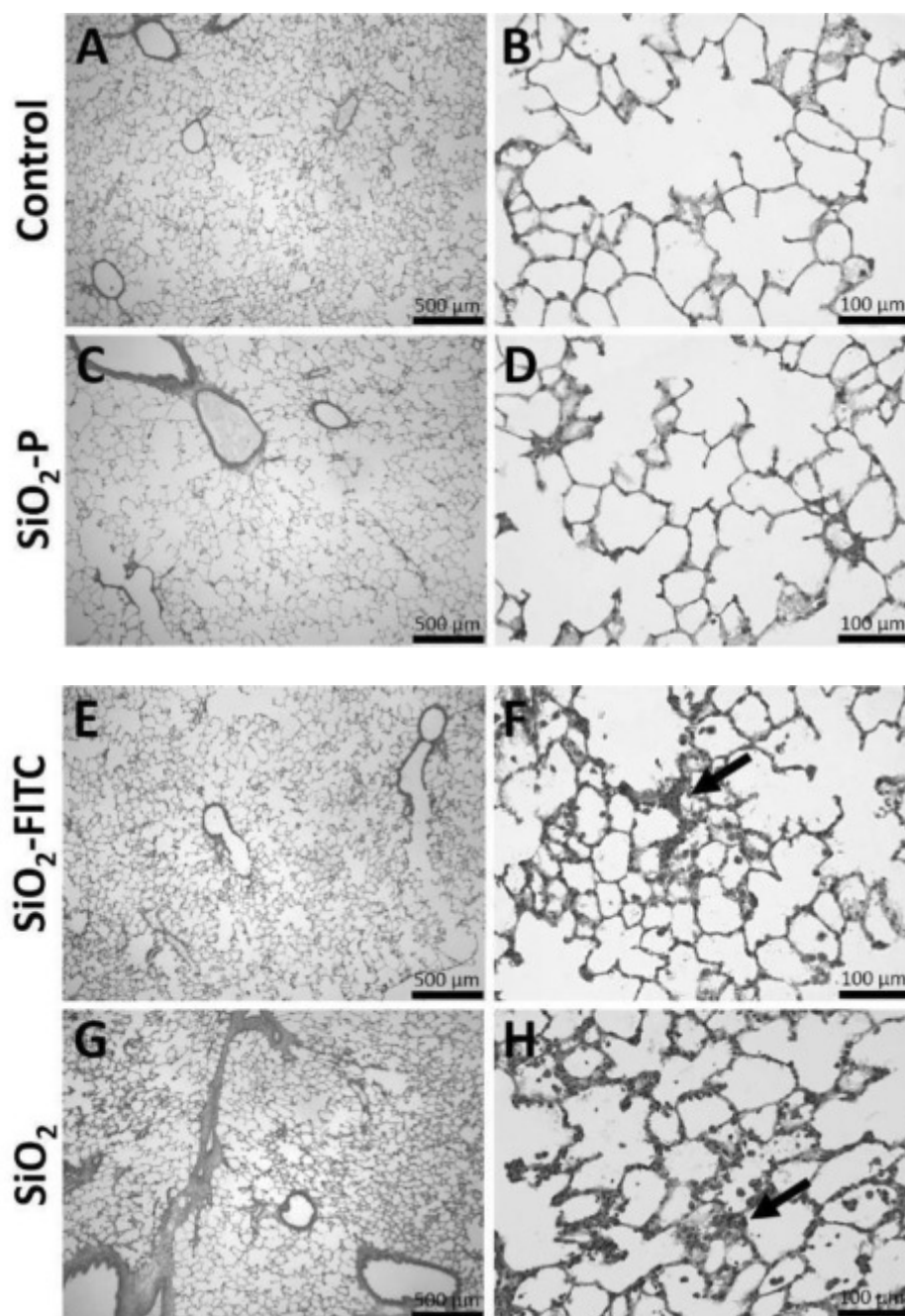


Figure S1. Effect of different SiO₂ NP on lung histology. Typical aspects from lung parenchyma 3 days after intratracheal instillation of 0.5 mL vehicle control fluid (A, B), 0.36 mg SiO₂-P (C, D), 0.36 mg SiO₂-FITC (E, F), or 0.36 mg SiO₂ (G, H). Hematoxylin-eosin stained cryo-sections. Note that SiO₂-FITC (F) and SiO₂ (H) leads to confined regions with increase macrophage numbers, slightly deteriorated septal structures and focal hypercellularity (Arrows in F and H). These changes were largely absent in lungs treated with vehicle control (B) or SiO₂-P (D).

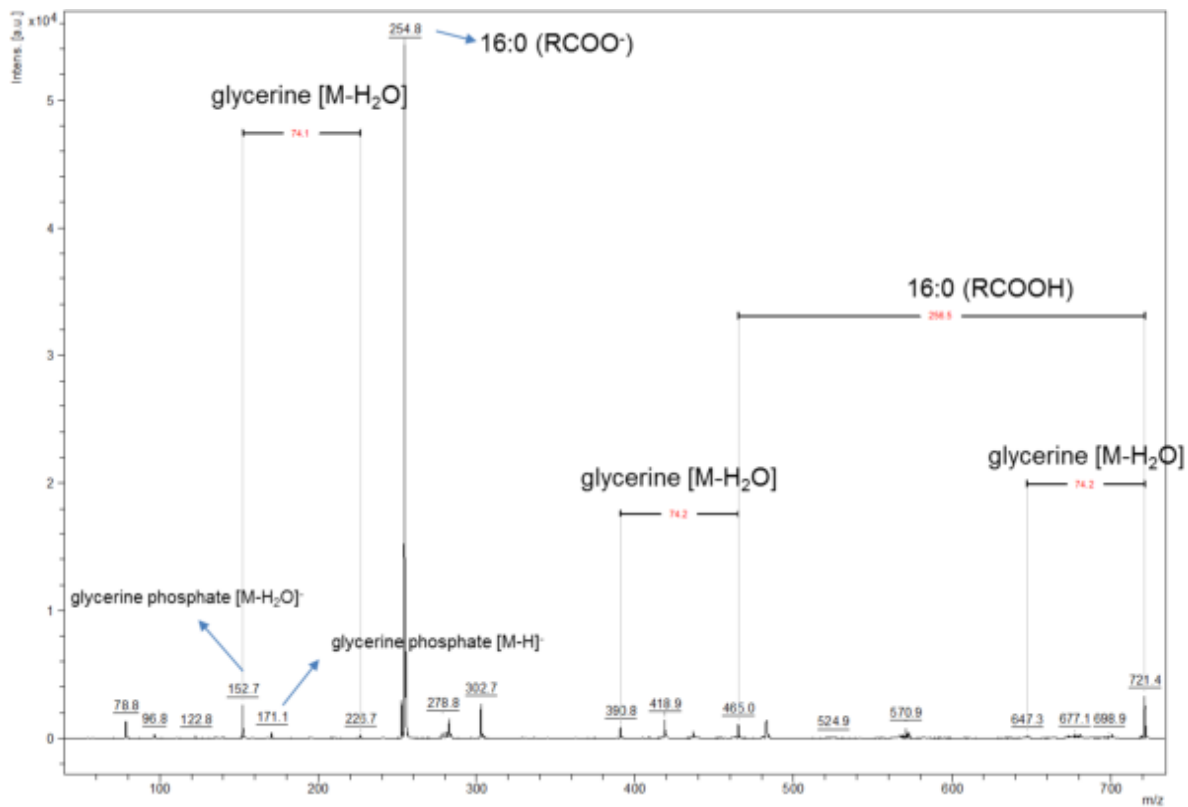


Figure S2. MALDI-MS/MS spectrum resulting from the fragmentation of precursor m/z 721.4. Fragment ions confirm the assignment of the respective MS ion image to PG (32:0) and indicate a fatty acyl composition of two (16:0) chains.

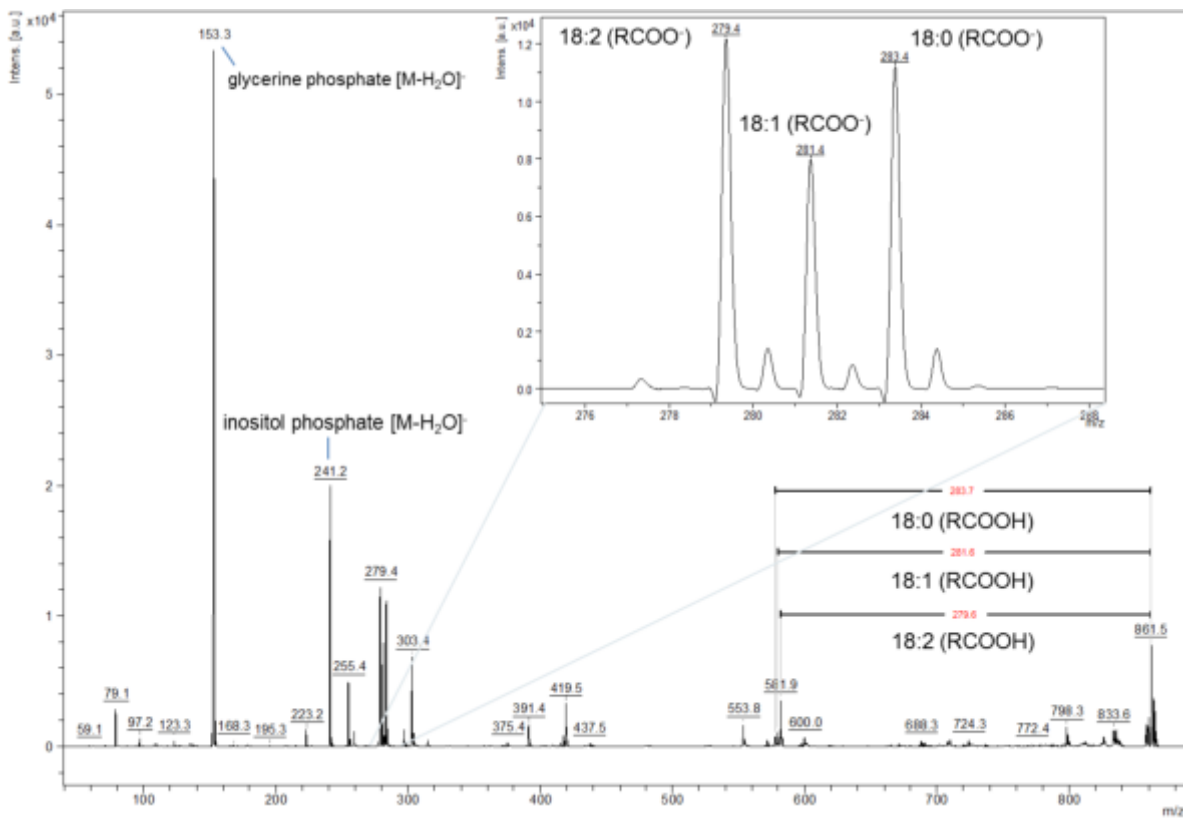


Figure S3. MALDI-MS/MS spectrum resulting from the fragmentation of precursor m/z 861.5. Fragment ions confirm the assignment of the respective MS ion image to PI (36:2), whereby both fatty acyl compositions, PI (18:1|18:1) and PI (18:0|18:2) are deduced.

ABBREVIATIONS

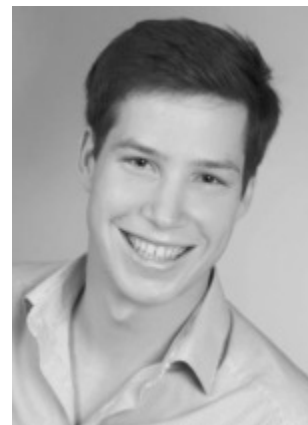
1,5-DAN	1,5-diaminonaphtalene
2,5-DHB	2,5-dihydroxybenzoic acid
9-AA	9-aminoacridine
ACE	acetone
ACN	acetonitrile
AcOH	acetic acid
AmAc	ammonium acetate
BALF	broncho-alveolar lavage fluid
CHCA	alpha-cyano-4-hydroxycinnamic acid
CMC	carboxymethylcellulose
DE	delayed extraction
DESI MS	desorption electrospray ionization mass spectrometry
EtOH	ethanol
FTICR	Fourier transform ion cyclotron resonance
FTIR	Fourier transform infrared
HCA	hierarchical cluster analysis
HRMS	high-resolution mass spectrometry
iPrOH	isopropanol
IS	internal standard
ITO	indium tin oxide
LA-ICP-MS	laser ablation inductively coupled plasma mass spectrometry
LC-MS/MS	liquid chromatography tandem mass spectrometry
LDI	laser desorption/ionization
m/z	mass to charge
MALDI MS	matrix-assisted laser desorption/ionization mass spectrometry
MMI	multi-modal imaging
MPM	malignant pleural mesothelioma
MS/MS	tandem mass spectrometry
MSI	mass spectrometric imaging
Nd:YAG	neodymium-doped yttrium aluminum garnet
Nd:YLF	neodymium-doped yttrium lithium fluoride
NP	nanoparticle
OCT	optimal cutting temperature
oTOF	orthogonal time-of-flight

PC	phosphatidylcholine
PCA	principal component analysis
PE	phosphatidylethanolamine
PI	phosphatidylinositol
PLC	phospholipid composition
qTOF	quadrupole time-of-flight
RDF	random decision forest
RMS	route-mean-square
ROI	region of interest
RSD	relative standard deviation
RTOF	reflectron time-of-flight
S/N	signal to noise
SA	sinapic acid, 3,5-dimethoxy-4-hydroxycinnamic acid
SIMS	secondary ion mass spectrometry
SiO ₂	silica
SM	sphingomyelin
TEC	tissue extinction coefficient
TIC	total ion current
TOF	time-of-flight
TPMP	3-(tri-hydroxysilyl)propyl methyl phosphonate

CURRICULUM VITAE

MATTHIAS HOLZLECHNER

Email: m.holzlechner@gmail.com
www.linkedin.com/in/matthiasholzlechner



EDUCATION

Technische Universität Wien, Vienna, Austria

03/2013 - 05/2018
Doctoral program in Technical Sciences - **TECHNICAL CHEMISTRY** (E 786 800)
PhD (Dr.techn.)
Thesis: *MALDI Mass Spectrometry Imaging – Aspects of Sample Preparation.*
Institute of Chemical Technologies and Analytics

University of Natural Resources and Life Sciences, Vienna, Austria

10/2010 - 03/2013
English Master program **BIOTECHNOLOGY** (H 066 418)
MSc (Dipl.Ing.), *summa cum laude*
Thesis: *General Unknown Screening of Whisky via LC-TOFMS.*
Division of Analytical Chemistry

Bachelor program **FOOD SCIENCE AND BIOTECHNOLOGY** (H 033 217)

10/2006 - 10/2010
BSc (Bakk.techn.)
Thesis: *Synthesis of precursor molecules for L- glycerol - D - mannose and D- glycerol -D- mannose.*
Division of Organic Chemistry

Bundesoberstufenrealgymnasium St. Johann im Pongau, Salzburg, Austria

2006
AHS Matura (Higher School Certificate)

EMPLOYMENT HISTORY

PROJECT ASSISTANT

11/2017 - 06/2018
Medical University of Vienna, Institute of Neurology, Center for Physiology and Pharmacology
Technische Universität Wien, Institute of Chemical Technologies and Analytics, Vienna, Austria

03/2017 - 10/2017
maternity / educational leave

UNIVERSITY ASSISTANT

03/2013 - 03/2017
Technische Universität Wien, Institute of Chemical Technologies and Analytics, Vienna, Austria

PUBLICATIONS, PEER-REVIEWED

M. Holzlechner, K. Strasser, E. Zareva, L. Steinhäuser, H. Birnleitner, A. Beer, M. Bergmann, M. Marchetti-Deschmann. IN SITU CHARACTERIZATION OF TISSUE RESIDENT IMMUNE CELLS BY MALDI MASS SPECTROMETRY IMAGING. *Journal of Proteome Research* (2017), 16(1), 65-76.

M. Holzlechner, S. Reitschmidt, S. Gruber, S. Zeilinger, M. Marchetti-Deschmann. MALDI MASS SPECTROMETRY IMAGING TO VISUALIZE FUNGAL METABOLITES DURING MYCOPARASITIC INTERACTION. *Proteomics* (2016), 16(11-12), 1742-1746.

PUBLICATIONS, SUBMITTED

M. Holzlechner, J. Frank, K. Piplits, T. Luidner, G. Allmaier, M. Marchetti-Deschmann. SUBLIMATION APPARATUS TO PUSH MALDI MS IMAGING BELOW THE CELLULAR LEVEL. Submitted to *Angewandte Chemie, International Edition*.

M. Holzlechner, M. Bonta, H. Lohninger, A. Limbeck, M. Marchetti-Deschmann. MULTI-SENSOR IMAGING – FROM SAMPLE PREPARATION TO INTEGRATED MULTI-MODAL INTERPRETATION OF LA-ICP-MS AND MALDI MS IMAGING DATA. Submitted to *Analytical Chemistry*.

M. Großgarten, **M. Holzlechner**, A. Vennemann, A. Babelkova, K. Wieland, M. Sperling, M. Marchetti-Deschmann, M. Wiemann, U. Karst. PHOSPHONATE COATING OF SiO₂ ABGROGATES INFLAMMATORY EFFECTS AND LOCAL CHANGES OF THE LIPID COMPOSITION IN THE RAT LUNG: A COMPLEMENTARY BIOIMAGING STUDY. Submitted to *Particle Fibre Toxicology*.

CONFERENCE PROCEEDINGS

M. Marchetti-Deschmann, B. Prentice, R. Van de Plas, **M. Holzlechner**, R. Oehler, J. Spraggins, R. Caprioli. HIGH PERFORMANCE IMAGING MS AND DATA-DRIVEN IMAGE FUSION TO CHARACTERIZE COLON STRUCTURES AND IMMUNE CELL IN. Poster: Proceedings of the 65th American Society of Mass Spectrometry Conference, Indianapolis, US; 04.06.2017 - 08.06.2017; in: "*Proceedings of the 65th American Society of Mass Spectrometry Conference*", (2017).

CONFERENCE CONTRIBUTIONS

S. Fröhlich, **M. Holzlechner**, J. Galehr, P. Rigger, M. Marchetti-Deschmann. MASS SPECTROMETRY BEYOND PROTEOMICS - MASS SPECTROMETRY IMAGING CORRELATES MATERIAL FAILURE WITH BIOMOLECULES. Talk: Institutseminar Analytische Chemie, Universität Wien; 23.10.2014.

M. Holzlechner, J. Frank, G. Allmaier, M. Marchetti-Deschmann. IMPROVED SPATIAL RESOLUTION IN MALDI MSI BY USING HIGHLY REPRODUCIBLE MATRIX SUBLIMATION. Talk: 27th Mass Spec Forum Vienna, Wien; 23.02.2016 - 24.02.2016.

M. Holzlechner, S. Reitschmidt, S. Gruber, S. Zeilinger-Migsich, M. Marchetti-Deschmann. VISUALIZING FUNGAL METABOLITES DURING MYCOPARASITIC INTERACTION BY MALDI MSI. Talk: 28th Mass Spec Forum Vienna, Vienna, Austria; 16.02.2017 - 17.02.2017.

M. Holzlechner, K. Strasser, R. Oehler, G. Allmaier, M. Marchetti-Deschmann. IMPROVED SPATIAL RESOLUTION IN MALDI MSI FOR LIPIDS, PEPTIDES AND PROTEINS BY USING HIGHLY REPRODUCIBLE MATRIX SUBLIMATION. Poster: OurCon III, Pisa, Italy; 27.10.2015 - 29.10.2015.

M. Holzlechner, K. Strasser, E. Zareva, L. Steinhäuser, H. Birnleitner, A. Beer, M. Bergmann, R. Oehler, M. Marchetti-Deschmann. "IMMUNE CELL CHARACTERIZATION AND IN SITU LOCALIZATION BY INTACT CELL MASS SPECTROMETRY AND MASS SPECTROMETRY IMAGING"; Talk: 10th Central and Eastern European Proteomic Conference, Budapest, H; 11.10.2016 - 14.10.2016.

M. Holzlechner, S. Theiner, S. Van Malderen, T. Van Acker, A. Legin, K. Keppler, F. Vanhaecke, G. Koellensperger, M. Marchetti-Deschmann. MULTIPLE MODES & SENSORS: POSITIVE/NEGATIVE ION MODE MALDI-TOF AND LA-ICP MS IMAGING OF TUMOR SPHEROIDS AND MESOTHELIOMA SAMPLES. Keynote Speaker: OurCon V, Doorn, NL; 25.09.2017 - 28.09.2017.

M. Holzlechner, S. Zoratto, S. Reitschmidt, S. Zeilinger-Migsich, M. Marchetti-Deschmann. MASS SPECTROMETRY IMAGING TO BETTER UNDERSTAND THE MYCOPARASITIC INTERACTION OF BIOCONTROL AGENTS. Poster: Proceedings of the 64th American Society of Mass Spectrometry Conference, San Antonio, Texas, United States; 05.06.2016 - 09.06.2016.

M. Marchetti-Deschmann, R. van de Plas, **M. Holzlechner**, K. Strasser, R. Oehler, J. Spraggins, R. Caprioli. HIGH MASS AND SPATIAL RESOLUTION IMAGING MS TO CHARACTERIZE COLON STRUCTURES AND IMMUNE CELL INFILTRATES ON THE PROTEIN LEVEL. Talk: 28th Mass Spec Forum Vienna, Vienna, Austria (invited); 16.02.2017 - 17.02.2017.

S. Reitschmidt, S. Zoratto, **M. Holzlechner**, M. Hartmanova, K. Lemr, G. Allmaier, M. Marchetti-Deschmann. STUDYING FUNGAL SURFACE CHANGES AND CHEMICAL COMMUNICATION DURING HOST-PATHOGEN INTERACTION. Poster: OurCon III, Pisa, Italy; 27.10.2015 - 29.10.2015.

K. Strasser, E. Zareva, **M. Holzlechner**, H. Birnleitner, M. Marchetti-Deschmann, R. Oehler. WHOLE-CELL MALDI-TOF MASS SPECTROMETRY AS A RAPID METHOD FOR LEUKOCYTE SUBTYPING. Poster: 4th European Congress of Immunology Vienna 2015, Wien; 06.09.2015 - 09.09.2015.